DOE-ER-0313/33
Distribution
Categories
UC-423, -424

FUSION MATERIALS
SEMIANNUAL PROGRESS REPORT
FOR THE PERIOD ENDING
December 31, 2002

Prepared for
DOE Office of Fusion Energy Sciences
(AT 60 20 10 0)

DATE PUBLISHED: MARCH 2003

Prepared for
OAK RIDGE NATIONAL LABORATORY
Oak Ridge, Tennessee 37831
Managed by
U.T.-Battelle, LLC
For the
U.S. DEPARTMENT OF ENERGY

FOREWORD

This is the thirty-third in a series of semiannual technical progress reports on fusion materials science activities supported by the Fusion Energy Sciences Program of the U.S. Department of Energy. This report focuses on research addressing the effects on materials properties and performance from exposure to the neutronic, thermal, and chemical environments anticipated in the chambers of fusion experiments and energy systems. This research is a major element of the national effort to establish the materials knowledge base of an economically and environmentally attractive fusion energy source. Research activities on issues related to the interaction of materials with plasmas are reported separately.

The results reported are the product of a national effort involving a number of national laboratories and universities. A large fraction of this work, particularly in relation to fission reactor irradiations, is carried out collaboratively with partners in Japan, Russia, and the European Union. The purpose of this series of reports is to provide a working technical record for the use of program participants, and to provide a means of communicating the efforts of fusion materials scientists to the broader fusion community, both nationally and worldwide.

This report has been compiled and edited under the guidance of Ron Klueh and Renetta Godfrey, Oak Ridge National Laboratory. Their efforts, and the efforts of the many persons who made technical contributions, are gratefully acknowledged.

S. E. Berk
Facilities and Enabling Technologies Division
Office of Fusion Energy Sciences

TABLE OF CONTENTS

1.0 VANADIUM ALLOYS

STRONGLY NON-ARRHENIUS INTERSTITIAL DIFFUSION IN VANADIUM – S. Han, R. Car, and D. J. Srolovitz (Princeton University), L. A. Zepeda-Ruiz (LLNL),

OBJECTIVE

Self-interstitial atoms (SIA), produced in the irradiation of metals, are key components of the micro-structural evolution of the material. The microstructural evolution of the irradiated material is largely determined by the migration, clustering, and annihilation of the SIAs. The objective of this research is to study self-diffusion via SIA migration in pure vanadium through a multiscale computational study.

SUMMARY

We perform molecular dynamics simulation to study the diffusion of SIAs in vanadium. The interatomic potentials employed were developed by fitting to first-principle, quantum mechanical results on SIA structure and energetics. The present results demonstrate that the SIA in vanadium exists in a <111>-dumbbell configuration and migrates along <111> directions, in agreement with first-principles calculations. At low and intermediate T, the diffusion is one-dimensional, but at higher temperatures, the dumbbell can rotate into other <111> directions, resulting in three-dimensional at high T. The apparent activation energy for migration increases with temperature as a result of a complex correlation effect even at temperatures before significant dumbbell reorientation occurs.

INTRODUCTION

Vanadium alloys are important candidate materials for future fusion reactors. Although it is the evolution of point defect distribution that determine the ultimate lifetime of these materials, there have been very few reliable experimental or theoretical studies of the fundamental point defect properties in vanadium. Earlier experiments have shown that SIA diffusion occurs down to temperatures as low as~4K with a migration energy of less than 0.01 eV. Extensive computer simulation studies of radiation damage in other metals have been performed. For example, simulations of bcc Fe have shown that SIAs and SIA clusters (small, perfect dislocation loops) are created along close-packed directions and tend to migrate along specific crystallographic directions. In these materials, the SIAs lie in <110> directions but rotate into the <111> in order to migrate. The resulting diffusion occurs via migration in a <111> direction, relaxation into a stable <110> orientation and then rotation into another <111> directions; this yields a 3D random walk diffusional trajectory with an Arrhenius temperature dependence with a very low activation energy, usually ~0.1 eV. Simulation studies of SIA migration have also been performed for V. These show that SIA migration in V is very similar to that in Fe. Unfortunately, these are not consistent with our own first principles calculations, which clearly demonstrate that the stable SIA structure in V is a <111> oriented dumbbell, rather than the <110> oriented dumbbell in Fe. Given this fundamental discrepancy, we are forced to conclude that SIA migration in Fe and V are fundamentally different and SIA diffusion in V is poorly understtod. Therefore, we have undertaken a study of SIA migration in V using our new interatomic potential, which is designed to ensure consistency with the first principles calculations.

COMPUTATIONAL METHOD

The diffusion of individual SIAs in vanadium was investigated using the molecular dynamics (MD) simulation code MDCASK using a new parameterization of a Finnis-Sinclair/EAM potential for vanadium. The reparameterization was performed in order to ensure that the point defect properties were consistent with the predictions of our first-principles calculations that suggest that the most stable SIA is a <111>-dumbbell, which is nearly degenerate with the crowdion configuration. The resultant potential has been extensively tested and successfully used to calculate static point-defect properties in vanadium.

All simulations were performed with a cubic system of 16000 + 1 mobile atoms ($20a_0$x$20a_0$x$20a_0$ computational cell; a_0=3.03Å), with periodic boundary conditions. Simulations were run at temperatures between 100 and 1600 K. The SIA was introduced in the form of a stable <111>-dumbbell followed by a

10 ps equilibration run using a constant temperature ensemble (N,V,T). The simulation was then switched to a microcanonical ensemble (N, V,E) in order to study the SIA migration dynamics. Because of the highly correlated nature of interstitial diffusion, long runs (1 ns) were required to ensure that the reliable diffusivites could be extracted. numerical convergence.

In order to calculate diffusivities, we followed the procedure employed by Guinan *et al*. The total run time is partitioned in *m* intervals of equal duration time τ, and within each the average interstitial positions and orientations determined at intervals $\Delta\tau$. The latter is chosen to ensure that the individual measurements were uncorrelated. This procedure allows us to calculate *D* as the average of all D_i calculated in each segment as

$$D = \frac{1}{m}\sum_{i=1}^{m} D_i$$
$$= \frac{1}{m}\sum_{i=1}^{m} \frac{\langle R^2 \rangle}{2d\tau_i}$$

where $\langle R^2 \rangle$ is the mean squared distance from beginning to end of a trajectory over the time period τ and *d* is the dimensionality of the diffusion path (1D or 3D). In order to assure consistency of the procedure, τ was varied from 5 to 100 ps with $\Delta\tau$ = 1ps. The activation energy and pre-exponential for the diffusivity were obtained via least square fits to the logarithm of the diffusivity vs. 1/*T*.

RESULTS

In order to investigate the migration mechanism of SIA in V, we first analyzed the interstitial trajectories as a function of temperature. Representative trajectories of the SIA center of mass are shown in Figure 1.

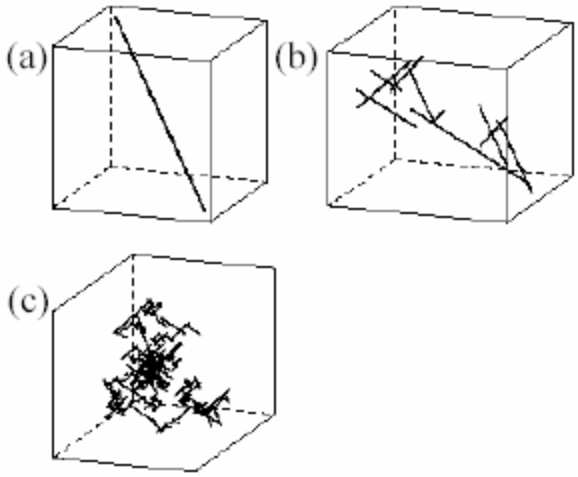

Figure 1: Typical trajectories of migrating SIAs at three different temperatures: (a) T = 100K, (b) T = 700K, and (c) T = 1300K.

We analyzed each trajectory to determine the migration mechanism and type of interstitial. For each temperature, more than 1000 jumps were observed. The interstitial migration mechanism was found to be temperature dependent. For low and intermediate temperatures (100-600 K) the SIA executes an essentially 1D random walk along a <111>-direction, as shown in Fig. 1(a). As temperature increases to T~700K, the SIA begins to make infrequent rotations from one <111>- to a different <111>-direction (passing through a <110>-dumbbell configuration). This results in a 3D trajectory that consists of long 1D

random walk segments with abrupt reorientations, as seen in Fig. 1(b). At very high temperatures, the rotation events become very frequent, such that the SIA is performing a truly 3D random walk (as shown in Fig. 1(c)). Although these results are similar to those reported for other bcc metals (i.e., Fe and Mo), it is fundamentally different. This difference is associated with the stable form of the interstitial - <111>-dumbbell in V and <110>-dumbbell in Fe and Mo. In the Fe and Mo cases, the reorientation or rotation events were associated with the relaxation of the dumbbells from their migration orientations <111> into their stable orientations <110>. Such relaxation events do not occur in the present V case, since the <111>-dumbbell is both the stable and migration form of the SIA. In fact, the <110>-dumbbell orientation corresponds to the saddle point in the V SIA rotation from one <111> orientation to another.

To obtain a more detailed understanding of SIA migration, we monitored the frequency for rotation from one <111>- to any other <111>-direction. Figure 2 shows the rotation frequency vs. $1/k_BT$ for temperatures between 700 and 1600 K (for T < 600K, no rotations were observed).

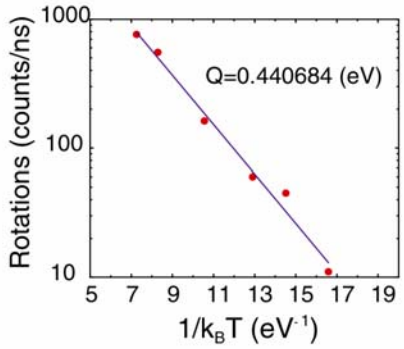

Fig. 2: Arrhenius plot of the SIA rotation frequency.

The logarithm of the rotation frequency is a linear function of the inverse temperature. This suggests that rotation is a thermally activated (Arrhenius) process. The activation energy obtained from Fig. 2, E_m=0.42eV, is consistent with first principles calculations and static calculations using the new interatomic potential which predict a rotational barrier for SIAs in V of 0.35 and 0.4 eV, respectively. The pre-exponential factor obtained from the fit was D_0=1.67x10^{13} rotations/s.

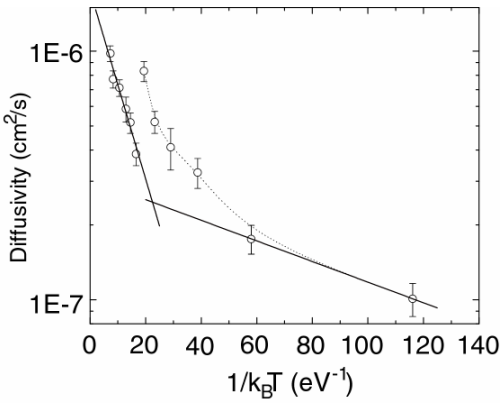

Fig. 3: Arrhenius plot of the SIA diffusion

The diffusivities, *D*, were obtained as described above over a range of temperatures. The results are shown in Fig. 3. Since we observe no rotations below 700K, we assume that the d=1 below 700K and d=3 above 700K. This switch in the value of d used in the determination of D is responsible for the abrupt

drop in D at 700K observed in Fig. 3. The data clearly show that the diffusivity is an Arrhenius function of temperature at high T and at low T, with a continuous transition from a low activation energy at low T to a higher activation energy at elevated T. For low temperatures we obtain D_0=3.0594x10^{-7} cm^2/s and E_m=0.0095 eV. This is in agreement with experimental data that shows that interstitial diffusion in V occurs even at 4 K with a migration energy < 0.01 eV. For high temperatures, we obtained D_0=1.7504x10^{-6} cm^2/s and E_m=0.0872 eV. We observe that at intermediate temperatures (200K < T < 600 K), *D* increases with T. This is interesting because the SIA undergo **NO** rotations during the course of this simulation until T is raised to 700K or above.

DISCUSSION AND CONCLUSION

The presence of a nonlinear regime in the Arrhenius diagram for temperatures between 200 and 600 K is surprising. As discussed above, previous studies of SIA migration in bcc metals showed that SIA migration is a multiple step process that involves not only translation of <111>-oriented dumbbells along a <111>-direction, but also rotations from the stable <110>- to <111>-oriented dumbbells. One could argue that the non-linearity observed in Fig. 3 is a result of the competition (over a certain temperature regime) of these thermally activated processes. But this is clearly not the situation in the case of V. As shown in Fig. 2 no changes in <111>-dumbbell orientation were observed for T< 700 K, *i.e.* SIA migration was purely 1D. Furthermore, analysis of atomic coordinates showed that in this temperature regime, the SIA exists only in a <111>-oriented dumbbell with only small angular deviations (these can be substantial at T~600 K. These deviations are consistent with first-principles results which show that the <111>-dumbbell configuration is stable relative to other dumbbell orientations, but the dumbbell energy varies slowly with misorientation around the <111>-orientation.

Since we have demonstrated that the transition from 1D to 3D diffusion is not responsible for the change in the apparent activation energy for SIA diffusion in V, we must look for another explanation. This can be found in the correlation factor for diffusion. Detailed examination of the SIA trajectories in V shows that SIA hops are correlated. At low temperature, the SIA has a higher probability of jumping back in the direction from whence it came, rather than forward along the same trajectory. We quantified this observation by measuring a correlation factor for SIA diffusion ψ, defined as

$$\psi = \frac{1}{m}\sum_{i=1}^{m}\sigma_i\sigma_{i+1}$$

where σ_i=1 if the SIA moves to the “left” and σ_i=-1 if the SIA moves in towards the “right”. In this way, a value of ψ=1 would mean that the SIA executed *m* jumps all in the same direction, a value of ψ=-1 would mean that the SIA jumps in the opposite direction than its previous jump, and a value of ψ=0 implies an uncorrelated random walk. A plot of ψ as a function of temperature is shown in Fig. 4.

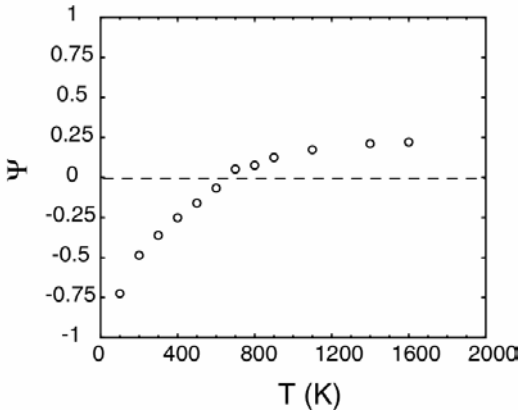

Fig. 4: Correlation factor versus temperature.

From this, we observe that at low T the SIA tends to jump back in the direction from whence it came, while at high T the random walk is more nearly perfect. At high T, there is a slight tendency for the hops to continue in the same direction (e.g.,, a small number of multiple site hops). At low T the SIA has very little thermal energy and hence tends to "bounce off" the next atom and return to its previous position while at high T the higher thermal energy gives rise to a 1D collision cascade. Thus, the non-Arrhenius behavior is not from competing thermally activated events as reported in Fe or Mo, but rather from a temperature-dependent correlation factor.

FABRICATION OF CREEP TUBING FROM THE US AND NIFS HEATS OF V-4Cr-4Ti – A.F. Rowcliffe, (Oak Ridge National Laboratory), W.R. Johnson (Rocket Science & Materials Engineering Services), D.T. Hoelzer (Oak Ridge National Laboratory)

OBJECTIVE

Utilize commercial–scale processing to fabricate small-diameter, thin-wall tubing from plate stock of V-4Cr-4Ti for both the US program heat no.832665 and the NIFS –HEAT-2 and produce sufficient tubing to meet foreseeable programmatic needs for investigating creep behavior in both lithium and vacuum environments and for carrying out irradiation creep measurements

SUMMARY

Commercial-scale fabrication of thin-walled tubing for thermal and irradiation creep testing of V4Cr-4Ti has been initiated at Century Tubes Inc, San Diego. In an effort to minimize the occurrence of the surface flaws and cracks which characterized the previous batch of tubing, the technical specifications have been extensively modified. In particular improvements have been made in the cleaning procedures and in the control of the vacuum during all stages of the annealing cycle; the levels of cold work applied during the final stages have been substantially reduced. Both the US program heat and the Japanese NIFS-HEAT-2 are being processed; interim examination shows significant increases in oxygen content for both heats in spite of the added precautions introduced. Surface defects similar to those observed in the previous batch of tubing were detected in one section of tubing from the US heat after 4 draw cycles while the NIFS heat was relatively free of surface defects.

PROGRESS AND STATUS

Introduction

The pressurized tube creep specimens adopted by the US and Japanese programs measures 25.4 mm long with a 4.57mm outside diameter, and a wall thickness of 0.25mm. In 1995, Argonne National Laboratory coordinated a campaign to fabricate ~ 6 meters of tubing from the US program heat no 832665 with Century Tubes Inc of San Diego as the primary contractor [1]. This campaign met with mixed success with a large fraction of the tubing developing cracks on both the inside and outside surfaces. These cracks were frequently linked together through the wall thickness. Since they were long enough to be visible to the naked eye, it was possible to select relatively sound segments of tubing to prepare a sufficient number of creep specimens to meet short term program needs. This tubing was used for an initial series of testing both in vacuum and in lithium environments [2] and also used to develop preliminary irradiation creep data in experiments conducted in the ATR[1] and in the HFIR [3]. It was also found that during processing, the level of interstitials elements increased significantly, with carbon increasing from 80 to 300 wppm, oxygen increasing from 310 to 700 wppm and nitrogen going from 85 to 95 wppm, a total increase in interstitial level of ~130%. The increase in oxygen was of particular concern since creep rate is sensitive to oxygen concentration in this range. However, in subsequent creep measurements using this tubing it was observed that the oxygen content decreased to ~100wppm in approx. 1500hrs during tests carried out at 800ºC in a Li environment. Thus it is not entirely clear that the in-Li creep data were compromised by the initially high oxygen level of the ANL batch of tubing since the oxygen concentration reverted to very low levels during testing. However, it has been suggested that the presence of the defects in the tube wall could be responsible for inconsistencies in the measured strains to failure [2].

Two small heats of V-4Cr-4Ti with low levels of interstitials have been produced in Japan under the direction of the National Institute for Fusion Science (NIFS). A small quantity of creep tubing was prepared from the NIFS-HEAT -2 material using a three-directional rolling process [4]. Problems were also encountered in the NIFS campaign with interstitial pick-up and the development of surface defects. Based upon the processing records from the previous batch of tubing from the US heat and

the experience gained from processing the NIFS heat, a new procedure was developed which incorporated a series of changes designed to minimize interstitial pick-up, improve initial surface quality, and to reduce the probability of surface cracking by reducing stress levels in the final drawing stages. Using the new procedure, fabrication of ~10 meters of finished tubing from both heats was initiated at Century Tubes in April 2003.

This report documents the new procedures and discusses the status of the tubing fabrication as it enters the final stages; a full evaluation of the finished tubing will be presented in the next semi-annual report.

Previous Tubing Fabrication Experience

US HEAT 832665

Tubing from the first campaign at Century Tube (subsequently referred to as Batch A tubing) has been used to provide the initial sets of biaxial creep data in vacuum, lithium, and lithium plus neutron radiation environments. During the final stages of drawing and sinking, difficulties were experienced with surface cracking and sometimes complete fracture of tubes. Metallography of several sections was carried out at ORNL. Five out of six randomly selected sections of tubing contained branching cracks at both the ID and OD surfaces penetrating inwards to depths from 20 to 200 microns**.** Longitudinally, these cracks extended from 2 to 200mm in length and so were often visible to the naked eye. Cracks penetrating from both surfaces were often connected by a band of severe macroscopic deformation in which grains were rotated and elongated in a direction 45 degrees to the through –wall radial direction as shown in Fig.1. Many smaller cracks simply penetrated 10-20 microns in from both surfaces. Chemical analysis of the finished tubing indicated that the carbon and oxygen concentrations increased during processing by 220 wppm and 389 wppm respectively. Because archival samples were not secured at each drawing stage it is not possible to say when the cracks developed. One plausible scenario is that the large defects in the OD developed first in the oxygen-contaminated surface region and that as the wall thickness was reduced, the cracks penetrated an ever greater fraction of the wall. The decrease in effective load –bearing cross section resulted in localized shear stresses sufficient to create a band of severe macroscopic deformation accompanied by grain rotation and elongation. Intersection of this band with the surface resulted in the development of a corresponding ID crack. The summary of the processing provided by ANL [1] and the notebook records at Century Tubes Inc. suggested a number of factors that could have resulted in the observed defects; these are discussed in the following.

The source material for Batch A tubing was the rectangular cross- section (63.5mmx190mm) as-extruded bar supplied by Teledyne Wag Chang Co. This material was used to produce the initial tube blank (27.9mm OD x 19.1mm ID x 200mm long) with the long direction parallel to the extrusion direction. The initial microstructure for Batch A was consequently very inhomogeneous and characterized by a mixture of small grains (20-60 microns),coarse equiaxed grains (100-200 microns) and banded regions of deformed (unrecrystallized) grains [7]. There is considerable evidence that Ti segregates strongly during ingot solidification and during extrusion at 1150ºC these regions become drawn out parallel to the extrusion direction and eventually give rise to the bands of Ti (CON) particles that characterize the subsequent cold worked and annealed microstructure.

During the processing of Batch A, the cold drawn tubing was encased in Ti foil and recrystallized at 1025ºC in a vacuum of ~7 x 10^{-5} torr. Furnace records show that because of the rapid heating rate employed, the vacuum quality often deteriorated into the 10^{-4} torr range as a result of out-gassing. The lack of control of the vacuum quality during heat-up is the most likely reason for the significant oxygen pick-up observed. Examination of the cleaning procedures used following each draw cycle suggested that the acrylic lubricant used was not completely removed during cleaning and was probably the source of the observed carbon pick-up.

The tube drawing cycle utilized in the production of Batch A is summarized in Table 1. A set of 10 draw cycles were used with intermediate recrystallization at 1025ºC for 1 hour; each draw cycle

consisting of 3 approximately equal passes. The reductions in area for the final 5 cycles were in the range 40-45%.and is it possible that these relatively high levels of work hardening coupled with oxygen pick-up could have led to the conditions which resulted in the development of the observed surface cracking. In addition, cycles 2-4 were drawn with a constant diameter mandrel so that the ID did not change ; this procedure necessitated a fairly heavy reeling operation to remove the tube from the mandrel prior to annealing and it is possible that this also contributed to the development of the surface cracks.

Table 1. Summary of drawing schedule used for Batch A tubing from US heat 832665 of V-4Cr-4Ti

Cycle No.	OD (ins)	ID (ins)	Wall (ins)	RA/Cycle (%)	Anneal No.
Tube blank	1.100	0.770	0.165		1
1	0.981	0.750	0.117	40.6	2
2	0.920	0.750	0.085	33.3	3
3	0.863	0.750	0.057	41.1	4
4	0.830	0.750	0.040	34.4	5
5	0.755	0.700	0.029	37.6	6
6	0.688	0.650	0.020	41.5	7
7	0.606	0.580	0.015	41.1	8
8	0.520	0.500	0.010	45.9	9
9	0.288	0.264	0.012	40.0	10
10	0.178	0.157	0.011	45.4	11

NIFS-HEAT-2

Before the second campaign at Century Tube was initiated, researchers at NIFS reported on the fabrication of a small quantity of pressurized creep tubing and some larger size tubing for tritium permeation studies using plate from the high purity NIFS-HEAT-2. A tube blank with a 25.0mm OD and 19mmID was machined from a cold-worked 26mm square section and initially recrystallized at 1000ºC. Tube reduction was carried using a 3-directional rolling process with intermediate annealing at 825ºC. This temperature was selected to minimize oxygen pick-up but is apparently sufficiently high to effect recrystallization with a final grain size of ~20 microns [4]. Creep tube fabrication was accomplished in 7 rolling passes, utilizing four anneals at 850ºC and one final anneal at 1000ºC resulting in a final grain size of 39 microns. The processing resulted in an increase in oxygen concentration of 200 wppm and an increase in carbon and nitrogen by 70 and 30 wppm respectively. Early problems with cracking were eliminated by a) lowering the heat treatment temperature of the initial plate to 1000ºC (finer grain size) and b) limiting the reduction in area per cycle to below 40%. The ID surface quality was improved by honing following gun drilling. The final creep tubing contained surface defects up to 20 microns deep and it was suggested that this cracking is related to the intersection of bands of Ti(CON) particles with the tube surfaces.

REVISED PROCEDURE FOR TUBING FABRICATION

Based upon the prior experience summarized above, a number of changes were introduced into the procedure for fabricating thin-wall tubing which were designed to decrease the magnitude of interstitial pick-up and to minimize the probability of generating the large surface defects which developed during the fabrication of Batch A of the US heat. The complete technical specification that is being followed in the current campaign to produce creep tubing from both the US and the NIFS heats of V-4Cr-4Ti is presented in the Appendix. The major changes introduced compared to the Batch A procedure are summarized below.

a) For the US heat, the initial as-extruded plate was cold worked 50-55% prior to recrystallizing at 1000ºC to give an average grain size of ~30 microns. Although this treatment did not improve chemical inhomogeneity or alter the distribution of Ti(CON) particles, the uniformity of the grain structure was greatly improved compared with Batch A. Gun drilling of tube blanks was followed by honing to a surface finish of 16 rms or better

b) A more rigorous cleaning operation was introduced after each draw cycle involving successive treatments in Alconox, acetone and ethyl alcohol followed by an acid cleaning.

c) Prior to annealing, the vacuum furnace was baked out at 100ºC above the annealing temperature to remove sources of contamination. Tubes were completely wrapped in tantalum foil and annealed in a vacuum of better than $2x10^{-5}$ torr; this vacuum was maintained during all out-gassing stages during heat-up. The first 4 annealing treatments were carried out at GA San Diego. Subsequently operations were transferred to a furnace that could accommodate up to 5ft tubing lengths at Bodycote Inc. where the vacuum was maintained in the 10^{-6} torr range.

d) To minimize stresses the drawing cycle was selected so that for the final 6 stages , the reductions in area did not exceed 30%. All draw cycles consisted of 3 approximately equal passes of mandrel draws using a series of mandrels of reducing diameter so that both the ID and OD were reduced in each cycle. Decreasing the reduction in area per cycle necessitated an increase in the number of annealing treatments with the corresponding risk of increase the amount of oxygen pick-up.

e) Archive samples for metallography and chemical analysis were removed after each draw and after each vacuum anneal.

INTERIM QUALITY ASSESSMENT

Tube Blanks

The starting material for the US Heat was a 28mm square cross-section measuring 230 mm long which had been cut from an extruded plate which had been cold rolled ~55%. A tube blank was machined measuring 25.7 mm OD and 15.7 mm ID. Ultrasonic testing and X-radiography failed to detect any defects in the tube blank. The source material for the NIFS-HEAT -2 was a 26mm thick plate, 28.6 mm wide and 200mm long from which a similar tube blank was machined. Ultrasonic testing of the NIFS tube blank indicated that several areas contained defects. Subsequent examination under low power stereo showed possible surface cracks 0.5-1.0mm long parallel to the rolling direction, several possible cracks at 45 degrees to the tube axis and several short 0.1-0.3mm circumferential defects. Nagasaka et. al also detected defects in the 26t plate material using ultrasonic methods and presented metallographic evidence for elongated cavities ranging up to 0.5mm long parallel to the extrusion direction [5].

Interstitial pick-up

Archive samples were removed after each draw cycle and after each annealing treatment. The results of chemical analysis for carbon oxygen and nitrogen up to the seventh drawing/eighth annealing cycle are shown in Table 3. At the end of the eighth anneal, the oxygen content of both heats has approximately doubled with very little change occurring in either nitrogen or carbon concentrations. With 5 more annealing treatments to complete the processing schedule, (Table 2), the increasing oxygen concentration is a concern. If the increase continues at the average rate of ~40 appm per cycle for the US Heat and ~30 wppm per cycle for the NIFS heat then the oxygen concentrations of the finished tubing could approach 850 and 530 wppm respectively. During the course of this study several anomalously high analyses were obtained for both oxygen and carbon and the origins of these results are difficult to pin down. It was established however that cutting specimens with a high speed saw produces surface oxidation and is a leading source of anomalously high oxygen analyses. This is probably not the only means of contaminating chemical analysis specimens and careful cutting

Table 2. Summary of drawing schedule for US heat 832665 (Batch B) and NIFS-HEAT-2 of V-4Cr-4Ti.

Cycle No.	OD (ins)	ID (ins)	Wall (ins)	RA/Cycle (%)	Anneal No.
Tube Blank	1.010	0.626	0.192		1
1	0.940	0.600	0.170	17.3	2
2	0.818	0.542	0.138	30.4	3
3	0.723	0.499	0.112	31.3	4
4	0.588	0.420	0.084	44.4	5
5	0.495	0.375	0.060	44.7	6
6	0.395	0.299	0.048	42.5	7
7	0.318	0.240	0.039	39.0	8
8	0.288	0.224	0.032	29.2	9
9	0.262	0.212	0.025	29.0	10
10	0.246	0.208	0.019	30.2	11
11	0.229	0.199	0.015	31.0	12
12	0.203	0.179	0.012	32.0	13
13	0.188	0.168	0.010	21.0	
SIZING	0.180	0.160	0.010	5.5	
				Final	

Table 3: Chemical analysis of tubing

Cycle No.	Wall (ins)	US HEAT			NIFS HEAT		
		C wppm	O wppm	N wppm	C wppm	O wppm	N wppm
Tube Blank	0.192	119	331	88	59	156	130
ANN 1	0.170	138	329	93	67	132	135
ANN 5	0.060	175	426	89	124	312	150
ANN 6	0.048	119	511	94			
ANN 7	0.039	155	494	84			
ANN 8	0.032	179	637	101	90	378	148

and cleaning procedures need to be rigorously followed to avoid contamination with oxygen or carbon.

Surface defects

At the end of the fifth drawing cycle numerous longitudinal surface defects were observed on the OD of the US heat tubing which at this stage had a wall thickness of 0.060 ins. One of the LT surfaces of the original plate was designated as the top surface (zero degrees), and the corresponding position on the tubing was tracked throughout the drawing sequence. The defects occurred in a band parallel to the drawing direction at a location 90 degrees from the original top surface of the plate. The defects appeared to consist of very shallow regions,1-2mm long, which had separated from the tube surface. Such defects are not uncommon in drawing tubes from BCC alloys and it is normal practice to remove them by local mechanical polishing before each draw. After the fifth draw the tube from the US heat was cut into 2 sections to fit into the annealing furnace. The region containing the defects

was confined to one tube (Tube A) while the second tube appeared to be defect-free (Tube A1). Despite careful polishing to remove the defects, they continued to appear in Tube A after each subsequent draw. After the tenth draw, it was possible to cut a sample from a region containing OD surface defects and a cross-section is shown in Fig.2. Comparison with Fig.1 shows that the surface defects are very similar to the type of defect frequently encountered in Batch A tubing from the US heat. Since these defects develop at an early stage in the drawing/annealing sequence and at a particular circumferential location, they are probably related to some macroscopic feature of the initial plate microstructure such as regions of highly banded microstructure, internal porosity or inclusions.

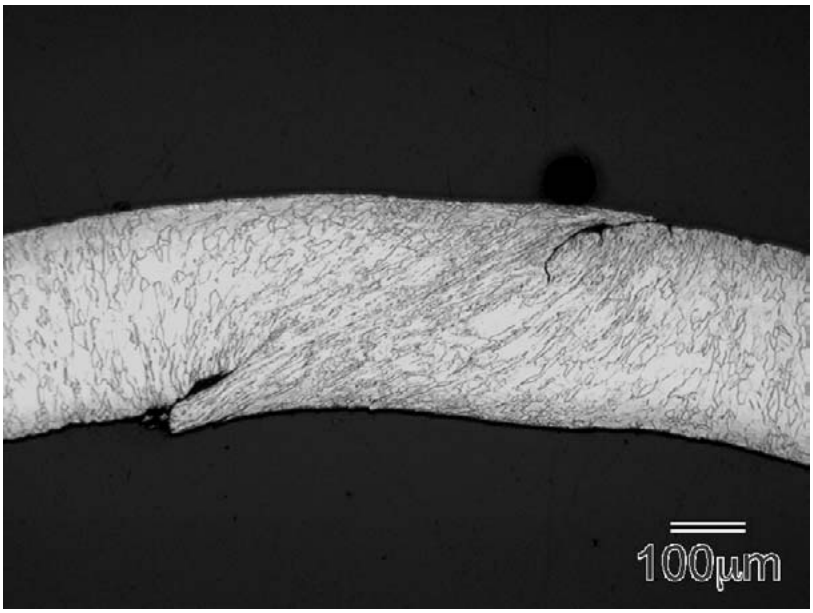

Figure 1. Surface defects in final tubing from US heat Batch A.

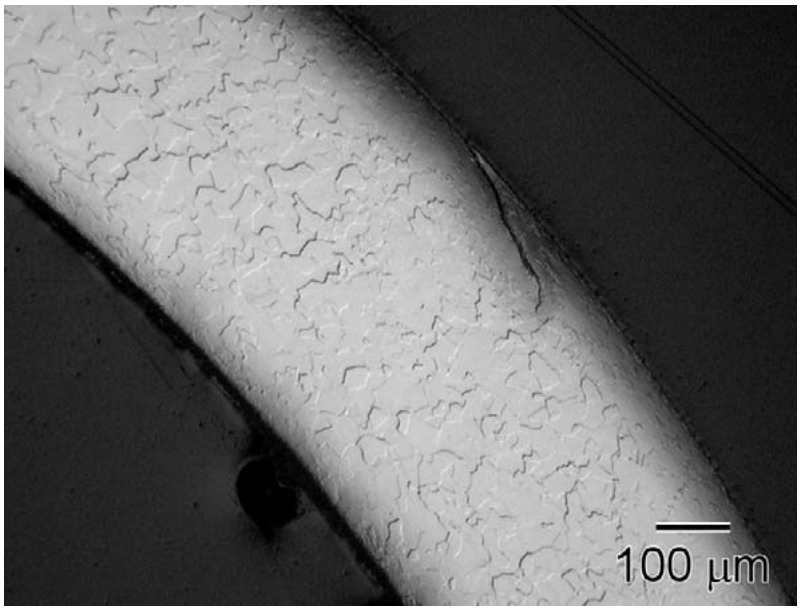

Figure 2. Surface defect in Tubing from US heat Batch B following the fifth drawing cycle.

Microstructure

Representative micrographs from both heats of tubing following the fourth draw cycle and fifth anneal are shown in Fig 3. The average grain size of the NIFS heat is very uniform with an average grain size of ~ 50 microns. The US heat contains a much higher fraction of small grains (5-10 microns) with an overall average size of ~ 28 microns. These differences are almost certainly related to the differences in initial interstitial content which is linked to the initial volume fraction and distribution of Ti(CON) particles. A cross section of the US heat following the third draw /fourth anneal is shown in Fig 4. This sample was stained during etching and at low magnification shows the macroscopic aspects of the deformation process during tube drawing. During etching, staining occurred along the bands of Ti(CON) particles revealing the significant macroscopic rotation of the grain structure which occurs as the outer surface is approached; the bands of particles apparently rotate with the deforming /rotating grains A similar phenomenon has been reported in the fabrication of NIFS heat tubing by 3-directional rolling and during cross-rolling of NIFS plate material [6]

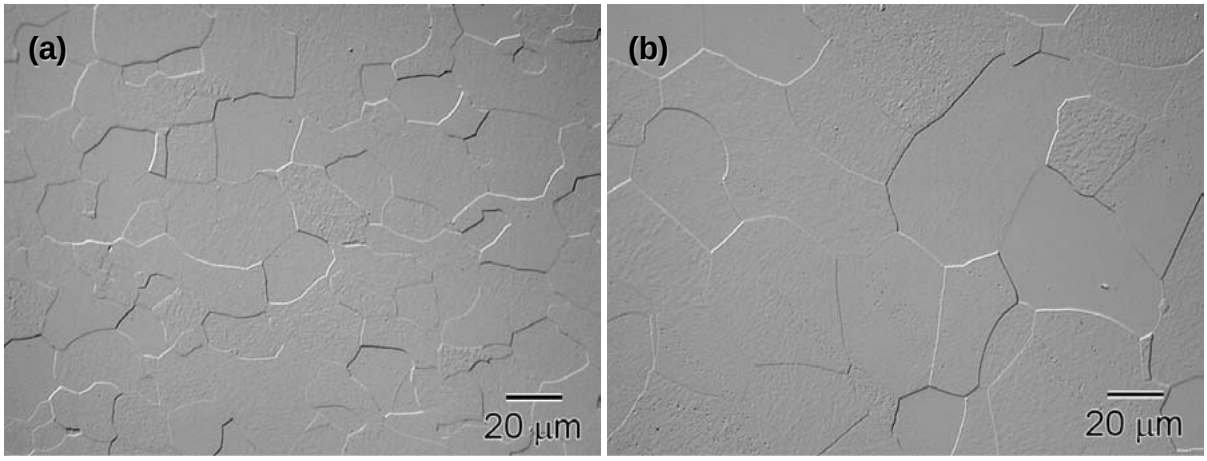

Figure 3. Grain structure of (a) US heat tubing (Batch B) and (b) NIFS heat tubing following the fifth annealing treatment.

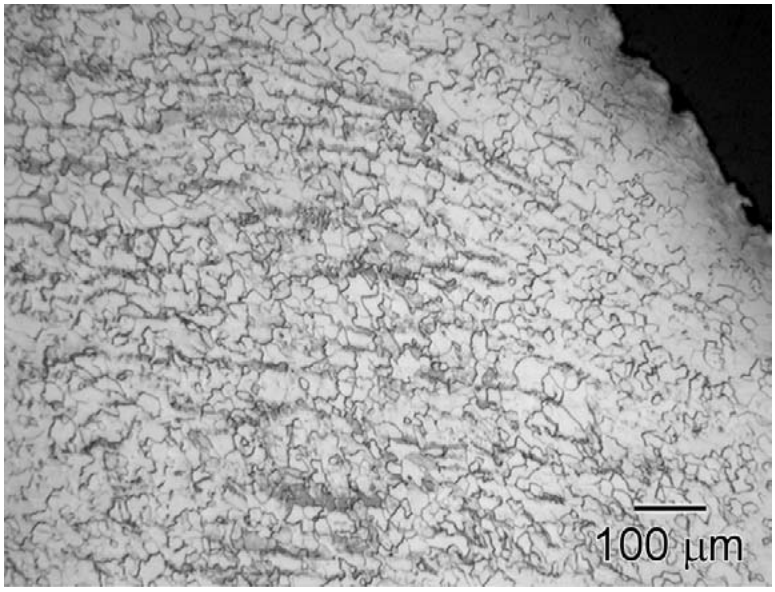

Figure 4. Optical micrograph with stain etch of the US heat (Batch B) following the 4th annealing treatment.

Future work

Fabrication of both heats will continue in accordance with the schedule shown in Table 2, paying close attention to the section of the US heat containing the visible defects and eliminating this section if necessary. Because of the development of different grain structures in the two heats it may be necessary to adjust the final heat treatment of the NIFS heat to reduce the grain size and ensure that there is a sufficient number of grains across the wall of the final creep tubing. A full evaluation of the finished tubing will be carried out including dimensional tolerance inspections, optical microscopy, TEM, chemical analysis, hardness, texture measurements and possibly ultrasonic and eddy current inspection.

REFERENCES

1. H. Tsai, M.C. Bilone, R.V. Strain, and D.L. Smith; Fusion Materials Semi-annual Progress Report DOE/ER-0310/23, December 1997, p149.
2. M.L. Grossbeck, R.J. Kurtz, L.T. Gibson and M.J. Gardner; Fusion Materials Semi-annual Report DOE/ER-0310/32, June 2002, p6.
3. H. Tsai, M.C. Billone, T.S. Bray and D.L. Smith; Fusion Materials Semi-annual Progress Report DOE/ER-0310/27,December 1999, p 65.
4. T. Nagaska, T. Muroga, T. Iikbo; “Development of Tubing Technique for High –Purity Low Activation Vanadium Alloys”, ANS Winter Meeting, Washington DC, Nov.2002, (to be published).
5. A.F. Rowcliffe and D.T. Hoelzer; Fusion Materials Semi-annual Progress Report DOE/ER-0310/25, December 1998, p42.
6. T. Nagasaka et. al, “Fabrication of High-Purity V-4Cr-4TiAlloy Products”; 2nd Workshop on the Development of Low Activation Vanadium Alloys for Fusion, NIFS, March 2002.

APPENDIX

TECHNICAL SPECIFICATION FOR FABRICATION OF THIN-WALL V-4Cr-4Ti ALLOY TUBING

TABLE OF CONTENTS

1.0 BACKGROUND

A V-4Cr-4Ti alloy is being studied as a possible structural material for first wall and blanket applications in Li-cooled fusion energy systems. Oremet Wah Chang of Albany, Oregon (OWCA), have produced a 500-kg heat (OWCA Heat 832665), for the United States Department of Energy (DoE)-funded Fusion Materials Sciences Program and a 1200-kg heat (OWCA Heat 832864) for General Atomics (GA), San Diego, California. A 30-kg heat (NIFS-HEAT-1) and a 166-kg. heat (NIFS-HEAT-2) with lower oxygen and nitrogen contents have been produced in Japan for the National Institute for Fusion Sciences. Thin-walled tubing of these alloys is needed to fabricate pressurized tube specimens for making creep property measurements in vacuum, liquid lithium, and neutron irradiation environments.

2.0 GENERAL INFORMATION

This specification establishes the requirements for the fabrication and heat treatment of thin-wall tubing to be used in the fabrication of specimens for irradiation creep experiments for the DoE Fusion Materials Sciences Program. Any additions or deletions to this specification shall be specified in applicable Oak Ridge National Laboratory (ORNL) service requests, memoranda, and/or drawings, and/or ORNL purchase orders/attachments. Should any conflicts develop between this specification and other technical documents referenced for the procurements or services indicated herein, this specification shall control. All such conflicts shall be resolved with the assigned ORNL representative before implementation. Any deviations to this specification by ORNL service organizations and/or outside contractors performing processes identified herein shall not be initiated without approval in writing by the assigned ORNL representative.

3.0 FABRICATION REQUIREMENTS

3.1 DEFINITION OF RESPONSIBILITIES

The assigned ORNL representative shall provide the raw material stock for fabricating the tubing. and provide certification of the chemistry of the raw material stock and any available fabrication history relative to same.

The assigned ORNL representative shall be responsible for the oversight of all processing steps in the fabrication of the tubing including characterization and preparation of the raw material stock, machining and dimensioning of the starting material (tube blank) for the initial tube fabrication, and fabrication, heat treatment, and dimensioning of the tubing .The ORNL representative shall also be responsible for the oversight of the characterization of the tubing at the designated hold points during processing and shall identify those ORNL service organizations or outside contractors who will be assigned to perform the characterization.

.

3.2 FABRICATION PROCEDURES

The specific procedures and requirements for the processing of tubing covered under this specification are defined in Section 5.0

3.3 MATERIAL CONTAMINATION PRECAUTIONS

The organizations identified herein for performing the various process steps in the fabrication of the tubing shall use necessary precautions to prevent exposure of the tubing material, during any process step, to any of the following:

The material shall not be exposed to any chlorine- or sulfur-bearing liquid, vapor, or grease during processing unless deemed specifically required for successful tubing fabrication, and which is known or can be shown to be removable by the cleaning processes designated herein prior to exposure to elevated temperatures (i.e. vacuum annealing or vacuum bakeout). The chemical nature of such required liquids, vapors, and/or greases with respect to the specific chemical species indicated herein shall be identified by the outside contractor prior to performing the work, and their specific use shall require approval by the assigned ORNL representative.

Except during tube drawing, expansion, and reduction (and mandrel removal) operations, the material shall not be allowed to come in contact with any metallic or non-metallic surface which may allow foreign particles of same to become embedded in its surface.

4.0 QUALITY ASSURANCE PROCEDURES

4.1 INSPECTION RIGHTS

The assigned ORNL representative shall have the right, during the working hours of the organization or outside contractor performing the work element, to witness inspections, perform product inspections, witness work operations in progress, and review quality documentation and records pertaining to the work indicated herein.

4.2 NOTIFICATION POINTS

Notification points shall be as a minimum the start of all processes designated in Section 5.0 Each notification point shall be witnessed at the option of the assigned ORNL representative who will be given two (2) working days advance notice. The outside contractor performing the work element shall not be required to hold up work once proper notification has been received by the assigned ORNL representative.

4.3 SAMPLING AND HOLD POINTS

At the end of each annealing cycle samples of tubing, to be specified by the ORNL representative, will be removed and placed in an archive. Samples will also be removed for chemical analysis and metallographic examination at ORNL. At the discretion of the ORNL representative, a hold time may be imposed until the results of chemical and microstructural analysis have been evaluated.

4.4 RECORDS MAINTENANCE

Outside contractors performing any of the work elements indicated herein shall submit inspection documentation, time-temperature and time-vacuum furnace charts, and other operations documentation and reports for inspection by the ORNL representative

5.0 FABRICATION PROCEDURES

5.1 CHARACTERIZATION OF THE RAW MATERIAL STOCK

The raw material stock to be used for fabrication of the tubing will be sections of cold–rolled plate measuring approximately 1.1 inches square and approximately 9 inches long. ORNL will provide material for three (3) sections of the US heat no.832665 and one (1) section of the Japanese heat NIFS-HEAT-2. The initial plate material will be characterized at ORNL in terms of optical microstructure, hardness and chemical analysis

5.2. MANUFACTURE OF TUBE BLANKS

The raw material stock shall be prepared for fabrication into material suitable for tubing (tube blank) as follows:

1) The raw material stock for the tubing shall be initially shaped and final machined using conventional machining methods to produce a tube blank (thick-walled tube) of dimensions suitable for processing into tubing of the required outside diameter (O.D.) and wall thickness. The method of machining and dimensions (O.D., wall thickness, and length) of the tube blank shall be agreed upon by the assigned ORNL representative and the vendor contracted to perform the processing of the tubing,. After machining, the finished tube blank shall be measured to record all physical dimensions and to determine its conformance to the specified dimensions. All measurements of these physical dimensions shall be documented. The finished tube blank shall be degreased in a solvent suitable

for removing visible traces of cutting debris and lubricants, and placed in a clean, dry, appropriately identified plastic bag.

2) The tube blank shall be cleaned in accordance with the procedure described in Section 5.3 and then annealed in accordance with the procedure described in Section 5.4 .

5.3 CLEANING TUBE BLANKS AND DRAWN TUBING

The starting material for fabrication of the tubing (tube blank) and subsequent as-fabricated tubing shall be cleaned prior to tube fabrication processes (drawing/expansion/reduction). Cleaning of the finished tube blank and as-fabricated tubing shall consist of solvent pre-cleaning, cleaning in a series of aqueous and solvent baths, and acid cleaning/etching (pickling), and shall be performed as follows:

5.3.1 SOLVENT CLEANING

The raw material stock for fabrication of tubing and as-fabricated tubing shall be solvent cleaned as follows:

1) Pre-clean the outer surfaces of the material to remove visual traces of any machining oils, marking ink, machining debris, etc., using a bristle brush or cloth and any suitable water-based or organic solvent cleaner (acetone, alcohol, etc.). Pre-clean the inner surfaces of the material to remove visual traces of any machining oils, machining debris, etc. by pulling or pushing multiple clean white solvent-soaked cotton or linen cloths through the internal bore of the material.

2) Clean external and internal surfaces of the material by immersion for a minimum of 5 minutes in each of the following series of solvent baths to remove all residues. Air dry material by placing on laboratory tissue (Kimwipes or equivalent) after each cleaning step. Verify removal of residues by surface wiping with a clean laboratory tissue moistened with ethyl alcohol.

   a) Bath 1 – Aqueous commercial cleaner (at >120ºF) [Alconox]

   b) Bath 2 - acetone (room temperature)

   c) Bath 3 - ethyl alcohol (room temperature)

3) If material has been saw cut (bandsaw, abrasive wheel, etc.), and saw-cut surfaces contain burrs, remove burrs by abrasive grinding saw-cut edges with #240 grit SiC paper (new).

4) If material has been electric discharge machined, abrasive grind machined surfaces with 600 grit SiC paper (new) to remove any discoloration and all evidence (by visual exam using 10X magnifier) of any brass residue from possible electrode interaction during discharge machining. Grind off a minimum of 0.0002 in. of surface material.

5) Wipe ground surfaces of material with ethyl alcohol-moistened tissue to remove all visual evidence of surface grinding debris. For tubular product forms, clean I.D. of tube by pulling or pushing ethyl alcohol-moistened cotton or linen cloth through tube to remove all visual evidence of surface grinding debris. Ultrasonically clean material in ethyl alcohol at room temperature. Air dry material on laboratory tissue (Kimwipes or equivalent). Handle cleaned material only with clean un-powdered rubber gloves or clean cotton or linen gloves.

6) Unless material is to proceed immediately through another process, e.g., pickling, annealing, etc., wrap material in laboratory tissue (Kimwipes or

equivalent) and place in a clean plastic bag appropriately identified as to sample identification, alloy designation, and material condition.

5.3.2 ACID CLEANING (PICKLING)

As soon as practical after solvent cleaning, all materials shall be acid cleaned as follows

1) Acid* clean/etch (pickle) material (maximum removal of 0.0005 in. of thickness) by immersion with agitation in a room temperature acid solution of 50 vol% deionized water - 30 vol% nitric acid - 20 vol% hydrofluoric acid for 30 seconds, followed by multiple rinses in deionized water at room temperature. Handle material with plastic tongs or by hand with clean un-powdered rubber gloves.

2) Wipe cleaned/etched and water-rinsed surfaces of material while still wet with deionized water-moistened cotton or linen cloth to remove all visual evidence of residue from acid cleaning/etching. For tubular product forms, clean I.D. of tube while still wet by pulling or pushing deionized water-moistened cotton or linen cloth through tube to remove all visual evidence of residue. For electric discharge machined materials remove all evidence of brass residue from prior machining (verify by visual exam using 10X magnifier). Ultrasonically clean material in ethyl alcohol at room temperature. Air dry material on laboratory tissue (Kimwipes or equivalent). Use clean un-powdered rubber gloves or clean cotton or linen gloves during etching/cleaning/wiping/handling of material. For electric discharge machined materials, repeat cleaning/etching/ rinsing/wiping procedure one additional time if visual evidence of brass residue persists. If repeat procedure is unsuccessful, hold at this point for review by the assigned ORNL representative.

3) Unless material is to proceed immediately through another process, e.g., vacuum annealing, etc., wrap fully-rinsed and dried material in laboratory tissue (Kimwipes or equivalent) and place in a clean plastic bag appropriately identified as to sample identification, alloy designation, and material condition.

**Caution: The acid etchant will generate some heat during its exposure to the material, and may cause severe burns from contact with unprotected tissue. A face shield and acid-resistant gloves should therefore be used at all times during handling of the acid and acid container(s).*

5.4 HEAT TREATMENT OF THE TUBE BLANK AND DRAWN TUBING

As soon as possible after cleaning as described above ,vacuum annealing should be carried out as follows:

1) Bake out vacuum furnace at a temperature at least 100ºC higher than the specified annealing temperature [see 4) below], and not more than 24 hours prior to the anneal.
2) Prior to annealing, wrap or shroud the material in a clean tantalum foil blanket such that no line of sight exists between the components of the vacuum furnace and any surface of the material to be annealed. Tantalum foil which has been previously used to anneal material in accordance with Section 5.4 or which has been baked out during or in a manner similar to the furnace bakeout step indicated in 1) above shall be acceptable. Support the material in the furnace to prevent distortion, or bowing. The material may be placed in the furnace either horizontally, vertically, or at an angle as long as proper support is provided.

3) Vacuum anneal the material using the following procedure:

a) Heat the material from room temperature to 525ºC at a rate commensurate with maintaining a vacuum of 2 x 10^{-5} torr or better. Hold at 525 ± 10ºC for 1 hour.

b) Heat the material from 525ºC to 1000ºC in a vacuum of 2 x 10^{-5} torr or better, and at a rate of 400ºC - 600ºC/hour. Hold at 1000 ± 10ºC for 1 hour.

c) Cool material to 50ºC in a vacuum of 2 x 10^{-5} torr or better, and at a rate of >1000ºC/hour (nominal). Do not remove material until temperature of material is <50ºC. Use clean cotton or linen gloves during handling.

d) Monitor the temperature and temperature uniformity of the material using a minimum of two (2) thermocouples (e.g., Type K, with Inconel 600 sheath) attached directly to the material or inserted into the tantalum-wrapped material/ package. If the uniformity of the furnace has been previously established and accepted by the assigned ORNL representative, only one (1) thermocouple attached to the material or inserted into the Ta-wrapped material/package is required.

5) Record temperature and vacuum level readings in a continuous fashion, or manually every 10 minutes, during heat up, elevated-temperature holds, and cool down of the material.

6) After removal of the wrapped material from the vacuum furnace, unwrap material. Wrap material in laboratory tissue (Kimwipes or equivalent) and place in a clean plastic bag appropriately identified as to sample identification, alloy designation, and material condition. Place tantalum foil in a clean plastic bag and provide to the assigned ORNL representative.

5.5 TUBING FABRICATION (TUBE DRAWING/EXPANSION/REDUCTION)

Tube blank material prepared in accordance with Sections 5.1 through 5.5 shall be fabricated into tubing of the required outside diameter (O.D.) and wall thickness. The dimensions of the tube blank required to produce the required finished tubing dimensions shall be agreed upon by the assigned ORNL representative and the vendor contracted to perform the fabrication of the tubing. The tube blank and finished tubing dimensions shall be specified in the ORNL purchase order for the processing of the tubing. Fabrication of the tubing shall be performed as follows:

1) The finished, cleaned, and annealed tube blank shall be fabricated into tubing by drawing at room temperature in accordance with the dimensions (O.D. and wall thickness) specified in the ORNL purchase order for the processing of the tubing. A step-by-step fabrication schedule to be followed in drawing the tubing, including die and mandrel sizes for each draw pass, shall be provided to the assigned ORNL representative by the outside contractor processing the tubing prior to the initiation of processing. The tolerance on the tube O.D. shall be ± 0.001 in. and the tolerance on the tube I.D. shall be ± 0.001ins.Finished tube ovality shall not exceed 0.002ins and eccentricity shall not exceed 0.0005ins. The fabrication of the finished tubing will require several draw cycles, of several draw passes each, and several intermediate cleanings/anneals.

2) Prior to initial drawing, one end of the tube blank shall be swaged (pointed) to facilitate entry into the drawing die. The swaged length (point) shall be minimized in order to facilitate the fabrication of the longest length of tubing possible, but shall not be made so short as to compromise the fabrication of the tubing itself. The tube blank shall be reduced through successively smaller dies until both its O.D. and wall thickness reach the final tube dimensions specified, or

reduced through successively smaller dies until its wall thickness reaches the specified wall thickness, and then expanded or reduced in diameter to the specified O.D. The reduction in area for each drawing pass shall be limited to 15 ± 2%. The total reduction for the first draw cycle shall be limited to 30 ± 5%; the total reductions for succeeding draw cycles up until the last two draw cycles shall not exceed 45%; and the total reductions for the last two draw cycles shall be limited to 30 ± 5%. The outside diameter, wall thickness, length, and hardness (near trailing end) of the tubing shall be measured and recorded after each draw (pass) to assess the progress of the processing. A report of the tubing dimensions and hardness values recorded after each pass shall be provided with the finished tubing.

3) After each draw cycle, and prior to cleaning/annealing, two (2) cross-sections (each ~1/4 in. in length) shall be taken from the trailing end (non-pointed end) of the tubing) using conventional cutting methods (abrasive wheel, bandsaw, EDM, etc). After cutting, the tubing sections shall be degreased in a solvent suitable for removing visible traces of machining debris and lubricants, and placed in a clean, dry, plastic bag appropriately identified as to sample identification, alloy designation, and material condition. The tube blank sections shall be provided to the assigned ORNL representative.

4) The remaining tubing shall be cleaned and vacuum annealed in accordance with the procedures described in Sections 5.3 and 5.4.

5) The step-by-step fabrication schedule may be necessarily changed or altered by the tube processing vendor during the actual fabrication process depending on the actual final dimensions of the starting tube blank, possible failure of the material to achieve the specified deformation levels, etc. Such changes shall require approval in writing by the ORNL representative prior to initiation.

6.0 PACKAGING AND SHIPMENT

6.1 IDENTIFICATION AND MARKING

The finished tubing shall be marked with the supplier's identification, lot number, nominal thickness or diameter and purchase order number. Markings shall be made on one surface of each product piece. Characters shall be of such size as to be clearly legible, and shall be applied using a suitable marking fluid capable of being removed with conventional cleaning solutions without excessive rubbing. The markings or their method of removal shall have no deleterious effect on the product or its intended performance, and shall be sufficiently stable to withstand normal handling.

6.2 PACKAGING AND PACKAGE MARKING

The product shall be prepared for shipment in accordance with commercial practice and in compliance with applicable rules and regulations pertaining to the handling, packaging, and transportation of the product to ensure carrier acceptance and safe delivery. Each piece of product form shall be individually wrapped in a protective material to preclude exposure to atmospheric conditions and/or improper handling which could inadvertently damage the material. Packaging shall conform to carrier rules and regulations applicable to the mode of transportation utilized for shipment of the product.

7.0 ACKNOWLEDGEMENT

The supplier shall specifically mention this specification number and revision letter in all quotations and when acknowledging contracts or purchase orders.

2.0 CERAMIC COMPOSITE MATERIALS

THERMAL DIFFUSIVITY/CONDUCTIVITY OF IRRADIATED SYLRAMIC™ 2D-SIC$_F$/SIC COMPOSITE

G. E. Youngblood, D. J. Senor and R. H. Jones (Pacific Northwest National Laboratory)*

OBJECTIVE

The primary objective of this task is to assess the thermal conduction properties of SiC$_f$/SiC composites made from SiC fibers (with various SiC-type matrices, fiber coatings and architectures) before and after irradiation, and to develop analytic models that describe the transverse and in-plane thermal conductivity of these composites as a function of constituent properties and geometry as well as temperature and dose.

SUMMARY

A 2D-SiC$_f$/SiC composite was made by Hypertherm with an ICVI-SiC matrix and with multilayer C/SiC coatings on high thermal conductivity Sylramic™ fibers woven into 5HS fabric layers. Thermal diffusivity measurements were made on representative samples of this Sylramic™ composite before and after irradiations in the HFIR reactor as part of the JUPITER 14J test series. The irradiations took place at about 290 and 800°C to equivalent doses of 4.2 and 7.0 dpa-SiC, respectively. The ratios of the transverse thermal conductivity after-to-before irradiation (K_{irr}/K_o) determined at the irradiation temperature were estimated from thermal diffusivity measurements to be about 0.12 and 0.37 at 290 and 800°C, respectively. However, the measured thermal diffusivity values of the unirradiated Sylramic™ composite with multilayer C/SiC fiber coatings were about 40% less than values predicted by the H2L model for this composite. This observation could be explained if the net interface conductance of the C/SiC multilayer was less than 0.1 of the interface conductance of a single layer PyC fiber coating.

PROGRESS AND STATUS

Introduction

The purpose of this study was to examine the effects of a C/SiC multilayer fiber coating on the thermal conduction properties of a SiC$_f$/SiC composite reinforced with a high conductivity SiC fiber. In particular, the H2L thermal conductivity model predicts that a composite with low fiber-matrix (f/m) interface conductance would thermally decouple the fiber from the matrix [1]. If the C/SiC multilayer interface, in fact, exhibits a low net interface conductance, the expected beneficial influence of using a fiber with a high thermal conductivity to achieve a composite with an overall high transverse thermal conductivity may be nullified.

It is noted that SiC$_f$/SiC composites with a multilayer interphase have exhibited improved toughness [2] and oxidation resistance [3] compared to composites similarly made except with a single layer PyC interphase. Furthermore, Snead and Lara-Curzio showed that for a set of similar SiC$_f$/SiC composites made with Hi-Nicalon™ fabric, but with a conventional single layer carbon, a pseudo-porous SiC, or a multilayer C/SiC interphase, the composite with the multilayer C/SiC interphase exhibited the least degradation (8-20%) in the ultimate bend stress after irradiation to 1.1 dpa at 385°C [4]. Thus, the multilayer C/SiC fiber coatings are expected in some cases to promote improved mechanical performance in both unirradiated and irradiated SiC$_f$/SiC composite.

In this companion report to [1], the H2L model is used to critically assess the overall transverse thermal conductivity before and after irradiation for a 2D-SiC$_f$/SiC composite made with a high thermal conductivity fabric and a C/SiC multilayer fiber coating. The examined composite was made by

* Pacific Northwest National Laboratory (PNNL) is operated for the U.S. Department of Energy by Battelle Memorial Institute under contract DE-AC06-76RLO-1830.

Hypertherm using a Sylramic™ fabric. The primary differences in this composite compared to the Hi-Nicalon™ composites discussed in the previous report were replacing the Hi-Nicalon™ fabric and its single layer PyC fiber coating with Sylramic™ fabric and its multilayer C/SiC fiber coating. Otherwise, the Sylramic™ and Hi-Nicalon™ composites had a similar ICVI-SiC matrix and similar bulk density values.

Composite Samples

The Sylramic™ fiber was prepared from a polymer-derived Si-C-O fiber by Dow Corning Corporation and had the following nominal properties: mean fiber diameter 10 μm, density 3.0-3.1 g/cc, tensile strength 3.2 GPa, tensile modulus 380 GPa, thermal conductivity 40-46 W/mK, crystallite grain size 100 nm, and thermal stability to 1600°C [5]. By using several processing steps including a high temperature sinter, a crystalline fiber results with essentially stoichiometric SiC (95% wt.), TiB_2 grains (3% wt.) at triple points and small amounts of B_4C (1% wt.) and BN. The high density and high degree of crystallinity in the fiber promote a high elastic modulus and thermal conductivity. Because the diameter is small, this fiber can be readily woven into 2D fabrics, even though the modulus of the Sylramic™ fiber is quite high.

The Sylramic™ composite, made by Hypertherm with a x4 C/SiC multilayer fiber coating applied by CVD prior to matrix infiltration by ICVI, was provided by G. Newsome (KAPL) as a 0.125" x 2.0" x 4.0" plate. The Sylramic™ fabric had 800 filaments/tow and was five-harness satin weave (5HS). In the composite plate, thirteen plies were stacked with a 0-90 lay-up. Prior to cutting out individual samples, the plate was diamond milled on one surface to a constant 2.26-mm thickness. Four thermal diffusivity samples (TS1-4, 9.3 mm dia. X 2.26 mm thick) and 21 flexural bars (30 x 6.0 x 2.26 mm) were diamond cored or sawed from the milled plate. The bulk density values, determined by simple weighing and measuring of the sample dimensions, were in a similar range as the composites made with Hi-Nicalon™ fabric (2.44-2.60 g/cc). These bulk density values suggest that the macroporosity values were in the 15-20% range for the Sylramic™ composites, whereas the Hi-Nicalon™ composites had macroporosity values in the 7-13% range.

Irradiation and Test Conditions

Thermal diffusivity measurements were made simultaneously on several sample discs at various temperature steps in air from RT to 400°C before and after irradiation using the "low temperature" laser flash diffusivity system as described previously [1]. By plotting the reciprocal of the measured thermal diffusivity values versus temperature in degrees K, the resulting linear fit was used to extend diffusivity values to higher temperatures for analysis. The Sylramic™ composite disc samples were irradiated in the HFIR reactor at ORNL as part of the JUPITER 14J test series (TS1-2 at 290 ± 20°C, 4.2 dpa-SiC and TS3-4 at 800 ± 5°C, 7.0 dpa-SiC). All diffusivity measurements were made in air, but no annealing treatments were given to these Sylramic™ composites (as were carried out for the Hi-Nicalon™ composites).

Results and Discussion

In Figure 1, the thermal diffusivity values as a function of temperature for the Sylramic™ ICVI-SiC composite with a multilayer C/SiC interface are presented for various conditions. The conditions were: [1] as-received sample TS4 with a bulk density of 2.60 g/cc, [2] samples TS3 and TS4 irradiated at 800°C to an equivalent dose of 7.0 dpa-SiC, and [3] samples TS1 and TS2 irradiated at 290°C to an equivalent dose of 4.2 dpa-SiC. Although not accurately determined by simple dimensional measurements, a volume change of the disc samples irradiated at 290°C and 800°C appeared to exhibit roughly a 2.5-4.0% and 1.5-2.5% expansion, respectively.

In general, the unirradiated samples with higher bulk density values exhibited higher thermal diffusivity values. Since sample TS4 had approximately the same bulk density (2.60 g/cc) as the previously tested

Hi-Nicalon™ samples with the “thin” interface, the thermal diffusivity data for this specific sample with a high thermal conductivity Sylramic™ fiber component was used for detailed analysis. The measured thermal diffusivity of this sample was about 0.076 cm^2/s at RT and decreased continuously with increasing temperature to about 0.04 cm^2/s at 500°C. The thermal diffusivity curve for sample TS4 approximately matches the curve determined for the Hi-Nicalon™ composite with a “thin” PyC interphase [1]. The corresponding transverse thermal conductivity values also approximately match the Hi-Nicalon composite values (14 and 9 W/mK at RT and 1000°C, respectively).

Assuming that the ICVI-SiC matrix in the Sylramic™ composite has the same thermal conductivity values as determined for the ICVI-SiC matrix in the Hi-Nicalon™ composite, the H2L model predicts thermal diffusivity values that should be about 40% higher than the observed values. This is the case even if the somewhat higher porosity factors in the Sylramic™ composite are considered. This observation can be explained if the net interface conductance for the x4 C/SiC multilayer fiber coating is less than 0.1 of the value determined for the single layer PyC fiber coating. At this time, microstructural analysis has not

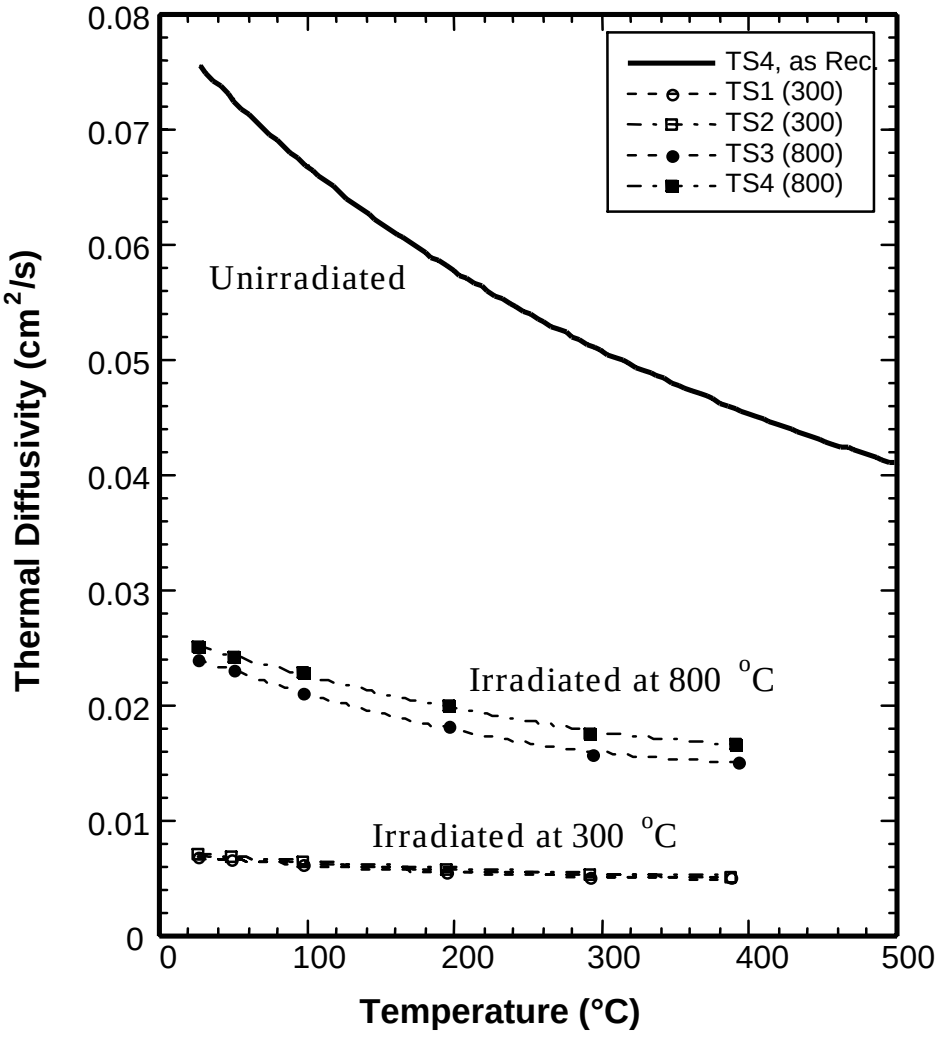

Figure 1. The measured thermal diffusivity values for representative Sylramic™ fiber-reinforced 2D-SiC_f/SiC composite samples made with multilayer C/SiC interphase before and after irradiation at 290°C (4.2 dpa-SiC) and 800°C (7.0 dpa-SiC).

been carried out on these Sylramic™ composites. Nevertheless, further analysis of this potential thermal conduction problem for other SiC_f/SiC composites made with multilayer fiber coatings is warranted.

After irradiation beyond saturation doses, the thermal diffusivity of the Sylramic™ composite was severely degraded as expected (Figure 1). Similar to the Hi-Nicalon™ composite case, the degradation was significantly larger for the irradiations at 290°C compared to those at 800°C. If it is assumed that the density and heat capacity values weren't significantly affected by the irradiation, then the ratio K_{effi}/K_{effo} is approximately 0.12 or 0.37 at 290 and 800°C, respectively. Again, the general trend that this ratio tends to gradually increase with increasing temperature for irradiated SiC_f/SiC composites and monolithic SiC is observed [6].

Further analysis of these data is not warranted until microstructural examinations have been carried out. Also, at this point the potential negative influence on the irradiation performance of the Sylramic™ composite due to the enhanced helium production in the Sylramic™ fibers with substantial boron content has not been considered.

FUTURE WORK

Detailed dimensional analysis will be performed on bar samples of the Sylramic™ composite irradiated in the 14J experiment. Also, if warranted flexural stress-strain measurements and microstructural examinations will be made and correlated with the thermal property results.

REFERENCES

[1] G. E. Youngblood, D. J. Senor and R. H. Jones, "Thermal diffusivity/conductivity of irradiated Hi-Nicalon™ 2D-SiC_f/SiC composite," in this Fusion Materials Semiannual Progress Report.

[2] Sebastien Bertrand, Rene Pailler and Jacques Lamon, "Influence of strong fiber/coating interfaces on the mechanical behavior and lifetime of Hi-Nicalon/(PyC/SiC)n/SiC minicomposites," J. Amer. Ceram. Soc. 84(4), 787-794 (2001).

[3] Y. Katoh, K. Hironaka, T. Hinoki and A. Kohyama, "Environmental effects of interfacial integrity of advanced SiC fiber-reinforced SiC matrix composites," Ceram. Eng. and Sci. Proc. 22 (4), 2001.

[4] L. L. Snead and E. Lara-Curzio, "Interphase integrity of neutron irradiated silicon carbide composites," p. 100 in Fusion Materials Semiannual Progress Report for period ending December 31, 1998 (DOE/ER-0313/25).

[5] R. E. Jones, J. Rabe and D. Petrak, "Sylramic™ SiC fibers for CMC reinforcement," p. 22 in the Proceedings of the 3rd IEA SiC/SiC Workshop, January 29-30, 1999, Cocoa Beach, FL.

[6] D. J. Senor, G. E. Youngblood, C. E. Moore, D. J. Trimble, G. A. Newsome and J. J. Woods, "Effects of neutron irradiation on thermal conductivity of SiC-based composites and monolithic ceramics," Fusion Technology 30(3), 943-955 (1996).

THERMAL DIFFUSIVITY/CONDUCTIVITY OF IRRADIATED MONOLITHIC CVD-SIC -
G. E. Youngblood, D. J. Senor and R. H. Jones (Pacific Northwest National Laboratory)*

OBJECTIVE

The primary objective of this task is to assess the thermal conduction properties of SiC before and after irradiation and after various high temperature heat treatments. Analytic models will be used to describe the fundamental behavior of the thermal conduction process in SiC as a function of microstructural properties as well as temperature and radiation dose.

SUMMARY

Several thermal diffusivity disc samples of high purity CVD-SiC were neutron-irradiated to equivalent doses of about 5-8 dpa-SiC at temperatures from 252 up to 800°C. For this temperature range, the degradation in the thermal diffusivity ranged from about 95% down to 89%, respectively. The reciprocal thermal diffusivity method was used to estimate the phonon mean free paths and defect concentrations before and after the irradiations for these materials. Even though the CVD-SiC material is an excellent monitor of certain neutron irradiation effects, the degradation in the thermal diffusivity (conductivity) appears to be more than a factor of two greater than predicted by recent theoretical model simulations.

PROGRESS AND STATUS

Introduction

A SiC material is exceptionally useful for monitoring some engineering aspects of neutron irradiation. For instance, in 1972 Price developed a method whereby SiC could be used to estimate the temperature inside a capsule during irradiation in a nuclear reactor by monitoring the recovery of its volume swelling after a series of high temperature anneals [1]. In 1995, a similar but more sensitive method for estimating the capsule irradiation temperature was examined at PNNL where the thermal diffusivity recovery rather than the volume swelling recovery was monitored also after a series of high temperature anneals [2]. This was possible because in SiC the thermal conductivity is determined by lattice or phonon conductivity, and in high purity SiC the phonon conductivity is extremely sensitive to the number of lattice imperfections. In high purity SiC neutron-irradiated at moderate temperatures (200-800°C), the lattice imperfections consist primarily of radiation-induced point defects (vacancies and interstitials). By measuring the temperature dependence of the thermal conductivity (or diffusivity) for the irradiated SiC, the phonon mean free path can be estimated and the spacing (or concentration) of the radiation-induced point defects deduced.

Originally, the analysis method developed at PNNL was used to estimate the phonon mean free path for high purity and Be-doped SiC by examining the temperature dependence of the reciprocal thermal diffusivity [3]. In this report, the reciprocal thermal diffusivity method is used to estimate the phonon mean free path for high purity Morton CVD-SiC before and after neutron irradiation at various temperatures. Then, from the calculated phonon mean free paths the radiation point defect concentrations are estimated and compared to some recent theoretical predictions by Li, et al [4].

CVD-SiC Material

The monolithic chemical vapor deposited (CVD) SiC material is a commercial product manufactured by Morton Advanced Materials (now Rohm and Haas) [5]. In the CVD process, methyltrichlorosilane (MTS)

* Pacific Northwest National Laboratory (PNNL) is operated for the U.S. Department of Energy by Battelle Memorial Institute under contract DE-AC06-76RLO-1830.

gas is decomposed onto a carbon substrate at about 1350°C. The CVD material is extremely pure, with typical impurity concentrations of less than 5 wppm. The crystal structure is cubic (3C polytype, commonly referred to as β-SiC) so provides isotropic characteristics. The grain size is between 5 and 10 μm in the plane parallel to the substrate, but the grains are elongated in the <111> growth direction perpendicular to the substrate. The material is homogeneous and typically free of microcracks or other large flaws, but atomic layer stacking faults on the {111} planes are common. There is no porosity in CVD-SiC, and the material is generally considered to be theoretically dense (approximately 3.21 g/cc). The material is stiff (elastic modulus 466 GPa), and has high chemical resistance, thermal conductivity and stability at high temperatures. Therefore, CVD-SiC makes an excellent reflective optics material or electronics substrate, and also an excellent reference material for analyzing neutron irradiation effects.

Reciprocal Thermal Diffusivity Method

The thermal conductivity (k) in SiC is determined by lattice or phonon conduction. An empirical approach, in analogy to the kinetic theory of gasses, relates k for an isotropic solid to the phonon mean free path (λ) via

$$k = 1/3VC_v\lambda \quad (1),$$

where V is the phonon group velocity and C_v is the specific heat at constant volume [6]. In turn, k also may be expressed in terms of the more easily measured thermal diffusivity of the material (α) as

$$k = \alpha\rho C_p \quad (2),$$

where C_p is the specific heat at constant pressure and ρ is the bulk density. By setting Eq. (1) = Eq. (2), the thermal diffusivity may be expressed as

$$\alpha = 1/3V\lambda \quad (3),$$

if the assumption that C_v is approximately equal to ρC_p (generally valid to within 10% up to the melting point of the material). Using α(T) for analysis rather than k(T) eliminates the complicating issue of considering the temperature dependence of C_v. Estimating λ then becomes a diffusion problem rather than an energy transport problem. For SiC, this is important since the temperature range of interest here covers 200°C <T<800°C and the Debye temperature (θ_D = 1080K) lies within this range [7]. The phonon group velocity, estimated from the speed at which vibrations propagate through an elastic material ($V = (E/\rho)^{1/2}$) is about 1.2 x 10^4 m/s for SiC and is only slightly temperature dependent. By inverting and expanding Eq. (3), the reciprocal thermal diffusivity is expressed as

$$1/\alpha = (3/V)\sum_i(1/\lambda_i) = (3/V)\{1/\lambda_o + 1/\lambda_d + 1/\lambda_p\} \quad (4),$$

where the subscripts o, d and p represent the phonon mean free paths associated with intrinsic defects, radiation-induced defects and phonon-phonon interactions, respectively. At higher temperatures ($T>\theta_D$), the phonon mean free paths for defects become temperature independent, and the temperature dependence of 1/α will be dominated by the temperature dependence of the phonon-phonon (Umklapp) interactions. Even at temperatures somewhat below θ_D, the temperature dependence of λ_o and λ_d can be considered temperature independent if the temperature dependence of λ_p is described by

$$\lambda_p = b/(T - T_o) \quad (5),$$

where b is a constant and $T_o = \theta_D/3$ = 360K for SiC. Substituting Eq. (5) into Eq. (4),

$$1/\alpha = (3/V)\{1/\lambda_o + 1/\lambda_d - T_o/b + T/b\} = A + B(T). \quad (6),$$

where $A = (3/V)\{1/\lambda_o + 1/\lambda_d - T_o/b\}$ (7a)

and $B = 3/Vb$ (7b)

If the distribution of the intrinsic and the radiation-induced point defects is assumed to be uniform, the cubic volume λ^3 surrounding each defect is given by a_o^3/NX where a_o is the lattice parameter for β-SiC (0.436 nm), N = 8 is the number of atoms in the unit cell defined by a_o, and X is the fractional concentration of point defects (intrinsic plus radiation-induced). Then the defect inverse mean free path ($1/\lambda$) can be calculated from Eqs. (7a) and (7b) by

$$1/\lambda = 1/\lambda_o + 1/\lambda_d = AV/3 + T_o/b \quad (8),$$

and the defect concentration (X) is

$$X = (1/\lambda)^3 a_o^3/N \quad (9)$$

Irradiation and Test Conditions

The thermal diffusivity of several unirradiated or irradiated CVD-SiC discs (9.5 mm dia. X 2.5 mm thick) was measured simultaneously in air as a function of temperature up to about 400°C by the laser flash method described previously [8]. Unirradiated samples on which the thermal diffusivity had already been measured were then irradiated in the HFIR reactor at ORNL as part of the JUPITER 11J-12J and 14J test series. The samples were irradiated in helium-filled capsules during seven HFIR-cycles at approximately constant, but different temperatures to doses well above saturation (for SiC saturation doses typically are <1 dpa-SiC). For doses above saturation, the SiC acquires a quasi-equilibrium concentration of radiation-induced defects, mostly vacancies and interstitials. After irradiation, the thermal diffusivity was remeasured on these same samples from RT to just below the irradiation temperature. The sample temperatures were held below the irradiation temperature to prevent defect annealing during the measurements.

In Table 1, the specific irradiation conditions for each sample are listed in order of increasing irradiation temperature. Temperature control during irradiation was more difficult for the lower temperatures, so the listed irradiation temperature is end-of-run temperature after seven cycles. The sample loading and irradiation cycle operation details are given in [9a-b].

Table 1. Irradiation conditions for CVD-SiC samples tested in JUPITER 11J or 14J.

Sample ID	Test	Eq. Dose (dpa-SiC)	Irrad. Temp.* (°C)	Est. $\Delta V/V_o$ (%)	α_{irr}/α_o ($\approx k_{irr}/k_o$)
M1	11J	7.9	252 ± 19	2.6	0.044
N5	14J	5.0	310 ± 20	2.5	0.050
N6	14J	5.1	310 ± 20	2.4	0.047
N7	14J	5.2	310 ± 20	2.5	0.046
M2	11J	7.1	355 ± 33	2.3	0.067
N3	14J	6.1	480 ± 20	2.2	0.062
N1	14J	6.8	800 ± 10	1.5	0.134
N2	14J	6.9	800 ± 10	1.5	0.113

*End-of-run temperature

Results and Discussion

In Table 1, the estimated relative volume changes (radiation-induced swelling, $\Delta V/V_o$) were determined from changes in the bulk density measurements made for each disc sample. The listed swelling estimates appear to be 20-30% higher than expected for each irradiation temperature. Nevertheless, the almost linear rate of swelling decrease with increasing irradiation temperature closely follows expected swelling behavior for SiC [10]. The dimensional measurements, carried out with a micrometer, were consistent but perhaps not very precise, which might explain the 20-30% discrepancy. Also, the irradiation temperatures monitored in the 300°C capsule tended to increase slightly (20-40°C) during each cycle [9a-b].

In Figure 1, the measured 1/α-data are graphically presented as a function of temperature (K) for each irradiated CVD-SiC sample listed in Table 1. For reference, the straight line fit to the average 1/α-data for unirradiated CVD-SiC is shown as a solid line near the bottom of the figure.

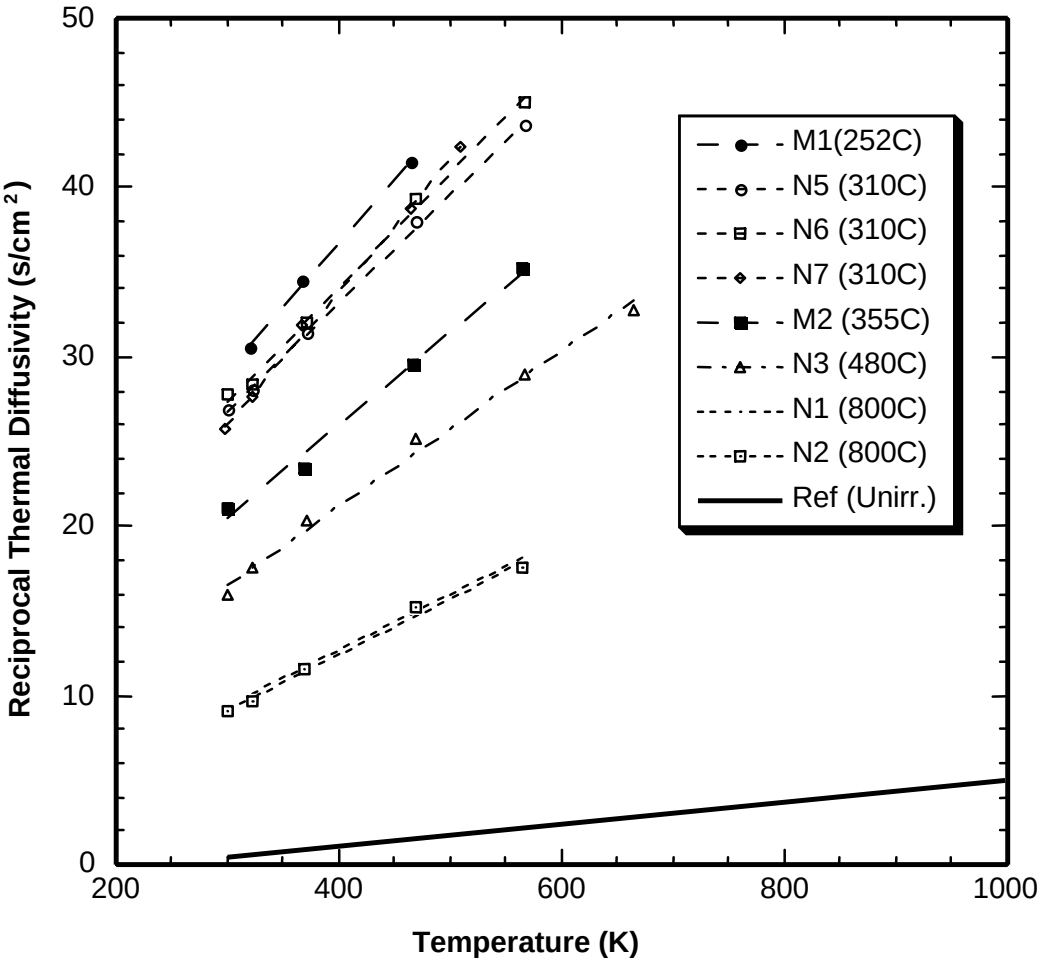

Figure 1. Comparison of the reciprocal thermal diffusivity values determined for several CVD-SiC samples irradiated at different temperatures (irradiation temperature shown in parenthesis) with reference values determined for unirradiated Morton™ CVD-SiC (solid line).

The solid reference line for CVD-SiC was calculated from the α(T)-curves measured before the irradiation for the six samples (N1-N7). The individual α(T)-curves for these unirradiated CVD-SiC samples exhibited characteristic ~1/T temperature dependence, but also a significant spread (±20%). Importantly, repeated measurements on the same sample typically reproduced α-values to ±5%. Apparently, the sample-to-sample variations were real and likely were caused by subtle differences in microstructure even though the sample discs were cut from the same plate. The ±20% spread in the α(T)-curves illustrates the importance of monitoring changes in diffusivity for the same sample before and after irradiation to properly assess changes in diffusivity due to radiation effects.

The intercepts A and slopes B, determined from a linear least squares fit to the 1/α-data for each sample according to Eq. (6) and shown as dashed lines in Figure 1, are listed in Table 2 along with their fit correlation factor R^2. Also listed are the λ- and X-values calculated by Eqs. (8) and (9), respectively.

Table 2. Phonon mean free path and point defect concentration calculations for CVD-SiC samples.

Sample ID	Irrad. Temp (°C)	A (s/cm^2)	B (s/cm^2K)	R^2	λ (nm)	X (appm)
M1	252 ± 19	6.497	0.0755	0.9993	0.74	25,300
N5	310 ± 20	7.624	0.0641	0.9986	0.81	19,200
N6	310 ± 20	7.257	0.0671	0.9957	0.80	20,500
N7	310 ± 20	2.743	0.0778	0.9984	0.81	19,300
M2	355 ± 33	4.016	0.0548	0.9948	1.05	8,900
N3	480 ± 20	2.827	0.0460	0.9931	1.29	4,800
N1	800 ± 10	-0.628	0.0332	0.9893	2.21	960
N2	800 ± 10	-0.745	0.0330	0.9937	2.25	920
Ref.	-	-0.824	0.0054	0.9986	22.2	0.9

The linear fits of the 1/α-data are exceptionally good with correlation coefficients near 0.99. The calculated λ-values decrease continuously from about 22 nm (~50 lattice constants) for the unirradiated reference CVD-SiC down to 0.74 nm (~2 lattice constants) for the sample irradiated at the lowest temperature (252°C). The calculated defect concentration for the reference sample is less than 1 appm, which is consistent with the manufacturer's value of <5 wppm impurities. The defect concentrations for the irradiated CVD-SiC samples decrease continuously from about 25,000 to 920 appm as the irradiation temperature increases from 252 to 800°C. The small concentration of intrinsic defects (<1 appm) in comparison to the extrinsic defect concentrations (>920 appm) illustrates why CVD-SiC makes an ideal irradiation damage monitor. Furthermore, these defect concentration estimates represent saturated values so should be relatively independent of dose.

In a theoretical study of the thermal properties of crystalline β-SiC, Li, et al, used a molecular dynamics simulation together with an empirical potential model to evaluate directly the heat capacity, thermal expansion and thermal conductivity for a perfect crystal, which were in excellent agreement with experimental data [4]. Then by introducing a single defect into the simulation cell (216 atoms, equivalent to 5000 appm defect concentration), they reevaluated their predictions. They found that the heat capacity and thermal expansion coefficients were little affected by the 0.5% defect concentration, in agreement with experimental data for neutron-irradiated SiC. In contrast, the thermal conductivity was markedly degraded by the dominant mechanism of defect scattering by phonons. The simulations predicted that the resulting conductivity would be essentially temperature independent from 1600K down to 436K. Interestingly, the relative conductivity degradation induced by the different types of point defects were ranked: Si interstitial at Tc site > Si antisite > C antisite > Si vacancy > C vacancy. For the 5000 appm defect concentration in β-SiC, the predicted thermal conductivity values ranged from about 15 up to 35 W/mK for the range of defect types listed above.

Listed in Table 2 for sample N3, the predicted concentration of radiation-induced defects is 4800 appm, which closely matches the 5000 appm defect concentration considered by Li, et al. However, at the irradiation temperature of 480°C the thermal conductivity calculated from the measured thermal diffusivity is only about 6.8 W/mK, more than a factor of two less than Li's conductivity predictions for any of the point defect types in SiC. An explanation for this discrepancy needs further investigation.

For engineering applications, the ratio of the irradiated to the unirradiated thermal conductivity values (k_{irr}/k_o) evaluated at the irradiation temperature is a useful quantity because k_{irr} represents the maximum degradation expected above saturation. Since neutron irradiation will have only a relatively small effect on the bulk density and heat capacity, $k_{irr}/k_o \approx \alpha_{irr}/\alpha_o$. This thermal diffusivity ratio was estimated for each irradiated CVD-SiC sample and is listed in Table 1. In Figure 2, the temperature dependence of k_{irr}/k_o is graphically presented for CVD-SiC, for the Hi-Nicalon™ and Sylramic™ composites reported earlier, and for similar values selected from the literature.

In Figure 2, the k_{irr}/k_o-data for CVD-SiC reported by Thorne, et al., Rohde, and Senor, et al. were similarly plotted in [11]. Likewise, k_{irr}/k_o-data for SiC/SiC composite made with first generation Nicalon™ CG fibers were given. The general trend is for the k_{irr}/k_o ratio to increase as the irradiation temperature increases. This trend reflects the relative dominance of temperature independent point defect phonon scattering in the lower temperature range, while the temperature dependent phonon-phonon scattering becomes relatively more important as the irradiation/test temperature increases. The curve for CVD-SiC represents the lower limit for irradiation degradation in SiC. In contrast, the phonon scattering in SiC/SiC composite materials is dominated by numerous structural defects even before irradiation, and the addition of irradiation point defects has a relatively small effect on the conductivity degradation. Thus, the curve through the Nicalon™ CG composite data marks an upper limit for the k_{irr}/k_o ratio for SiC-based materials. The new k_{irr}/k_o data for the SiC/SiC composite made with second generation Hi-Nicalon™ or Sylramic™ fiber generally fall in between the two limits.

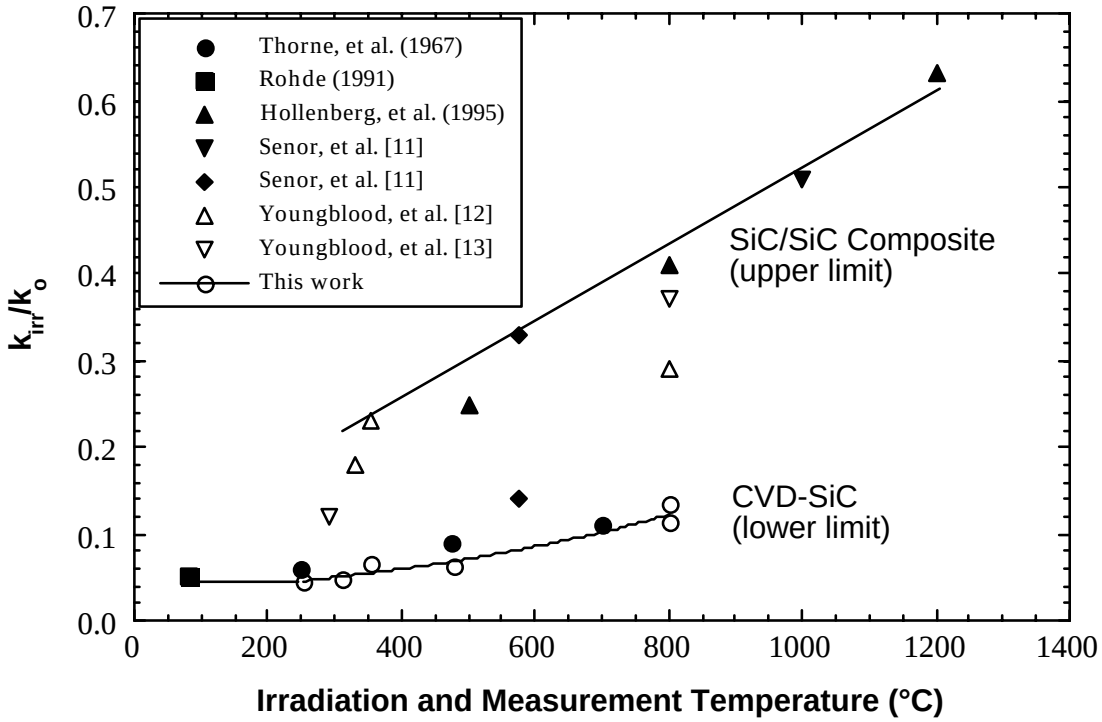

Figure 2. Conductivity degradation as a function of irradiation and test temperature for CVD-SiC and SiC/SiC composite.

FUTURE WORK

An attempt will be made to examine the kinetics of the thermal diffusivity recovery during annealing for the CVD-SiC samples irradiated at different temperatures and containing vastly different concentrations of point defects. Appropriate TEM analysis will accompany the thermal diffusivity recovery studies.

REFERENCES

[1] J. Price, "Annealing behavior of neutron-irradiated SiC temperature monitors," Nuclear Technology 16, 536-542 (1972).

[2] G. E. Youngblood, "Passive SiC irradiation temperature monitor," p. 324 in Fusion Materials Semiannual Progress Report (FMSPR) for period ending December 31, 1995. (DOE/ER-0313/19)

[3] G. E. Youngblood and W. Kowbel, "Improvements of the thermal conductivity of SiCf/SiC composite," p. 107 in *ibid*.

[4] Li, Lisa Porter and Sydney Yip, "Atomistic modeling of finite-temperature properties of crystalline β-SiC: II. Thermal conductivity and effects of point defects," J. Nucl. Mater. 255, 139-152 (1998).

[5] Morton Advanced Materials, 1996. CVD Silicon Carbide, technical Publication 107, Morton Advanced Materials (now Rohm and Haas), Woburn, MA 01801.

[6] D. R. Flynn, "Thermal conductivity of ceramics," p. 63 in Mechanical and Thermal Properties of Ceramics, ed. J. B. Wachtman, Jr., NBS Special Publication 303, Washington D.C., May, 1969.

[7] J. S. Haggerty and A. Lightfoot, "Opportunities for enhancing the thermal conductivities of SiC and Si3N4 ceramics through improved processing," Ceram. Eng. Sci. Proc., 475-487 (1996).

[8] D. J. Senor, G. E. Youngblood, D. V. Archer and C. E. Chamberlin, "Recent progress in thermal diffusivity testing of SiC-based materials for fusion reactor applications," p. 102 in the Proceedings of the 3rd IEA SiC/SiC Workshop, January 29-30, 1999, Cocoa Beach, Florida.

[9a] A. L. Qualls, "HFIR-MFE-RB-14J specimen loading listing and operational summary," p. 241 in FMSPR for period ending June 30, 2000. (DOE/ER-0313/28)

[9b] M. L. Grossbeck, K. E. Lenox and M. A. Janney, "The Monbusho/U.S. experiment: HFIR-MFE-RB-11J and 12J," p. 254 in FMSPR for period ending June 30, 1997. (DOE/ER-0313/22)

[10] S.J. Zinkle and L.L. Snead, "Thermophysical and mechanical properties of SiC/SiC composites," p. 93 in FMSPR for period ending December 31, 1998. (DOE/ER-0313/24)

[11] D. J. Senor, G. E. Youngblood, C. E. Moore, D. J. Trimble, G. A. Newsome and J. J. Woods," Effects of neutron irradiation on thermal conductivity of SiC-based composites and monolithic ceramics," Fusion Technology 30(3), 943-955 (1996).

[12] G. E. Youngblood, D. J. Senor and R. H. Jones, "Thermal diffusivity/conductivity of irradiated Hi-Nicalon™ 2D-SiC$_f$/SiC composite," in this FMSPR.

[13] G. E. Youngblood, D. J. Senor and R. H. Jones, "Thermal diffusivity/conductivity of irradiated Sylramic™ 2D-SiC$_f$/SiC composite," in this FMSPR.

EVALUATION OF TRANSTHICKNESS TENSILE STRENGTH OF SiC/SiC COMPOSITES - T. Hinoki, E. Lara-Curzio and L.L. Snead (Oak Ridge National Laboratory)

OBJECTIVE

The objective of this work is to develop experimental technique for measuring transthickness tensile strength using diametral compression and to understand usability of the experiment and specimen size effect.

SUMMARY

The transthickness tensile strength (TTS) of 2-D CVI-SiC/SiC composites reinforced with Tyranno SA fibers was evaluated by the diametral compression test. The effects of specimen size and specimen shape on the magnitude of the TTS were studied and the results were analyzed using an analysis of variance (ANOVA) and Weibull statistics.

Specimens failed along an interlaminar plane adjacent to the line of action of the applied load and fractographic analyses revealed that the crack had propagated through matrix pores and along interfaces between the fiber, fiber coating and matrix. The magnitude of the TTS was found to be independent of specimen size or shape for the range of specimen dimensions investigated, although the amount of scatter was largest for the results obtained from the evaluation of the smallest specimens. The characteristic value of the TTS and the Weibull modulus for the distribution of TTS values were 24.9 MPa and 6.48, respectively.

PROGRESS AND STATUS

Introduction

SiC/SiC composites are considered for use in extremely harsh environments primarily due to their excellent thermal, mechanical and chemical stability, and the exceptionally low radioactivity following neutron irradiation [1-2]. In particular, recent improvement in the crystallinity and purity of SiC fibers, the developments and improved composite processing have improved physical and mechanical performance under harsh environments [3-5]. The tensile strength perpendicular to the lay-up planes of 2D laminated composites (transthickness tensile strength: TTS) is typically much lower than the strength of the composite on the lay-up plane. Therefore, it is likely that the design of engineering components utilizing these materials will be limited by strength in this direction. Recently, the American Society for Testing and Materials (ASTM) standardized test method C1468 to evaluate the TTS of continuous fiber-reinforced ceramic matrix composites (CFCCs). Because this test method relies on the use of adhesively-bonded extenders to transfer load to the specimen, its applicability is limited by the properties of the adhesive and can only be used at low temperatures. The diametral compression test [6-9], also known as Brazilian test, overcomes the limitations imposed by the adhesive and, therefore, can be applied at high temperatures. This test method is based on the fact that tensile stresses develop when a circular disk is compressed by two diametrically opposed forces as shown in Fig. 1. These tensile stresses exist perpendicularly to the loading direction and are proportional to the applied compressive force. The preparation of test specimens and the actual tests are relatively straightforward, making this test method

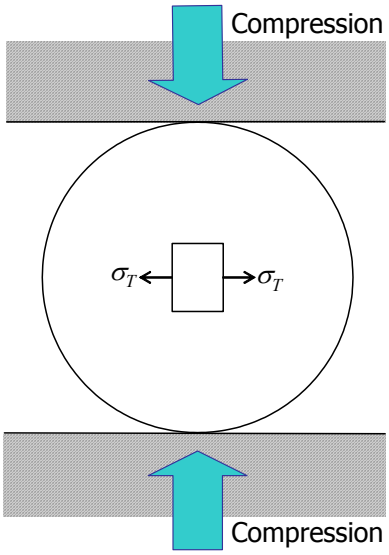

Fig. 1: Transthickness tensile strength by diametral compression

amenable for use. Because of these reasons, this test method is currently being considered for ASTM standardization.

In this paper we report the TTS results from the evaluation of a 2-D SiC/SiC CFCC by diametral compression. The effects of specimen size and shape on the magnitude of the TTS were investigated and the results were analyzed using Weibull statistics. A discussion regarding the determination of the TTS from the magnitude of the applied load and specimen dimensions is also included.

Experimental

The material used in this investigation consisted of plain-weave Tyranno™ SA fabric, stacked in [0°/90°] direction, and a SiC matrix synthesized by forced-flow thermal-gradient chemical vapor infiltration [10]. A dual coating of approximately 80 nm-thick SiC and 570 nm-thick C was applied to the fiber prior to matrix infiltration. Pieces with 75 mm diameter and 12.5 mm thick were obtained with 22.6 % porosity. Details of the material and its fabrication can be found elsewhere [6]. Disk specimens of various sizes (diameter: 3.2, 6.4, 9.4 mm, thickness: 1.7, 3.1, 4.5, 6.0 mm) were obtained from the composite piece by core-drilling using a diamond-impregnated tool. Truncated disk specimens (diameter: 6.5 mm, thickness: 3.1 mm, width: 3.2 mm) were also obtained as illustrated in Fig. 2.

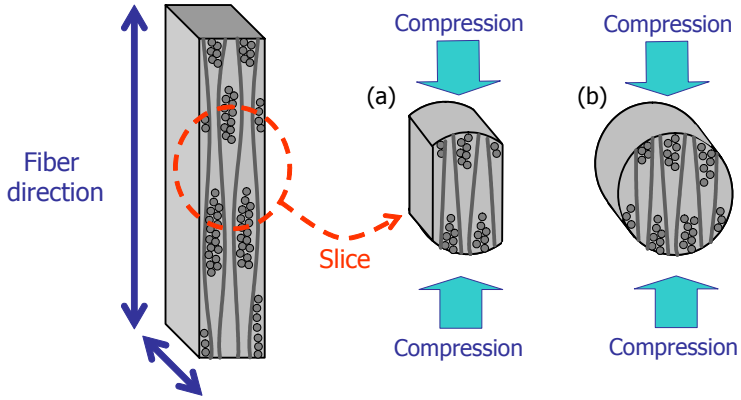

Fig. 2: Specimen types for diametral compression tests, (a) truncated disk, (b) disk

Transthickness tensile tests were carried-out at ambient conditions (20°C/35% RH) using an electromechanical testing machine at a constant cross-head displacement rate of 10 μm/s. The test specimens were subjected to diametral compression using two parallel plates of Hexoloy® SA SiC. This material was selected due to its low Poisson's ratio (0.14) and high elastic modulus (390 GPa) to minimize radial expansion at the contact area. The specimens were aligned and fixed with double-sided tape on the bottom plate. Fig. 2 illustrates the relation between the fabric orientation and the loading direction. At the end of the tests, the fracture surfaces were examined by scanning electron microscopy.

Result and discussion

Fig. 3 shows typical stress-displacement curves for specimens of various sizes. In every case the load increased monotonically to a peak value, which was followed by an abrupt drop and an audible indication that the sample had failed. Every specimen failed by a crack that propagated along the loaded diameter, along an interlaminar region through large pores in the matrix, and along the fiber/fiber coating/matrix interfaces. Fig. 4 is an SEM micrograph of a typical fracture surface. Debonded fibers and CVI coated fiber-bundle surfaces without matrix infiltration were evident on the fracture surfaces.
The TTS (σ_T) was determined according to Eq. (1).

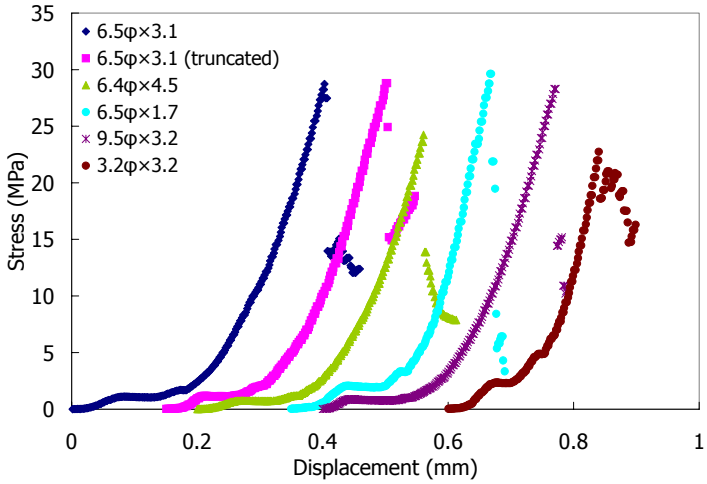

Fig. 3: Typical loading curves of various size specimens

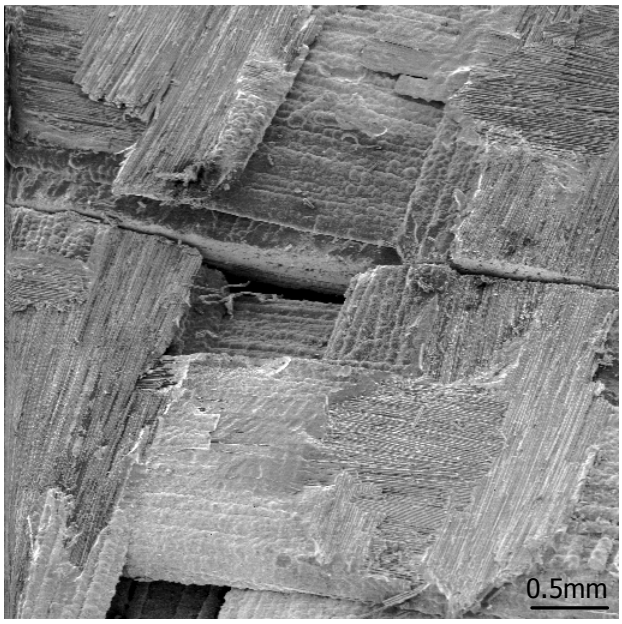

Fig. 4: Fracture surface after the diametral compression test

$$\sigma_T = \frac{2P}{\pi dt} \qquad (1)$$

where *P* is the load at failure, *d* is the diameter, and *t* is the thickness of the specimen [7,8]. However, this relationship between the TTS and the failure load is only valid for isotropic materials and, therefore, it needs to be corrected to account for the transverse isotropy of the material evaluated. This work is in progress and will be reported in the future.

Fig. 5(a) shows the effect of diameter on the TTS of SiC/SiC test specimens 3.1 mm-thick, while Fig. 5(b) shows the effect of thickness on the TTS of SiC/SiC 6.5 mm-diameter test specimens. The error bars represent one standard deviation about the mean value. In the thickest specimens, it was difficult to identify the magnitude of the load at which failure ocurred, since the curves showed multiple load drops. Two values of TTSs were obtained for these specimens from two critical loads in the curves. An analysis of variance (ANOVA) [11] of all the test results revealed that there are no significant differences among these mean

values at the 95 % confidence level. Therefore, for the range of values examined, there are no apparent size effects on the magnitude of the TTS of the material evaluated. It was found, however, that scatter was largest for the TTS values obtained with small-diameter (3.2 mm) specimens, which can be attributed to lack of precision in the alignment of the test specimen during the test, and the reduced number of fabric unit cells in the gauge section of the test specimen.

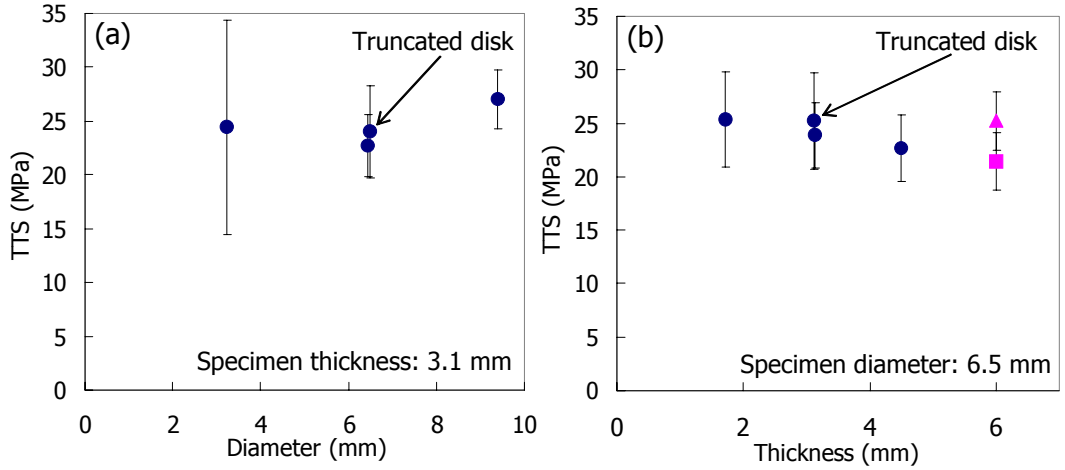

Fig. 5: Size effects on transthickness tensile strength, (a): effect of diameter, (b): effect of thickness

The TTS results were analyzed using Weibull statistics. Fig. 6 shows Weibull plots for (a) TTS of standard size specimens (diamter: 6.4 mm, thickness: 3.1 mm); (b) TTS of all specimens without the thickest specimens (thickness: 6.0 mm). The Weibull modulus and scale parameter for the standard specimens are 9.41 and 25.1 MPa, respectively, while those for the entire data set are 6.48 and 26.7 MPa, respectively. The Weibull modulus of the strength data set that includes all specimens is smaller than that of standard size specimens, and this is attributed to the large scatter of the data obtained from the evaluation of small diameter specimens. The Weibull modulus for a data set that excludes the small diameter specimens is 8.15. This relatively large value of the Weibull modulus is consistent with materials that contain large-sized defects that are responsible for failure.

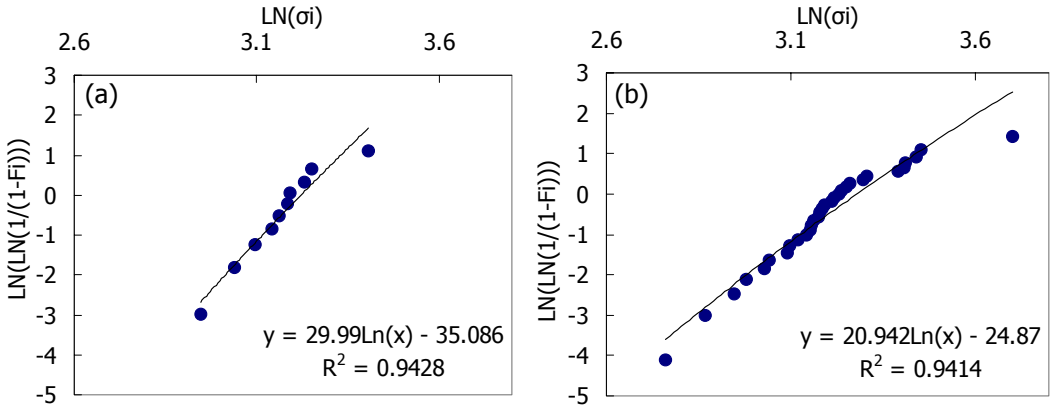

Fig. 6: Weibull plots of transthickness tensile strength of (a): standard size specimens and (b): all specimens

It was also found that the TTS of the material evaluated was independent of specimen geometry, i.e.- disk-shaped versus truncated disk-shaped specimens. This is important because for the range of dimensions investigated in this work, these results validate the use of truncated-disks specimen geometries when the material is available only as a thin plate and the diameter of the disk is larger than the thickness of the plate. Therefore, these results support the validity of this test method for the evaluation of the

transthickness tensile strength of 1-D and 2-D CFCCs.

CONCLUSION

The TTS of CVI-SiC reinforced with Tyranno™ SA fibers was evaluated by diametral compression using specimens of various sizes (diameter and thickness) and shapes (disks vs. truncated disks). All specimens failed along an interlaminar plane adjacent to the diametral plane of the applied load. Analysis of the fracture surfaces revealed that the dominating crack grew along large pores in the matrix and along the fiber/fiber coating/matrix interfaces. It was found that for the range of specimen dimensions investigated, the magnitude of the TTS was independent of size or specimen geometry (disk vs. truncated disk). It was also found that there was considerable scatter in the TTS results obtained from the evaluation of the smallest disk specimens, and this could be attributed to reduced precision in the alignment of the specimen during the test, and the reduced number of fabric unit cells in the gauge section. The average TTS, the one standard deviation, the Weibull modulus and the scale parameter for the entire data set were 24.9 MPa, 4.77, 6.48 and 26.7 MPa, respectively. Although the magnitude of TTS was determined from the peak load using the elastic solution for isotropic materials and, therefore, needs to be corrected to account for the transverse isotropy of the material, these results demonstrate the applicability of this test method to determine the TTS of CFCCs. On-going work is focused on the determination of correction factors to account for anisotropy and the implementation of this test method at elevated temperatures.

ACKNOWLEDGEMENTS

The material used in this work was fabricated under the collaboration program of Oak Ridge National Laboratory, Japan Atomic Energy Research Institute, and Kyoto University. This work was supported by the office of Fusion Energy Science, US DOE under contract DE-AC-05-00OR22725 with UT-Battelle, LLC.

REFFERENCES

[1] A. Kohyama and Y. Katoh, Ceramic Transactions, 144 (2002) 3-18.
[2] L.L. Snead, R.H. Jones, A. Kohyama and P. Fenici, J. Nucl. Mater., 233-237 (1996) 26-36.
[3] M. Takeda, A. Urano, J. Sakamoto and Y. Imai, J. Nucl. Mater., 258-263 (1998) 1594-1599.
[4] T. Ishikawa, S. Kajii, T. Hisayuki, K. Matsunaga, T. Hogami and Y. Kohtoku, Key Eng. Mater., 164-165 (1999) 15-18.
[5] T. Hinoki, L.L. Snead, Y. Katoh, A. Hasegawa, T. Nozawa and A. Kohyama, J. Nucl. Mater., 307-311 (2002) 1157-1162.
[6] A. Okada, J. Mater. Sci., 25 (1990) 3901-3905.
[7] S. P. Timoshenko and J. N. Goodier, Theory of Elasticity, McGraw-Hill, NY (1970)
[8] T.V. Parry and A.S. Wronski, J. Mater. Sci., 25 (1990) 3162-3166
[9] T. Hinoki and E. Lara-Curzio, 104th annual meeting of Am. Ceram. Soc., St. Louis, Apr., 2002.
[10] T. Hinoki, L.L. Snead, T. Taguchi, N. Igawa, W. Yang, T. Nozawa, Y. Katoh and A. Kohyama, Ceramic Transactions, 144 (2002) 55-68.
[11] R.L. Scheaffer and J.T. McClave, Statistics for Engineers, PWS Publishers, Boston, (1982).

DEVELOPMENT OF REFRACTORY ARMORED SILICON CARBIDE - T. Hinoki, L.L. Snead, C.A. Blue, M.L. Santella, D.C. Harper and N. Hashimoto (Oak Ridge National Laboratory), H. Kishimoto (Kyoto University)

OBJECTIVE

The objective of this work is to develop refractory armor on silicon carbide for fusion applications.

SUMMARY

Tungsten (W) and molybdenum (Mo) were coated on silicon carbide (SiC) as refractory armor using high power plasma arc lamp at powers up to 23.5 MW/m^2. Both W powder and Mo powder were melted and formed coating layers on silicon carbide. The effect of pretreatment (vapor deposition of titanium (Ti), W and Mo and annealing) and sample heating conditions on microstructure of the coating and coating/substrate interface were investigated. The microstructure was observed by scanning electron microscopy (SEM) and optical microscopy (OM).

A uniform strong W coating was successfully formed. Tungsten vapor deposition and pre-heating at 5.2 MW/m^2 made for a refractory layer containing no cracks which propagated into the SiC substrate. This layer was formed without the thick reaction layer (WC and W_5Si_3) reported in previous studies. Moreover the thinner interface transition layer and armor avoid coefficient of thermal expansion (CTE) mismatch driven failure previously reported. For this study, small W_xC_y grains were observed adjacent to interface. Silicon carbide grains and W_xSi_y grains were observed within W coating. By contrast, Mo was not successfully formed. Most of Mo coating debonded at reaction layer due to too much absorbed energy for Mo and larger CTE mismatch than that of W and SiC. Further study at lower absorbed powers would be required to carry the Mo coating further.

PROGRESS AND STATUS

Introduction

Silicon carbide can be used in extremely harsh environment due to its excellent thermal, mechanical and chemical stability. Silicon carbide also provides exceptionally low radioactivity following neutron

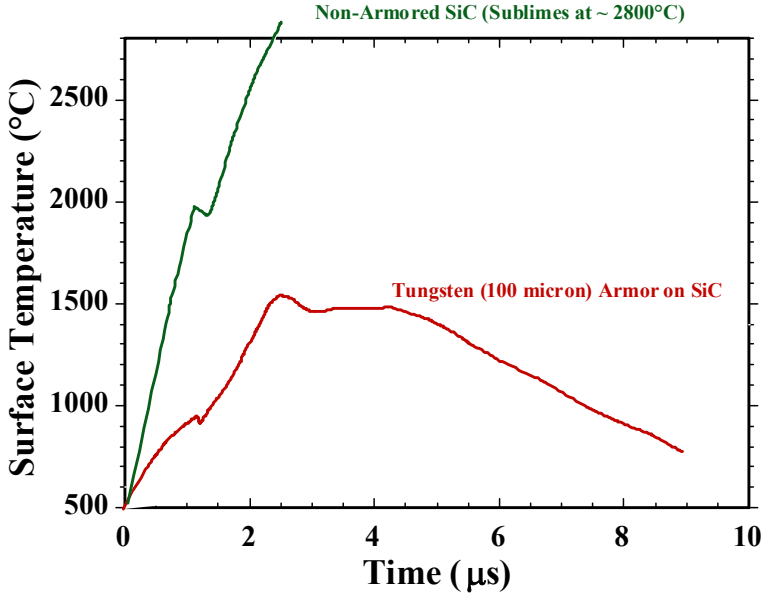

Figure 1: Effect of W armor on the calculated surface temperature of SiC*

* Data provided by R. Raffray, UCSD, 2002.

irradiation [1]. The intrinsic features of SiC make SiC fiber reinforced SiC matrix composites (SiC/SiC composites) significantly attractive structural material for nuclear application [2].

Refractory armored materials (RAM's) have been previously considered in the magnetic fusion energy community to reduce the introduction of power-sapping impurities into the plasma [3], and to reduce erosion. Recently RAM's have been considered for inertial fusion energy systems as a means to absorb and handle the very high impulse heat loading expected. Figure 1 shows the effect of W armor on the calculated surface temperature of non-armored SiC and W armored SiC.

To select the refractory armor material for SiC, CTE is one key to obtain a strong bond between substrate and refractory armor, since CTE mismatch causes residual stress at the interface. To reduce the CTE mismatch, W and Mo were selected as the refractory armor materials for SiC. Table 1 shows the thermal properties of SiC used, W and Mo.

Table 1: Thermal properties of substrate and coating materials

Material	CTE (RT, 10^{-6}/K)	Melting point (°C)	Thermal conductivity (RT, W/mK)
Hexoloy SA SiC	4.02	2797 (α-SiC)	125.6
W	4.4	3370	163.3
Mo	5.35	2617	138

There are many techniques to apply refractory metals to ceramic substrates including plasma spraying, chemical and plasma vapor deposition. However, the chemical bonding, hence mechanical strength of layers produced with those techniques is low. A novel approach to forming this refractory layer using the Oak Ridge National Laboratory (ORNL) 300 kW infrared plasma arc lamp (IR processing) [4] was used. This facility can apply up to 35 MW/m^2 over an area of 35 cm by 3.175 cm in transient or continuous mode. The assumption driving application of this system for SiC/W was that by applying transient infrared power a layer of W powder could melt and react with the surface of the SiC while keeping the bulk SiC below its sublimation temperature.

Experimental

The substrate material for this study was Hexoloy® SA SiC (sintered α-SiC). Substrates with dimension 25 mm (long) × 15 mm (wide) × 3 mm (thick) were machined from plate. As refractory armor material, W and Mo powder were brushed or sprayed on the SiC to an approximate thickness of 100 μm. Several kinds of pretreatments including vapor deposition of Ti, W and Mo, and pre-melt substrate annealing were applied prior to forming the armor. The thickness of vapor deposition of Ti, W and Mo was 0.20 μm, 2.00 μm and 1.18 μm, respectively. The annealing temperatures after the vapor deposition were 1300 °C or 1500 °C for 72 hours in a vacuum. The conditions of the pretreatments are summarized in Table 2.

Table 2: Pretreatment conditions

Vapor deposition (μm)	Annealing (°C)
W (2.00)	
Ti (0.20) + W (2.00) or Mo (1.18)	
W (2.00)	1300 (72 hours)
Ti (0.20) + W (2.00) or Mo (1.18)	1300 (72 hours)
W (2.00)	1500 (72 hours)
Ti (0.20) + W (2.00) or Mo (1.18)	1500 (72 hours)

The plasma arc lamp used by IR processing is mounted on a Cincinnati-Milacron model T3-776 robotic arm. Using the robotic arm in conjunction with the Plasma Arc Lamp allows for a variety of experiments to be performed in a short amount of time. The powder on SiC was heated by the lamp with 23.5 MW/m^2 for 2~5 sec at argon flow environment. Pre-heating and post-heating at lower power were also applied to optimized IR processing conditions.

The refractory armored SiC was sliced, and the coating and interface were observed by OM and SEM with EDS.

Result and discussion

Both W and Mo on SiC melted in a couple of seconds by IR processing and formed coating on SiC. It is most likely that this SiC was removed by sublimation of the surface of the SiC prior to, ordering the W powder melt. An OM image is given if Figure 2, along with a micrograph of the as-machined substrate to allow comparison of the surface roughness. No diffusion of W into SiC was observed.

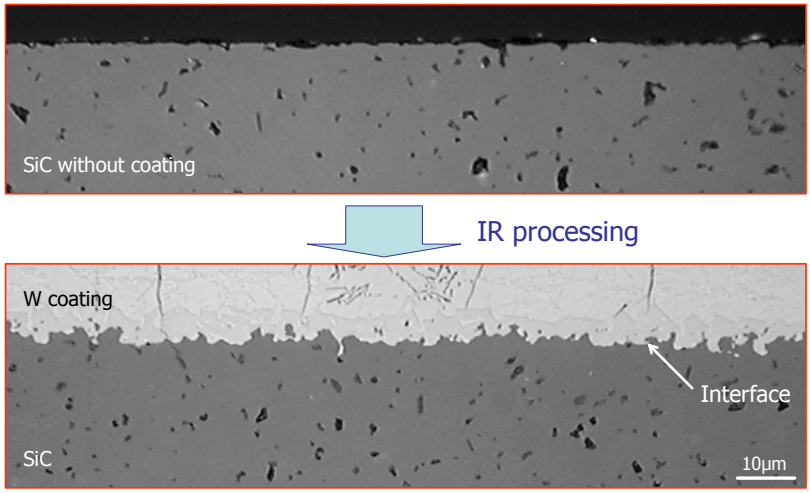

Figure 2: Effect of IR processing on SiC surface roughness (OM images)

All W coated specimens with pretreatments were stable following IR processing, while most of specimens without the pretreatments broke following IR processing. In the “pretreated” cases, the critical ingredient appears to be the vapor deposited W layer. The addition of very thin Ti layer under the vapor deposited W was used in the hope of aiding the wetting of W to SiC. It has been reported that reaction between W and SiC occurs above 1200 °C leading to a bulk diffusion path $W/W_5Si_3/WC/SiC$ [5]. The thickness of those regions depends on temperature and time. In this work it was assumed that a reaction layer several microns thick was formed at interface. However, given the apparent removal of surface SiC through sublimation and the absence of Ti (using EDS) it is felt that the use of Ti and the annealing were unnecessary.

IR processing conditions were optimized using a series of specimens without pretreatments. Maximum power to melt powder was fixed to 23.5 MW/m^2 for 3 seconds. Pre-heating and post-heating at reduced power was used to decrease thermal shock. Post-heating did not improve stability of specimens following IR processing with all samples fracturing. In contrast, pre-heating at 5.2 MW/m^2 for 20 seconds improved stability of specimens, and the specimens with the pre-heating was stable following IR processing. Figures 3 are OM (Nomarski) images showing the effect of W vapor deposition and pre-heating on crack propagation into SiC. In the specimen without W deposition and pre-heating, large cracks induced from W surface propagated into substrate SiC (a), while cracks induced from W surface did not reach the W/SiC interface in the specimens with W vapor deposition (b) and pre-heating (c). It is considered that W powder was porous prior to IR processing allowing part of the energy to be absorbed by the SiC directly, and the energy caused expansion of SiC near interface with crack propagation at cooling. Slowing down the cool down by slowing down the lamp power did not reduce the armor and substrate cracking. However if the whole SiC substrate is allowed to absorb energy at low power not to melt W powder prior to W coating formation, it will expand with temperature increasing. Relative expansion of SiC near surface caused by high energy to melt W was reduced by pre-heating. As a result pre-heating reduced the crack into SiC. By adding the thin W layer by vapor deposition, it is thought that IR power was not effectively coupled to the SiC substrate reducing expansion of SiC near surface.

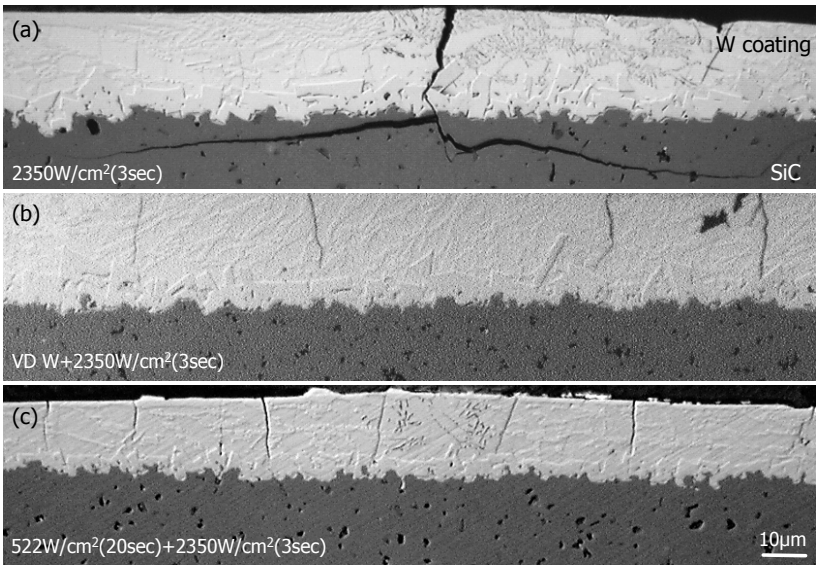

Figure 3: Effect of vapor deposited W and pre-heating on crack propagation into SiC

Figure 4 shows back scattering (composition) electron image of a specimen with pre-heating (5.2 MW/m^2 + 23.5 MW/m^2). SEM observation reveals a complicated microstructure within the W coating. Through EDS analysis, grains it was found that grains adjacent to W/SiC interface within W coating was W_xC_y. The W_xSi_y grains were found near surface. SiC grains were also found within W coating. It is considered that the sublimated SiC at interface decomposed and reacted within the melted W. It has been reported that W was coated on SiC successfully by other methods. However those W coatings included relatively thick reaction layers of WC and W_5Si_3 [5]. Even with strong bonding at room temperature, those reaction layers cause fracture at the interface by stress concentration attributed to mismatch of CTE at high temperature. For this reason W coating with thin reaction layers are preferred. By IR processing the reaction layer was not formed at W/SiC interface, although relatively small reacted grains were observed. This grain structure can reduce the crack initiation by CTE mismatch compared with the reaction layers, since the stress caused by CTE mismatch distributes to each grain boundary.

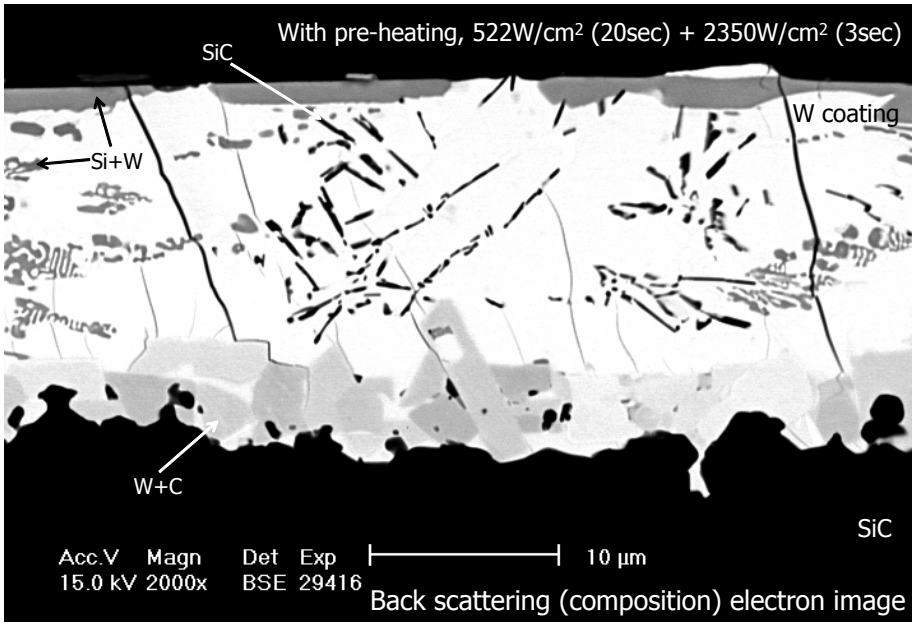

Figure 4: SEM image (back scattering electron image) of W coating on SiC

Molybdenum coating was applied by IR processing at the same power used for W coating. Most of Mo coating disappeared due to application of too high a power density for Mo. Figures. 5 show OM images

of the remaining Mo coating (a, b) and debonded interface (c). The reaction layer was formed at Mo/SiC interface. It was found that debonded substrate surface did not have the reaction layer and most of Mo coating debonded at the reaction layer. The difference of CTE of Mo and SiC is larger than that of W and SiC. Even with optimization of IR processing, it might be difficult to obtain strong bonding with Mo coating compared with W coating.

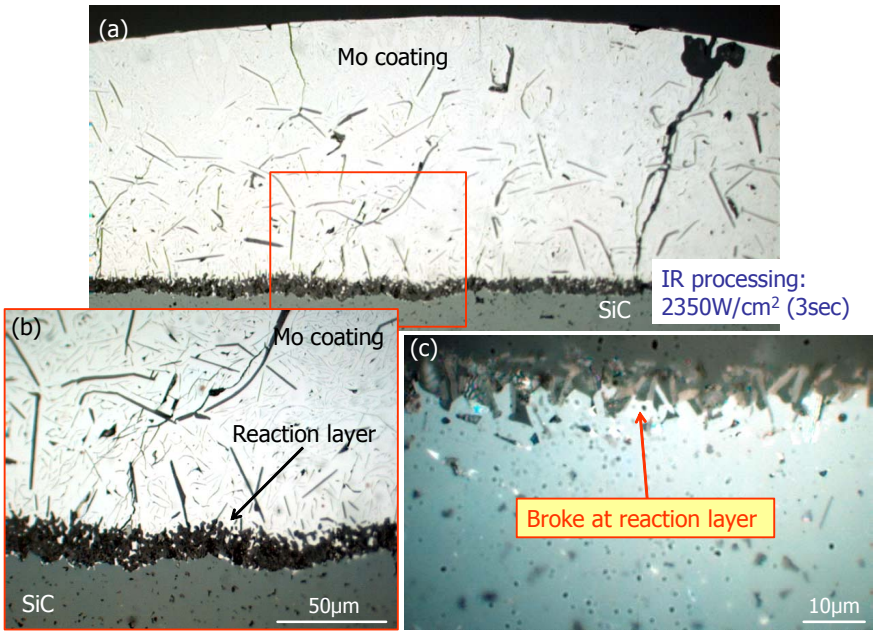

Figures 5: Mo coating on SiC (a,b) and debonded surface of SiC (c)

CONCLUSION

1. Tungsten coating was formed successfully on a SiC substrate. The SiC substrates without pretreatments or pre-heating were broken by IR processing. It was found that vapor deposition of W and pre-heating significantly reduced cracks within the silicon carbide. The W_xC_y grains were formed near interface within W coating in all specimens, while SiC grains and the W_xSi_y grains were observed in middle and surface of W coating. It was found that a thick reaction layer which causes fracture due to CTE mismatch was not formed by the coating method used in this work.
2. Most of Mo coating disappeared due to application of too high a power density. Furthermore a reaction layer which may have enhanced crack propagation was observed.

ACKOWLEDGEMENT

This program was supported by under the DOE High Average Power Laser Program.

REFFERENCE

[1] T. Noda, J. Nucl. Mater., 233-237 (1996) 1475-1480.
[2] L.L. Snead, R.H. Jones, A. Kohyama and P. Fenici, J. Nucl. Mater., 233-237 (1996) 26-36.
[3] V. Barabash, G. Federici, M. Rodig, L.L. Snead and C.H. Wu, J. Nucl. Mater., 283-287 (2000) 138-146.
[4] C. A. Blue, V. K. Sikka, E. K. Ohriner, P.G. Engleman, and D.C. Harper, JOM-e, 52[1] (2000).
[5] F. Goesmann and R. Schmid-Fetzer, Mater. Sci. Eng., B34 (1995) 224-231.

TOTAL DPA CROSS SECTIONS FOR SIC AS A FUNCTION OF NEUTRON ENERGY - H. L. Heinisch, L. R. Greenwood, W. J. Weber and R. E. Williford (Pacific Northwest National Laboratory)*

OBJECTIVE

The objective of this work is to calculate total DPA cross sections for SiC as a function of neutron energy using the best available input for stopping powers and displacement threshold energies.

SUMMARY

Total DPA cross sections for SiC as a function of neutron energy have been calculated using the latest and best knowledge about damage production in SiC. We encourage the adoption of these cross sections as the standard to be used for calculating radiation damage production in DPA for all neutron-irradiated SiC samples, including those in past irradiations.

PROGRESS AND STATUS

This is an extended abstract of a paper entitled “Displacement Damage And Transmutation Calculations For Neutron-Irradiated Silicon Carbide” by H. L. Heinisch, L. R. Greenwood, W. J. Weber and R. E. Williford, which has been submitted for publication in the Journal of Nuclear Materials.

Introduction

The standard damage parameter for nuclear materials is displacements per atom (DPA), which incorporates information on the response of the material, i.e. displaced atoms, as well as simply the (fast) neutron fluence to which it was exposed. The concept of DPA was initially developed for monatomic metals, where the definition of DPA is somewhat simpler than in multi-component ceramic materials where the various atom displacement energies are not easily measured. In the past few years significant progress has been made in modeling displacement damage in SiC using molecular dynamics computer simulations to determine displacement threshold energies [1] and employing improved models for stopping powers [2]. This information has been utilized for the calculation of DPA cross sections for SiC as a function of neutron energy [3].

To be most useful, the DPA damage parameter should be defined and calculated the same way by all concerned, and preferably for all past, present and future experiments, models and analyses. To that end, we include here the DPA cross sections as a function of neutron energy for SiC in tabulated form, Table 1. This function, along with neutron flux and energy spectrum information, can be used to calculate the DPA value for SiC in any irradiation.

Displacements per Atom

Displacements per atom is a calculated, hypothetical measure of radiation damage that reflects not only the dose and type of irradiation, but also includes some measure of the material’s response to the irradiation. DPA is not a measure of the residual crystal lattice defects actually created in a material, but rather it is a measure of the “damage energy” deposited in the material by the irradiating particles in terms of how many atoms could possibly be permanently displaced from their lattice sites to stable interstitial sites by this damage energy. In each individual radiation damage event, the primary knock-on atom (PKA, an atom that has received kinetic energy through interaction with an irradiating neutron) imparts energy to neighboring atoms, producing a cascade of collisions. Within the affected volume of the collision cascade many atoms are displaced significantly from their lattice sites, creating a near-molten zone in the crystal. But within picoseconds many of the displaced atoms return to vacant sites, healing

* Pacific Northwest National Laboratory (PNNL) is operated for the U.S. Department of Energy by Battelle Memorial Institute under contract DE-AC06-76RLO-1830.

much of the damage. The actual number of lattice defects ("permanently" displaced atoms) remaining after the cascade region cools is usually a small fraction of the atoms initially displaced in the cascade. This fraction is often referred to as the "efficiency" of defect production relative to the calculated DPA value, and it can vary considerably depending on the material and the irradiating conditions, including neutron energies and irradiation temperature. Although it does not reflect the actual residual defects produced in the material, DPA has been found to be an extremely useful damage parameter for correlating the effects of radiation damage in the same material irradiated in different neutron environments, and it is the standard damage parameter for nuclear structural materials.

The original model for displacement damage, developed initially for simple metals, is due to Kinchin and Pease [4], and the standard formulation of it by Norgett et al [5], often referred to as the "NRT" model, is

$$\begin{aligned} \nu(T) &= 0 && T < E_d \\ &= 1 && E_d < T < 2E_d \\ &= 0.8\ T/2E_d && T > 2E_d \end{aligned} \qquad (1)$$

where $\nu(T)$ is the number of displaced atoms produced by a recoil atom of energy E and damage energy T, and E_d is the average threshold displacement energy for an atom in the metal. Damage energies T(E) can be calculated for each recoil energy E using an analytic expression due to Robinson [6]. The threshold displacement energy E_d can be determined experimentally for simple metals, while for more complicated materials, such as polyatomic materials or those with complex crystal structures, where there may be several different displacement energies, the values of E_d are best determined with the aid of computer simulations. The energies required to displace Si and C atoms from their lattice sites to interstitial positions in SiC have been determined using atomic-scale molecular dynamics and first principles calculations [1]. The values of displacement energies averaged over all directions in SiC have been determined to be 20 eV for C and 35 eV for Si, and it is recommended that these values be used universally for calculating DPA in irradiated SiC [7]. There are actually four minimum recoil damage energies required to create displacements in SiC, depending on the projectile/target combinations: 41 eV (C/Si), 35 eV (Si/Si), 24 eV (Si/C) and 20 eV (C/C) [3]. Thus, a C atom must have kinetic energy of at least 41 eV to provide the 35 eV to a Si atom that is necessary to displace it.

Treating polyatomic materials introduces other complications to the formulation of damage functions due to the interactions among sublattices. Thus, in the present work displacement functions for polyatomic materials, $\nu_{ij}(E)$, for the average number of atoms of type j initiated by a PKA of type i and energy E, were obtained by numerical solutions of the coupled integro-differential equations for $\nu_{ij}(E)$ devised by Parkin and Coulter [8-10] and using the displacement energies discussed above. Atomic scattering cross sections based on the Ziegler, Biersack, and Littmark (ZBL) universal screening potential [11] were used in the calculation of the displacement functions, and the electronic stopping powers used in the calculations were generated from the SRIM 2000 electronic stopping power database [12]. The use of these representations of the scattering and stopping powers in the calculation of displacement functions for SiC is demonstrated and discussed in Reference [2].

The damage functions $\nu_{ij}(T)$ are integrated over the PKA damage energy spectrum for a neutron of energy E_n in the material, to yield the Si, C and total (Si + C) displacement cross sections for neutrons of energy E_n. This has been done for SiC using the SPECOMP code [13], and the results for total DPA cross sections are tabulated in Table 1 and shown graphically in Figure 1 as a function of E_n.

Spectrally Averaged DPA Cross Sections

When the displacement function is integrated over the flux spectrum of neutron energies for a given reactor location, the result is a cross section for total DPA in SiC averaged over the neutron energy spectrum. The total DPA obtained by a SiC specimen in a specific irradiation is then the product of the spectrally averaged DPA cross section for SiC and the total neutron fluence received by the specimen.

Table 1. Total DPA cross sections in barns for SiC as a function of neutron energy in MeV.

E,MeV	σ_d, b
1.00E-10	4.14E+00
1.00E-09	1.31E+00
1.00E-08	6.84E-01
2.30E-08	4.58E-01
5.00E-08	3.44E-01
7.60E-08	2.80E-01
1.15E-07	2.30E-01
1.70E-07	1.88E-01
2.55E-07	1.54E-01
3.80E-07	1.27E-01
5.50E-07	1.04E-01
8.40E-07	8.43E-02
1.28E-06	6.86E-02
1.90E-06	5.66E-02
2.80E-06	4.61E-02
4.25E-06	3.75E-02
6.30E-06	3.11E-02
9.20E-06	2.57E-02
1.35E-05	2.10E-02
2.10E-05	1.72E-02
3.00E-05	1.42E-02
4.50E-05	1.15E-02
6.90E-05	9.46E-03
1.00E-04	8.02E-03
1.35E-04	7.03E-03
1.70E-04	6.25E-03
2.20E-04	9.53E-02
2.80E-04	3.56E-01
3.60E-04	1.60E+00
4.50E-04	1.34E+00
5.75E-04	1.15E+00
7.60E-04	2.86E+00
9.60E-04	3.74E+00
1.28E-03	2.91E+00
1.60E-03	4.32E+00
2.00E-03	6.89E+00
2.70E-03	9.07E+00
3.40E-03	1.06E+01
4.50E-03	1.38E+01
5.50E-03	1.95E+01
7.20E-03	2.36E+01
9.20E-03	2.69E+01
1.20E-02	3.06E+01
1.50E-02	3.91E+01
1.90E-02	4.91E+01
2.55E-02	5.90E+01
3.20E-02	7.26E+01
4.00E-02	8.86E+01
5.25E-02	1.79E+02
6.60E-02	1.51E+02
8.80E-02	1.54E+02
1.10E-01	1.54E+02
1.35E-01	1.51E+02
1.60E-01	4.67E+02
1.90E-01	6.32E+02
2.20E-01	5.04E+02
2.55E-01	4.62E+02
2.90E-01	4.16E+02
3.20E-01	4.08E+02
3.60E-01	4.53E+02
4.00E-01	4.25E+02
4.50E-01	4.75E+02
5.00E-01	4.89E+02
5.50E-01	5.28E+02
6.00E-01	4.67E+02
6.60E-01	4.78E+02
7.20E-01	5.20E+02
7.80E-01	8.01E+02
8.40E-01	5.75E+02
9.20E-01	7.22E+02
1.00E+00	5.19E+02
1.20E+00	5.95E+02
1.40E+00	6.08E+02
1.60E+00	6.03E+02
1.80E+00	8.27E+02
2.00E+00	6.02E+02
2.30E+00	6.60E+02
2.60E+00	7.15E+02
2.90E+00	7.09E+02
3.30E+00	6.92E+02
3.70E+00	9.96E+02
4.10E+00	7.96E+02
4.50E+00	8.46E+02
5.00E+00	7.04E+02
5.50E+00	7.01E+02
6.00E+00	6.49E+02
6.70E+00	6.42E+02
7.40E+00	9.25E+02
8.20E+00	7.31E+02
9.00E+00	8.08E+02
1.00E+01	7.99E+02
1.10E+01	8.57E+02
1.20E+01	8.86E+02
1.30E+01	8.79E+02
1.40E+01	8.70E+02
1.50E+01	9.21E+02
1.60E+01	9.05E+02
1.70E+01	8.72E+02
1.80E+01	9.36E+02
1.90E+01	9.20E+02
2.00E+01	

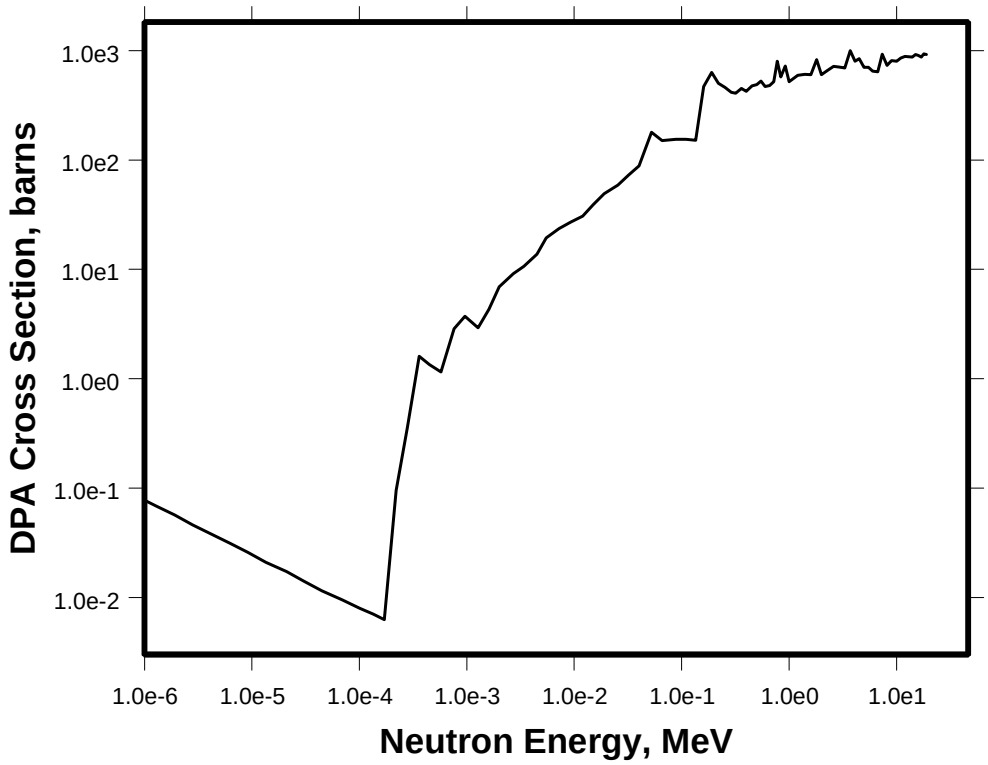

Figure 1. Total DPA cross sections in barns for SiC as a function of neutron energy in MeV.

Conclusions

The DPA cross sections in Table 1 represent the latest and best knowledge about damage production in SiC. We encourage the adoption of these cross sections as the standard to be used for calculating radiation damage production in DPA for all neutron-irradiated SiC samples, including those in past irradiations if possible.

ACKNOWLEDGEMENTS

The authors are indebted to Dr. J. Stephen Herring of INEEL for numerical values of the MPBR reactor neutron spectrum. This work was supported in part by each of the U.S. Department of Energy Offices of Nuclear Energy, Basic Energy Sciences, and Fusion Energy Sciences.

REFERENCES

[1] R. Devanathan and W. J. Weber, J. Nucl. Mater. 278 (2000) 258.

[2] W. J. Weber, R. E. Williford and K. E. Sickafus, J. Nucl. Mater. 244 (1997) 205.

[3] H. Heinisch, L. R. Greenwood, W. J. Weber and R. E. Williford, J. Nucl. Mater. 307-311 (2002) 895.

[4] G. H. Kinchin and R. S. Pease, Rep. Prog. Phys. 18 (1955) 1.

[5] M. J. Norgett, M. T. Robinson and I. M. Torrens, Nucl. Eng. Design 33 (1975) 50.

[6] M. T. Robinson, Nuclear Fusion Reactors, Proc. British Nuclear Energy Soc., UKAEA, London, (1970) 364.

[7] R. Devanathan, W. J. Weber, and F. Gao, J. Appl Phys. 90 (2001) 2303.

[8] D. M. Parkin and C. A. Coulter, J. Nucl. Mater.101 (1981) 261.

[9] D. M. Parkin and C. A. Coulter, J. Nucl. Mater.103-104 (1981) 1315.

[10] D. M. Parkin and C. A. Coulter, J. Nucl. Mater.117 (1983) 340.

[11] J. F. Zeigler, J. P. Biersack and U. Littmark, The Stopping and Range of Ions in Solids (Pergamon Press, New York, 1985).

[12] J. F. Zeigler, SRIM-2000, code and manuals available on the Internet at http://www.srim.org, (2001).

[13] L. R. Greenwood, Reactor Dosimetry: Methods, Applications, and Standardization, ASTM STP 1001(1989) 598.

STRENGTH OF NEUTRON IRRADIATED SILICON CARBIDE AND SILICON CARBIDE COMPOSITE - L. L. Snead and T. Hinoki (ORNL) and Y. Katoh (Kyoto University)

OBJECTIVE

The objective of this paper is to compare recently generated data on the effect of irradiation on stoichiometric SiC with previous results on stoichiometric and non-stoichiometric forms of SiC and SiC composites.

SUMMARY

Specimens of monolithic SiC and SiC composite have been irradiated with fission neutrons in the temperature and dose range of 90-1000°C and 1.1- 7.7 x 10^{25} n/m^2 (E>0.1 dpa), respectively. Materials included stoichiometric chemically vapor deposited SiC and composites containing SiC-based fibers chemicaly vapor infiltrated with SiC. For the case of the monolithic SiC and the composite containing the near-zero oxygen content fibers, no degradation in bend strength was observed. Composite materials containing the higher oxygen content fibers exibited significant degradation. These results are compared with data from the literature on the irradiation effects on the properties of stoichiometric and non-stoichiometric SiC-based materials.

PROGRESS AND STATUS

Introduction

Silicon carbide (SiC) has been widely used as a pressure vessel for fuel-particles in high-temperature gas cooled reactors. One design of such a pressure vessel is the TRISO system. The TRISO coating system contains internal gas pressures generated during fissioning of the fuel kernel material and acts as a diffusion barrier to metallic fission products. Figure 1 (left) gives a schematic representation of the TRISO fuel particle. The coating layer adjacent to the fuel kernel is a low density PyC (buffer layer) containing about 50% porosity. This layer absorbs fission product recoils from the kernel, provides a reservoir for fission product gases, and accommodates kernel swelling limiting forces transmitted to the outer coatings. The next layer is a high-density, isotropic PyC layer that protects the kernel from reactions with chlorine present during deposition of the SiC layer, provides structural support for the SiC layer, and protects the SiC from fission products and carbon monoxide during operation. The outermost layer is another high-density, isotropic PyC layer that protects the SiC during the remainder of the fabrication process and provides structural stability to the particle during irradiation. High Density PyC and SiC layers are impervious to fission gases at normal operating temperatures and the SiC layer is an effective barrier to both gaseous and metal fission products. A polished section of an actual fuel kernel, with SiC shown as the brightest ring, is shown in Figure 1(right). Typical high temperature gas cooled reactors employing this fuel would operate in a temperature range of 800-1300°C and be subjected to up to ~ 5x10^{25} n/m^2 (E>0.1 MeV.)

A more recent (proposed) application of SiC is as a structural material for fusion reactors. In this case, SiC would be used in the form of woven composites and formed into very large structures. An example of the scale and design for a SiC fusion reactor structure is described in the recent work of Giancarli [1]. In that design, concentric shells of SiC/SiC on the order of a few square meters are nested to form the first wall and blanket structure. Such structures are building blocks to surround the toroidal plasma. For such a fusion power system application, the SiC composite would receive as much as 100 dpa over its lifetime and be expected to operate at temperatures as high as 1000°C.

For both SiC coated nuclear fuels and structural applications, knowledge of the effects of irradiation on mechanical properties are critical. This paper will present new results on the effect of neutron irradiation on the strength of chemically vapor deposited SiC as applied for the TRISO system, and SiC/SiC composites as proposed for fusion structural materials. Particular emphasis is placed on the importance of stoichiometry of the SiC materials on the degradation in strength of these materials due to neutron irradiation.

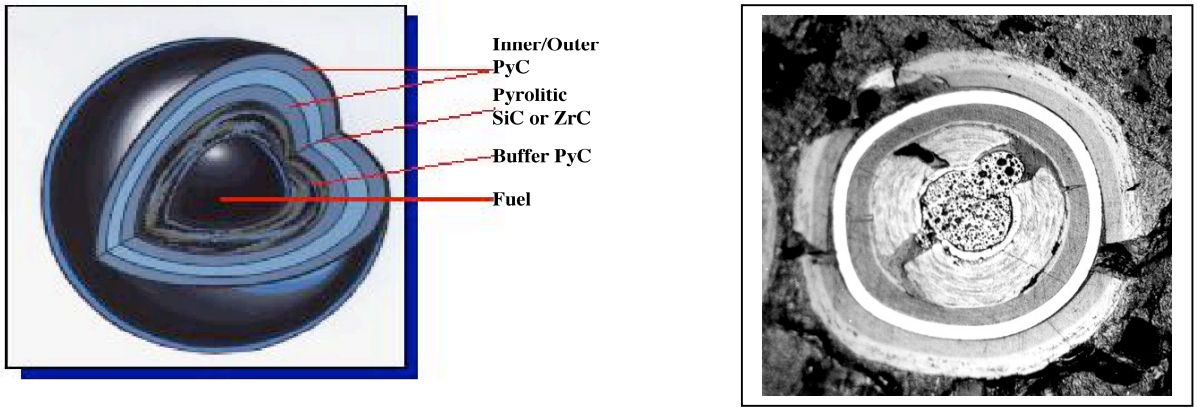

Figure 1: Schematic and polished section of TRISO fuel particle.

Experimental

The chemically vapor deposited (CVD) SiC was obtained from Morton Advanced Ceramics (now Rohm Haas) in plate form. Impurities in this material are at or less than the ppm level. Grain size varies from 5-10 μm with a 100% theoretical density (3.21 g/cc.) The crystal structure is highly faulted FCC β-SiC. The strength as provided by the manufacturer is 470 MPa at ambient, and 575 MPa at 1400°C using a four-point fixture and a 0.5 nm RMS surface finish. The Weibull parameters as provided by the manufacturer are modulus of 11.45 and scale factor of 460 MPa. Bend bars were machined into 1 x 1 x 25 mm and tested at room temperature in four-point bending with a load and support span of 6.25 and 19.05 mm, respectively. The cross-head displacement rate was 0.0085 mm/s. Data was analyzed using a two-parameter Weibull treatment. Density was measured using a density gradient column technique [2] utilizing a mixture of methylene iodide and ethylene bromide. Density samples were soaked in hydrofluoric acid for period of 1 hour to remove any surface silica.

Composite materials were fabricated in the High Temperature Materials Laboratory at the Oak Ridge National Laboratory. Fabric was layed-up in a 0/90° pattern and infiltrated by forced flow chemical vapor infiltration [3]. Fibers chosen were from the Nicalon™ family: Hi and Type-S. Properties are listed in Table 1. For each case a carbon interphase was applied between the fiber and the matrix. Composite bend bars were machined in the as-received condition (2.3 x 6 x 30 mm) and baked at 200°C in air prior to loading into graphite holders for irradiation. Bend testing was carried out at room temperature at a cross-head displacement of 0.0085 mm/s. Load and support spans were 6.45 and 19.05 mm, respectively. Due to a lack of materials the use of thermal control specimens was not possible. However, previous work which included limited thermal control samples for CVD SiC/C interphase/Hi-Nicalon composite fabricated with the identical process to the composites in this study and held for 30 days at ~300 and 1000°C in an inert cover gas. No significant effect of the thermal treatment was seen in that work.

Nicalon™ Fiber Type	C/Si Atomic Ratio	Oxygen Content (wt/%)	Tensile Strength (GPa)	Tensile Modulus (GPa)	Density (g/cm3)	Diameter (μm)
Ceramic Grade	1.31	11.7	3.0	220	2.97	2.55
Hi	1.39	0.5	2.8	270	7.77	2.74
Type-S	1.05	0.8	2.6	410	24.1	3.1

Table 1: Properties of Nicalon™ family fibers.

Irradiation was carried out in both the flux trap of the High Flux Isotope Reactor (HFIR) at ORNL and the V-15 core position of High Flux Beam Reactor (HFBR). The High Flux Beam Reactor irradiation of the CVD SiC material was a thermocouple-monitored experiment with a static helium fill gas surrounding samples inserted into vanadium holders. The calculated neutron fluence was 1.1 dpa. A conversion of $1x10^{25}$ n/m^2 (E>0.1 MeV) is assumed equivalent to 1 dpa in both reactors. The high fluence (14J experiment, 6 and 7.7 dpa) HFIR irradiation was carried out for 8 cycles in a thermocouple-controlled capsule with 300, 500 and 800°C zones. Heaters and sweep gas was used to maintain target irradiation temperature.

Results

CVD SiC Data

Table 2 gives the reduced data for the CVD SiC including the Weibull parameters and density change. The quoted temperatures for the 14J experiment have an uncertainty of less than 10°C, while those from the SiC-1 experiment have a larger range (as listed.) The temperature for this experiment tended to increase throughout the irradiation. It is important to note that the plates from which the bend bars were taken for the 14J and SiC-1 experiments were different, and the machining was conducted at different times. This may explain the difference in non-irradiated strengths between the two experimental batches, though the difference is still within the standard deviation listed.

ID	Tirr (°C)	Dose dpa, or $x10^{25}$ n/m^2 (E>0.1MeV)	Density Change (%)	Weibull Mean (MPa)	Weibull Standard Deviation (MPa)	Weibull Modulus	Size Parameter (MPa)	Number of Samples
HFIR-14J								
Non-irr	-	-	-	353	72	13	368	29
14J	300±10	7.7	2.0	399	117	5	434	10
	500±10	6	1.65	576	133	10	607	20
	800±10	7.7	.82	540	138	8	588	31
HFBR SiC-1								
Non-irr	-	-	-	416	109	7	444	30
	80-90	1.1	3.09	424	114	7	455	17
	250-270	1.1	1.8	407	109	7	437	25
	385	1.1	1.37	392	112	6	485	23
	960-1150	1.1	.45	448	145	4	495	23

Table 2: Reduced data for CVD SiC.

The normalized strength data ($\sigma_{irr}/\sigma_{non\text{-}irr}$) for the CVD SiC as a function of irradiation temperature are given in Figure 2. The error bars represent ± 1 Weibull's standard deviation while the temperature uncertainty is the measured range in temperature during irradiation. For the ~1000°C data point, the temperature band is weighted towards the lower temperature end reflecting the greater exposure time at this lower (~1000°C) temperature.

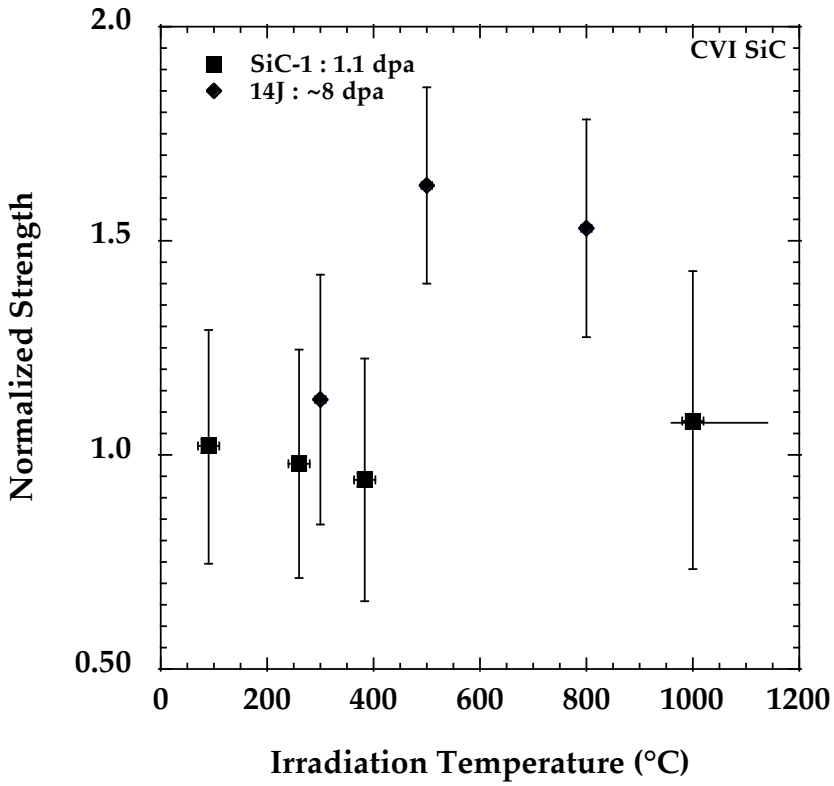

Figure 2: Effect of temperature on normalized strength ($\sigma_{irr}/\sigma_{non\text{-}irr}$) of neutron irradiated CVD SiC.

SiC/SiC Composite

The effect of irradiation on the composite materials tested in this study is given in Table 3. For the Type-S Nicalon™ composite both plain and satin weave fabrics were employed. For the FCVI process employed in this work, the satin weave composites had lower fiber volume fractions and higher resulting porosity. This was typical of Results for Type-S satin weave composite include interphase thickness of 150 and 500 nm. It was observed that composites fabricated from the satin weave fabric tended to have a higher porosity and correspondingly larger scatter in mechanical properties. The mean strength and standard deviation values given in Table 3 assume a normal distribution as the number of samples was limited. The mean strength given is the ultimate bend strength.

Fiber	Weave	C thickness (nm)	Fiber Fraction (%)	Void (%)	Irr. temp. (°C)	Length Change* (%)	Mean strength (MPa)	Standard deviation	Number of samples
Type-S	Plane	150	36	14	Non-irrad.	-	425	12.2	2
					300	.64	469	22.9	2
					800	.25	474	12.9	3
Type-S	Satin	150	29	20	Non-irrad.	-	271	-	3
					300	.72	314	22.1	3
					800	.30	267	58.1	4
Type-S	Satin	500	30	19	Non-irrad.	-	344	23.4	4
					300		406	36.7	2
Hi-Nicalon	Plane	150	37	11	Non-irrad.		442	18.1	4
					800		278	18.2	2

* In-plane length change.

Table 3: Reduced data for high-dose irradiated SiC composites

Discussion

Monolithic SiC

Due to the lack of data available on irradiation effects for the CVI SiC shells, and more generally, monolithic pyrolytic SiC in the temperature ranges of interest for gas cooled reactors, a number of assumptions have been made with respect to material performance of SiC. These assumptions have been outlined in the CEGA(Combusion Engineering-General Atomics) report, which summarizes properties of interest for modeling TRISO fuel particles [4]. As described by CEGA, the non-irradiated room temperature strength of CVD SiC in the literature ranges from 60 Mpa [5] to over 3100 Mpa [6]. This variability is due to many factors, including both material and test dependent parameters. Strength was obtained using several techniques including three and four-point bending and ring compression testing.

Based on the review of the original papers on the subject Yavuz [5,6], it appears that the presence of free silicon (as much as 6%), which becomes molten at the high temperatures, would serve to seriously degrade strength. The presence of free silicon in the TRISO fuel particles SiC was known [8], though its importance not fully recognized. Such degradation in non-irradiated strength at high temperatures due to the presence of free silicon has also been studied in detail by Lara-Curzio [9]. As will be mentioned later, previous work on powder processed SiC [10-13] clearly indicates that the presence of free silicon causes anisotropic dimensional change under irradiation resulting in strength reduction. Additionally, it is clear for all ceramics that factors such as surface condition, machining, and test orientation with respect to grinding can have and influence on strength. As example, Cockeram [14] has measured the four point bend strength for both Morton and Coors stoichiometric CVD SiC and found a significant difference in strength between the two materials and a dependence of strength on orientation with respect to the grinding direction. He also reports small or insignificant effect of orientation with respect to the CVD growth direction. The Morton material of Cockeram's work is equivalent to the CVD SiC of the present study.

The effect of irradiation on SiC strength is similarly limited by sparse data. CEGA discusses the use of two experimental studies and the model proposed by Allelein [15] for TRISO shell evaluation. The data used in Allelein's empirical model were based on a single irradiation at 1165°C to a fluence of 2.88 x 10^{25} n/m^2 (E>0.18 MeV.) With this data a Weibull's mean strength reduction from 834 to 687 MPa was found. However, as CEGA points out, the model does not compare well with the earlier work by Price[16] which shows no affect for irradiation at 630°C and 1020°C. CEGA goes on to show the unfavorable comparison of the model with the Price data and concludes: "These inconsistencies need resolution before any recommendation on correction for the irradiation effect. For the interim, we assume that there is no effect of irradiation on strength."

There have been several studies of the effect of irradiation on the mechanical properties of monolithic SiC [10-13,16-24]. When considering the irradiation effects on strength of SiC it is important to differentiate between the stoichiometric and non-stoichiometric ceramics. Forms include reaction bonded, sintered, pressureless sintered, SiC converted from reaction of graphite with molten Si or silicon monoxide, SiC derived from polymer precursors, and materials formed from the decomposition of gasses such as methyl or ethyltrichlorosilane (MTS or ETS.) In each case, chemical impurities are present at some levels within the SiC grains. The highest purity materials tend to be those manufactured from gas phase transition. As example, the Morton CVD material used in this study has a manufacturer quoted chemistry of less than a part per million for metallic impurities (http://www.cvdmaterials.com/sicprop1.htm). However examples of CVD SiC deposited from MTS with as much as 6.3 wt/% free silicon have been studied and results indicate that both high-temperature and irradiation performance suffers [5]. In some forms, such as the commercial reaction-bonded Norton NC-430, molten silicon is added to SiC and graphite powder resulting in 8-10% free silicon which resides at crystallite boundaries. Sintered materials have been made with either boron (eg ~0.4 wt/% Carborundum □-SiC), Si or Al as sintering aids, with the sintering-aid primarily residing at the grain boundary in the final form.

Figure 3 shows a comparison of the normalized bend strength data from the present work and of Price [10,16] and Dienst [23] on pyrolitic, CVI SiC. For all cases, the values are for Weibull's mean with error bars indicating ±1 Weibull's standard deviation. However, while the work of Dienst [22,23] references the use of ten samples per condition and gives Weibull's mean and modulus, no standard deviation was given. The dotted lines of the figure are approximations of this standard deviation as calculated using Weibull data provided by Dienst [22,23]. From the

compilation data of figure 3 it is clear that for doses less than ~10 dpa no degradation, and possibly a slight increase, in mean strength has occurred. In all cases (cf Table 2) irradiation reduces the Weibull's modulus. For doses greater than 10 dpa the effect of irradiation on strength is less clear in that the data of Price[10] and Dienst[23] are contradictory. Unfortunately, the stoichiometry and density of the material used are not given, so the presence of free silicon cannot be dismissed as the mechanism responsible for the strength reduction.

Recent work has been carried out on samples taken from the same CVD SiC samples in this work. Nogami[25] reports Vicker's harness increasing for all dose levels and temperatures for the samples. For the 7.7 dpa, 800°C irradiation a hardness increase of ~ 20% was reported. Also of interest is that the indentation fracture toughness is increased at this level supporting the apparent increase in strength given in this work.

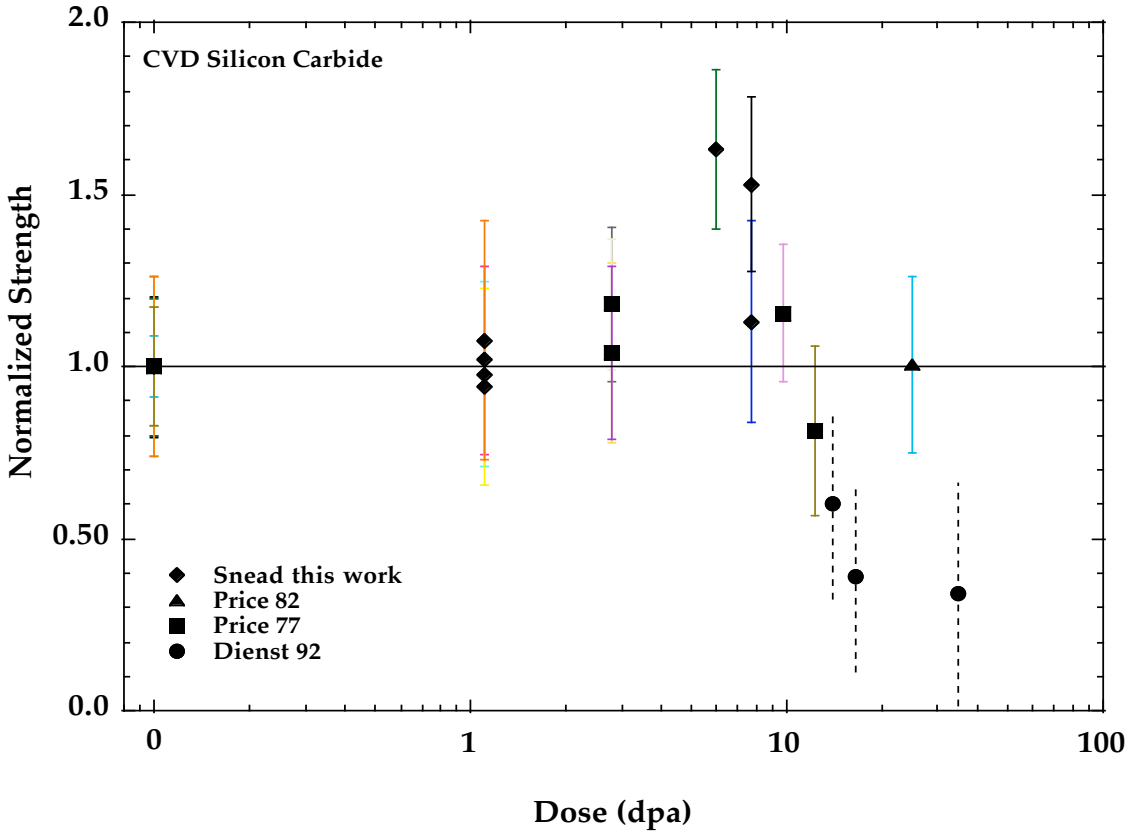

Figure 3: Normalized strength ($\sigma_{irr}/\sigma_{non\text{-}irr}$) of CVD SiC data as a function of dose for this study and literature data.

As mentioned earlier, the presence of free silicon in pyrolitic SiC, or the presence of Si or other sintering aids has a great influence on strength and other mechanical properties of irradiated SiC.[10-13,16-24] This point can be illustrated by inspection of Figure 5, which contains a compilation of data on powder processed forms of SiC. Clearly, normalized strength is substantially degraded at relatively low fluence. For the case of materials (such as Norton NC-430) with free silicon at the grain boundary, anisotropic swelling between the Si and SiC causes disruption at the grain boundary reducing mechanical properties of strength, elastic and Weibull's modulus.[12,20] Other materials which contain boron as sintering aids further suffered from the additional recoil damage due to the (n,α) reaction and the corresponding presence of helium bubbles near the grain boundaries.

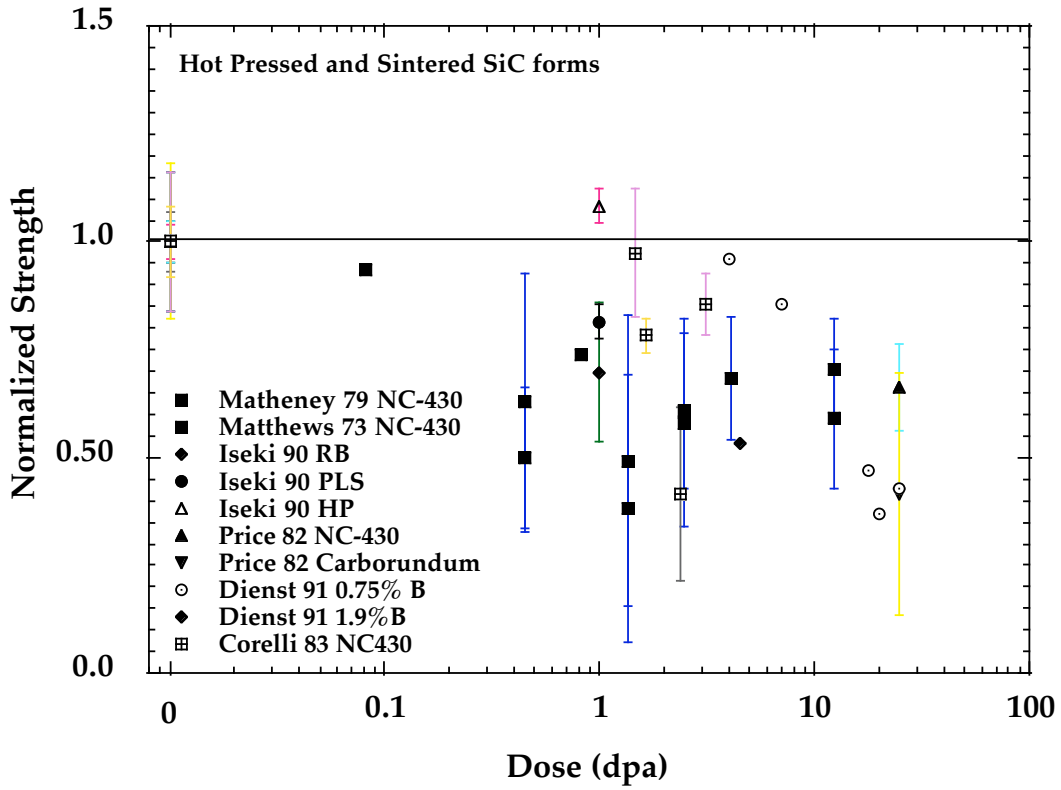

Figure 4: Effect of irradiation on powder processed monolithic SiC.

Silicon Carbide Composites

The effect of neutron irradiation on SiC matrix SiC fiber composites have been studied for more than ten years with early materials exhibiting significant degradation in mechanical properties following neutron irradiation.[26] It was recognized that the cause of this degradation was debonding between the fiber and the chemically vapor infiltrated matrix.[26] This disruption of the carbon interphase layer compromised the load transfer between the high-stiffness matrix and the high-strength fibers. It is an important note that due to the presence of excess oxygen and carbon, these fibers are more correctly classified as SiC-based fibers, rather than SiC fibers. The manufacturer's quoted composition for Nicalon™ NLM-202, which is close to figures given by Yajima[27] for pre-production fibers, is 65 % □-SiC with 23 % SiO_2 and 11 % free carbon. The microstructure of these fibers are of dispersed □-SiC crystallites of a few nanometers in size embedded in a continuum glassy silicon oxycarbide matrix (Si-O_x-C_y , where x+y is approximately 4). Second generation Nicalon™ fibers were then produced by improving the method of cross-linking the spun polymer, though there was still substantial excess oxygen (0.5%) and a C/Si imbalance (1.31). The density of the second-generation (Hi-Nicalon™) fiber was increased from 2.55 g/cc (ceramic grade Nicalon fiber) to 2.74 g/cc, which is approximately 85 % theoretical SiC density. Of interest for nuclear applications, the Hi-Nicalon™ fiber density was seen not to undergo the dramatic densification seen in ceramic grade Nicalon™ fiber, at least for low-dose neutron irradiation[28]. It is the densification of these fibers that was identified early on as the source of the poor irradiation performance of SiC composites.[26] Recently, a further improvement in the Nicalon™ system has been achieved (Type-S Nicalon™.) Essentially, the Hi-Nicalon™ process has been taken a step further with the result of a near theoretical density fiber with very low excess carbon and oxygen (< 0.1%). Table 1 gives a chemical comparison of the Nicalon™ family fibers.

The impact of the evolution from SiC-based fibers with high oxygen content and excess silicon to near stoichiometric fibers on the performance following neutron irradiation is given in Figure 5. It is seen that the earliest fibers exhibited ~ 40% loss in ultimate bend strength at irradiation doses of a few dpa, which corresponds to

only a few months operation in a fusion power reactor. While the Hi-Nicalon™ fiber composites showed slightly better performance mechanical properties still sharply degraded and debonding was still clearly seen through direct TEM observation of the interphase region.[29] Results from the current work are also provided in this plot and clearly indicate that degradation in strength does not occur. Moreover, it appears that a moderate increase in composite strength has occurred, though this observation is tempered by the statistical limitations.

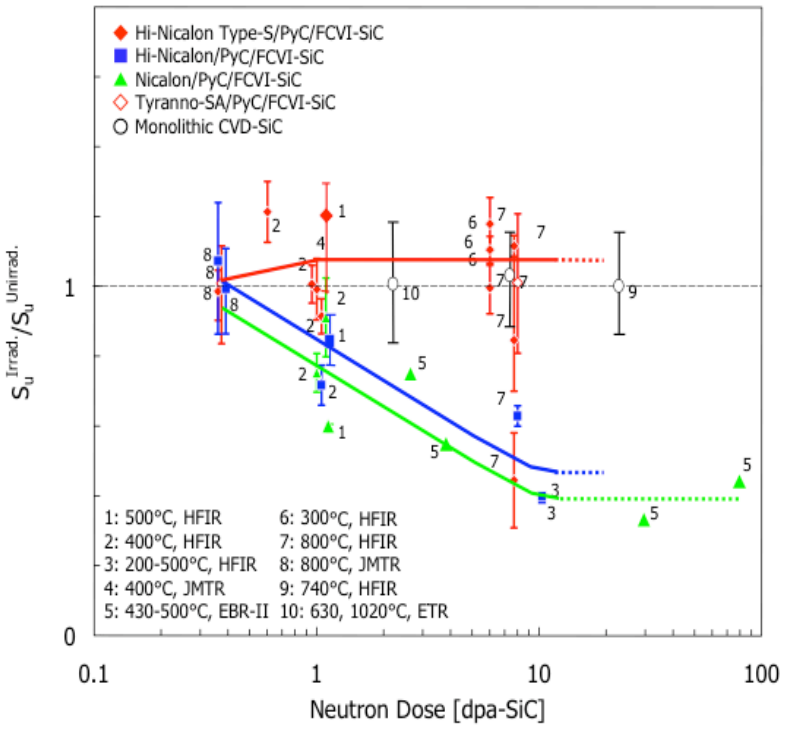

1,2: L.L. Snead, et al., J. Nucl. Mater., 283-287 (2000) 551-555.
3,4: T. Hinoki, et al., Mater. Trans., JIM, 43 [4] (2002) to be published.
5: R.H. Jones, et al., 1st IEA-SiC/SiC (1996).
6,7: T. Hinoki, et al., J. Nucl. Mater., (2002) to be published.
8: T. Nozawa, et al., J. Nucl. Mater., (2002) to be published.
9: R.J. Price, et al., J. Nucl. Mater., 108-109 (1982) 732-738.
10: R.J. Price, J. Nucl. Mater. 33 (1969) 17-22.

Figure 5: Effect of irradiation on Nicalon™ family SiC composites.

Conclusions

Over the neutron dose range of this study of (1.1 to 7.7 x 10^{25} n/m^2 (E>0.1 MeV)) Weibull mean bend strength of stoichiometric pyrolitic silicon carbide remains unchanged or exhibits slight strengthening. Data is consistent with hardening and increased indentation fracture toughness measurements made previously on identical materials. A point of ambiguity exists at high doses because of an apparent contradiction in the literature between two high-dose studies. Another, high-dose experiment is called for on the newest, stoichiometric CVD SiC to address this discrepancy. As with the CVD SiC, composites fabricated from stoichiometric fibers and matrix undergo no change in proportional limit or ultimate bend strength, and may undergo a slight increase in strength. For both cases it is clearly important that elements in the form of impurities or second phases occurring at grain boundaries or within the crystallites. be minimized to retain as-irradiated strength of silicon carbide.

Acknowledgement

Research sponsored by the Office of Fusion Energy Sciences, U.S. Department of Energy under contract DE-AC05-00OR22725 with UT-Battelle, LLC.

REFERENCES

[1] L. Giancarli, M. Ferrari, M.A. Futterer, S. Malang, Fusion Engineering and Design 49 (2000) 445.
[2] ASTM., D1505-85. Standard Test Method for Density of Plastics by Density Gradient Technique. 1985.
[3] T. M. Besmann, J.C. McLaughlin, H.T. Lin, J. Nucl. Mat. 219 (1995) 31.
[4] CEGA,, Report CEGA-002820, Rev 1 (July 1993).
[5] B. O. Yavuz, R.E. Tressler, Ceram. International 8 (1992) 19.
[6] A. Briggs, J. Nucl. Mat. 61 (1976) 233.
[7] T. D. Gulden, J. Am. Ceram. Soc. 52 (1969) 585.
[8] A. Naoumidis, R. Benz, J. Rottman, High-Temp High-Press. 14 (1982) 53.
[9] E. Lara-Curzio, Ph.D Thesis, Dept. of Materials Science, Rensselaer Polytechnic Institute, 1992.
[10] R. J. Price, G. R. Hopkins, J. Nucl. Mat. 108-109 (1982) 732.
[11] J. C. Corelli, J. Hoole, J. Lazzaro, C.W. Lee, J. Amer. Ceram. Soc. 66 (1983) 529.
[12] R. Matthews, J. Nucl. Mater. 51 (1974) 203.
[13] W. Dienst, Fus. Eng. and Design 16 (1991) 311.
[14] B. V. Cockeram, J. Am. Ceram. Soc. 85 (2002) 603.
[15] H. J. Allelein, in:, SMiRT 7, Chicago Illinois, 1983 p. 203.
[16] R. Price, Nucl. Tech. 35 (1977) 320.
[17] R. J. Price, J. Nucl. Mat. 33 (1969) 17.
[18] A. M. Carey, F. J. Pineau, C. W. Lee, J. C. Corelli, J. Nucl. Mat. 103-104 (1981) 789.
[19] S. D. Harrison, J. C. Corelli, J. Nucl. Mat. 99 (1981) 203.
[20] R. A. Matheny, J. C. Corelli, J Nucl Mat 83 (1979) 313.
[21] T. Iseki, T. Maruyama, T. Yano, T. Suzuki, T. Mori, J Nucl Mat 170 (1990) 95.
[22] W. Dienst, T. Fett, R. Heidinger, H. D. Roehrig, B. Schulz, J. Nucl. Mater. 174 (1990) 102.
[23] W. Dienst, J. Nucl. Mater. 191-194 (1992) 555.
[24] F. Porz, G. Grathwohl, T. Thummler, Mater. Sci. Eng. 71 (1985) 273.
[25] S. Nogami, A. Hasegawa, L. L. Snead, J. Nucl. Mat. in press (2002).
[26] L. L. Snead, S. J. Zinkle, D. Steiner, J. Nucl. Mat. 191-194 (1992) 560.
[27] S. Yajima, K. Okamura, T. Matsuzawa, Y. Hasegawa, T. Shishido, Nature 279 (1979) 706.
[28] L. L. Snead, M. Osborne, K. L. More, J. Mater. Res. 10 (1995) 736.
[29] L. L. Snead, E. Lara-Curzio, in: eds. G. E. Lucas, R. C. Ewing, J. S. Williams, Microstructure of Irradiated Materials, Boston MA, vol. 540, MRS Warrendale PA, 1999 p. 273.

3.0 FERRITIC/MARTENSITIC STEELS

FRACTURE TOUGHNESS CHARACTERIZATION OF IRRADIATED F82H IN THE TRANSITION REGION— M. A. Sokolov, R. L. Klueh (Oak Ridge National Laboratory), G. R. Odette (University of California, Santa Barbara), K. Shiba, and H. Tanigawa (Japan Atomic Energy Research Institute)

OBJECTIVE

The objective of this work is to characterize the fracture behavior of ferritic/martensitic steels.

SUMMARY

The ferritic-martensitic steel F82H is a primary candidate low-activation material for fusion applications, and it is being investigated in the joint U.S. Department of Energy-Japan Atomic Energy Research Institute collaboration program. As part of this program, two capsules containing a variety of specimen designs were irradiated at two different temperatures in the Oak Ridge National Laboratory (ORNL) High Flux Isotope Reactor. The bottom and top parts of these capsules were loaded with disk-shaped compact tension [DC(T)] specimens that were used for fracture toughness characterization. This small (12.5 mm in diameter with thickness of 4.6 mm) DC(T) specimen was developed at ORNL for testing irradiated materials. Six specimens were irradiated in each "low-" and "high-" irradiation temperature capsule up to ~3.8 dpa. Irradiation temperatures were measured by thermocouples. In the low-temperature capsule, three specimens were irradiated at an average temperature of 261°C and another three at 240°C; temperature variation during irradiation was within ±19°C for a given specimen. In the high-temperature capsule, all six specimens were irradiated at an average temperature of 377°C in the bottom part of the capsule; temperature variation during irradiation was within ±30°C for a given specimen. All irradiated specimens failed by cleavage instability. From these data, fracture toughness transition temperatures were evaluated for irradiated F82H steel and compared to unirradiated values. Specimens irradiated at the higher temperature exhibited a relatively modest shift of the fracture toughness transition temperature of ~57°C. However, the shift of fracture toughness transition temperature of specimens irradiated at 250°C was much larger, ~191°C. These results are compared with available tensile and impact Charpy data for this material.

PROGRESS AND STATUS

Introduction

The ferritic-martensitic steel F82H is a primary candidate low-activation material for fusion applications, and it is being investigated in the joint USA-JAERI collaboration program. As part of this program, two capsules containing a variety of specimen designs were irradiated at two different temperatures in the ORNL High Flux Isotope Reactor (HFIR). Two capsules with europium oxide (Eu_2O_3) thermal neutron shield were irradiated in the HFIR removable beryllium (RB) positions. Details of the irradiation conditions and the contents of the capsules can be found elsewhere [1]. The bottom and top parts of these capsules were loaded with disk-shaped compact tension [DC(T)] specimens that were used for fracture toughness characterization. The small (12.5 mm in diameter with thickness of 4.6 mm) DC(T) specimen was developed at ORNL for testing irradiated materials [2]. Six specimens were irradiated in each "low-" and "high-" irradiation temperature capsule up to ~3.8 dpa. Irradiation temperatures were measured by thermocouples. In the low-temperature capsule, three specimens were irradiated at an average temperature of 261°C in the bottom part of the capsule and another three at 240°C in the upper part of the capsule; temperature variation during irradiation was within ±19°C for a given specimen. In the high-temperature capsule, all six specimens were irradiated at an average temperature of 377°C in the bottom part of the capsule; temperature variation during irradiation was within ±30°C for a given specimen.

In addition to DC(T) specimens, miniature SS-3 type sheet tensile specimens (7.62 mm in gage length, 1.52 mm in gage width and 0.76 mm in gage thickness), and 1/3-size Charpy specimens (3.3 x 3.3 x 25.4 mm^3 with 0.51 mm deep 30°C V-notch and a 0.05-0.08 mm root radius) were irradiated in both capsules. However, tensile and Charpy specimens were irradiated in the middle sections of their capsules. In the "low-temperature" capsule, tensile specimens were irradiated at an average temperature of 307°C and 1/3-size Charpy specimens were irradiated at an average temperature of 288°C to ~4.7 dpa. In the "high-temperature" capsule, tensile specimens were irradiated at an average temperature of 497°C and 1/3 size Charpy specimens were irradiated at an average temperature of 509°C to ~4.8 dpa.

Testing Procedure

The fracture toughness tests were conducted in general accordance with the American Society for Testing and Materials (ASTM) E 1921-02 [3] Standard Test Method for Determination of Reference Temperature, T_o, for Ferritic Steels in the Transition Range, with a computer-controlled test and data acquisition system [4]. The specimens were fatigue precracked before irradiation to a ratio of the crack length to specimen width (a/W) of about 0.5, and then side-grooved by 20% of their thickness (10% from each side). The unloading compliance method used for measuring the J-integral using these specimens is outlined in Ref. [2]. Unirradiated specimens were tested in the laboratory on a 98-kN (22-kip) capacity servohydraulic machine, and irradiated specimens were tested in a hot cell with a 490-kN (110-kip) capacity servohydraulic machine with a 22-kN (5-kip) load cell. All tests were conducted in strain control, with an outboard clip gage having a central flexural beam that was instrumented with four strain gages in a full-bridge configuration. The broken unirradiated specimens were examined with a calibrated measuring optical microscope to determine the initial and final crack lengths. The irradiated specimens were photographed, and enlarged prints of the fracture surfaces were fastened to a digitizing table to allow the crack length to be measured.

Values of J-integral at cleavage instability, J_c, were converted to their equivalent values in terms of stress intensity K_{Jc} by the following equation [3]:

$$K_{Jc} = \sqrt{J_c \frac{E}{1-\nu^2}} \qquad (1)$$

where E is Young's modulus and ν = 0.3 is Poisson's ratio.

It was assumed that the transition fracture toughness of F82H steel complied with the master curve concept. Therefore, a K_{Jc} datum was considered invalid if this value exceeded the $K_{Jc(limit)}$ requirement of the ASTM Standard E 1921 [3]:

$$K_{Jc(limit)} = \sqrt{\frac{b_o \sigma_{YS}}{30} \cdot \frac{E}{1-\nu^2}} \qquad (2)$$

where b_o was the remaining ligament and σ_{YS} was the yield strength of the material at the test temperature. All invalid data were censored and substituted by the $K_{Jc\ (limit)}$ values for calculation of the transition fracture toughness temperature, T_o. After that, all K_{Jc} data (valid and substituted) were converted to 1T equivalence, $K_{Jc(1T)}$, using size adjustment procedure of the ASTM Standard E1921 [3]:

$$K_{Jc(1T)} = 20 + \left[K_{Jc(x)} - 20\right] \cdot \left(\frac{B_x}{B_{1T}}\right)^{1/4} \qquad (3)$$

where $K_{Jc(x)}$ = measured K_{Jc} value,
B_x = gross thickness of test specimen,
B_{1T} = gross thickness of 1T C(T) specimen.

The reference fracture toughness transition temperature, T_o, was determined using the multi-temperature equation from E1921 [3]:

$$\sum_{i=1}^{N} \delta_i \frac{\exp\left[0.019\left(T_i - T_O\right)\right]}{11+77\exp\left[0.019\left(T_i - T_O\right)\right]} - \sum_{i=1}^{N} \frac{\left(K_{Jc(i)} - 20\right)^4 \exp\left[0.019\left(T_i - T_O\right)\right]}{\left\{11+77\exp\left[0.019\left(T_i - T_O\right)\right]\right\}^5} = 0 \qquad (4)$$

where δ_i = 1.0 if the datum is valid or zero if datum is a dummy substitute value,
T_i = test temperature corresponding to $K_{Jc(i)}$.

Results

The unirradiated DC(T) specimens were examined in two orientations, L-T and T-L, while only T-L-oriented DC(T) specimens were irradiated. Twenty-three T-L specimens were tested in the unirradiated condition in the temperature range from -100°C to -20°C and 16 L-T specimens were tested in the unirradiated condition in the temperature range from -140°C to -50°C. Only two T-L and one L-T specimens exhibited stable crack growth and did not demonstrate any unstable fracture. From their full J-R curves, values of the critical integral at the onset of the stable crack growth, J_{Ic}, were determined using ASTM Standard E 1820 [5]. However, these values could not satisfy the validity requirements of E1820 because of the relatively small dimensions of the DC(T) specimens, and they were designated as J_q on the Figures. These three tests were censored for T_o determination and substituted with the $K_{Jc(limit)}$ values from Eq. (2). All other specimens failed by cleavage instability. From these data, using Eqs1-4, fracture toughness transition temperatures were evaluated for the F82H steel.

The size-adjusted to 1T fracture toughness data of F82H steel in the T-L orientation are presented in Figure 1. This figure illustrates the temperature dependence of the transition fracture toughness data relative to its master curve with 5 and 95% tolerance bounds. While 5 and 95% tolerance bounds provide a reasonable description of the transition fracture toughness data, there are a noticeable number of data points outside the bounds. Two J_q values were converted to their stress-intensity factor equivalent using Eq. (1) and plotted as filled symbols on Figure 1 to indicate the upper end of the transition region. The temperature dependence of $K_{Jc(limit)}$ is also plotted on Figure 1. It can be seen that for a given strength of F82H, this specimen design (b_o) leaves a relatively narrow test temperature window to obtain valid K_{Jc} data. For example, out of 21 specimens that failed by cleavage, nine specimens exceeded the validity limit, $K_{Jc(limit)}$, and were censored for T_o determination.

Figure 2 compares the fracture toughness data of F82H in the T-L and L-T orientations. It is apparent from the Fig. 2 that both the transition region and the upper shelf fracture toughness have a distinct orientation dependence. The reference transition temperature is lower in the L-T orientation; -109°C compared to -68°C in the T-L orientation. The upper-shelf toughness is higher in the L-T orientation compared to T-L. Thus overall, the F82H steel is tougher in the L-T orientation than in T-L. Such orientation dependence is typical for many ferritic steels, and the L-T orientation is usually the toughest orientation. It needs to be pointed out that the optical microscopy did not reveal an orientation dependence in the microstructure of this steel.

As mentioned above, tensile properties were determined by testing miniature SS-3 sheet-tensile specimens with a 7.62-mm gage length, a 1.52-mm gage width, and a 0.76-mm in gage thickness. Figure 3 provides the temperature dependence of the yield strength of F82H steel before and after irradiation. These results were used in the present study to evaluate the fracture toughness data. Irradiation at ~300°C to 4.5 dpa resulted in significant hardening of F82H. Room temperature yield strength increased by 368 MPa (from 528 MPa in the unirradiated condition to 896 MPa after irradiation). Specimens tested after irradiation at ~500°C to 5.0 dpa did not show any noticeable hardening as result of irradiation.

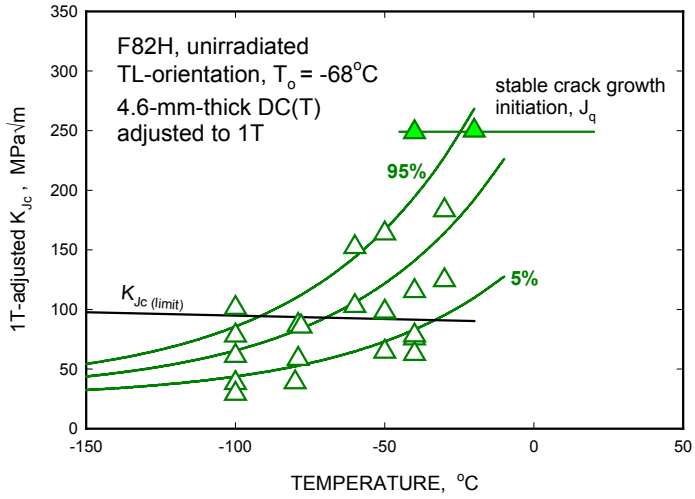

Fig. 1. Temperature dependence of fracture toughness data of F82H in T-L orientation relative to its master curve.

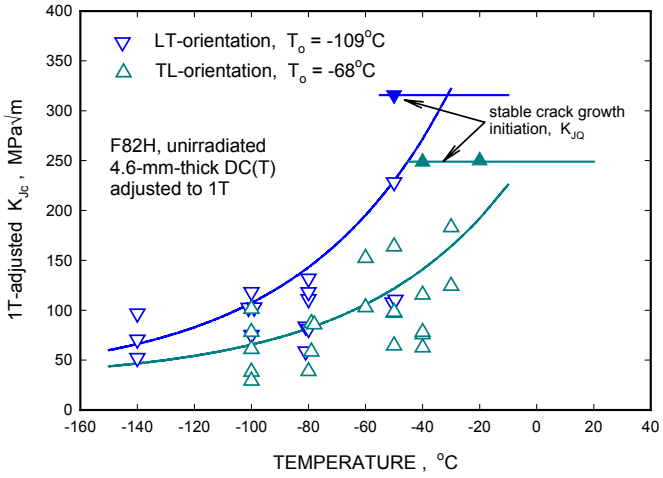

Fig. 2. Size-adjusted to 1T fracture toughness data of F82H steel in two orientations, T-L and L-T, relative to their master curves.

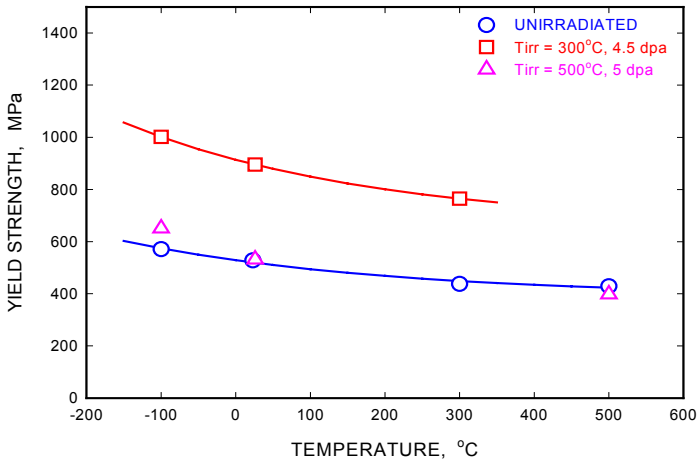

Fig. 3. Temperature dependence of yield strength of F82H Steel in the unirradiated condition and after irradiation at 300 and 500°C.

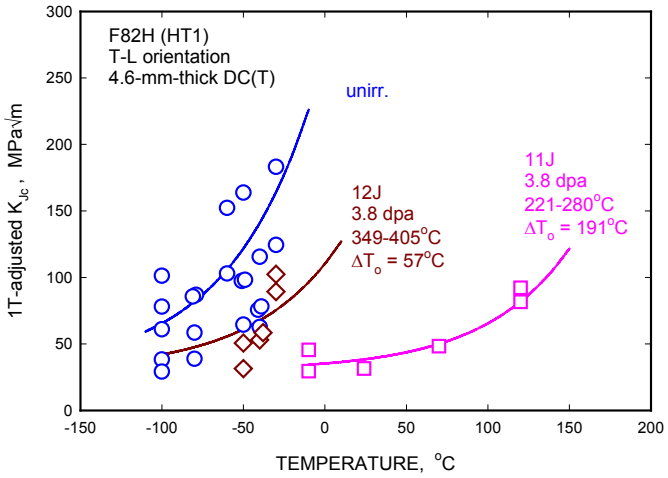

Fig. 4. Fracture toughness data of F82H steel (size-adjusted to 1T) in T-L orientation before and after irradiation.

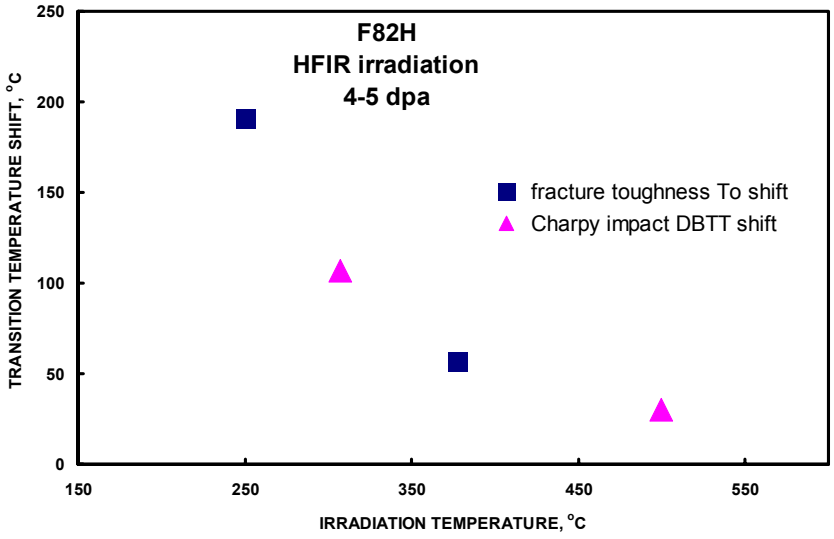

Fig. 5. Comparison of fracture toughness reference temperature T_o shifts derived from DC (T) specimens and Charpy impact DBTT shifts derived from third-sized specimens of F82H steel after irradiation in HFIR at different temperatures.

Using the following correlation between hardening and fracture toughness transition temperature shift from Ref. [6]:

$$\Delta T_o = 0.7 \cdot \Delta\sigma_{YS}\,, \qquad (5)$$

it was estimated that the shift of fracture toughness transition temperature, ΔT_o, after irradiation at 300°C might be about 260°C. This estimate was used to select test temperatures for irradiated fracture toughness specimens taking into account differences in irradiation temperatures of the DC(T) and tensile specimens.

Every irradiated specimen failed by cleavage instability. It turned out that all generated K_{Jc} values satisfied the validity requirement in Eq. 2. From these data, fracture toughness transition temperatures were evaluated for irradiated F82H steel and compared to the unirradiated T_o, see Fig. 4. Specimens irradiated at the higher temperature exhibited a relatively modest shift of the fracture toughness transition temperature of 57°C. However, the shift of fracture toughness transition temperature of specimens irradiated at ~250°C was much larger at 191°C.

While the shift of T_o after irradiation at an average temperature of ~250°C is relatively large, 191°C, it is still smaller than expected from correlation Eq. 5 and tensile data after irradiation at ~300°C. The same correlation also suggests a larger than 51°C shift of T_o after irradiation at an average temperature of 377°C. The correlation in Eq. 5 was based entirely on low-alloy reactor pressure vessel (RPV) steels data [6], and the present results do not support direct application of this correlation to ferritic-martensitic steels like F82H, suggesting a different relationship between embrittlement and hardening than in RPV steels. It appears that 8%Cr-based steels, like F82H, have a smaller shift of T_o per the same amount of hardening than 0.3%Cr-based RPV steels. On the other hand, shifts of the fracture toughness transition temperature, T_o, and the Charpy ductile-to-brittle transition temperature, DBTT, appear to be comparable if the irradiation temperature is taken into account (see Fig. 5).

Summary and Conclusions

Disk compact tension specimens of F82H steel of T-L orientation were irradiated in the HFIR removable beryllium (RB) positions in capsules with a europium oxide (Eu_2O_3) thermal neutron shield to 3.8 dpa at average temperatures of ~250°C and ~77°C. The master curve methodology was applied to characterize the transition fracture toughness of this steel before and after irradiation. Application of the master curve methodology in accordance with ASTM standard E1921 showed that even for such a relatively large number (for fusion irradiation experiments) of specimens, there is a very narrow test temperature range where K_{Jc} values could be qualified as valid values per E1921. In this study, all irradiated specimens exhibited cleavage fracture with E1921 valid fracture toughness values.

In the unirradiated condition, both the transition range and the upper-shelf fracture toughness exhibited strong orientation dependence. The F82H steel was tougher in the L-T orientation than in T-L orientation.

Specimens irradiated at ~377°C exhibited a modest shift of reference fracture toughness temperature, T_o (57°C). However, the T_o shift of specimens irradiated at ~250°C was much larger (191°C).

The present results show that relatively high-Cr ferritic-martensitic steels, like F82H, exhibit smaller embrittlement in terms of T_o shift for the same amount of hardening (yield strength increase) than low-Cr ferritic RPV steels. Shifts of T_o and Charpy DBTT temperatures appear to be the same (taking into account irradiation temperature).

References

[1]. K.E. Lenox and M.L. Grossbeck, "Operating History of the HFIR MFE-RB-11J and –12J (P3-2 and P3-3) Experiments," *DOE/ER-0313/25 Fusion Materials*, 30 December, 1998, pp.307-23.

[2]. D.J. Alexander, "Fracture Toughness Measurements with Subsize Disk Compact Specimens," *Small Specimen Test Techniques Applied to Nuclear Reactor Vessel Thermal Annealing and Plant Life Extension, ASTM STP 1204*, W.R. Corwin, F.M. Haggag, and W.L. Server, Eds., ASTM, Philadelphia, 1993, pp.130-142.

[3]. Standard Test Method for Determination of Reference Temperature, T_o, for Ferritic Steels in the Transition Range, Designation E 1921-02, Annual Book of ASTM Standards, Vol. 03.01.

[4]. R.K. Nanstad, D.J. Alexander, R.L. Swain, J.T. Hutton, and D.L. Thomas, "A Computer Controlled Automated Test System for Fatigue and Fracture Testing," *Applications of Automation Technology for Fatigue and Fracture Testing, ASTM STP 1092*, A.A. Braun, N.E. Ashbaugh, and F.M. Smith, Eds., ASTM Philadelphia, 1990, pp. 7-20.

[5]. Standard Test Method for Measurement of Fracture Toughness, ASTM E1820-99a, ASTM, Philadelphia, Annual Book of Standards, Vol. 3.01.

[6]. M.A. Sokolov and R.K. Nanstad, " Comparison of Irradiation-Induced shifts of K_{Jc} and Charpy Impact Toughness for Reactor Pressure Vessel Steels," *Effects of Radiation on Materials: 18th International Symposium, ASTM STP 1325*, R.K. Nanstad, M.L. Hamilton, F.A. Garner, and A.S. Kumar, Eds., American Society for Testing and Materials, Philadelphia, 1999, pp. 167-190.

CHARPY IMPACT PROPERTIES OF REDUCED-ACTIVATION FERRITIC/MARTENSITIC STEELS IRRADIATED IN HFIR UP TO 20 DPA — H.Tanigawa (Japan Atomic Energy Research Institute), M.A. Sokolov (Oak Ridge National Laboratory), K. Shiba (JAERI), R.L. Klueh (ORNL)

OBJECTIVE

The objective of this work is to (1) analyze the results of Charpy impact tests on HFIR 11J-, 12J- JP25-irradiated CVN specimens, (2) investigate the DBTT shift saturation of F82H, (3) determine the validity of the TIG welding process, (4) investigate He and grain size effects.

SUMMARY

The effects of irradiation up to 20 dpa on the Charpy impact properties of reduced-activation ferritic/martensitic steels (RAFs) were investigated. The ductile-brittle transition temperature (DBTT) of F82H-IEA shifted up to around 50°C. TIG weldments of F82H showed a fairly small variation on their impact properties. A finer prior austenite grain size in F82H-IEA after a different heat treatment resulted in a 20°C lower DBTT compared to F82H-IEA after the standard heat treatment, and that effect was maintained even after irradiation. Helium effects were investigated utilizing Ni-doped F82H, but no obvious evidence of helium effects was obtained. ORNL9Cr-2WVTa and JLF-1 steels showed smaller DBTT shifts compared to F82H-IEA.

PROGRESS AND STATUS

Introduction

Reduced-activation ferritic/martensitic steel (RAF) is one of the candidate structural materials for a fusion power plant reactor. It is being investigated in the Japan Atomic Energy Research Institute (JAERI) and DOE collaboration program with the emphasis on F82H (Fe-8Cr-2W-VTa), which was developed by JAERI and NKK Corporation, Kawasaki, Japan. To validate the potential of RAFs as the structural material for fusion power plants, it must be ensured that the materials have adequate fracture toughness at the application temperature, including the welded joints. It is also important to establish the effect of the presence of gas atoms (hydrogen and helium) formed by transmutations induced by 14MeV neutron bombardment from the fusion reaction.

Previous irradiation test results after irradiation up to 11 dpa at temperatures below 400°C indicated that the shift of ductile-brittle transition temperature (DBTT) to a higher temperature depends on irradiation dose. This is important because 100°C is expected to be the lowest temperature of fusion blankets [1-3]. Current interest is to determine whether there is a saturation dose level or not, and to know the degradation level of toughness after saturation. Additionally, the effect of transmutation-formed helium on the mechanical properties, especially fracture toughness, is one of the most important issues that needs to be understood for expected power plant reactor application. In this study, the effects of irradiation up to 20 dpa on the Charpy impact properties of RAFs were investigated.

Experimental

The material used for this research was IEA-modified F82H (F82H-IEA), nominally Fe-7.5Cr-2W-0.15V-0.02Ta-0.1C. Base metal with two heat treatment variations (standard IEA heat treatment and another heat treatment designated HT2) and TIG weldments (weld metal and weld joint) of F82H were irradiated. Details of weld conditions were shown elsewhere [4]. F82H doped with 2%Ni (F82H+2Ni) was also irradiated to study the effect of helium produced from a two-step reaction involving ^{58}Ni and thermal neutrons, along with chemical effects of nickel itself. For the maximum dose of 20 dpa, 200 appm He were formed in the nickel-doped material. ORNL9Cr-2WVTa and JLF-1 steels were also

irradiated for comparison. The details of the chemical compositions and heat treatments of these materials are listed in Table1 and Table2.

Table 1. Chemical compositions of RAFs (wt%)

	C	Cr	W	V	Ta	Ti	N	Ni
F82H- IEA :	0.11	7.7	2.00	0.16	0.02	0.01	0.008	-
F82H+2Ni :	0.1	7.9	1.99	0.19	0.06	0.005	0.004	1.9
9Cr-2WVTa:	0.1	8.8	1.97	0.18	0.065	<0.01	0.023	-
JLF-1 :	0.1	8.9	1.95	0.20	0.09	0.002	0.0215	-

Table 2. Heat treatment conditions

F82H-IEA : 1040°C/40min/AC + 750°C/1hr
F82H HT2 : (F82H-IEA) + 920°C/1hr/AC + 750°C/1hr
F82H +2Ni : 1040°C/30min/AC + 750°C/1hr
9Cr-2WVTa : 1050°C/1hr/AC + 750°C/1hr
JLF-1 : 1050°C/1hr/AC + 780°C/1hr

Miniature Charpy specimens (3.3 x 3.3 x 25.4 mm with 0.51 mm V-notch) were used for the impact tests, and SS-3 tensile specimens (gage section : 7.62 x 0.76 x 1.5 mm) were used to evaluate the relation between hardening and DBTT shift. Irradiation was performed in the Oak Ridge National Laboratory (ORNL) High Flux Isotope Reactor (HFIR). Two capsules (RB-11J and RB-12J) were irradiated to ≅5 dpa at 300°C and 500°C in the boron reflector position, and another capsule (JP25) was irradiated in the target position to ≅20 dpa at 380°C and 500°C. The two RB capsules contained a europium thermal neutron shield for neutron spectrum tailoring.

Charpy impact tests were carried out with an instrumented Charpy impact machine in the Irradiated Materials Examination and Testing (IMET) hot cell facility at ORNL. Testing temperatures ranged from -20°C to 100°C to obtain DBTT and upper-shelf energy (USE) values. SEM observations were made on selected tested specimens. Tensile tests were carried out at room temperature with a strain rate of 0.01 /s.

Table 3. Summary of Charpy impact properties and tensile results.

Material	*Nominal irradiation condition*		*Mid-Trans. DBTT, °C*	*Δ DBTT, °C*	*USE, J*	*σ_y, MPa*	*Δ σ_y, MPa*
	Dose, dpa	Temp., °C					
F82H-IEA	-	-	-84	-	11.58	528	-
	5	300	23	107	10.13	898	370
		500	-54	30	11.56	527	-1
	20	380	50	134	8.7	-	-
		500	-46	38	12.03	-	-
F82H (HT#2)	-	-	-101	-	14.09	501	-
	5	300	3	104	11.76	865	364
		500	-92	9	12.0	485	-16
	20	380	33	133	8.31	-	-
F82H + 2Ni	-	-	-103	-	9.11	651	-
	5	300	137	240	4.09	1281	630
		500	-82	11	10.36	613	-44
	20	380	11	114	5.57	-	-
		500	-77	26	11.56	-	-
Weld Metal	-	-	-83	-	10.88	637	-
	5	300	50	133	9.11	963	326
		500	-37	46	12.74	-	-
	20	380	33	115	7.71	-	-
Weld Joint	-	-	-110	-	10.73	-	-
	5	300	22	132	10.47	-	-
9Cr-2WVTa	-	-	-94	-	10.96	577	-
	5	300	-31	63	9.5	1040	463
		500	-78	16	10.47	569	-8
JLF-1	-	-	-85	-	9.9	525	-
	5	300	-37	48	10.48	839	314
		500	-66	19	12.04	-	-

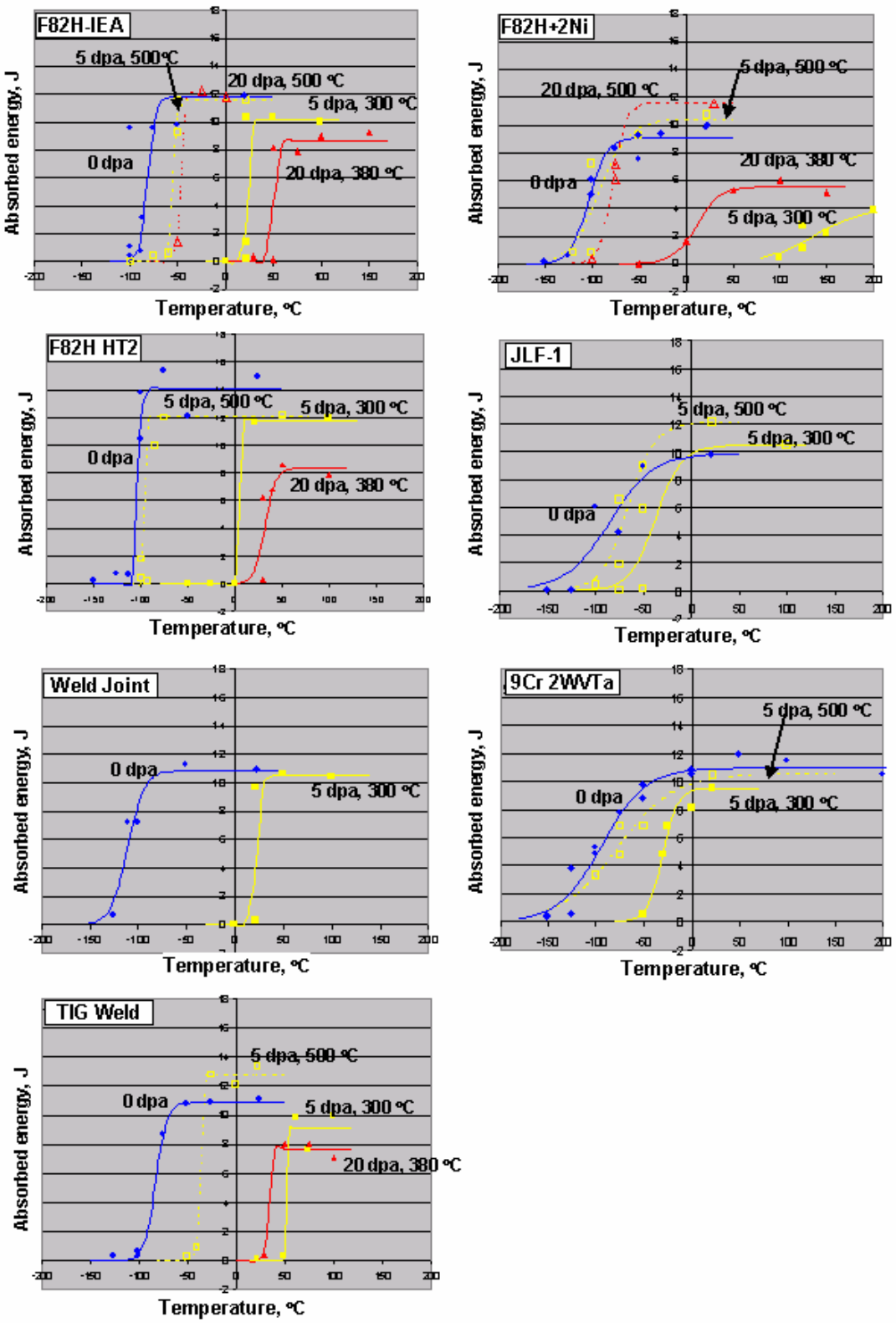

Fig. 1. Charpy curves obtained in this research.

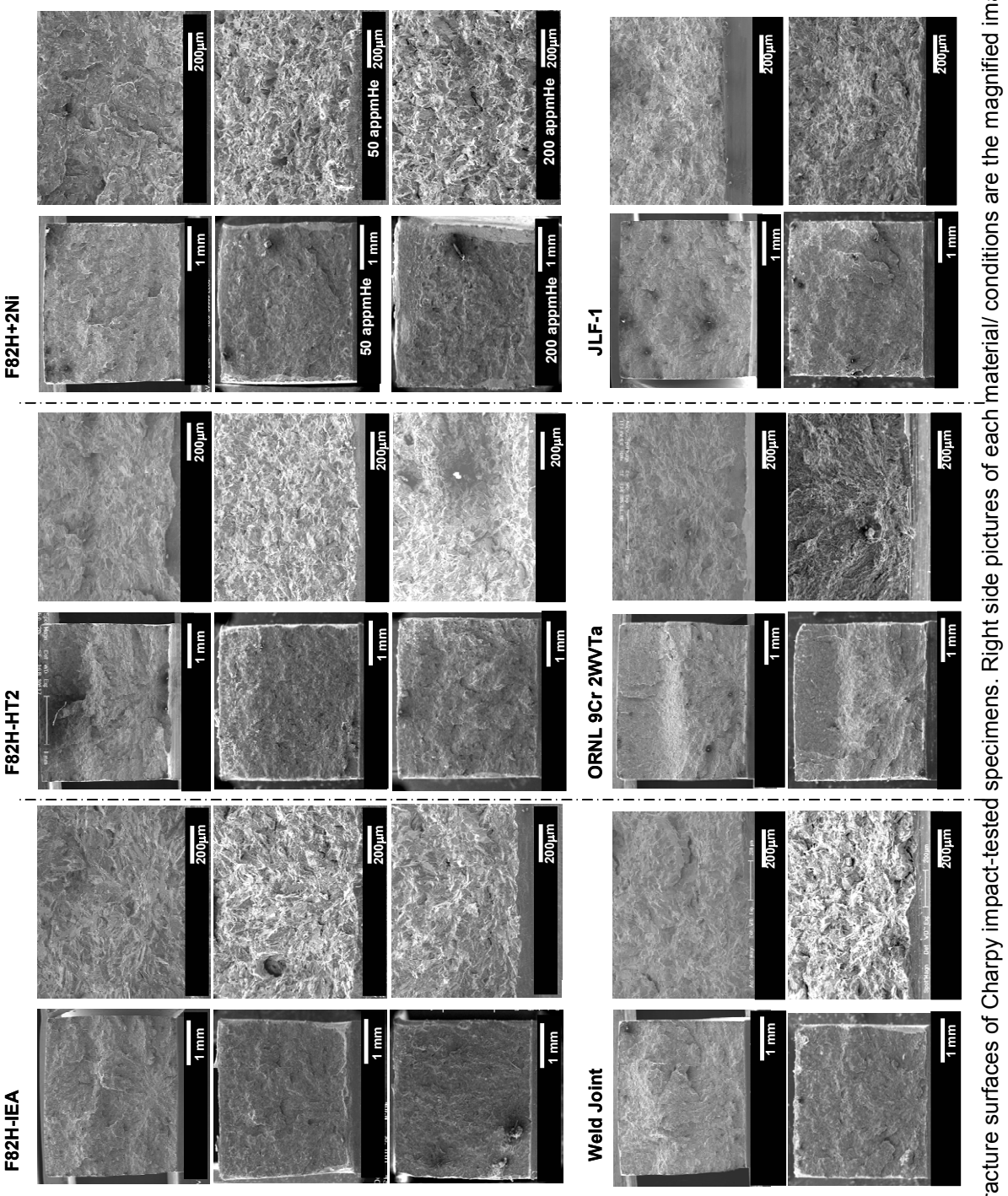

Fig. 2 Fracture surfaces of Charpy impact-tested specimens. Right side pictures of each material/ conditions are the magnified images of fracture initiation points

Results and discussion

Results for the Charpy tests and tensile tests are given in Table 1. Charpy curves and SEM observations of fracture surfaces obtained in this research are shown in Fig. 2 and Fig. 3, respectively. The DBTT was obtained at half the USE value. The DBTT of each of the steels was shifted to a higher temperature after irradiation.

Irradiation dose dependence of the shift in DBTT (ΔDBTT) of F82H-IEA is summarized in Fig. 3. Irradiation up to 5 dpa at 300°C shifted the DBTT up to around room temperature, and there was no obvious indication which suggests a DBTT shift saturation. On the other hand, the DBTT was not further shifted by an increase in irradiation from 11 dpa [3] to 20 dpa at 380°C. This result indicates the ΔDBTT induced by irradiation around 380°C was saturated at 11 dpa.

The DBTT and USE of the weldments before and after irradiation at 300°C up to 5 dpa are summarized in Fig. 4. Base metal (F82H-IEA), weld metal (TIG weld) and weld joint material exhibited about the same shifts of DBTT after irradiation under similar conditions. The USE for all irradiated weldments exhibited only a small drop from the unirradiated level. From these results, it was concluded that TIG weldments have acceptable impact properties, even after the irradiation.

The effects of prior austenite grain size on DBTT shift were investigated by comparing F82H-IEA (ASTM grain size 3.3) to F82H-HT2 (ASTM grain size 6.5). The fine grain structure in F82H-HT2 was obtained by renormalizing F82H-IEA using a lower austenitization temperature (920°C) (see Table 2). The results show that the DBTT of both unirradiated and irradiated HT2 are slightly (~20°C) lower than for F82H-IEA, and the finer-grain F82H-HT2 has a higher USE than F82H-IEA. (see Fig. 5). From these results, it is concluded that F82H-HT2 benefited from the fine grain size after irradiation compared to F82H-IEA steel.

Helium effects on Charpy impact properties were investigated with the Ni-doped F82H. A large DBTT shift and drop of USE were obtained with F82H+2Ni irradiated up to 5 dpa at 300°C (see Fig. 1) . The DBTT of the F82H+2Ni irradiated up to 20 dpa at 380°C is lower than that irradiated up to 5 dpa at 300°C, although 200 appm helium was

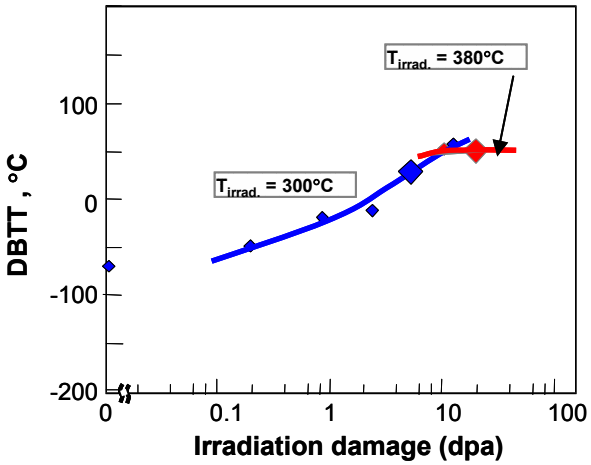

Fig. 3. Irradiation damage dependence of the DBTT of F82H-IEA irradiated at 300°C and 380°C. Data points indicated by small squares were reported elsewhere [3, 5].

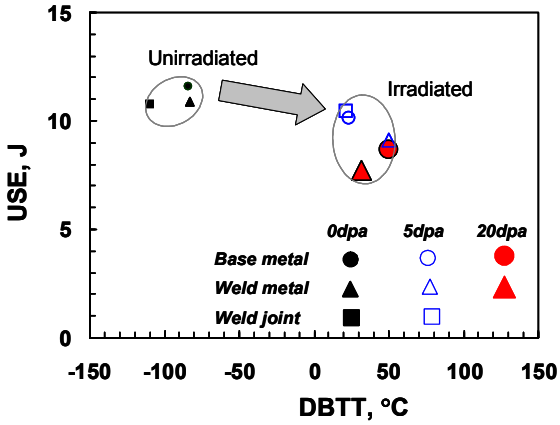

Fig. 4. DBTT and USE changes of base metal, weld metal, and weld joint caused by irradiation.

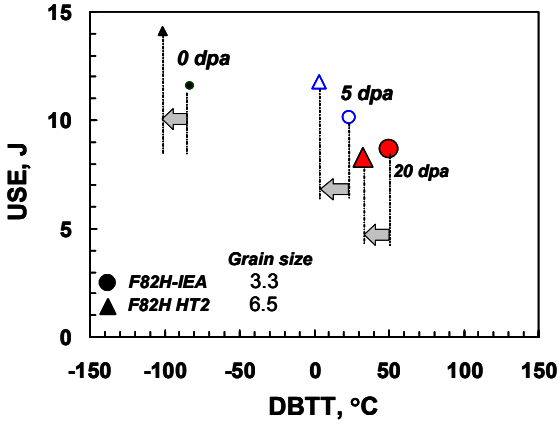

Fig. 5, Effect of prior austenite grain size on Charpy impact properties.

produced for the former case. This could be explained in terms of irradiation temperature. Fracture surfaces were observed for each irradiation condition on specimens that fractured in a brittle mode (~ 0.1J) on the lower shelf (see Fig.3). All specimens showed typical brittle cleavage fracture surfaces, and there was no evidence of intergranular fracture. From these results, it was concluded that helium up to 200 appm did not affect the fracture mode.

Correlation between ΔDBTT and yield stress increase ($\Delta\sigma_y$) is shown in Fig. 6 for F82H-IEA, F82H-HT2, F82H+2Ni, 9Cr-2WVTa and JLF-1. The three F82H vaiations follow the same trend. Ni-doped specimens are also on the same trend. From this, the large ΔDBTT of Ni-doped F82H could be explained as the effect of radiation hardening, just as the other steels. The values for 9Cr-2WVTa and JLF-1 are slightly lower than the main trend. The reason for this difference between F82H and the two 9Cr steels was not clarified in this study, and this will be investigated further in the future.

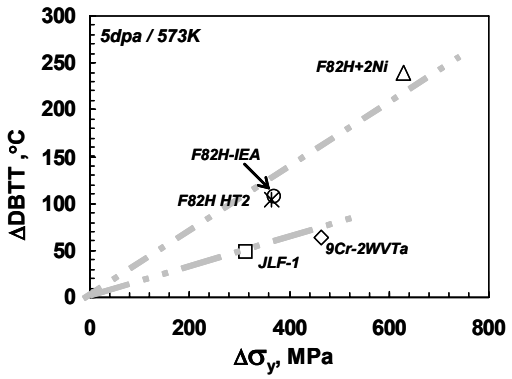

Fig. 6 Relation between DBTT shift and yield stress increase.

Charpy impact properties changes for the specimens irradiated at 500°C are summarized on Fig. 7. The weld metal shows a large ΔDBTT and USE increase compared to those of the base metal (F82H-IEA). This indicates that there could be a better post-weld heat treatment that would make the weld metal much more like the base metal than the current condition. Ni-doped F82H showed an increase in USE which is not understood in light of the hardening. JLF-1 also showed an increase in USE, and this can be explained as the result of the martensitic lath structure recovery, which appears in JLF-1 at higher irradiation temperatures [6].

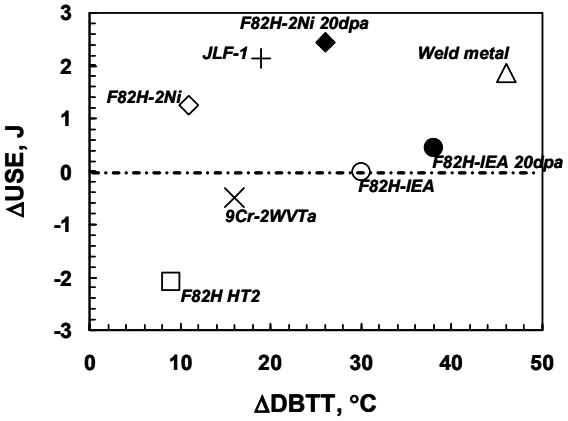

Fig. 7 Charpy impact properties changes of RAFs irradiated at 500°C up to 5 and 20 dpa.

SUMMARY AND CONCLUSIONS

Reduced-activation ferritic/martensitic steels (RAFs) are being investigated in the JAERI/DOE collaboration program with the emphasis on F82H (Fe-8Cr-2W-VTa) to validate the potential of RAFs as the structural material for fusion power plants. The effects of irradiation up to 20 dpa on the impact properties of RAFs were investigated in this study. The following is a summary of the important conclusions:

1. Irradiation of F82H-IEA up to 5 dpa at 300°C shifted the DBTT up to room temperature.
2. No obvious results were obtained which suggested a DBTT shift saturation after irradiation at 300°C to 5 dpa.
3. TIG weldments have acceptable impact properties even after the irradiation.
4. The use of a lower austentization temperature to produced a finer grain size improved the properties of F82H-IEA.
5. All Ni-doped F82H specimens showed typical brittle fracture surfaces, and there was no evidence of intergranular fracture.
6. The large ΔDBTT of Ni-doped F82H could be explained as the effect of radiation hardening, just as

the other steels.

ACKNOWLEDGEMENT

The authors would like to thank R.L. Swain and E.T. Manneschmidt for conducting the impact tests. This research was sponsored by the Japan Atomic Energy Research Institute and the Office of Fusion Energy Sciences, US Department of Energy under contract DE-AC05-96OR22464 with UT-Battelle.

REFERENCE

[1] K. Shiba, M. Suzuki and A. Hishinuma, J. Nucl. Mater. 233-237 (1996) 309
[2] K. Shiba and A. Hishinuma, J. Nucl. Mater. 283-287 (2000) 474
[3] R.L. Klueh, M.A. Sokolov, K. Shiba, Y. Miwa and J.P. Robertson, J. Nucl. Mater. 283-287 (2000) 478
[4] K. Shiba, R.L. Klueh, Y. Miwa, N. Igawa, and J.P. Robertson, Fusion Materials semiannual progress report, DOE/ER-0313/28 (2000) 131
[5] M. Rieth, B. Dafferner, and H.D. Röhrig, J. Nucl. Mater. 258-263 (1998) 1147
[6] Y. Kohno, A. Kohyama, M. Yoshino, K. Asakura, J. Nucl. Mater. 212-215 (1994) 707

DEFORMATION MICROSTRUCTURE OF A REDUCED-ACTIVATION FERRITIC/MARTENSITIC STEEL IRRADIATED IN HFIR - N. Hashimoto (Oak Ridge National Laboratory), M. Ando (Japan Atomic Energy Research Institute), H. Tanigawa (JAERI), T. Sawai (JAERI), K. Shiba (JAERI) and R.L. Klueh (ORNL)

OBJECTIVE

To determine the contributions of different microstructural features to strength and to deformation mode, transmission electron microscopy (TEM) specimens were prepared from the gage sections of the strained flat tensile specimens of irradiated F82H BM and its TIG weldments (weld metal and weld joint); fracture surfaces were examined by scanning electron microscopy (SEM).

SUMMARY

In order to determine the contributions of different microstructural features to strength and to deformation mode, the microstructures of deformed flat tensile specimens of irradiated reduced activation F82H (IEA heat) base metal (BM) and its tungsten inert-gas (TIG) weldments (weld metal and weld joint) were investigated by transmission electron microscopy (TEM), following fracture surface examination by scanning electron microscopy (SEM). After irradiation, the fracture surfaces of F82H BM and TIG weldment showed a martensitic mixed quasi-cleavage and ductile-dimple fracture. The microstructure of the deformed region of irradiated F82H BM contained dislocation channels. This suggests that dislocation channeling could be the dominant deformation mechanism in this steel, resulting in the loss of strain-hardening capacity. While, the necked region of the irradiated F82H TIG, which showed less hardening than F82H BM, showed deformation bands only. From these results, it is suggested that the pre-irradiation microstructure, especially the dislocation density, could affect the post-irradiation deformation mode.

PROGRESS AND STATUS

Introduction

For structural applications in fusion energy systems, ferritic/martensitic steels have several advantages based upon their resistance to void swelling, good thermal stress resistance, and well-established commercial production and fabrication technologies. Ferritic/martensitic steels, however, undergo radiation-induced hardening during neutron irradiation at temperatures up to 673-725K. Radiation hardening is often accompanied by a reduction in strain-hardening capacity and uniform elongation, and an increase in the temperature delineating the transition from quasi-cleavage to ductile fracture.

To investigate irradiation temperature dependence of hardening in ferritic/martensitic steels, F82H IEA base metal (BM) and its TIG weldments were irradiated in the High Flux Isotope Reactor (HFIR) of the Oak Ridge National Laboratory (ORNL). Irradiation conditions and further information on the experiment can be found elsewhere [1-4]. Stress-strain curves of F82H IEA base metal (BM) and the TIG weldment (TIG) irradiated at 573K and 773K in tests at RT are shown in figure 1(a) and (b), respectively [5,6]. In both F82H BM and TIG, the irradiation at 573K led to significant hardening and loss of strain-hardening capacity, while the specimens irradiated at 773K did not show irradiation hardening or degradation in ductility. The TIG specimen irradiated at 573K, however, showed a somewhat smaller irradiation hardening (e.g.; yield stress) compared to the BM specimen.

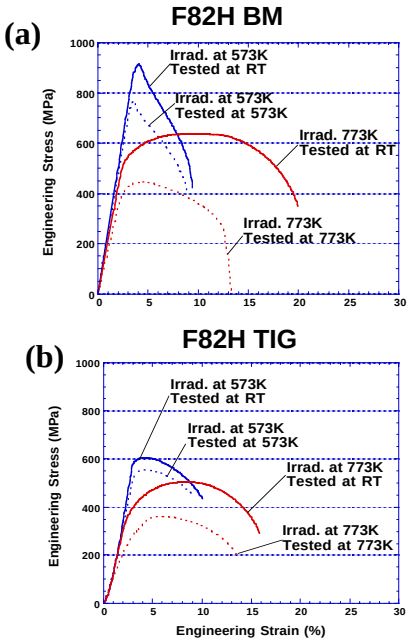

Fig. 1 Stress-strain curves of F82H BM (a) and TIG (b) irradiated at 573K and 773K in tests at RT

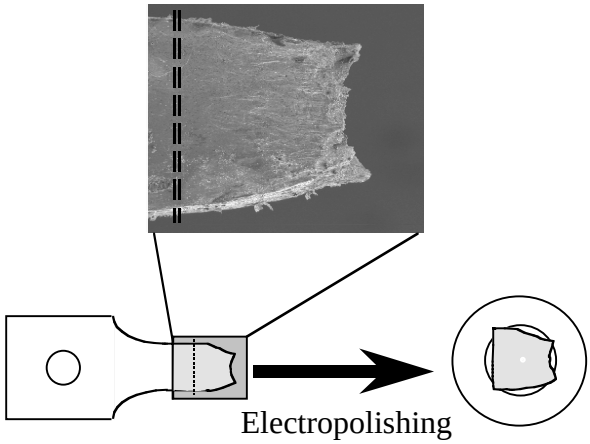

Fig. 2 Fabrication of TEM sample from the gauge section of F82H BM tensile specimen.

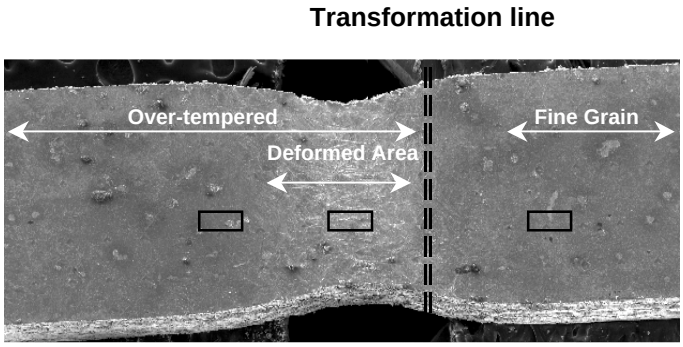

Fig. 3 TEM samples where taken from the over-tempered region, deformed area, and fine grain region of the deformed TIG specimen using FIB.

Experimental

The 8Cr-2WVTa steel F82H IEA was hot-rolled at 1473K and normalized at 1313K for 0.63 hrs followed by tempering at 1023K for 1 hr. TIG weldments were annealed at 993K for 1 hr. Chemical compositions of F82H IEA BM and TIG are given in the Ref.5. Neutron irradiation was performed up to 5 dpa at 573K and 773K in HFIR of ORNL. After post-irradiation tensile tests and SEM, TEM samples of BM and TIG were taken from the deformed specimen, followed by electropolishing (Fig.2) and fabrication using the Focused Ion Beam (FIB) (Fig.3) at Japan Atomic Energy Research Institute (JAERI). An FIB processor (Hitachi FB-2000A) with a microsampling system was used for ion machining and specimen manipulation. The fabrication with FIB has advantages of reducing ferromagnetism and radioactivity of irradiated ferritic steels. Further information on the FIB fabrication can be found in ref. 7.

A ferritic/martensitic steel weldment consists of weld metal, heat-affected zone (HAZ), and base metal. The HAZ is base metal that was affected by heating during welding, and the microstructural regions formed can be determined from the phase diagram. Immediately adjacent to the fusion line the base metal was heated to $T_{\gamma\delta}<T<T_m$, where $T_{\gamma\delta}$ is the temperature at which a two-phase region of austenite (γ) and δ-

ferrite begin to form on heating and T_m is the melting temperature. On cooling, the γ transforms to martensite. Next to this region is a region of base metal that transforms to γ on heating. The next region was heated to $A_{C1}<T<A_{C3}$ (A_{C1} is the temperature at which γ begins to form on heating), and it contains untempered martensite from the base metal that transformed to γ and over-tempered martensite. The remainder of the HAZ was heated to $T_T<T<A_{C1}$, where T_T is the tempering temperature of the base metal. This region contains over-tempered martensite.

Deformation and necking was shown (ref. 8) to occur in the over-tempered region immediately adjacent to the region where part of the microstructure transformed to austenite (Fig.3). TEM specimens were obtained from the deformed region and the over-tempered and transformed regions immediately adjacent to the deformed region.

Results and discussion

Fracture Surface

Fracture surfaces of F82H BM and TIG specimens irradiated at 573K and tested at RT at a strain rate of $1x10^{-3}$ s^{-1} are shown in Fig. 4. Fracture surfaces showed a typical martensitic mixed quasi-cleavage and ductile-dimple fracture in the center in both specimens. The sizes of large and small dimples were about 20-30mm and 10nm, respectively. The BM specimen seemed to include more large dimples than the TIG specimen.

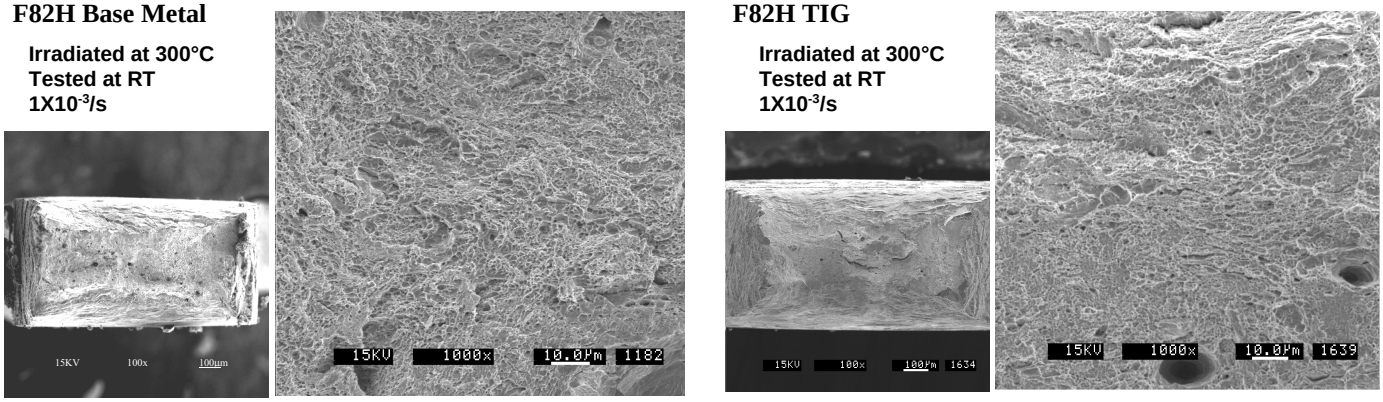

Fig. 4 Fracture surface of F82H base metal (BM) and TIG weldment specimens irradiated at 573K and tested at RT.

Microstructural Examination

Microstructure of Non-irradiated Specimens

Figure 5 shows microstructure of non-irradiated F82H BM, over-tempered region and fine grain region of TIG. The fine grain region showed finer grains than the BM and the over-tempered region. The BM and the fine grain region showed dislocations with a high density. Conversely, over-tempered region had a much lower dislocation density compared to the others.

Microstructure of As-irradiated Specimens

Figure 6 shows microstructure of the BM, the over-tempered region, and the fine grain region irradiated at 573K to 5 dpa in HFIR. In the BM, irradiation-induced dislocation loops were observed with a high number density. However, irradiation-induced precipitates and cavities were not observed.

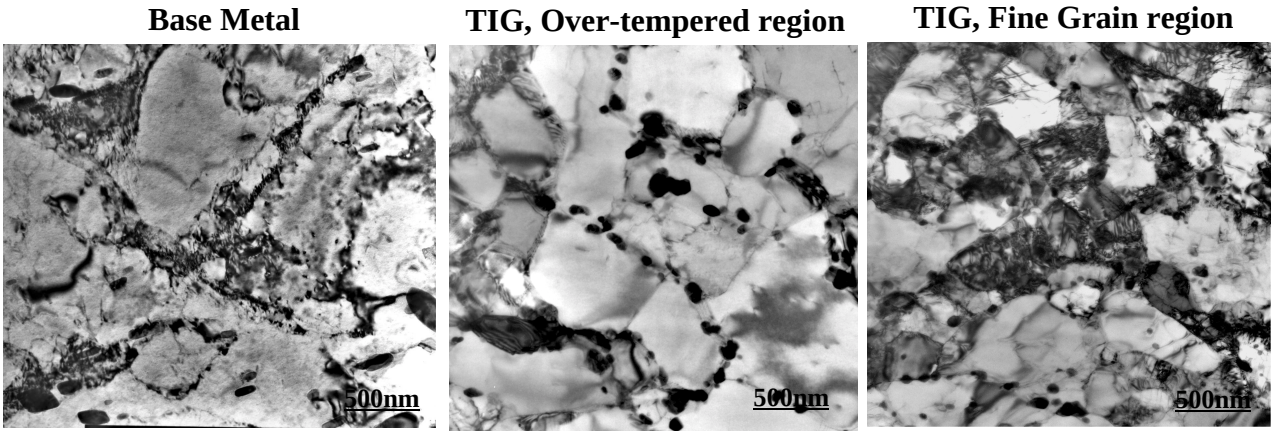

Fig. 5. Microstructure of non-irradiated F82H base metal., over-tempered region, and fine grain region of TIG weldment

Assuming the irradiation-induced obstacles to be dislocation loops only, the approximate value of α = 0.6, barrier strength of obstacles, was obtained for 573K, where a is defined by [9,10]

$\alpha = \Delta\sigma_y / M\mu b(Nd)^{1/2}$

where $\Delta\sigma_y$, M, b, N, d, and m are the increase in YS, the Tailor factor [11], the Burger's vector of dislocation, the number density of obstacles, the mean diameter of obstacles, and the shear modulus, respectively. Hardening contributions due to submicroscopic cavities or precipitates would reduce this calculated upper limit for the dislocation loop α.

On the other hand, the irradiated over-tempered and fine grain region showed no visible dislocation loops, while dislocation lines and helical dislocations decorated with defect clusters were observed, as seen in Fig.6. Furthermore, the number density of defect clusters in the TIG specimens was much smaller than in the BM. This could suggest that irradiation-introduced point defects such as vacancies and interstitials formed defect clusters along preexisting screw type dislocation lines and were absorbed by the screw dislocations.

Basically, there is no tensile and compressive stress field around a screw-type dislocation, but a shear stress is present, so that a screw-type dislocation is incapable of absorbing vacancies and interstitials. However, a screw-type dislocation could have a tensile and compressive stress field due to making edge components partially, and transform into helical dislocation by absorbing point defects. Therefore, the existence of a screw-type dislocations before irradiation could lead to a small number density of defect clusters and a lack of dislocation loops after irradiation, which would be barriers to moving dislocations during deformation. This is in good agreement with the tensile test results, showing that a lack of irradiation-induced dislocation loops led to a small yield stress increase (Fig.1).

Deformation Microstructure of Iirradiated Specimens

Figure 7 shows the microstructure of the deformed BM and TIG (over-tempered region) specimens irradiated at 573K to 5 dpa in HFIR. The microstructure in the necked region of the irradiated BM showed defect-free bands, indicative of dislocation channels (Fig.7(a)). The main deformation mode observed in the BM was dislocation channeling. The slip systems were identified as (110) $[\bar{1}11]$ and $(0\bar{1}1)$ [111], and the width and spacing of the channels was 100-120 nm and 480-520 nm, respectively. The moving dislocation sweeps the defects in the slip plane, leaving the slip plane depleted of them in its wake. Succeeding dislocations in the same plane will find fewer obstacles in their way, provoking a strong localization of the deformation in channel-like regions in the crystal. Gelles reported the deformed microstructure of irradiated Fe-9Cr uniaxial tensile specimens, showing elongated cavities in poorly defined narrow bands but no clear channels [12].

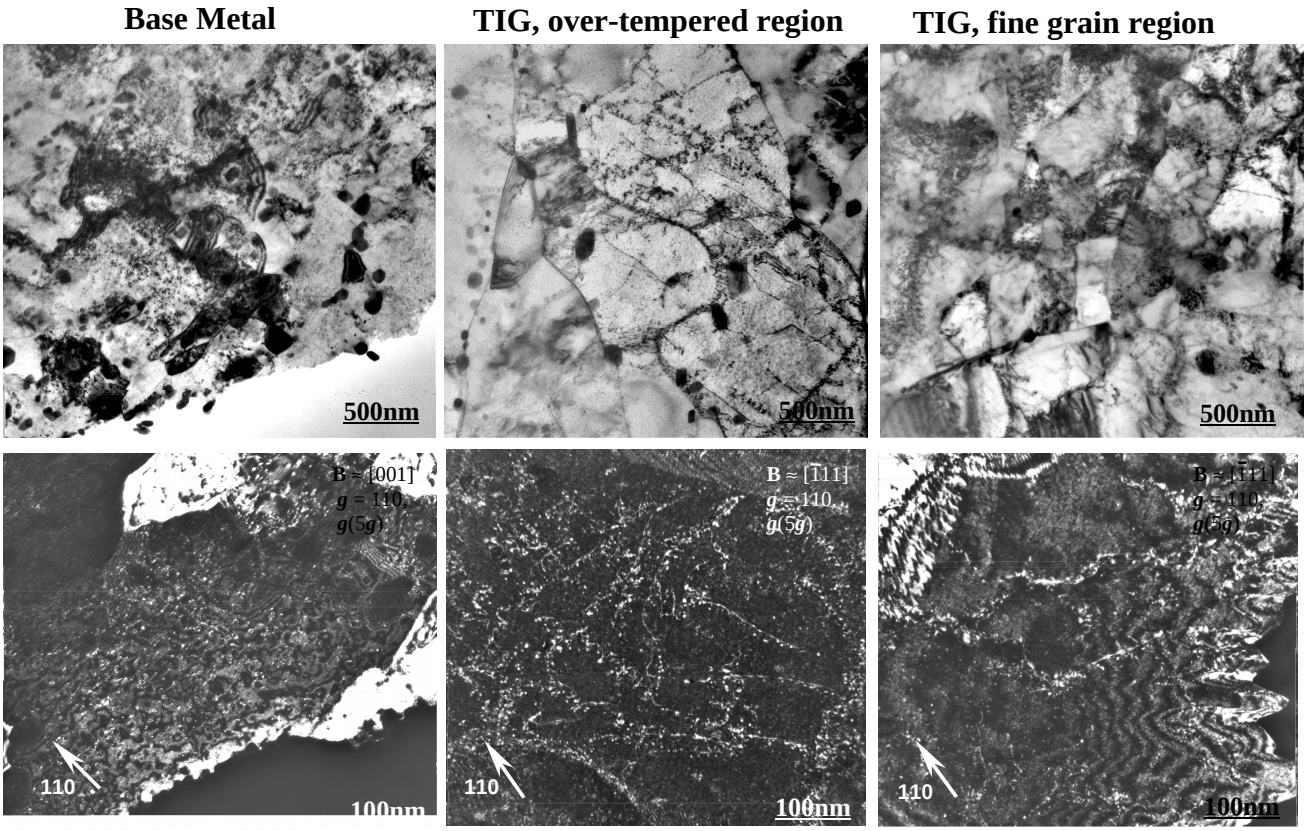

Fig. 6. Microstructure of irradiated F82H base metal, over-tempered region, and fine grain region of TIG weldment.

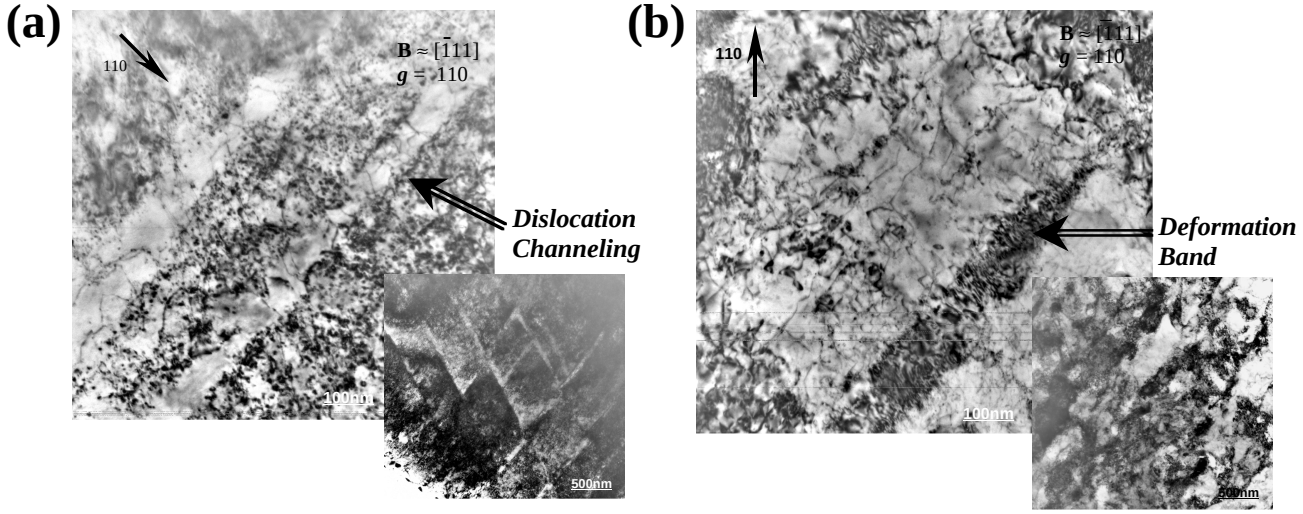

Slip plane: (110) and (0$\bar{1}$1)
Slip direction: [111] and [$\bar{1}$11]

Fig. 7. Microstructure of deformed F82H base metal (a) and over-tempered region of TIG weldment (b) irradiated at 573K to 5 dpa.

In contrast, the deformation microstructure of the irradiated TIG (over-tempered region) showed not dislocation channels but deformation bands (Fig.7(b)). Deformation bands with a 100 nm in width were lying on the (110). Since the irradiated TIG specimen had no dislocation loops and less defect clusters, dislocation channeling was not the dominant deformation mode.
These results suggest that the microstructure before irradiation could affect the development of secondary defects during irradiation, and also affect the dominant deformation mechanism.

Summary

In order to determine the contributions of different microstructural features to strength and to deformation mode, neutron-irradiated F82H (IEA heat) base metal and TIG weldments were investigated by transmission electron microscopy.

The microstructure of the deformed region of irradiated F82H BM showed dislocation channels, suggesting that dislocation channeling could be the dominant deformation mechanism in this steel, resulting in the loss of strain-hardening capacity. The necked region of irradiated F82H TIG (over-tempered region), which has less hardening than F82H BM, showed deformation bands. From these results, it is suggested that the pre-irradiation microstructure, especially one consisting of screw-type dislocations, could affect irradiation-induced secondary defect formation, leading to not only a lower yield stress but also a change in deformation mode after irradiation.

Acknowledgement

This research was sponsored by the Office of Fusion Energy Sciences, US Department of Energy under contract DE-AC05-96OR22464 with UT-Battelle, and the Japan Atomic Energy Research Institute.

REFERENCE

1) J.E. Pawel, K.E. Lenox, and I. Ioka, *Fusion materials semiannual progress report*, DOE/ER-0313/**19**, 312 (1995).
2) J.E. Pawel, K.E. Lenox, I. Ioka, and E. Wakai, *Fusion materials semiannual progress report*, DOE/ER-0313/**21**, 249 (1996).
3) M.L. Grossbeck, K.E. Lenox, M.A. Janney, T. Muroga, W.W. Heatherly, and K.R. Thoms, *Fusion materials semiannual progress report*, DOE/ER-0313/**22**, 254 (1997).
4) K.E. Lenox and M.L. Grossbeck, *Fusion materials semiannual progress report*, DOE/ER-0313/**25**, 307 (1998).
5) K. Shiba, R.L. Klueh, Y. Miwa, N. Igawa, and J.P. Robertson*, Fusion materials semiannual progress report*, DOE/ER-0313/**28**, 131 (2000).
6) N. Hashimoto, S.J. Zinkle, R.L Klueh, A.F. Rowcliffe, and K. Shiba, “Deformation Mechanisms in Martensitic Steels Irradiated in HFIR”, Microstructural Process in Irradiated Materials–2000, Mat. Res. Soc. Symp. Proc. Vol. **650** (2000) R1.10.
7) H. Tanigawa, M. Ando, Y. Katoh, T. Hirose, H. Sakasegawa, S. Jitsukawa, A. Kohyama, T. Iwai, J. Nucl. Mater. **297**, 279 (2001).
8) H. Tanigawa, N. Hashimoto, M. Ando, T. Sawai, K. Shiba, R.L. Klueh, in this proceedings
9) U.F. Kocks, *Metall. Trans.* **1**, 1121 (1970).
10) P.M. Kelly, *Int. Metal. Rev*. **18**, 31 (1973).
11) R.J. Asaro, Advances in *Applied Mechanics*, vol. **23**, Academic Press, New York, 1993, pp.1.
12) D.S. Gelles, R.E. Schäublin, *Mater. Sci. and Eng*. A **309-310**, 82 (2001).

CRACK TIP MICROSTRUCTURES IN F82H ON THE LOWER SHELF - D. S. Gelles (Pacific Northwest National Laboratory)[*], G. R. Odette (University of California at Santa Barbara) and P. Spätig (École Polytechnique Fédérale de Lausanne, – Centre de Recherches en Physique des Plasma, Villigen PSI, Switzerland)

OBJECTIVE

The objective of this effort is to better understand deformation behavior in low activation ferritic steels with regard to fracture toughness testing.

SUMMARY

Dislocation microstructures have been examined near the crack tip of a compact tension specimen of unirradiated F82H loaded to 25.6 MPa $m^{1/2}$ at –196°C after fatigue precracking. A specimen was prepared by sectioning, dimple grinding and ion milling in order to produce electron transparency just behind the crack tip. The tip was found to have trifurcated with moderate dislocation densities ahead and to the side of each tip extending at least 4 to 5 μm, but regions adjacent to the fatigue crack but back from the tip displayed only minor dislocation rearrangement of lath boundaries.

PROGRESS AND STATUS

Introduction

Observation of microstructure at cracks in metals has only recently been considered viable with the development of ion milling techniques suitable for preparation of metallic specimens. Recent work at PNNL has utilized the ion milling procedure to allow observation of microchemistry and microstructure in irradiated austenitic steels undergoing stress corrosion cracking[1] and to allow dislocation and very small bubble examination in ^{3}He injected palladium foils.[2] Given recent advances in our understanding of post-irradiation deformation response in ferritic steels based on miniature tensile specimens,[3-4] the opportunity to study plane strain deformation behavior at a crack tip generated during a fracture toughness test was deemed appropriate. For example, it has not yet been demonstrated that post-irradiation deformation behavior under tensile loading, which can lead to channel deformation, will be duplicated under plane strain conditions. The present effort is intended to show that deformation at a crack tip can be studied. As procedures are in place to prepare similar specimens of irradiated austenitic steels, it is hoped that this work will be expanded to include examination of a similar sample of F82H following irradiation.

Experimental Procedure

Two 0.4T compact tension specimens of F82H (0.35x0.84x0.89 $in.^3$) in the fully tempered precracked condition were loaded in order to produce crack tip deformation. The first, P4-2, was loaded at room temperature to 100 MPa $m^{1/2}$ and the second, P4-10, was loaded to 25.6 MPa $m^{1/2}$ in a liquid nitrogen bath. Specimen P4-2 contained a remaining ligament of only ~0.03 in. with a crack tip microstructure therefore affected by the back surface, whereas P4-10 was cracked approximately half way through, so only P4-10 was prepared for examination.

Specimen P4-10 was sectioned using a slow speed diamond-impregnated-blade to provide a central longitudinal slice perpendicular to the crack surface and a 3 mm disk was cut with the crack tip located at the midpoint. One side was ground and polished to a high polish using 1-2 μm BN grinding compound and the other side was dimple ground to a thickness of ~10 μm with a similar final polish. Final thinning was performed on an ion mill using ultra high purity (99.999%) argon. Milling was centered just behind the crack tip with conditions for thinning 1 h at ±6º and 5 kV, and for final polishing 15 min at ±4º and 2 kV.

---

[*] Pacific Northwest National Laboratory (PNNL) is operated for the U.S. Department of Energy by Battelle Memorial Institute under contract DE-AC06-76RLO-1830.

Both the Dimple Grinder model 656 and Precision Ion Polishing System (PIPS) model 691 were obtained from Gatan, Inc of Pleasanton, CA and the procedures used are based on those developed by Gatan.

Microscopy was performed using either a JEM-840 Scanning Electron Microscope (SEM) operating at 20 KeV or JEOL 1200EX or Tecnai 30 Transmission Electron Microscopes (TEM) operating at 120 and 300 KeV, respectively. All images are digitized, either directly or from scanned negatives. Image processing included electronic dodging to compensate for low magnification negatives with very high contrast.

Results

Metallography

In order to ensure that the 3 mm disk contained the crack tip at the center, the central slice was polished and etched to show grain boundary and lath structure. The microstructural features found are provided in Figures 1 and 2.

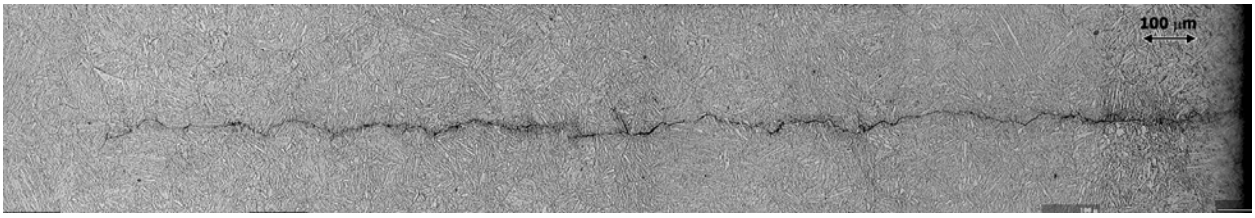

Figure 1. Etched metallographic section showing the crack in specimen P4-10.

Figure 1 shows that in cross section the fatigue crack is not straight, with deviations on the order of 50 µm. The crack follows some prior-austenite grain boundaries, but transgranular cracking tends not to produce straight sections, in contradiction to what might be expected based on fractographic examinations. A central section of the fatigue crack shows both a vertical secondary crack and a step. From the higher magnification image in Figure 2, it can be estimated that the crack stopped at a prior-austenite grain boundary. However, another crack appears to have formed ahead of the propagating crack, shown at the upper left. It is possible that the two are linked, but the crack is not revealed by etching. Note that the step at the center of Figure 1 also shows poor crack definition.

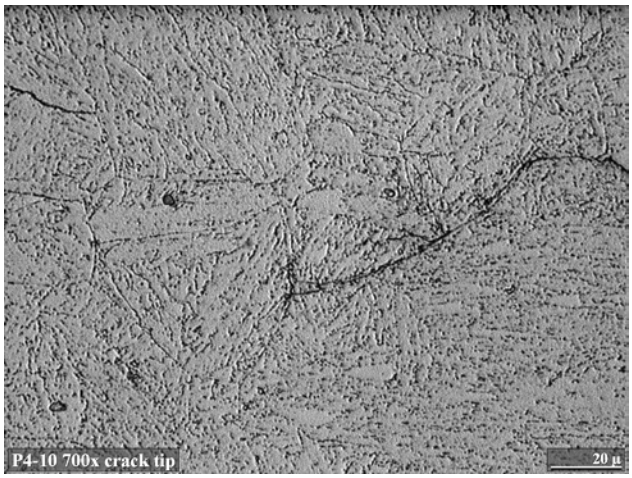

Figure 2. Crack tip of Figure 1 at higher magnification

Microscopy

Ion milling produced a perforation that was as much as 15 µm wide. An SEM montage of the crack and perforation is provided in Figure 3. In this case, several crack sections are found to be quite straight, and a secondary crack again can be noted near the center of the montage. The ion milled perforation shows a darker electron-transparent region adjacent.

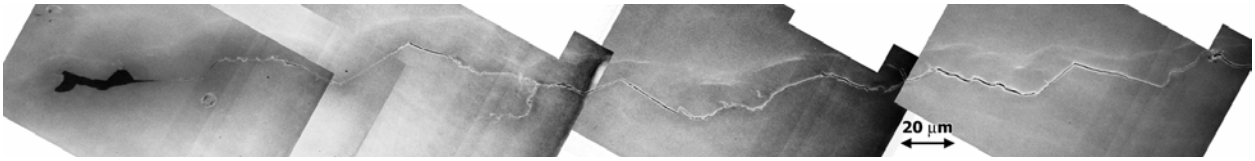

Figure 3. SEM montage of the crack tip following ion milling.

A low magnification TEM image of the perforation is provided in Figure 4. The image was developed to show the microstructure adjacent to the perforation at low magnification, and as a result the edge of the perforation is not visible. This image defines three cracks at the crack tip and a fourth secondary crack, marked 1, 2, 3, and 4 respectively. Therefore, it is possible that this crack tip developed three (or four) small cracks on loading.

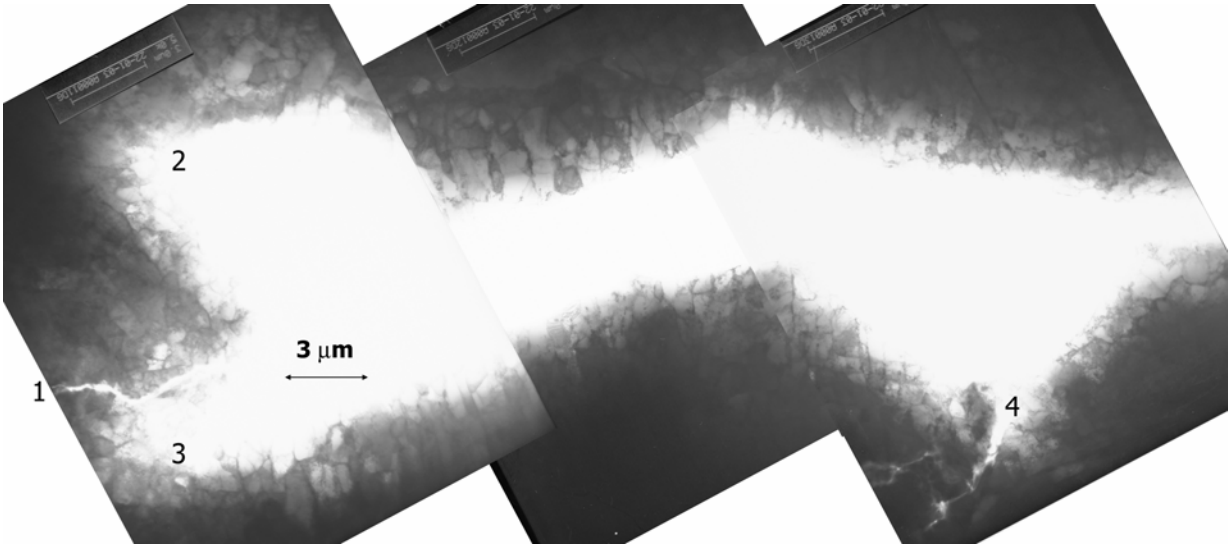

Figure 4. Low magnification montage of the perforation behind the crack tip.

Examination of the regions around the perforation but away from cracks showed microstructure characteristic of as-tempered treatments except for two features. Evidence of surface restructuring from the ion milling could be found that produced wide darker parallel wavy bands, and the dislocation structure at lath boundaries appeared to be rearranged. Three examples are provided in Figure 5 using g=200 so all (a/2)<111> dislocations are visible. The images are anaglyphs requiring colored glasses to see the structures in stereo. The ion milling artifacts are most visible in Figure 5c running from the upper left to lower right as wavy dark bands in the central sub-grain. In comparison, a dislocation slip band can be identified in a similar region in Figure 5b. However, the sub-boundary structure, most apparent towards the bottom of Figure 5a, consists of dislocations that extent a short distance from the subgrain boundary. In comparison, the as-tempered sub-boundary structure is simpler and more planar. This extended structure indicates that the dislocations in the original sub-boundary moved as a result of the stresses from the nearby fatigue crack tip.

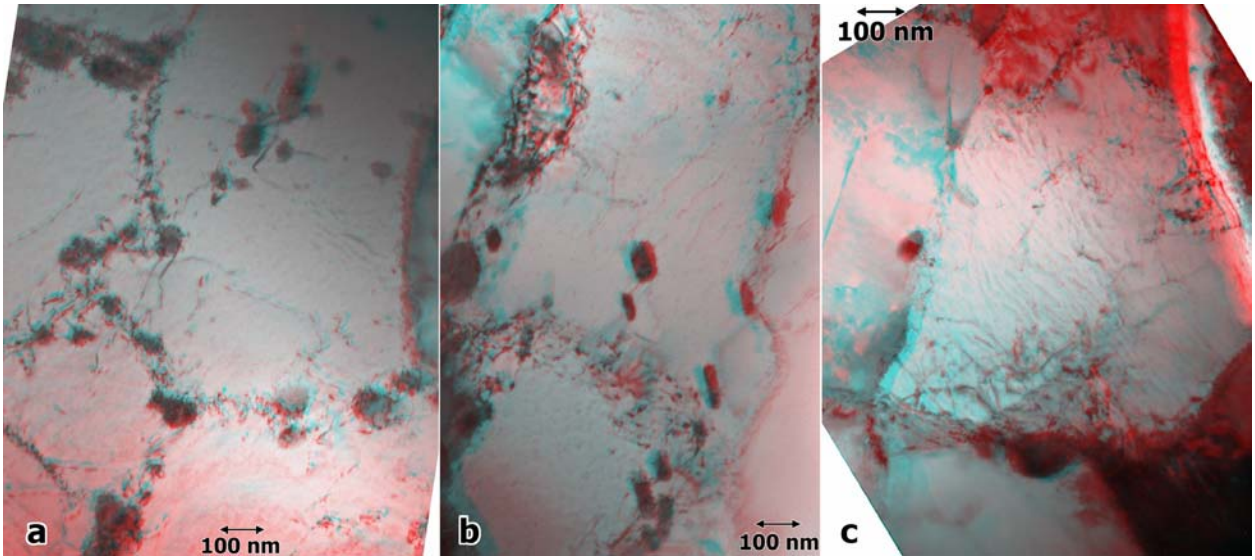

Figure 5. Anaglyph examples of the dislocation structures away from the crack tips.

In comparison, the dislocation structure ahead of the crack tip was more complex. The dislocation density was higher, but individual dislocations could be imaged clearly at higher magnifications. An example is shown as a low magnification montage in Figure 6. The dislocation density below the crack tip in Figure 6 is shown to be much higher than that found in Figure 5 but regions back from the tip are at a more moderate density. Note that local shear has occurred to allow the crack tip to open and the crack is about 200 nm wide near the tip.

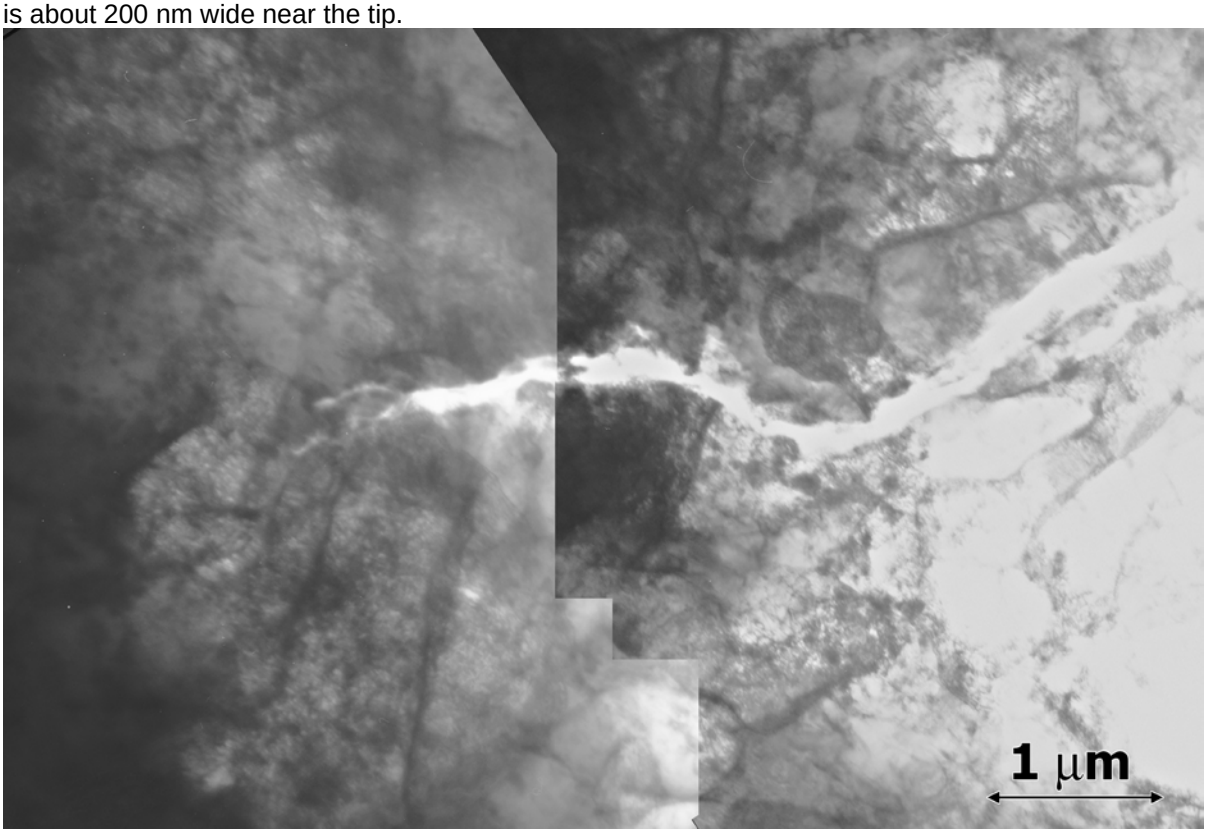

Figure 6. Dislocation structures near blunted crack tip 2.

In order to define the extent of the deformation, a low magnification montage has been prepared for this crack tip, shown in Figure 7. The crack tip appears dark on the right. Many carbide particles can be identified in lighter areas (diffracting weakly), but darker regions in dislocation contrast show fine dislocation structure. The upper portion of this figure approaches the area affected by crack 1, but similar deformation can be identified on either side of the crack. Therefore, Figure 7 demonstrates that significant dislocation damage has occurred at least 4 to 5 μm from the crack.

Discussion

The results obtained for dislocation behavior at a crack tip in a compact tension specimen of F82H tested at -196°C (on the lower shelf) demonstrate that such experiments are viable. Ion milling provides specimens that retain deformation microstructures with few artifacts. It can therefore be anticipated that similar examinations are possible on irradiated specimens. However, it should be emphasized that such experiments are quite difficult. Specimen miniaturization procedures such as 1 mm specimen geometries can simplify microstructural studies of magnetic materials due to reduced magnetic mass, but preparation of the crack tip within a 1 mm sample is expected to be very difficult. Therefore, magnetic effects complicate imaging. The nature of the lath martensite structure requires tilting of each lath in order to optimize dislocation imaging, and deformation within a lath further complicates imaging procedures. In order to understand crack tip deformation, imaging must extend over many lath distances, and therefore, a display of the dislocation structure requires montage techniques that are difficult to optimize. We expect to continue examination of specimen P4-10 after further ion mill thinning, so that the extent of deformation beyond the blunted crack tip can be better understood.

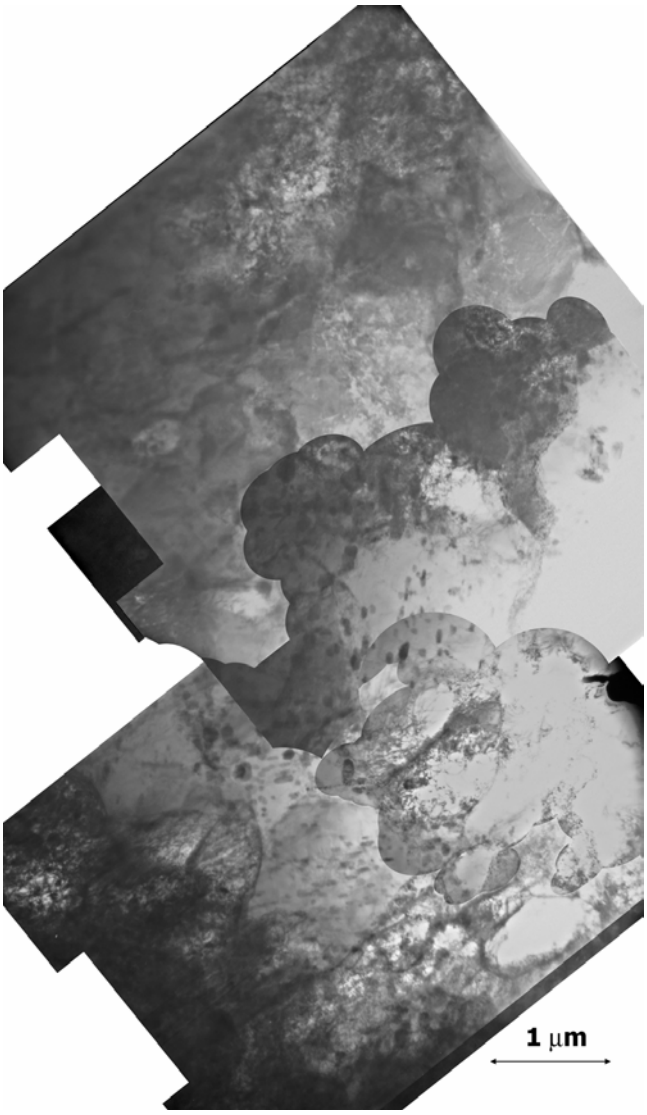

Figure 7. Low magnification montage of microstructure around crack 2.

Results obtained thus far demonstrated that fatigue pre-cracking can proceed with very minor effects on nearby dislocation structures. Only minor rearrangements of sub-grain boundary dislocations are observed. However, crack propagation from further loading of a fatigue pre-crack produces local plastic deformation. One example showed widening of the crack tip to 200 nm. The density of dislocations at a crack tip can be described as moderate; individual dislocations can be imaged in bright field. But the extent of the deformation from a crack tip is at least 4 to 5 μm, but the extent of the plastic zone size is not yet determined. Therefore, this effort must be considered a beginning.

Conclusions

Dislocation microstructures have been examined near the crack tip of a fatigue pre-cracked compact tension specimen of F82H loaded at -196°C to 25.6 MPa $m^{1/2}$. The tip was found to have trifurcated with moderate dislocation densities ahead and to the side of each tip extending at least 4 to 5 μm, but regions adjacent to the crack but back from the tip in the fatigue pre-cracked region displayed only minor dislocation rearrangement of lath boundaries.

FUTURE WORK

The effort is expected to continue and eventually shift to examination of a specimen tested following irradiation in HFR, Petten.

REFERENCES

[1] L. E. Thomas and S. M. Bruemmer, Corrosion, V 56 (2000) 572.

[2] D. S. Gelles, R. Causey, K. Hertz, D. F. Cowgill, and R. Schäublin, "Bubble Microstructures in Helium Injected Palladium Foils**,"** submitted for publication in Effects of Radiation on Materials: 21th International Symposium*,* ASTM STP 1447*,* M. L. Grossbeck, Ed., ASTM International, West Conshohocken, PA, 2003.

[3] D. S. Gelles, M. L. Hamilton and R. E. Schäublin, "Post-Irradiation Deformation Microstructures in Fe-9%Cr," in Effects of Radiation on Materials: 20th International Symposium, ASTM STP 1405, S. T. Rosinski, M. L. Grossbeck, T. R. Allen, and A. S. Kumar, Eds., American Society for Testing and Materials (2001) 523.

[4] S. Gelles and R. Schäublin "Examination of Postirradiation Deformation Microstructures in F82H," DOE/ER-0313/31, July-December 2000, 85.

IRRADIATION EFFECTS ON IMPACT TOUGHNESS OF HIGH-CHROMIUM FERRITIC/MARTENSITIC STEELS—R. L. Klueh and M. A. Sokolov (Oak Ridge National Laboratory)

OBJECTIVE

The objective of this work is to develop an understanding of the effect of irradiation on fracture behavior the reduced-activation ferritic/martensitic steels that are of interest for fusion applications and to use that knowledge to develop steels with improved properties.

SUMMARY

Charpy specimens of four ferritic/martensitic steels were irradiated at 376-405ºC in the Experimental Breeder Reactor (EBR-II) to 23-33 dpa. The steels were the ORNL reduced-activation 9Cr-2WVTa and that steel containing 2% Ni (9Cr-2WVTa-2Ni), modified 9Cr-1Mo, and Sandvik HT9 (12Cr-1MoVW). The steels were normalized and then the 9Cr-2WVTa and 9Cr-2WVTa-Ni were irradiated after tempering 1 hr at 700ºC and after tempering 1 h at 750ºC; the 9Cr-1MoVNb and 12Cr-1MoVW were tempered 1 h at 760ºC. Based on the change in ductile-brittle transition temperature and the upper-shelf energy, the results again demonstrated the superiority of the 9Cr-2WVTa steel over the two commercial steels, which were replaced by the reduced-activation steels. The Charpy properties of the 9Cr-2WVTa-2Ni steel were similar to those of the 9Cr-2WVTa steel for both heat treatments, indicating no adverse effect of the nickel on the properties after irradiation.

PROGRESS AND STATUS

Introduction

The 9Cr reduced-activation ferritic/martensitic steels are being considered for applications as first wall and blanket structural materials for future fusion reactors. Displacement damage by neutron irradiation of these types of steel below 425-450ºC hardens the steel lattice, causing an increase in strength and a decrease in toughness. The effect on impact toughness is measured in a Charpy test as an increase in the ductile-brittle transition temperature (DBTT) and a decrease in the upper-shelf energy (USE).

The possible effect of helium on hardening and embrittlement is important because large amounts of transmutation helium will form in the ferritic/martensitic steel first wall of a fusion reactor. Nickel-doped 9 and 12 Cr steels have been irradiated in a mixed-spectrum reactor such as the High Flux Isotope Reactor (HFIR) to study the effect of helium on fracture [1]. Helium is formed in a mixed-spectrum reactor by a two-step transmutation reaction between ^{58}Ni and the thermal neutrons in the mixed-neutron spectrum. This technique allows for the simultaneous production of displacement damage and helium in the steel matrix, thus simulating what will happen in a first wall. Results from such irradiation experiments at 400ºC have been interpreted to indicate an effect of helium on embrittlement. This conclusion was based on the comparison of the steels with and without nickel and on the differences between the behavior of the nickel-doped steels in a mixed-spectrum reactor, where considerable helium forms, and in a fast reactor, where little helium forms [1].

More-recent irradiation experiments of nicked-doped 9Cr reduced-activation steels have indicated that the nickel-doped steels hardened more than steels without the nickel addition [2,3]. A 9Cr-2W steel with and without 1% Ni was irradiated in the Japanese Materials Test Reactor (JMTR) to 0.15 dpa at 170ºC, and an increase in the room temperature yield stress of up to 350 MPa was observed for the nickel-containing steel, compared to a 120 MPa increase for the steel without nickel. However, no difference in the strength increases was observed for the steels irradiated at 220ºC [2]. Irradiation of these steels to 2.2 and 3.8 dpa at 270 and 348ºC, respectively, in the Advanced Test Reactor (ATR) indicated that the nickel-containing steel hardened about 20% more than the steel without nickel at 270ºC, but strengths were similar after the irradiation at 348ºC [3]. Likewise, there was a larger shift in DBTT for the nickel-containing steel than the one without nickel when irradiated at 270ºC, but not after irradiation at 348ºC. TEM analysis indicated that nickel refined the size of the defect clusters, which were more numerous in the nickel-containing steel [3].

These results indicate that the nickel-doping simulation technique should be used below about 300ºC with caution. The results using nickel doping that most strongly indicated that helium caused an increase in the DBTT above that caused by displacement damage alone were on nickel-doped steels irradiated in HFIR to high fluences at 400ºC [1]. Tensile tests of specimens irradiated under similar conditions gave no indication of hardening due to helium (or nickel) [1]. Also, when the same steels were irradiated at similar conditions in the Fast Flux Test Facility (FFTF), no difference was observed in the embrittlement of the nickel-doped and undoped specimens [4]. Transmission electron microscopy (TEM) studies of nickel-doped steel irradiated in HFIR and FFTF showed that a high density of M_6C formed in the nickel-doped steel but not in the undoped steel [5]. Since the shift in DBTT in HFIR, where helium forms, was larger than in FFTF, where little helium forms, the results were taken to mean that helium caused the shift [1].

In this report, Charpy properties are reported for the reduced-activation steel ORNL 9Cr-2WVTa and this steel containing 2% Ni (9Cr-2WVTa-2Ni) after irradiation in the Experimental Breeder Reactor (EBR-II). The commercial non-reduced-activation steels modified 9Cr-1Mo (9Cr-1MoVNb) and Sandvik HT9 (12Cr-1MoVW) steels were also irradiated and tested.

Experimental Procedure

Compositions and designations of the steels used in this experiment are given in Table 1. In the original Oak Ridge National Laboratory (ORNL) alloy development program for development of reduced-activation steels [6], an 18-kg heat of the electroslag-remelted heat of the 9Cr-2WVTa steel was prepared by Combustion Engineering Inc, Chattanooga, TN. Material from that heat was used as the master alloy to prepare 450-g vacuum arc-melted button heats of 9Cr-2WVTa and 9Cr-2WVTa-2Ni steels. The 9Cr-2WVTa heat was a remelt of the master alloy so that the steels could be compared after similar processing.

Table 1. Chemical composition of the steels tested

Element[a]	9Cr-2WVTa	9Cr-2WVTa-2Ni	9Cr-1MoVNb[b]	12Cr-1MoVW[c]
C	0.098	0.098	0.092	0.20
Si	0.19	0.19	0.15	0.17
Mn	0.39	0.38	0.48	0.57
P	0.014	0.014	0.012	0.016
S	0.003	0.003	0.004	0.003
Cr	8.71	8.55	8.32	12.1
Mo	<0.01	<0.01	0.86	1.04
W	2.17	2.15	<0.01	0.61
Ni	0.02	2.01	0.09	0.51
V	0.23	0.23	0.20	0.29
Nb	<0.01	<0.01	0.06	<0.001
Ta	0.06	0.06		
N	0.016	0.016	0.054	0.027

[a] Balance iron
[b] Modified 9Cr-1Mo steel
[c] Sandvik HT9

The small heats were cast as 25.4 mm x12.7mm x 152 mm ingots, after which they were rolled to 6.4-mm plate and 0.76 mm sheet. The steels were normalized by austenitizing for 0.5 h at 1050ºC in a helium atmosphere, after which they were quickly cooled in flowing helium. Specimens were irradiated in two tempered conditions: 1 h at 700ºC and 1 h at 750ºC.

The modified 9Cr-1Mo (9Cr-1MoVNb) and Sandvik HT9 (12Cr-1MoVW) steels were from large commercial-size heats that have been irradiated previously and were included in this experiment as benchmarks for the reduced-activation steels.

One-third-size Charpy specimens measuring 3.3 x 3.3 x 25.4 mm with a 0.51-mm-deep 30º V-notch and a 0.05- to 0.08-mm-root radius were machined from normalized-and-tempered 6.4-mm plates. Specimens were machined with the longitudinal axis along the rolling direction and the notch transverse to the rolling direction (L-T orientation). The absorbed energy vs. temperature values were fit with a hyperbolic tangent function to permit the USE and DBTT to be consistently evaluated. The DBTT was determined at an energy level midway between the upper- and lower-shelf energies. Details of the test procedure for the subsize Charpy specimens have been published [7-9].

Six Charpy specimens of each heat and each heat-treated condition were irradiated in the COBRA experiment in EBR-II at temperatures of 378 to 405ºC. Fluence was determined from flux monitors in the irradiation canisters. There was some variation for different specimens, depending on their position in the canisters, but the individual sets of specimens for a given steel and heat treatment were kept together in the canisters and experienced the same irradiation conditions. Specimens were irradiated to 5.1×10^{26} to 6.9×10^{26} n/m^2 (E>0.1 MeV), which produced between 23 and 33 dpa. Helium concentrations were calculated to be between about 3 and 6 dpa, depending on the dose and composition (the 6 dpa was for the steel containing 2% Ni).

Results

The Charpy data are summarized in Table 2. First, the results for the reduced-activation 9Cr-2WVTa steel with and without nickel will be discussed to examine the effect of the tempering and the effect of nickel. After this, the results for the 9Cr-2WVTa steels will be compared with the commercial modified 9Cr-1Mo (9Cr-1MoVNb) and Sandvik HT9 (12Cr-1MoVW) steels.

Table 2. Charpy data for unirradiated and irradiated steels

Steel	Temper	Irrd Temp	Dose	Uirrd DBTT	Irrd DBTT	DBTT Shift	Uirrd USE	Irrd USE
9Cr-2WVTa	700ºC	376ºC	23 dpa	-77ºC	-26ºC	51ºC	9.6 J	7.1 J
	750ºC	390ºC	33 dpa	-81ºC	-98ºC	0ºC	14.0 J	9.0 J
9Cr-2WVT-2Ni	700ºC	404ºC	26 dpa	-97ºC	-81ºC	16ºC	9.1 J	7.6 J
	750ºC	390ºC	33 dpa	-125ºC	-86ºC	39ºC	12.8 J	7.1 J
9Cr-1MoVNb	760ºC	405ºC	24 dpa	-17ºC	31ºC	48ºC	10.0 J	8.0 J
12Cr-1MoVW	760ºC	405ºC	24 dpa	-34ºC	54ºC	84ºC	5.4 J	3.5 J

<u>9Cr-2WVTa and 9Cr-2WVTa-2Ni Steels</u>

Both the 9Cr-2WVTa steel with and without the nickel after either the 700 or 750ºC tempers have low DBTTs in the unirradiated condition, with the steel containing nickel having the lowest values. Figure 1 shows the DBTTs for the two steels given the different tempers before and after irradiation. Nickel has a beneficial effect on the transition temperature prior to irradiation, for in both heat-treated conditions, the nickel-containing steel had the lowest value.

After irradiation of the two steels tempered at 700ºC, the 9Cr-2WVTa steel showed the larger shift in DBTT. For the steels tempered at 750ºC, the steel without nickel showed no shift in DBTT, while the nickel-containing steel showed a relatively small shift of 39ºC. The final DBTT values for the 9Cr-2WVTa and 9Cr-2WVTa-2Ni were quite similar (-98 and -86), because of the lower DBTT of the latter steel in the unirradiated condition.

Before irradiation, the 9Cr-2WVTa and 9Cr-2WVTa-2Ni had similar USE values (Fig. 2); as expected, the values after the 750ºC temper were higher than after the 700ºC temper. Irradiation caused a decrease in the USE, with the largest decrease occurring after the 750ºC. As a result, after irradiation there was little difference in the USE of the steels given the different tempering treatments.

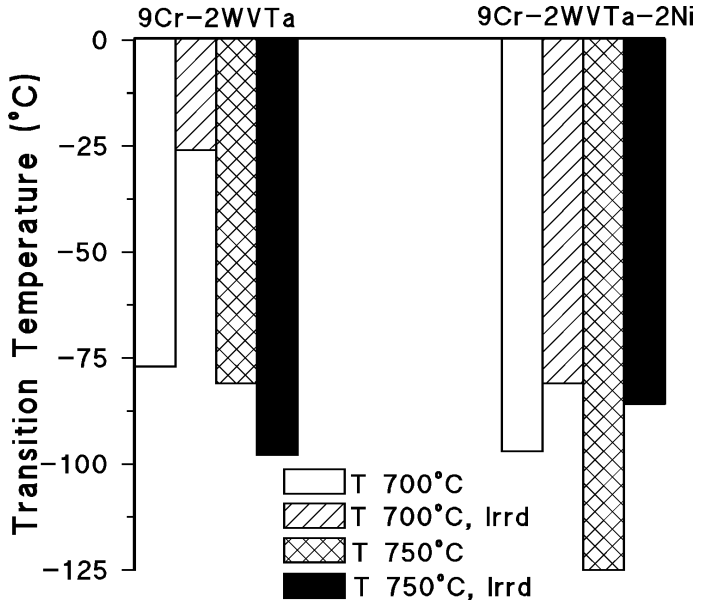

Fig. 1. Transition temperature of 9Cr-2WVTa and 9Cr-2WVTa-Ni steels in the unirradiated and irradiated conditions.

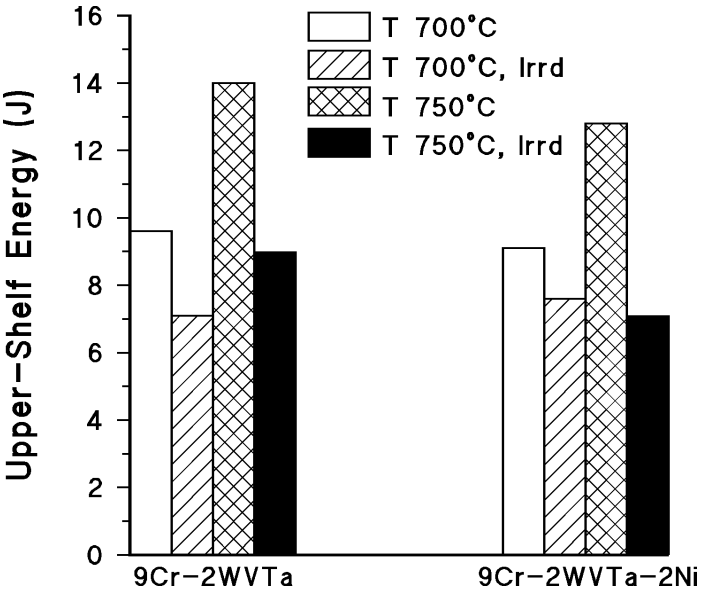

Fig. 2. Upper-shelf energy of 9Cr-2WVTa and 9Cr-2WVTa-Ni steels in the unirradiated and irradiated conditions.

Comparison of Reduced-Activation and Commercial Steels

For a comparison of the reduced-activation 9Cr-2WVTa 9Cr-2WVTa-2Ni steels with the 9Cr-1MoVNb and 12Cr-1MoVW steels, the comparison was made for the 9Cr-2WVTa and 9Cr-2WVTa-2Ni steels tempered 1 h at 750ºC. The commercial steels were both tempered 1 h at 760ºC. In both the unirradiated and irradiated conditions, the transition temperatures of the 9Cr-2WVTa and 9Cr-2WVTa-2Ni steels have a definite advantage over the commercial steels (Fig. 3). After irradiation, the 9Cr-1MoVNb and 12Cr-1MoVW steels have DBTT values above room temperature, whereas the values for the other two steels are well below 0ºC. This occurs dispite the fact that the 9Cr-1MoVNb and 12Cr-1MoVW steels were irradiated at a higher temperature and to a lower dose (Table 2). Indeed, after irradiation the transition temperature values of the 9Cr-2WVTa and 9Cr-2WVTa-2Ni tempered at 700ºC are much better than for either of the commercial steels (Fig. 1). Likewise, in the unirradiated condition, the 9Cr-2WVTa and 9Cr-2WVTa-2Ni steels tempered at 700ºC have much lower transition temperatures than the commercial steels.

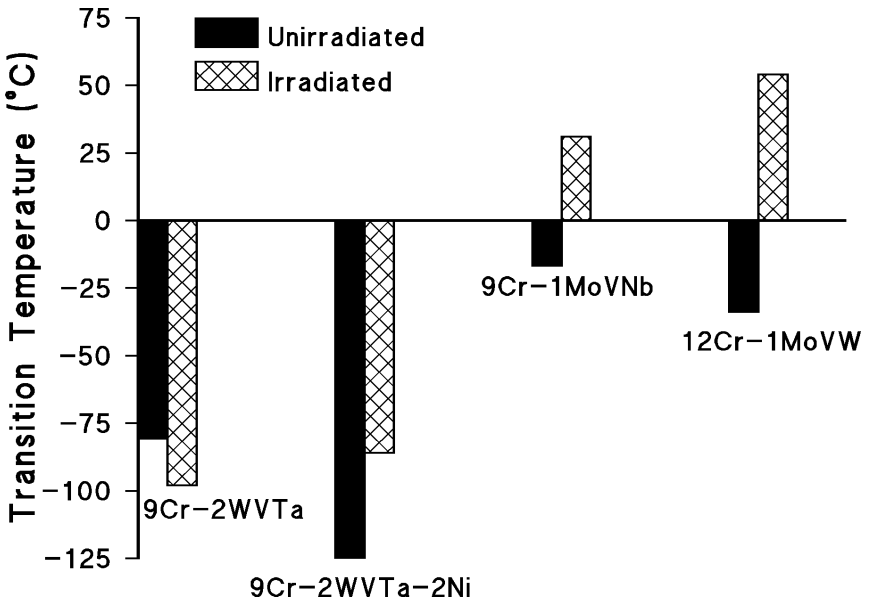

Fig. 3. Transition temperature of 9Cr-2WVTa, 9Cr-2WVTa-Ni, modified 9Cr-1Mo (9Cr-1MoVNb), and Sandvik HT9 (12Cr-1MoVW) steels in the unirradiated and irradiated conditions.

Before irradiation, the USE values of the 9Cr-2WVTa and 9Cr-2WVTa-2Ni are also better than those of the 9Cr-1MoVNb and 12Cr-1MoVW steels (Fig. 4). After irradiation, the USEs of the 9Cr-2WVTa, 9Cr-2WVTa-2Ni, and 9Cr-1MoVNb steels are similar, and all three are considerably higher than for the 12Cr-1MoVW steel. Both before and after irradiation, the values for the 9Cr-2WVTa and 9Cr-2WVTa-2Ni steels tempered at 700ºC (Fig. 2) have USE values that are comparable to the commercial steels before and after irradiation, even though the latter steels were tempered at a higher temperature.

Discussion

In the normalized-and-tempered condition, the results demonstrate the excellent impact properties of the 9Cr-2WVTa steel compared to the modified 9Cr-1Mo and Sandvik HT9 commercial steels. For the nickel-containing version of the steel, the well-known effect of nickel on decreasing the transition temperature is also demonstrated, especially after the 750ºC temper. Even for the 700ºC temper, the 9Cr-2WVTa and 9Cr-2WVTa-2Ni steels have excellent impact properties relative to the commercial steels.

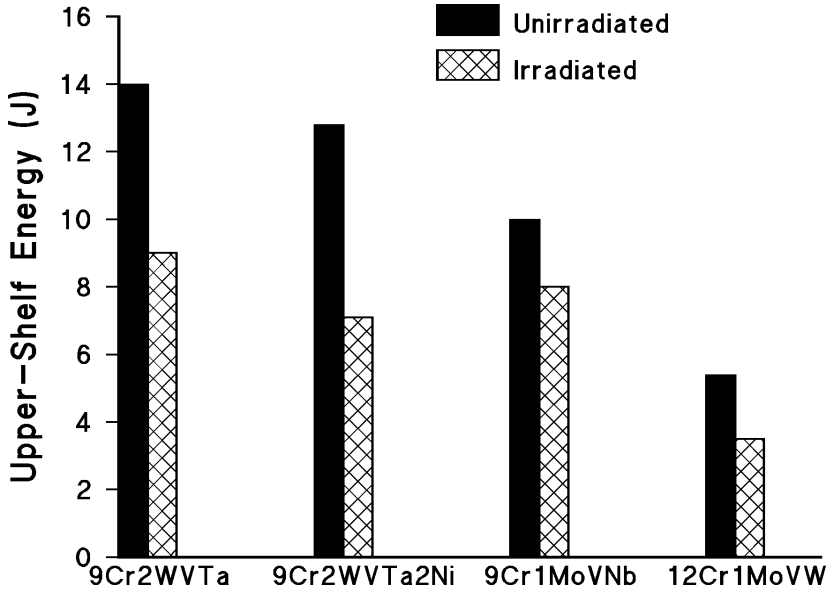

Fig. 4. Upper-shelf energy of 9Cr-2WVTa, 9Cr-2WVTa-Ni, modified 9Cr-1Mo (9Cr-1MoVNb), and Sandvik HT9 (12Cr-1MoVW) steels in the unirradiated and irradiated conditions

The results again demonstrate the high irradiation resistance of the 9Cr-2WVTa steel relative to the commercial steels. The irradiation resistance of the 9Cr-2WVTa-2Ni is as good (after the 750ºC temper) or better (after the 700ºC temper) than the steel without nickel. As discussed earlier, nickel has been added to the steel primarily to study helium effects by comparing the effect of irradiation on the steel with and without the nickel addition in a fast reactor such as EBR-II, where very little helium forms, and in a mixed-spectrum reactor such as HFIR, where a transmutation reaction with ^{58}Ni and thermal neutrons produces much higher helium concentrations [1]. Observations on the 9Cr-1MoVNb and 12Cr-1MoVW steels with and without nickel indicated that there was no increased hardening or enhanced shift in DBTT for the steels when irradiated in FFTF, a fast reactor [4]. However, when irradiated in HFIR where over 200 appm He formed, a larger shift with little difference in hardening was observed for the nickel-containing steel. The additional shift was attributed to helium [1].

In recent years, data obtained at 200-250ºC indicated that the nickel addition to these types of steel could affect the properties by producing excess hardening and a larger shift in DBTT even in a reactor where no significant amount of helium formed [2,3]. There was no indication that the nickel-containing steel in this experiment hardened excessively, which would be expected to result in a larger DBTT for the nickel-containing steel than for the steel without nickel if it had [2,3]. Tensile tests are required to determine if there was more hardening in the nickel-containing steel. The difference in hardening behavior for the present tests and the previous tests that showed no hardening effect caused by nickel when irradiated in a fast reactor [8] and the tests that showed hardening [2,3] would appear to be due to the different test temperatures. The hardening in the low-temperature tests that indicated nickel-enhanced irradiation hardening was attributed to finer defect clusters in the nickel-containing steels [3]. It may be that such clusters are not stable at the higher temperatures.

Future Work

Tensile specimens were also irradiated in the capsules that contained the Charpy specimens discussed in this report. These will be tested to determine the relationship of the shift in DBTT to hardening. Transmission electron microscopy specimens of unirradiated and irradiated 9Cr-2WVTa and 9Cr-2WVTa-2Ni in the two tempered conditions used in this experiment have been examined. An attempt will be made to relate the microstructures of the steels to the mechanical properties.

References

[1] R. L. Klueh and D. J. Alexander, J. Nucl. Mater. 187 (1992) 60.
[2] R. Kasada, A. Kimura, H. Matsui, and M. Narui, J. Nucl. Mater. 258-263 (1998) 1199.
[3] A. Kimura, Report of IEA Workshop on Reduced-Activation Ferritic/Martensitic Steels, JAERI-Conf 2001-007, p. 348.
[4] W. R. Corwin, J. M. Vitek, and R. L. Klueh, J. Nucl Mater. 149 (1987) 312.
[5] P. J. Maziasz, R. L. Klueh, and J. M. Vitek, J. Nucl. Mater.141-143 (1986)929.
[6] R. L. Klueh and P. J. Maziasz, Met. Trans. 20A (1989) 373.
[7] D. J. Alexander, R. K. Nanstad, W. R. Corwin, and J. T. Hutton, in: Applications of Automation Technology to Fatigue and Fracture Testing, ASTM STP 1092, Eds. A. A. Braun, N. E. Ashbaugh, and F. M. Smith (American Society for Testing and Materials, Philadelphia, 1990) p. 83.
[8] D. J. Alexander and R. L. Klueh, in: Charpy Impact Test: Factors and Variables, ASTM STP 1072, ed. J. M. Molt (American Society for Testing and Materials, Philadelphia, 1990) p. 179.
[9] M. A. Sokolov and R. K. Nanstad, in: Effects of Radiation on Materials: 17th International Symposium, ASTM STP 1270, eds. D. S. Gelles, R. K. Nanstad, A. S. Kumar, and E. A. Little (American Society for Testing and Materials, Philadelphia, 1996) p. 384.

MICROSTRUCTURE AND HARDNESS VARIATION IN A TIG WELDMENT OF IRRADIATED F82H —
H. Tanigawa (Japan Atomic Energy Research Institute), N. Hashimoto (Oak Ridge National Laboratory), M. Ando, T. Sawai, K. Shiba (JAERI), R.L. Klueh (ORNL)

OBJECTIVE

The objective of this work is to identify the part of a weld joint that exhibited lower hardening on a HFIR11J irradiated (5dpa 573K) weld joint tensile specimen and investigate the mechanisms occurring by analyzing the corresponding microstructure.

SUMMARY

Previous work reported that a TIG weld joint of F82H exhibited low irradiation hardening in a tensile test, compared to the base metal. Microhardness tests and microstructure observation on the neutron-irradiated TIG weld joint of F82H revealed that the over-tempered zone in the heat-affected zone (HAZ) exhibited this good performance. The region in the HAZ where the prior austenite grain became very fine during welding also exhibited lower irradiation hardening. Hypotheses for these low-hardening mechanisms were proposed based on the phase diagram and grain orientation.

PROGRESS AND STATUS

Introduction

To validate the potential of reduced-activation ferritic/martensitic steel (RAF) as a structural material for fusion power plants, the methodology for joining the steel to form welds with adequate toughness before and after irradiation must be developed. In this study, an irradiated tungsten inert-gas (TIG) weldment (weld metal, base metal and HAZ) of the IEA-modified F82H (F82H-IEA) was investigated. Previous post-irradiation tensile test results of F82H-IEA TIG weldment specimens suggested that the weld metal exhibited almost the same amount of irradiation hardening as the base metal, but the HAZ showed far less hardening than the base metal (Fig. 1) [1]. In this study, a hardness profile across the irradiated weld joint was determined to investigate the location of the weldment that was involved with this low hardening. The mechanisms responsible for this low hardening were investigated in order to provide guidelines for the improvement of radiation resistance of F82H by heat treatment.

Experimental

The materials used for this research were normalized-and-tempered F82H-IEA steel, nominally Fe-7.5Cr-2W-0.15V-0.02Ta-0.1C, in wt%, and an F82H TIG weldment. The TIG welding was performed using pulsed direct current with filler wire for 5 to 6 passes on pre-heated and U-shape grooved 15mm thick plate. The TIG weldment was annealed at 993K for 1 hour. SS-3 type tensile specimens were machined with the HAZ in the middle of the gage section. The details of the welding conditions and specimens were explained in a previous paper [1]. Irradiation was performed in the Oak Ridge National Laboratory (ORNL) High Flux

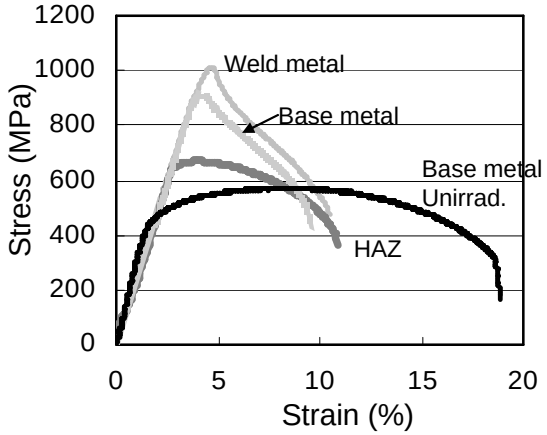

Fig. 1 Tensile results of irradiated weldments and unirradiated base metal [1].

Isotope Reactor (HFIR) up to 5 dpa at 573K. Vickers hardness tests (500 gf load) were carried out along the gage section of the tensile specimens at 254μm (0.010 in) intervals from the weld metal region to the base metal region in order to obtain the micro hardness profile. Five as-prepared specimens and four irradiated specimens were tested, and in total 8 hardness profiles were obtained for each conditions. Specimens were etched with 88% H_2O/10% HNO_3/2% HF prior to the hardness tests in order to perform metallography after the hardness tests to determine hardness-microstructure correlation. Post-irradiation tensile tests were carried out at room temperature at a strain rate of $1x10^{-3}$ s^{-1} on the hardness-tested specimens to identify in which microstructural region the tensile fracture occurred.

Surface observations were performed by Scanning Electron Microscopy (SEM) using FE-SEM (Philips XL30) for unirradiated specimens and conventional SEM (TOPCON ABT-32) for irradiated specimens. For unirradiated specimens, the Orientation Image Mapping (OIM) system (Tex SEM Laboratories) and X-ray energy-dispersive spectrometry (XEDS) system were used to analyze the grain orientation distribution and precipitate distribution, respectively. The OIM analysis was performed with a resolution of 200 nm and a 0.05 s exposure time per spot. The XEDS mapping was done with a resolution of 200 nm and a 4.0 s dwell time per spot.

Results and discussion

The microstructure of the TIG weldment is shown in Fig. 2. The microstructure consisted of 3 regions; i.e., weld metal, HAZ, and base metal. The HAZ can be further divided into 3 regions with obviously different microstructures, and those regions are denoted with a circled number in Fig. 2. Here we call the boundary line between region 1 and region 2 the transformation line, since the α–γ transformation occurred during welding within the region inside these lines. It should be noted that the microstructure of the weld metal was rather fine except for the last pass region, and the HAZ was wider than that of a single-pass weldment, since a multi-pass TIG weld was used in this study.

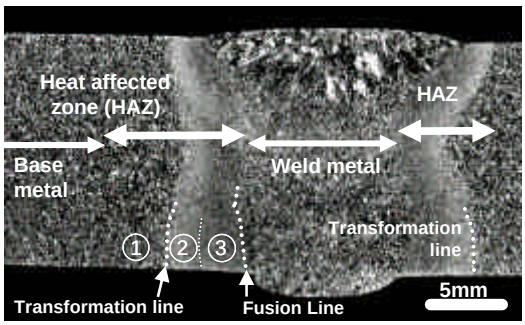

Fig. 2 Micrstructure of TIG weldment and the definitions of the different regions.

The HAZ microstructure of a singe-pass weld on a martensitic steel can be defined as follow [2] (see Fig. 3):

HAZ1 (T_T<T<Ac_1) — The original tempered martensite was heated above the tempering temperature (T_T=1023K), i.e. it was over-tempered. The microstructure is quite similar to that of the base metal as the region was never heated over Ac_1 (the temperature at which austenite begins to form on heating ≅1113K).

HAZ2 (Ac_1<T< Ac_3) — Over-tempered martensite and freshly formed martensite constitute the very fine microstructure, as this region was heated between Ac_1 and Ac_3 (the temperature at which the austenite transformation is complete ≅1193K). The prior austenite grains are generally very fine and ambiguous.

HAZ3 (Ac_3<T<$T_{γδ}$) — The microstructure is freshly formed martensite. The grains are finer than that of base metal, but larger than in HAZ2. The fine

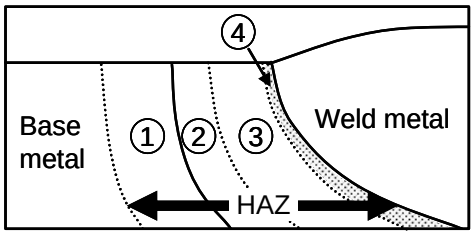

Fig. 3 Schematic diagram of HAZ microstructure which is formed by a single-pass TIG weld.

grains were observed at the region near HAZ2 and coarse grains were observed near region HAZ4 as this region was heated to just below $T_{\gamma\delta}$ (the temperature at which δ phase began to form)

HAZ4 ($T_{\gamma\delta}$<T< T_m) — Fresh martensite and δ-ferrite was formed during welding in this region as this is located next to the fusion line.

Fig. 4 shows the schematic diagram of the multi-pass TIG welding process and the thermal history of a weldment, and Fig 5 shows the magnified microstructure of the HAZ which was formed by the multi-pass weld and tested in this study. This microstructure can be interpreted on the basis of the highest temperature (T_{max}) achieved during welding as follows:

Region 1 (T_T<T_{max}<Ac_1) — This region was over-tempered several times during welding. The microstructure is the same as HAZ1.

Region 2 (Ac_1<T_{max}<Ac_3) — The microstructure of this region is the same as HAZ2 as it was once heated between Ac_1 and Ac_3, but also over-tempered several times by subsequent passes during welding.

Region 3 (Ac_3<T_{max}<$T_{\gamma\delta}$) — HAZ3 would correspond to this region, but no larger grains were observed probably because this region was also heated between Ac_1 and Ac_3 and over-tempered a few times.

Region 4 ($T_{\gamma\delta}$<T_{max}<T_m) — This region must form martensite and δ-ferrite during welding, as this is located next to the fusion line. δ-ferrite was not obvious, and the microstructure was similar to that of region 3. This is probably because this region was also heated over Ac_3 or Ac_1 once or twice, and over tempered several times by the multi-pass welding.

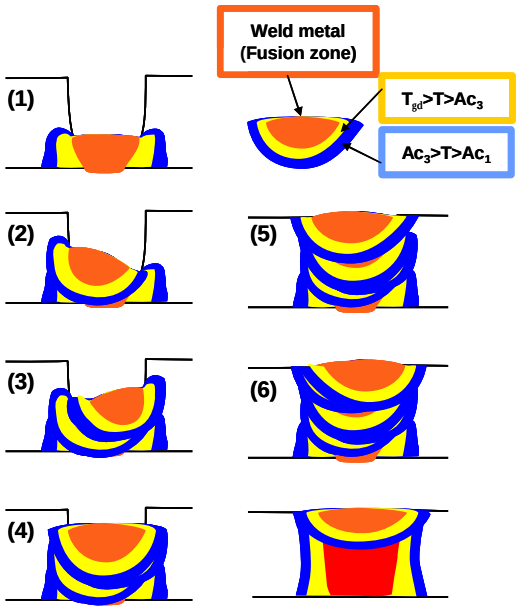

Fig. 4 Schematic diagram of the multi-pass TIG welding process and the thermal history of weldment

The microhardness profiles across the weld joint are shown in Fig. 6. Figure 6 (a) shows that minimum hardness was obtained for both unirradiated and irradiated specimens in the “over-tempered region,” the region just next to the transformation line in region 1, which is denoted as A in Fig. 5. On the other hand, as shown in Fig. 6 (b), both minimum ΔHv and minimum hardening ratio were obtained at the “fine-grain region,” the region which is located at about 1 mm from the transformation line in region 2, denoted as B in Fig. 5. The same hardness profile changes were also obtained in ion-irradiated TIG weldments [3].

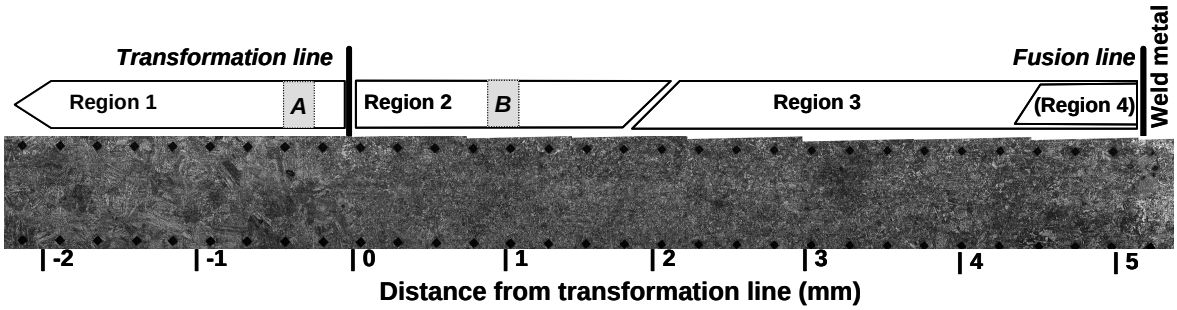

Fig. 5 Magnified image of HAZ and the definitions of the regions.

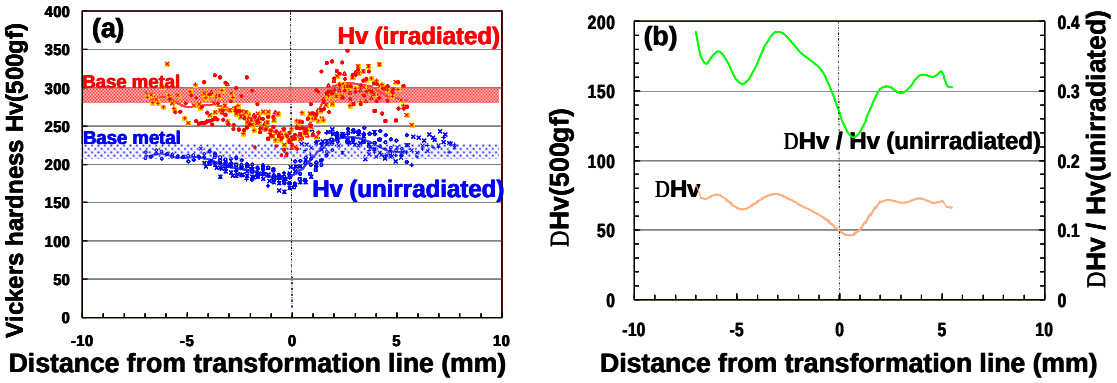

Fig. 6 The profile of (a) hardness and (b) hardness increase and the ratio of increase over irradiated and unirradiated weldments .

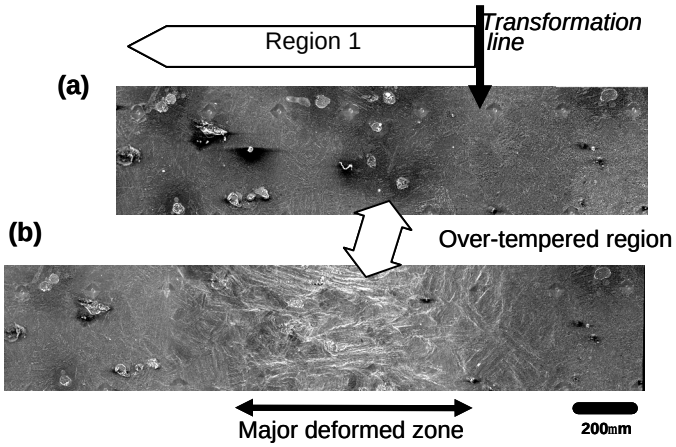

Fig. 7 Microstructure of (a) as-hardness-tested and (b) deformed weld joint tensile specimens .

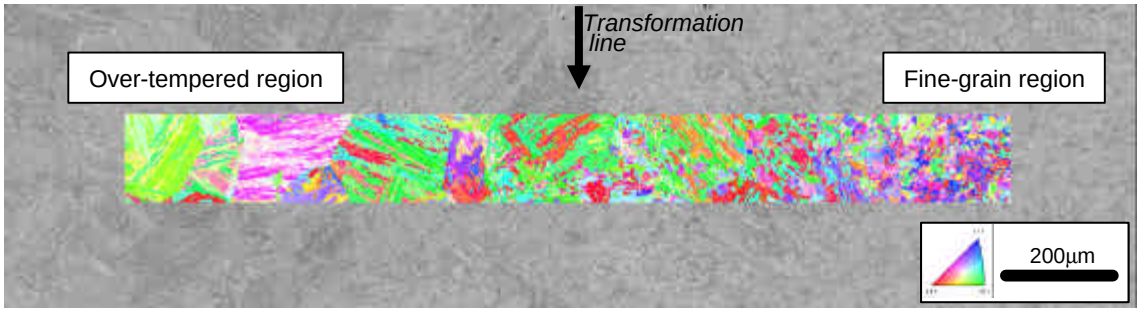

Fig.8 BSE images and OIM results plotted on the corresponding location of the weldment.

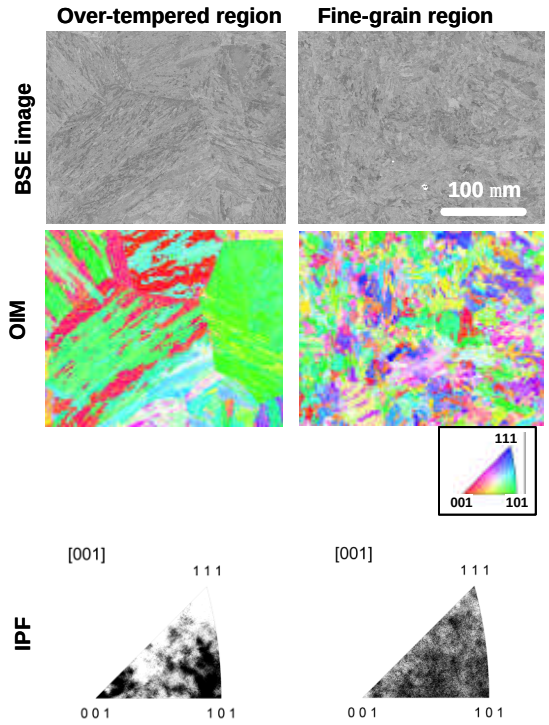

Fig. 9 BSE images with OIM and IPF results on over-tempered region and fine-grain region.

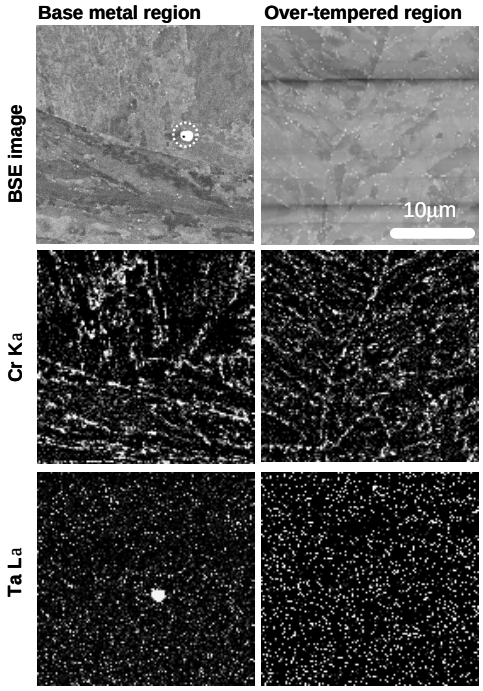

Fig. 10 BSE images and XEDS mapping results on base metal region and over-tempered region. The white dashed circle indicates the BSE image of a Ta-rich precipitate.

A tensile test was performed using the hardness-tested and observed tensile specimen to confirm the region where the major deformation occurred by stopping the tensile test before fracture. The region was identified by the hardness indents near by. As shown in Fig. 7, the major deformation occurred in the over-tempered region.

These results clearly indicate that the tensile results obtained from the weld joint specimen represent the tensile property of the over-tempered region, and the tensile property of the fine-grain region, which exhibited the minimum hardening ratio, is better than the over-tempered region.

Mechanism of low irradiation hardening

Figure 8 shows the OIM results across the transformation line placed on the back-scattered electron (BSE) image. The results show that the grains become fine and isotropic in the fine-grain region. The magnified images of the mapping of each region and inversed pole figure (IPF) are shown in Fig. 9. A triple point of the grain structure is included in both cases, although they are nondistictive in the fine-gain region. The fine-grain region consisted of isotropically oriented grains in which the shapes are related to the former lath or packet structure. IPF also suggests that those fine grains have an isotropic orientation, while the results from the over-tempered region suggest an anisotropic tendency. These results indicate that there are more high-index grain boundaries in the fine-grain region than in the base-metal, as there is no distinctive difference in grain structure between the base-metal region and the over-tempered region.

XEDS mapping was performed to analyze Cr-rich and Ta-rich precipitate distributions on the base-metal region and the over-tempered region (Fig.10). The Cr K_α and Ta L_α peaks were selected for mapping. The

results showed that the distribution of Cr-rich precipitates was similar in each region. The results also indicated that there were no detectable small-sized Ta-rich precipitates. On the other hand, precipitates with bright contrast in the BSE image turned out to correspond to large-sized (>1nm) Ta-rich precipitates, mainly consisting of Ta, Ti and V. These images are dominant both in the over-tempered region and base metal region, but not in the fine-grain region.

From these results, the following hypothetical mechanisms of low hardening for each region were derived:

The fine-grain region — Fine grain structures act as neutral sinks, where induced point defects have high probability to be absorbed and re-combined.

The over-tempered region — No clear evidence was obtained to explain the mechanism of low hardening in this region. One possible explanation which could be indicated from Fe-C phase diagram is that the heating during welding increased the solute carbon concentration. It has been postulated that the local strain field around carbon atoms can act as re-combination sites for irradiation-induced point defects.

Active point defect absorption and re-combination in these regions may result in far less hardening compared to the base metal region.

Hashimoto et.al. performed transmission electron microscopy to analyze the microstructures of these regions of the irradiated weldments [4], and it turned out that no visible dislocation loops were observed in the over-tempered region and the fine-grain region. Small dislocation loops were the main microstructural features in F82H irradiated up to 5 dpa at 573K. This result indicates that more active point defect absorption and re-combination took place in those regions, and this conforms to the hypothetical mechanisms proposed above.

SUMMARY AND CONCLUSIONS

An irradiated TIG weld joint of F82H IEA, which showed far less hardening than the base metal in previous post-irradiation tensile tests, was investigated by taking a hardness profile across the irradiated weld joint to locate the region that was involved with this low hardening. The following summarizes the observations and conclusions:

1. The hardness profile and the metallography indicated that the weakest part of the HAZ is in the over-tempered zone located in the region of the HAZ that was heated to just below the Ac_1, the temperature at which austenite begins to form on heating.
2. A tensile test halted before fracture revealed that the plastic deformation occurred at the lowest hardness region.
3. There is a low-hardening region in the fine-grain region that was heated between Ac_1 and Ac_3 during welding.
4. SEM observations and OIM analyses revealed that the fine-grain region consisted of isotropically oriented fine prior austenite grains.
5. The hypothetical mechanisms proposed for these low hardening regions is that those microstructures involve a high concentration neutral sinks for point defect recombination.

ACKNOWLEDGEMENT

The authors would like to thank E.A. Kenik for helping with the SEM analysis at SHaRE Collaboration Research Center at Oak Ridge National Laboratory. This research was sponsored by the Japan Atomic Energy Research Institute and the Office of Fusion Energy Sciences, US Department of Energy under contract DE-AC05-96OR22464 with UT-Battelle.

REFERENCE

[1] K. Shiba, R.L. Klueh, Y. Miwa, N. Igawa, and J.P. Robertson, Fusion materials semiannual progress report, DOE/ER-0313/28 (2000) 131
[2] R.L. Klueh and D.R. Harries, “High-Chromium Ferritic and Martensitic Steels for Nuclear Applications” ASTM, PA USA (2001), p72
[3] M. Ando, T. Sawai, E. Wakai, JAERI-Research (2002), to be published
[4] N. Hashimoto, M. Ando, H. Tanigawa, T. Sawai, K. Shiba, R.L. Klueh, to be published in this report.

NEUTRON-INDUCED SWELLING OF Fe-Cr BINARY ALLOYS IN FFTF at ~400°C - F. A. Garner and L. R. Greenwood (Pacific Northwest National Laboratory)* T. Okita and N. Sekimura (University of Tokyo) and W. G. Wolfer (Lawrence Livermore National Laboratory)

OBJECTIVE

The purpose of this effort is to determine the influence of dpa rate, He/dpa ratio and composition on the void swelling of simple binary Fe-Cr alloys.

SUMMARY

Contrary to the behavior of swelling of model fcc Fe-Cr-Ni alloys irradiated in the same FFTF-MOTA experiment, model bcc Fe-Cr alloys do not exhibit a dependence of swelling on dpa rate at ~400°C. This is surprising in that an apparent flux-sensitivity was observed in an earlier comparative irradiation of Fe-Cr binaries conducted in EBR-II and FFTF. The difference in behavior is ascribed to the higher helium generation rates of Fe-Cr alloys in EBR-II compared to that of FFTF, and also the fact that lower dpa rates in FFTF are accompanied by progressively lower helium generation rates.

Introduction

In a previous publication it was shown that simple binary Fe-Cr alloys irradiated in the in-core region of FFTF at ~400°C required much higher dpa levels to approach the steady-state swelling condition than that required to reach this condition when the same alloys were irradiated in in-core regions of EBR-II, as shown in Figure 1 (1). Based on comparisons with various austenitic alloys, the different swelling behavior in the two reactors was interpreted to be a consequence of the large difference in swelling rates in the two reactors. For instance, simple Fe-Cr-Ni model austenitic alloys irradiated in FFTF over a wide range of dpa rates in a later experiment were shown to exhibit progressively longer transient regimes of swelling as the displacement rate increased (2). This behavior is shown in Figure 2.

It must be recognized, however, that comparative irradiations of simple Fe-Cr binary alloys conducted in two different reactors are potentially influenced by differences in other important spectral or operating variables, and the observed difference in transient behavior can not be ascribed simply to differences in dpa rate without eliminating the possible role of these other variables.

Since the transient regime of Fe-Cr-Ni austenitic alloys irradiated in FFTF showed such a clear dependence on dpa rate, it was natural to turn to another experiment included in the same FFTF irradiation series to assess the effect of dpa rate. Fortunately, the simple austenitic and ferritic alloys were both irradiated in the same comprehensive experiment.

Experimental Details

Relatively pure Fe-9Cr and Fe-12Cr (at %) with no added solute were prepared by arc melting from high purity Fe and Cr. The binary alloys was rolled to sheets of 0.25 mm thickness, cut into 3 mm disks, wrapped with Zr foil and annealed for 60 minutes at 900°C in high vacuum.

Two sets of identical specimens are placed in sealed, helium-filled packets at each of seven different capsule positions of the Materials Open Test Assembly (MOTA), ranging from below the core to above the core of the Fast Flux Test Facility (FFTF). The packets in general contained four identical specimens of each of the two alloys. In many cases the Fe-Cr-Ni and Fe-Cr alloys were located side-by-side in the

* Pacific Northwest National Laboratory (PNNL) is operated for the U.S. Department of Energy by Battelle Memorial Institute under contract DE-AC06-76RLO-1830.

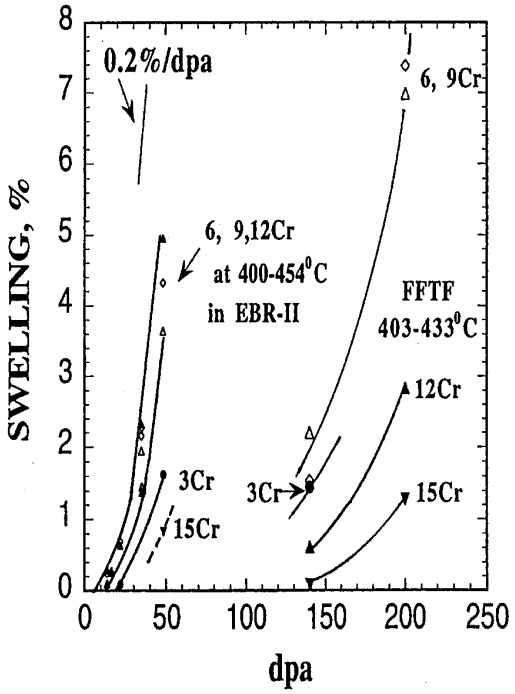

Figure 1. Comparison of swelling of Fe-Cr binary alloys at ~400°C in in-core regions of EBR-II and FFTF, as observed by Garner and coworkers (1). These results were interpreted to arise from the sensitivity of the swelling transient regime on displacement rate, which is lower by a factor of 3-4 in the in-core regions of EBR-II.

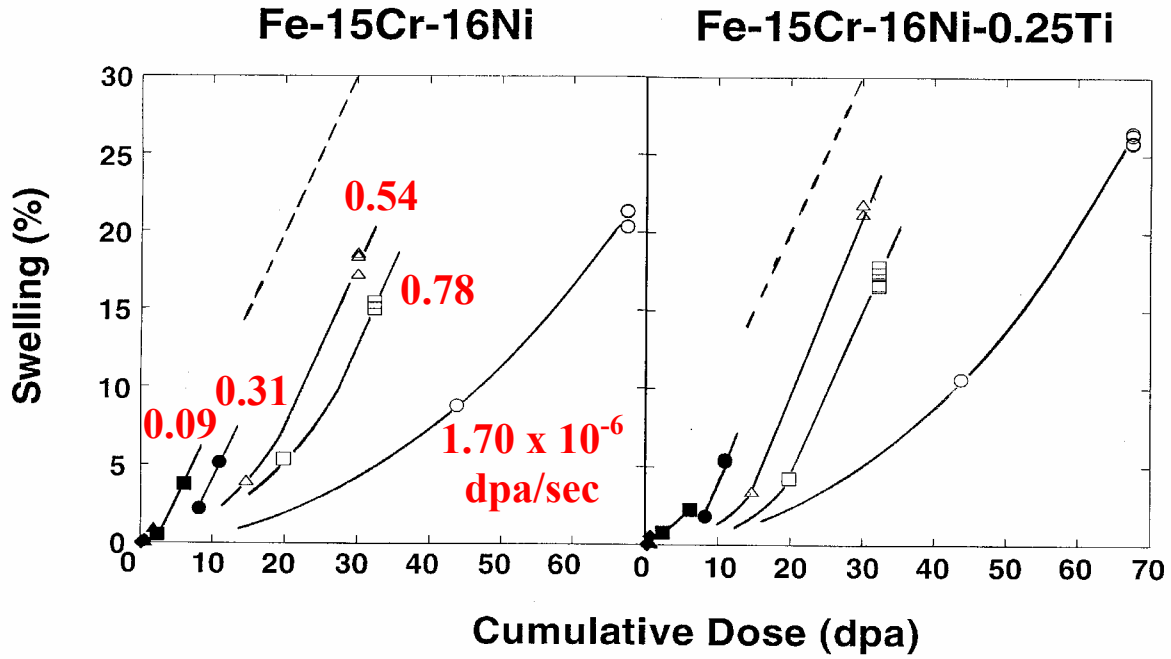

Figure 2. Swelling of simple model fcc Fe-Cr-Ni alloys in FFTF-MOTA at ~400°C, as observed by Okita and coworkers (2), showing that the transient regime of swelling increases progressively as the dpa rate increases.

same packet. Two or more identically-loaded packets were placed in each capsule, with the dpa rate dependent on the axial location in MOTA.

With the exception of the below-core canister, the temperatures in MOTA capsules are actively controlled to ±5°C of the nominal target, although the nominal target temperatures varied a little from capsule to capsule.

The first irradiation sequence occurred in Cycle 11 of MOTA-2A for 2.58 x 10^7 sec, and a subset of specimen packets was then removed. Other identical specimen packets continued in Cycle 12 of MOTA-2B for 1.71 x 10^7 sec. The dose rates in the various capsules ranged from 1.4 x 10^{-8} to 1.7 x 10^{-6} dpa/sec. The dose levels attained by the specimens varied from 0.37 to 43.8 dpa in Cycle11 and an additional 0.24 to 24.0 dpa in Cycle12. Table 1 summarizes the irradiation conditions.

The starting and post-irradiation densities were measured using an immersion density technique known to be accurate to ±0.2 % change in density. In some cases it was not possible to clearly identify and retrieve all four specimens, but in general there were at least two identical specimens measured in each capsule. Determination of microstructural evolution in these specimens using a transmission electron microscope has not yet been initiated.

Results

Figure 3 shows the measured changes in density observed in the irradiation series. Surprisingly, the results are quite different than expected. There is no obvious effect of dpa rate for either of the two alloys. There is some small range of data scatter among nominally identical specimens, but with only a few exceptions, the individual data points are relatively consistent with each other, especially considering that voids are not the only contribution to the density change.

There appears to be some densification occurring in both alloys which is visible at the lowest dpa levels. Such densification is expected as a consequence of α' formation, known to form in these alloys during irradiation (3). The swelling rate of the Fe-9Cr alloy appears to be ~0.05%/dpa, much less than the ~0.2%/dpa observed at steady state in the earlier FFTF/EBR-II comparative experiment (1). The swelling rate for the Fe-12Cr alloy appears to be slightly smaller, but may reflect the larger amount of α' phase formation and densification expected at the higher chromium level. The failure to attain a swelling rate of 0.2%/dpa is thought to indicate that steady-state swelling has not yet been attained in this experiment. Since the earlier FFTF experiment conducted at high dpa rates required almost 200 dpa before approaching 0.2%/dpa, this is not a surprising result.

Discussion

When this series of measurements was initiated it was expected that a clear effect of dpa rate on the duration of the transient regime would be seen, since the model Fe-Cr-Ni alloys in the same FFTF packets exhibited such a behavior. One would reasonably expect the Fe-Cr alloys to exhibit a flux-dependent behavior in the current FFTF experiment as was observed in the earlier FFTF/EBR-II comparative irradiation.

What might account for this lack of expected behavior? Was it reasonable to expect an experiment conducted only in FFTF would yield a result similar to that conducted in EBR-II and FFTF? What other differences in variables beside dpa rate might be operating to produce such a result?

The earlier experiment utilized specimens produced in the USA while the recent experiment utilized specimens prepared in Japan. Whereas the current Japanese experiment involved a heat treatment of 60 minutes at 900°C in high vacuum, the earlier experiment utilized 1040°C/I hr/air cool + 760°C/2 hr/air cool treatment for both the EBR-II and FFTF irradiations. Differences in impurity and gas content in the

Table 1. Irradiation conditions for Fe-Cr alloys irradiated in FFTF Cycles 11 and 12 (MOTA-2A and MOTA-2B). Note that in three of the seven cases the specimens irradiated in both cycles did not experience completely identical conditions with single cycle packages.

Dose Rate, dpa/sec		Dose, dpa		Temperature, ˚C	
#11	#12	#11	#11 & #12	#11	#11 & #12
1.7×10^{-6}	1.4×10^{-6}	43.8	67.8	427	408
7.7×10^{-7} *1	9.6×10^{-7}	20.0 *1	34.5	390	387
8.2×10^{-7} *2	8.4×10^{-7}	21.1 *2	28.8	430	424
3.2×10^{-7} *3	3.5×10^{-7}	8.22 *3	13.1	373	373
1.5×10^{-7}	1.3×10^{-7}	3.87	6.12	430	431
4.6×10^{-8}	4.2×10^{-8}	1.18	1.91	434	437
1.4×10^{-8}	1.4×10^{-8}	0.37	0.61	436	444

*1: 6.8×10^{-7} dpa/sec and 17.7 dpa in #11 for 2 cycle irradiation specimens
*2: 5.4×10^{-7} dpa/sec and 14.0 dpa in #11 for 2 cycle irradiation specimens
*3: 2.7×10^{-7} dpa/sec and 6.90 dpa in #11 for 2 cycle irradiation specimens

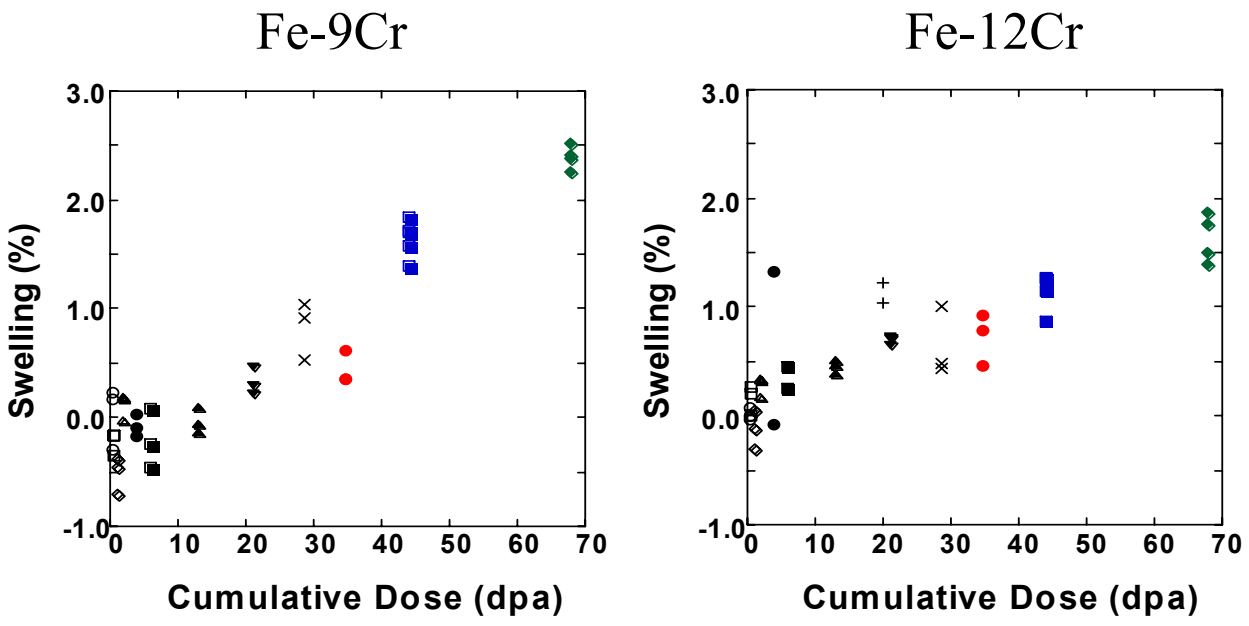

Figure 3. Swelling of simple model bcc Fe-Cr alloys in FFTF-MOTA at ~400°C, as observed in the current experiment, showing no apparent dependence of swelling on dpa rate. See Table 1 to identify dpa rates temperature, etc. for each data point.

U.S. and Japanese prepared alloys have not yet been defined. This possibility of preparation differences contributing to the different swelling response is now being explored in more depth.

The details of temperature history might have had a strong effect. The rise to power and the temperature history are somewhat different between EBR-II and FFTF. This possibility has been explored previously and shown to sometimes exert a strong impact on microstructural evolution (4).

However, the authors suspect that another subtler difference may be operating in the two sets of irradiation experiments. In the earlier work it was proposed that the flux and temperature sensitivity of swelling in Fe-Cr binaries reflected a greater difficulty of void nucleation in the bcc Fe-Cr system compared to that of the FCC Fe-Cr-Ni system (1, 5). It was further speculated that such a difficulty in void nucleation might reflect a potentially greater role for helium to stabilize voids, especially under fusion or spallation neutron conditions. In fact, the difference in transient duration observed in the original FFTF and EBR-II irradiations might reflect differences in helium generation rate in addition to any impact of differences in dpa rate.

In the current experiment, differences in dpa rates are accompanied by differences in helium generation rate with lower dpa rates accompanied by lower helium generation rates as shown in Figure 4. Might the potential effects of lower dpa rate to shorten the transient duration be cancelled by the associated lower helium generation rate?

In every case, however, the helium generation rates in Fe-Cr alloys in the current experiment are lower than those in EBR-II. All of the EBR-II data were generated at He/dpa ratios on the order of ~0.17 appm/dpa, while the FFTF irradiations proceeded at ~0.02 to 0.08 appm He/dpa.

It is proposed that model austenitic alloys irradiated in the same FFTF packets of the current experiment are able to exhibit their potential flux sensitivity much easier, since nucleation is not only easier in the fcc system, but the helium generation rates in FFTF are larger in Fe-15Cr-16Ni due to the larger contribution of nickel to helium generation.

If void nucleation in bcc Fe-Cr alloys is indeed dependent on helium availability, then one can not expect EBR-II results from the previous experiment to be comparable to FFTF results, even at the same dpa rate.

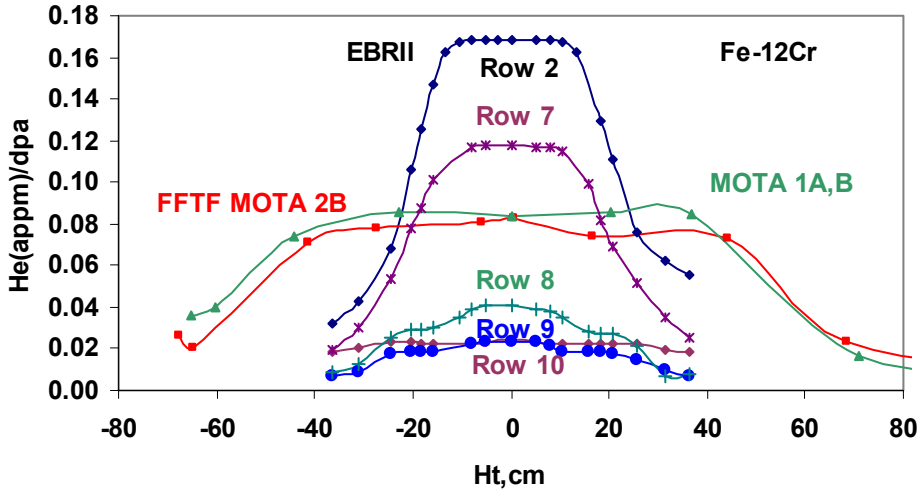

Figure 4. Calculated He/dpa ratios for Fe-12Cr irradiated in EBR-II and FFTF. The earlier EBR-II experiment was conducted in-core in Row 2 at ~0.18 appm He/dpa while the current FFTF experiment was conducted both in and out-of-core, with He/dpa ratios falling from 0.08 to 0.02 appm/dpa.

These results and conclusions require further study and some indication of the reasons for the observed behavior may be obtained after microstructural examination is completed.

Conclusions

An experiment conducted in FFTF-MOTA to determine the effect of dpa rate on void swelling of Fe-9Cr and Fe-12Cr model binary alloys appears to indicate that there is no effect of dpa rate on the evolution of swelling, which is contrary to the result observed in model Fe-Cr-Ni alloys irradiated in the same experiment. This result is also contrary to that of an earlier comparative irradiation experiment on nominally similar Fe-Cr alloys irradiated in EBR-II and FFTF.

While differences in alloy preparation or operational history may have contributed to this surprising result, the authors favor an interpretation based on the strong differences in helium generation rate in EBR-II and FFTF, especially in the out-of-core FFTF capsules, and the possible sensitivity of void nucleation to helium availability.

REFERENCES

[1] F. A. Garner, M. B. Toloczko and B. H. Sencer, “Comparison of Swelling and Irradiation Creep Behavior of fcc-Austenitic and bcc-Ferritic/Martensitic Alloys at High Neutron Exposure,” proceedings of Workshop on “Basic Differences in Irradiation Effects Between fcc, bcc and hcp Metals and Alloys,” Congas de Onis, Spain, 15-20 October., 1998, J. of Nuclear Mater., 276 (2000) 123-142.

[2] T. Okita, N. Sekimura, F. A. Garner, L. R. Greenwood, W. G. Wolfer and Y. Isobe, “Neutron-Induced Microstructural Evolution of Fe-15Cr-16Ni Alloys at ~ 400°C During Neutron Irradiation in the FFTF Fast Reactor,” 10th International Conference on Environmental Degradation of Materials in Nuclear Power Systems – Water Reactors, 2001, issued on CD format, no page numbers. Also in Fusion Materials Semiannual Progress Report for Period Ending June 30, 2001, vol. 30, pp. 148-164.

[3] D. S. Gelles, "Void Swelling in Binary Fe-Cr Alloys at 200 dpa," in J. of Nucl. Mater. 225 (1995) 163.

[4] F. A. Garner, N. Sekimura, M. L. Grossbeck, A. M. Ermi, J. W. Newkirk, H. Watanabe, M. Kiritani, "Influence of Details of Reactor History on Microstructural Development During Neutron Irradiation," J. of Nucl. Mater. 205 (1993) 206-218.

[5] B. H. Sencer and F.A. Garner,”Compositional and Temperature Dependence of Void Swelling in Model Fe-Cr Base Alloys Irradiated in EBR-II,” 283-287 (2000) 164-168.

ON THE EFFECTS OF PRECRACKING TECHNIQUE ON TRANSITION FRACTURE TOUGHNESS VALUES DERIVED FROM SMALL 3-POINT BEND SPECIMENS — M.A.Sokolov (Oak Ridge National Laboratory) and H.Tanigawa (Japan Atomic Energy Research Institute)

OBJECTIVE

The objective of this work is to verify the validity of a new precracking method of small 3 point bend specimens for fracture toughness measurement.

SUMMARY

Small 3-point bend specimens of F82H steel were precracked using the “plate-precracking” and traditional “specimen-precracking” techniques. The “plate-precracking” technique guarantees crack front that is straight and practically perpendicular to the sides for all specimens in the group. The results suggest that the plate-precracked specimens were in higher constraint during the fracture toughness test than in the "specimen-precracked" specimen. However, difference in T_0 value is within statistical scatter of fracture toughness. Additional testing on different materials is needed to validate the effects.

PROGRESS AND STATUS

Introduction

The fracture toughness specimens for irradiation studies within the fusion program are becoming smaller and smaller due to a variety of reasons. Validity of the fracture toughness values derived from these specimens is always a critical issue. Among different types of specimens, 3-point bend specimens are gaining popularity for the transition fracture toughness characterization of bcc alloys mostly because of the convenience of the their geometry for placement within small-volume irradiation capsules. For example, a 18-mm long, 3.3-mm wide, and 1.6-mm thick V-notched bar is currently the specimen of choice within the DOE-JAERI fusion program although it is not the smallest fracture toughness specimen within this program.

For these small specimens, the straightness and perpendicularity of the crack tip are two of the critical validity issues for experimental fracture toughness determination. In fact, the ASTM standard E1921for transition fracture toughness determination spells out the validity requirements for straightness and perpendicularity.

In practice, the specimen should be carefully monitored during fatigue precracking. Sometimes, precracking may start and grow only on one side without any crack initiation on the other side. In such cases, the fatigue cycling should be stopped to try to determine the cause and find a remedy for the asymmetric behavior. Sometimes, simply turning the specimen around in relation to the fixture will solve the problem for a relatively large specimen. However, for small-size specimens such as those described above for fusion irradiation experiments this may not apply. Because of the small size, fatigue precrack length may not exceed even 1 mm and, thus, there is not enough crack length to fix such a problem. Secondly, even if the fatigue crack is symmetrical on both sides, it is very likely that the crack front has characteristic curvatures near the side edges of the crack tip.

Prof. G.R. Odette from UCSB suggested a special precracking technique to ensure proper or, at least, not to decrease, constraint conditions ahead of the crack tip in these small specimens compared to larger specimens. The basic concept of this technique is that instead of precracking each specimen individually, a relatively large plate is fatigue precracked and then sliced and cut by order into individual small specimens. According to Odette, this plate-precracking technique provides a crack that is straight and perpendicular to the sides without any curvature at the sides. For example, a large piece of test material,

let's say 25-mm-thick, has a fatigue precrack that may have some curvature along its 25 mm length. However, slicing this piece into several 1.6 mm thick (or smaller depending on the specimen design) portions makes the crack front in each small portion practically straight and symmetrical.

Very often for large specimens, sharp side grooves provide a simple solution to this problem by removing these curvatures and providing additional stress concentration at the side edges to increase constraint. Typically, side groves are 20% of the thickness (10% from each side). But again for small, 1.6-mm thick and smaller specimens, it means that side grooves would be only a portion of a mm in depth. This makes side groves technologically challenging. Thus, the benefit from this technique is questionable for small fracture toughness specimens.

Overall, a concern is that with small specimens these problems with fatigue precracking would be magnified. From this point of view, the plate-precracking technique offers a unique solution for all these problems. The purpose of this exercise was to exam the advantages of this technique in comparison with the traditional precracking techniques using ferritic steel F82H.

Specimen preparation

It was decided to prepare three groups of specimens (18-mm long, 3.3-mm wide, and 1.6-mm thick V-notched bars). One group, named "plate-precracked", would contain specimens precracked by the technique proposed by UCSB. The second group, named "specimen-precracked", would contain specimens precracked individually by the traditional method. The third group named "side-grooved", would contain specimens individually precracked by the traditional method and then 20% side-grooved. The side grooves were made with a broach typically used for the standard Charpy V-notch specimens which has a 45^{o} angle and 0.25 mm radius. Thus, the root radius of the side grove was larger than the depth of it which diluted the idea of the side groove as the constraint increaser. Instead, such side grooving simply reduced the thickness of the specimens in the vicinity of the crack propagation.

Experimental

All fracture toughness tests were performed at one temperature, -165^{o}C. A total of 11 specimens was tested in the "specimen-precracked" group, 10 specimens in the "side-grooved" group, and 9 specimens in the "plate-precracked" group. All data were treated using the ASTM E1921 master curve methodology.

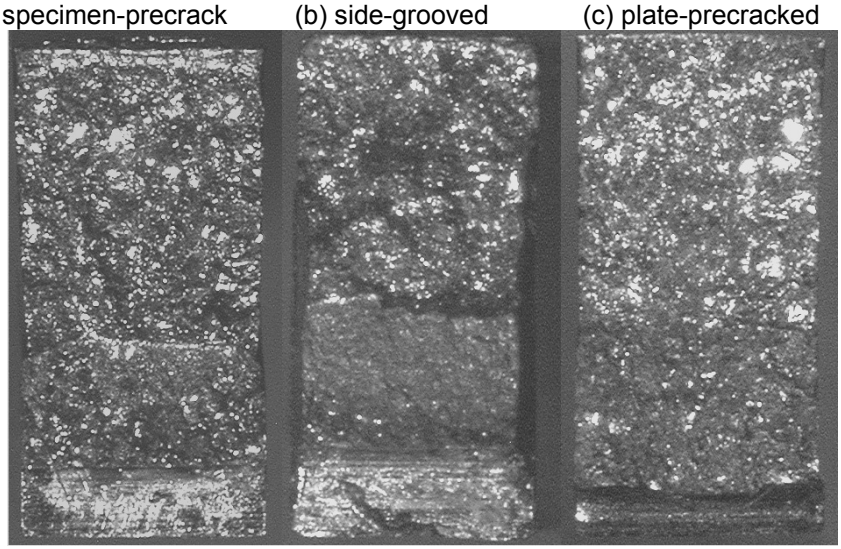

Fig. 1. Optical micrographs of fracture surfaces of a typical specimen from each group tested. Crack propagated from the bottom to the top.

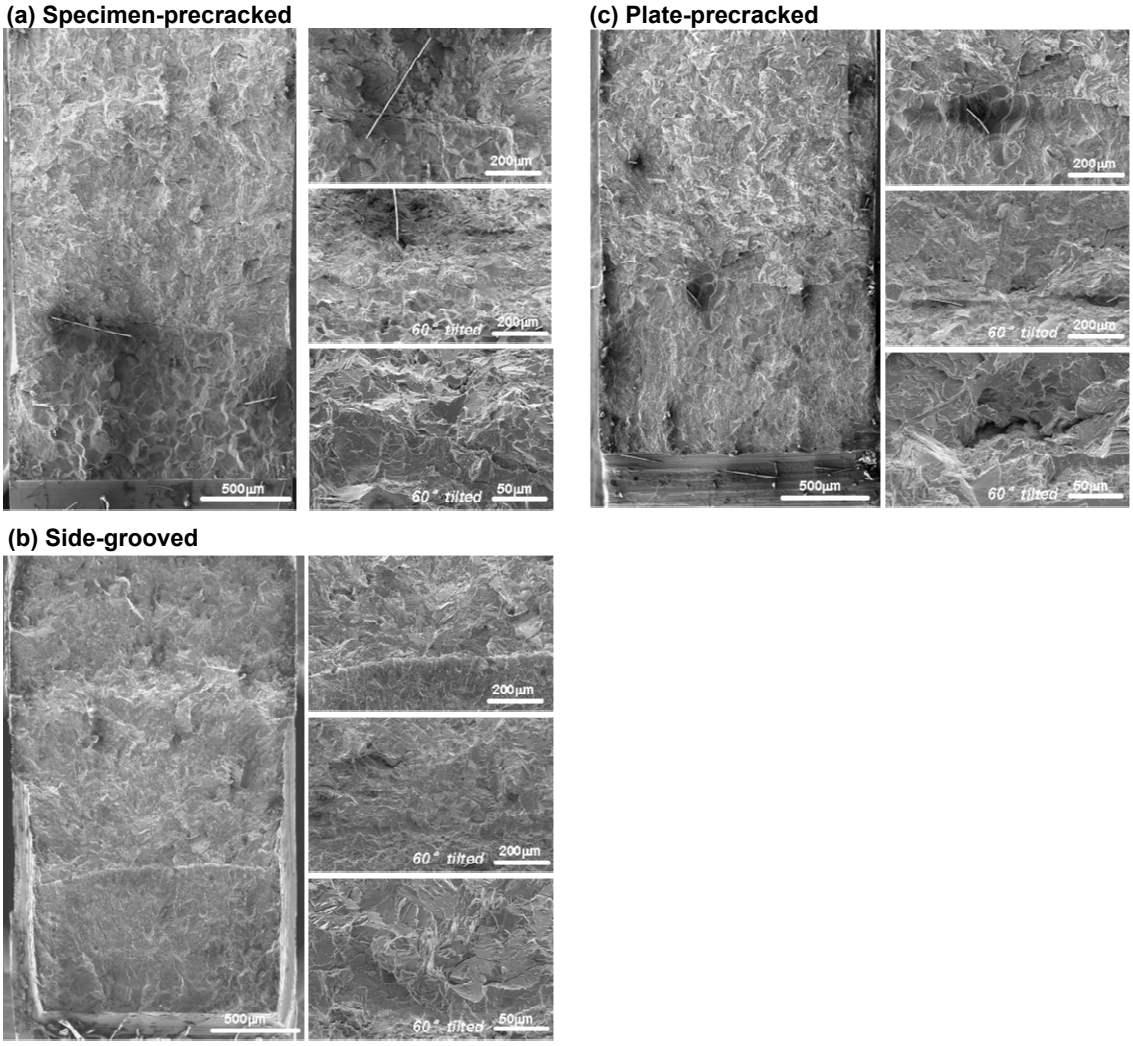

Fig. 2 SEM micrographs of fractured specimen from each group. Right side pictures of each group are the magnified images of fractre initiation points.

Thus comparison can be made in terms of fracture toughness reference temperature, T_o, or $K_{Jc(med)}$.

Results and discussion

Optical micrographs and SEM micrographs of the fracture surface of a typical specimen in each group are shown Fig. 1 and Fig. 2. Tables 1-3 are the tables that contain experimental results, average crack length(a_o) measurements, and results of the master curve analysis for each group examined. Elastic modulus and yield stress used in the calculations are 226GPa and 612.12MPa, respectively.

The master curve analysis shows that the “plate-precracked” group has the highest T_o value (the lowest $K_{Jc(med)}$) followed by the “specimen-precracked” group while the “side-grooved” group has the lowest T_o value (the highest $K_{Jc(med)}$). As discussed above, the highest $K_{Jc(med)}$ value from the “side-grooved” group could be the result of a relatively large root radius used in these side-grooves. In this case, side-grooves could thin the operational region of the specimen instead of providing additional constraint. Thus, the

Table 1. Summary of fracture toughness tests of "plate-precracked" group performed at –165ºC.

I.D.	J_c, kJ/m^2	K_{Jc}, MPa√m	K_{Jc} -1T, MPa√m	$K_{Jc(limit)}$, MPa√m	δ_i	$K_{Jc(med)}$, MPa√m	T_o, ºC	a_o, mm	W, mm	a/W
1S	32.81	90.39968436	55.6538469	98.60053648	1	50.4	-99.8	1.412	3.325	0.424662
3S	39.97	99.77709906	60.40302882	98.08375862	0			1.429	3.322	0.430163
6S	31.31	88.30907438	54.59505965	91.82162745	1			1.658	3.317	0.499849
7S	25.92	80.34915198	50.56376523	100.6916002	1			1.32	3.315	0.39819
8S	25.4	79.53909719	50.15351383	95.72373951	1			1.524	3.327	0.45807
9S	27.15	82.2334888	51.51808566	96.88470933	1			1.468	3.315	0.442836
10S	9.49	48.61797938	34.49354588	99.37066432	1			1.359	3.302	0.411569
11S	33.1	90.79831639	55.85573368	99.52397477	1			1.371	3.32	0.412952
12S	7.43	43.01879149	31.657843	101.144828	1			1.307	3.32	0.393675
									AVER=	0.430218
									STDEV=	0.033207

Table 2. Summary of fracture toughness tests of "specimen-precracked" group performed at –165ºC.

I.D.	J_c, kJ/m^2	K_{Jc}, MPa√m	K_{Jc} -1T, MPa√m	$K_{Jc(limit)}$, MPa√m	δ_i	$K_{Jc(med)}$, MPa√m	T_o, ºC	a_o, mm	W, mm	a/W
H1	45.21	106.1160443	63.61338105	102.194543	0	54.6	-109.9	1.275	3.317	0.384383
H2	18.19	67.31008646	43.96014407	101.0694312	1			1.32	3.317	0.39795
H3	18.78	68.39299035	44.50857962	99.72802209	1			1.373	3.315	0.414178
H4	22.47	74.81097848	47.75896303	104.8455622	1			1.167	3.317	0.351824
H5	40.91	100.9435418	60.99377252	100.4136206	0			1.346	3.32	0.405422
H6	50.32	111.9525822	66.56928959	101.1950614	0			1.315	3.317	0.396443
H7	26.56	81.33506802	51.06308139	100.5147931	1			1.342	3.32	0.404217
H8	26.22	80.81279779	50.79857817	103.4548788	1			1.224	3.317	0.369008
H9	20.71	71.821397	46.2448926	102.0452449	1			1.281	3.32	0.385843
A11	16.95	64.97535338	42.77772093	98.65206538	1			1.417	3.332	0.42527
H10	71.67	133.6080117	77.53665934	96.35872982	0			1.503	3.317	0.45312
									AVER=	0.398878
									STDEV=	0.027271

Table 3. Summary of fracture toughness tests of "side-grooved" group performed at –165ºC.

I.D.	J_c, kJ/m^2	K_{Jc}, MPa√m	K_{Jc} -1T, MPa√m	$K_{Jc(limit)}$, MPa√m	δ_i	$K_{Jc(med)}$, MPa√m	T_o, ºC	a_o, mm	W, mm	a/W
A1	79.45	140.6730001	81.11471535	93.57599025	0	59.7	-119.9	1.609	3.332	0.482893
A2	43.79	104.4362505	62.76265125	101.9206627	0			1.291	3.335	0.387106
A3	34.15	92.22722743	56.57940419	100.8680975	1			1.33	3.332	0.39916
A4	29.31	85.44205951	53.14306295	95.82986342	1			1.528	3.335	0.458171
A5	64.83	127.0725689	74.22679112	95.6440693	0			1.532	3.332	0.459784
A6	26.09	80.61221201	50.69699171	99.6005415	1			1.38	3.332	0.414166
A7	46.35	107.4456081	64.28673724	96.91093337	0			1.482	3.33	0.445045
A8	35.46	93.97950744	57.46684458	97.32955706	1			1.468	3.332	0.440576
A9	93.61	152.695037	87.20326343	95.80334347	0			1.529	3.335	0.458471
A12	25.03	78.95765175	49.85904139	94.68279798	1			1.568	3.332	0.470588
									AVER=	0.441596
									STDEV=	0.031573

effective thickness of this specimen would be less than the nominal and that could lower the size-adjustment value of $K_{Jc(med)}$. From this point of view, the comparison of the “plate-precracked” and “specimen-precracked” groups is straightforward, since both groups have specimens of the same thickness. It is a well known fact that less constrained specimens exhibit higher toughness. The fact that the specimens precracked by the traditional technique exhibited higher $K_{Jc(med)}$ value than the “plate-precracked” group indicates that the “specimen-precracked” specimens might have less constraint than the “plate-precracked” specimen. The difference in the $K_{Jc(med)}$ values of two groups is about 10%. However, it is not clear at this point whether the entire difference can be attributed to the advantages of the precracking technique or it is also part of a scatter in properties.

Summary

Small 3-point bend specimens of F82H steel were precracked using the “plate-precracking” and “specimen-precracking” techniques. It was observed that the “plate-precracking” technique simplifies the precracking process and complicates the machining process in comparison with the traditional precracking technique. In return, however, the “plate-precracking” technique almost guarantees a fatigue crack front that is straight and practically perpendicular to the sides for all specimens in the group. This may result in higher constraint during the fracture toughness test than in the "specimen-precracked" specimen. The present results support this postulate. The “plate-precracked” group of specimens exhibited a lower $K_{Jc(med)}$ value than the traditional group. The difference in the $K_{Jc(med)}$ values of the two groups is about 10%. Additional testing on different materials is needed to validate the effects.

4.0 COPPER ALLOYS

STATUS OF COLLABORATIVE RESEARCH PROGRAM BETWEEN PNNL AND RISØ NATIONAL LABORATORY - D. J. Edwards (Pacific Northwest National Laboratory)* and B. N. Singh (Risø National Laboratory, Denmark)

OBJECTIVE

The primary objective of this collaboration is to conduct fundamental studies of radiation effects on pure metals and alloys of interest to the fusion materials community. Pure copper and its alloys (all FCC metals) are the primary focus of this collaboration, but other metals and alloys such as pure Fe, Mo and ferritic steels (BCC materials) and Ti (HCP materials) are included for comparison.

SUMMARY

PNNL and Risø have been collaborating since 1994 on a series of irradiation experiments on pure copper and various alloys of interest to the fusion materials community. The collaboration has been of great benefit to both institutes by sharing resources and experience. Past research has concentrated on examining the microstructural evolution during neutron irradiation and the influence this microstructural change exerts on the deformation response. Post-irradiation annealing experiments of both irradiated pure copper and CuCrZr yielded unique insights into the relationship between the microstructure and the deformation response. The results of that experiment also raised further questions regarding the stability and structure of the small defects produced during irradiation, particularly regarding the stability of these defects during annealing and how they interact with mobile dislocations. The focus of ongoing work has now shifted to examining the issues of defect stability in irradiated materials, dislocation generation from stress concentrations at interfaces in irradiated materials, and a new experiment on in-situ straining during irradiation and how this affects microstructural evolution and the relationship to mechanical properties.

PROGRESS AND STATUS

Introduction

PNNL and Risø have been collaborating since 1994 on a series of irradiation experiments on pure copper, molybdenum, iron and other metals and alloys of interest to the fusion materials community. The collaboration has been of great benefit to both institutes by sharing resources and experience. Past research has concentrated on examining the microstructural evolution during neutron irradiation and the influence these microstructural changes exert on the deformation response. The irradiated materials have been investigated using a wide variety of techniques including transmission and scanning electron microscopy (TEM and SEM, respectively), tensile testing, electrical resistivity measurements and positron annihilation spectroscopy. The irradiation experiments have been both fundamental in nature as well as more engineering oriented, the latter in particular for those experiments involving materials being considered for use in ITER (International Thermonuclear Experimental Reactor).

One experiment in particular that yielded unique insights involved the post-irradiation annealing of pure copper irradiated at 100°C. The original intent of this experiment was to explore the possibility that in-reactor bakeouts (performed to restore the vessel vacuum in ITER) could remove or at least mitigate the radiation hardening that occurs in copper and its alloys during reactor operation. This radiation hardening involves substantial increases in yield strength and severe loss of uniform elongation and work hardening ability that manifests itself as a yield point phenomenon and early onset of plastic instability. In the more extreme cases the tensile curves for irradiated copper and some of its alloys can exhibit plastic instability

* Pacific Northwest National Laboratory (PNNL) is operated for the U.S. Department of Energy by Battelle Memorial Institute under contract DE-AC06-76RLO-1830.

upon yielding and immediately begin necking in tension. The annealing conditions of 300°C for 50 hrs were chosen to reflect this bakeout procedure. The results of the PI annealing experiment proved that the vacancy-type defects in the irradiated copper (stacking fault tetrahedra in this case) were more stable than expected, especially at doses of 0.1 dpa and above where the defect density had essentially saturated. Annealing produced observable changes in the microstructure including a new distribution of interstitial loops. However, more significant was the fact that the SFT distribution coarsened only slightly after annealing, that is, the density decreased slightly and the average size of the SFT increased, proving that the SFT microstructure was quite resistant to annealing. After annealing the tensile properties reflected these microstructural changes by losing the yield point phenomenon that occurred at doses of 0.1 dpa and higher and restoring some work hardening ability. However, the overall ductility of the PI annealed materials did not significantly improve after annealing if the specimens were irradiated to doses of ≥ 0.1 dpa. In the as-irradiated condition, the appearance of a yield point phenomenon is thought to be a consequence of suppression of homogenous production and propagation of dislocations by the pinning of pre-existing dislocations of small dislocation loops, clusters of defects and impurities formed during irradiation. The restoration of work hardening and removal of the yield point phenomenon is therefore related to the post-irradiation annealing lowering the degree of dislocation pinning, allowing more homogenous plastic flow. While the annealing lowered the yield stress and allowed some degree of homogenous deformation to promote work hardening, dislocation channeling still occurred in the post-irradiation annealed samples. The presence of even a small amount of dislocation channeling appeared to be more than enough to prevent the full recovery of ductility back to the unirradiated levels. The experiment demonstrated the bakeout condition to be of limited use for restoring the mechanical properties to unirradiated levels, particularly since subsequent exposure of the PI annealed material would involve a starting microstructure composed of pre-existing loops and SFTs not present in the unirradiated condition. For further details on this experiment the reader is referred to reference 1.

This experiment in turn produced new directions of research that have led to continued experimental collaborations between PNNL and Risø. One key issue is to examine the deformation microstructures after tensile testing and attempt to discover more about the dislocation channeling phenomenon such as where the channels originate, how they get started, what leads to the continued production of new channels with increasing strain and why existing channels appear to get shut down as new channels are formed. Deformation studies have been started in both pure copper and CuCrZr irradiated below 100°C to further investigate dislocation channeling. The stability of the SFT raised new questions and reopened issues related to how they interact with mobile dislocations, an issue of particular importance for modeling the generation and movement of dislocations to produce cleared channels. Finally, the past experiments led to a new experiment aimed at investigating the microstructure of irradiated metals that were strained in-situ and how this influenced the mechanical properties compared to materials that were only tested after being removed from the reactor.

A brief description of current experiments is provided in the following sections. The results of these experiments are to be presented either at the next ICFRM-11 in Japan or published separately in the Journal of Nuclear Materials.

Status of Present Experiments

Recently, a number of TEM samples were examined with the objective of characterizing the microstructures in pure copper and CuCrZr neutron irradiated at 60°C to 0.3 dpa. The CuCrZr alloy had been processed before irradiation to yield a much different size distribution of precipitates than produced during the conventional prime ageing heat treatment. In addition, the deformation microstructures were characterized for most of the irradiated conditions to better understand the formation and interaction of dislocation channeling, a phenomenon that severely limits the deformation to discrete volumes and substantially reduces the uniform elongation.

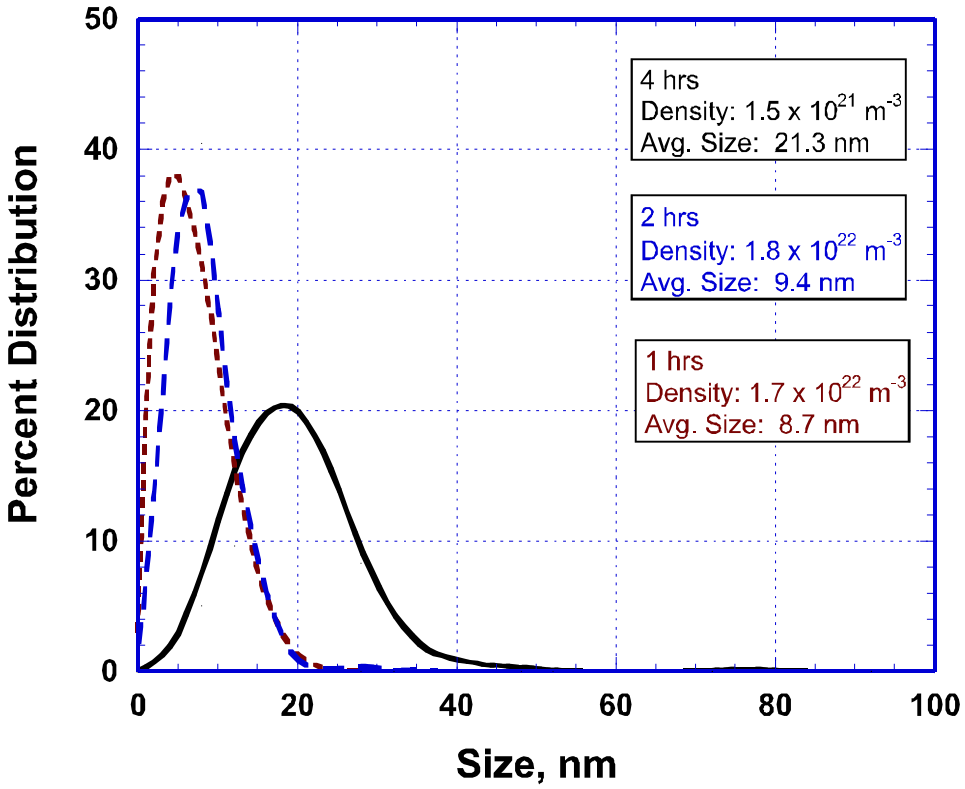

Figure 1. Size distributions were measured of the precipitates produced during the overageing treatment at 600°C. The samples aged for 2 and 4 hours were included in the irradiation experiment.

The irradiation experiment on the CuCrZr concluded a set of experiments started in 2001 that involved overageing the CuCrZr to produce a much coarser precipitate distribution than observed in prime aged CuCrZr, the normal condition when using this material. In 2001 a series of heat treatments were explored to choose two overageing conditions that would yield a reasonable density of precipitates of larger diameter that might alter the response of the alloy during subsequent post-irradiation testing. The hope was that a precipitate distribution could be produced that yielded average sizes on the order of 4-10 nm in diameter with a density around 10^{22} m^{-3}, a density similar to that of the oxide particles present in the oxide dispersion strengthened GlidCop alloy. Note that the prime aged condition for CuCrZr (this involves solution annealing, water quenching, then ageing at ~475°C for 3-4 hours) generally yields a precipitate distribution of 3-5 nm diameter precipitates in a density of ~10^{23} m^{-3}. Ultimately the goal was to see if it was possible to mitigate or remove the extreme effects of radiation hardening and restore some semblance of uniform elongation and work hardening to the CuCrZr alloy by manipulation of the starting microstructure before irradiation. The larger precipitates may be more stable and resistant to irradiation, therefore serving as effective obstacles to dislocation motion and prevent or minimize dislocation channeling. The exploratory research, which has been reported in prior Fusion Material Semi-Annual Reports [2,3], found that an additional thermal exposure of 600°C for 2 hrs and 4 hrs to samples initially given the prime aged heat treatment produced a precipitate distribution in the desired range indicated above. The size distributions are shown in Figure 1. These two conditions, along with samples of CuCrZr given only the prime aged heat treatment and samples of pure copper provided for a baseline comparison, were placed in neutron irradiation experiment at 60°C to a total dose of 0.3 dpa.

These samples were removed from reactor in 2002 and were tested and examined recently at Risø. The tensile results demonstrated that the alteration of the precipitate distribution before irradiation did indeed influence the tensile behavior and achieved some increase in work hardening, although the upper/lower

yield point phenomenon was not removed. The microstructural characterization was performed on both the as-irradiated and the as-irradiated and deformed samples, however, the analysis of the results is still in progress and will be reported in detail at a later date. The initial impression, based on a strictly qualitative inspection of the images and the tensile response, is that the different precipitate distributions obviously influenced the deformation behavior, but the microstructural relationship is not so obvious and requires careful analysis.

In an experiment involving interrupted tensile tests on pure copper irradiated at ~50°C to 0.3 dpa, a new feature has been observed in deformed samples that offers potential insight into the deformation behavior of irradiated copper. The samples were tested at Risø and sent to PNNL for characterization in the SEM and TEM. In samples where the tensile test was stopped just before yield (~80% of the yield strength or ~270 MPa), distinct defect-free zones (DFZs) were observed in the TEM at many of the grain boundaries in the deformed pure copper. Four different examples of these DFZs are provided in Figure 2. By examining TEM samples taken from the grip area of the tested samples, the defect-free zones were confirmed to be a consequence of the applied stress during post-irradiation tensile testing. The lack of DFZs at the grain boundaries implies that the DFZs in the strained samples were due to grain boundary

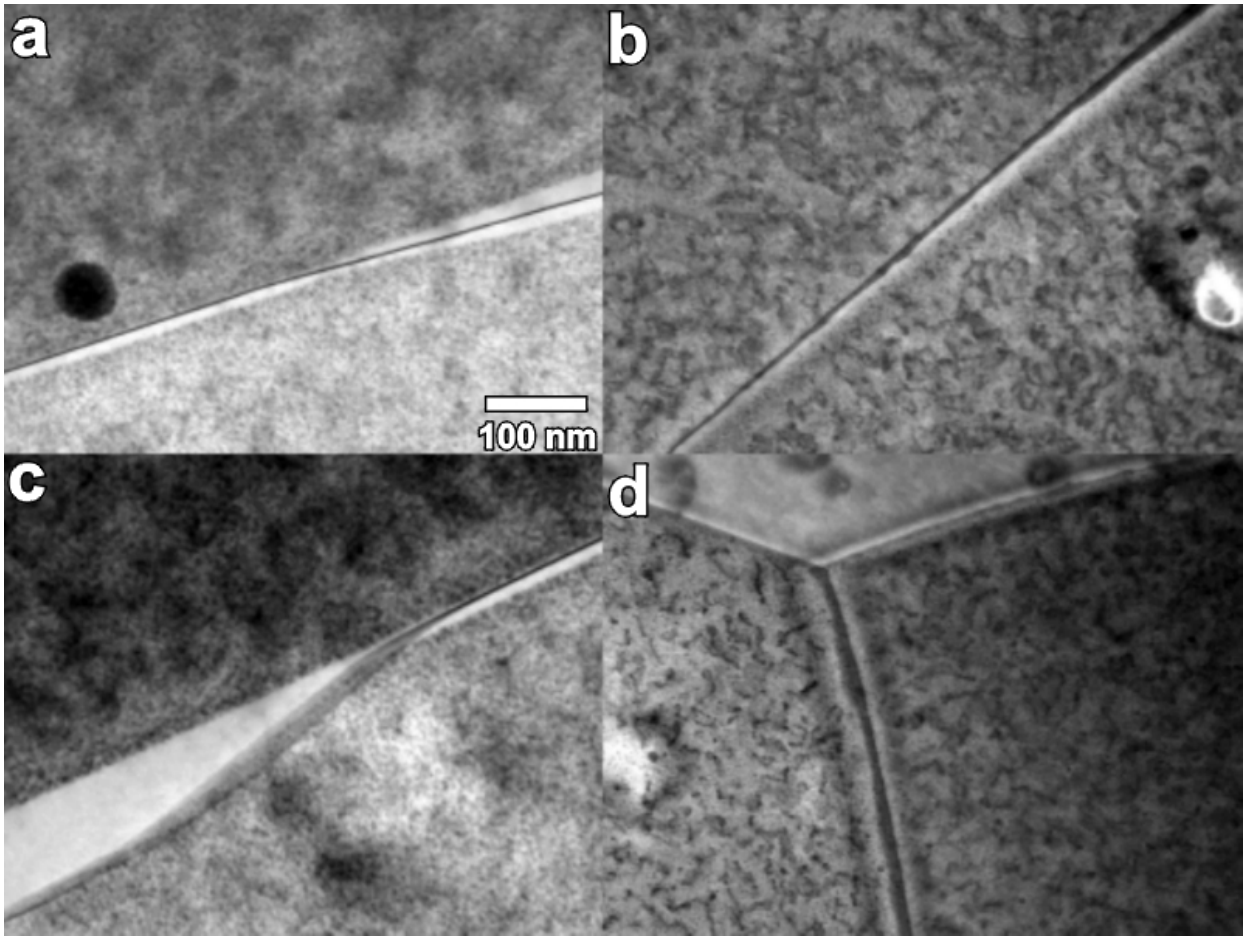

Figure 2. Examples are shown of defect-free zones observed along grain boundaries in irradiated OFHC copper. The sample was irradiated and tested at 50°C, but the test was stopped just before the macroscopic yield point. These defect-free zones were not observed in the untested samples. Note that the DFZ can undulate across the grain boundaries, varying in width at different positions.

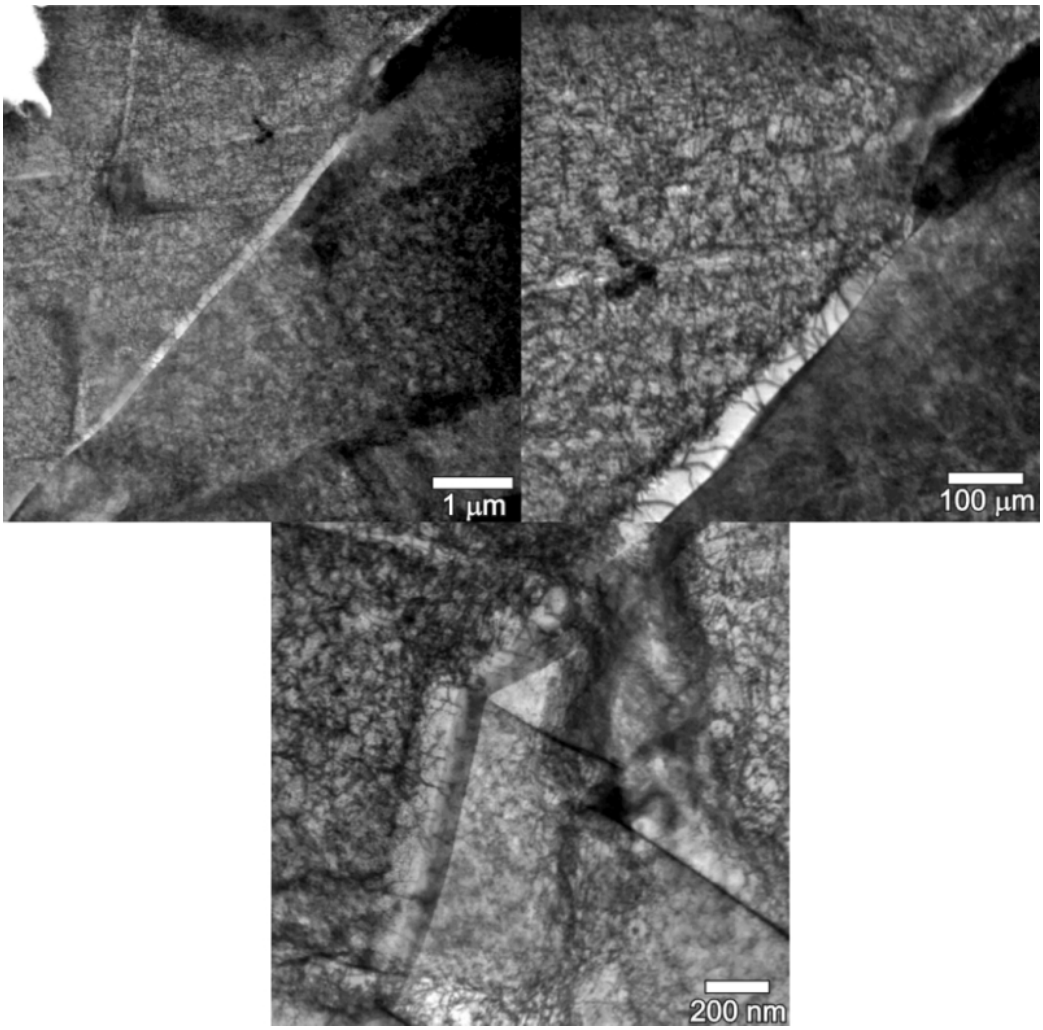

Figure 3. Three examples are shown for the DFZ as they appeared in sample where the tensile test was stopped at the ultimate tensile strength. Dislocation channeling was more prevalent at this level of strain, and the DFZ often contained dislocations produced by deformation. No wide scale homogenous deformation is present in the grain interiors, but the dislocations are present that are thought to have formed during deformation and percolated through the SFTs present in the matrix without removing a substantial fraction of these defects.

sliding and/or migration under the applied load. Note that the yield stress in the as-irradiated samples was near 300 MPa, so the applied loads at which the DFZs were first observed was quite high for pure copper. At this stage of the tensile test, dislocation channeling, the dominant deformation mechanism observed at higher strains, was very rare, often limited to 1-2 channels per grain in the area examined with no deformation-induced dislocation motion evident in grain interiors. Figure 3 shows DFZs in a sample irradiated and tested under the same conditions, but in this case the tensile test was stopped just before the ultimate tensile strength. Dislocation channeling was far more prevalent in this condition and the DFZs often contained line dislocations possibly produced from a source near or within the grain boundary. Note that even though the matrix contained a significant density of dislocations resulting from the irradiation, no homogenous annihilation of the defects could be identified, indicating that most of the strain was accommodated within the dislocation channels and the dislocations were only able to “percolate” through the SFTs.

The DFZs were found to be present in both the pure copper and the CuCrZr samples mentioned earlier that were irradiated at 60°C. However, because the samples examined had been taken to failure and were not interrupted tests, the DFZs were difficult to see because the impingement of the dislocation channels distorted the grain boundary areas and produced large plastic strains in the softer DFZ regions. In a few isolated cases, grain boundaries were found that had not been heavily deformed by channel intersection and the DFZs were more obvious. These results offer further confirmation of the DFZs being a generic feature in irradiated and tested copper, and illustrate that it would be easy to overlook these DFZs in samples taken to failure. The impact of these DFZs requires further evaluation, but the immediate implication is that deformation occurred at the grain boundaries at macroscopic stresses lower than that needed to initiate significant dislocation channeling. The relationship between the dislocation channeling and the DFZs is unknown at this time as many of the grain boundaries had clear DFZs around them, but only rarely were channels found in the grains and these often came from boundaries with no DFZs.

Another experiment recently completed extended the previously described post-irradiation annealing experiment to TEM samples of pure copper that were neutron-irradiated at 200 and 250°C. Post-irradiation annealing was then conducted on separate specimens at 300, 350, 400 and 450°C for 2 hours for each irradiation temperature. These two irradiation temperatures bracket a transition in microstructural evolution where void swelling and small defects form during irradiation at 250°C, but only small defects (stacking fault tetrahedra and small loops) form at 200°C. The objective of this experiment was to investigate the stability of the stacking fault tetrahedra (SFT) in the absence or presence of voids, another sink/source of vacancies during the annealing. The importance of this type of research is two-fold since it first helps to understand why in-situ annealing treatments may be ineffective as a means for mitigating radiation hardening, especially in those situations where the component will be irradiated in the next cycle. Secondly, understanding the stability of the SFT may provide insights into their structure and how they can be destroyed by the passage of dislocations during deformation. In the post-irradiation annealing experiment conducted on samples irradiated at 100°C, it was noticed that the SFT appeared to become more “perfect” after annealing, i.e. more triangular in appearance, suggesting that the SFT produced from displacement cascades were not as “structurally perfect” as often assumed. This is an issue that requires further verification since a high fraction of non-perfect SFT could alter the overall deformation response if they are more easily destroyed by mobile dislocations. Recent modeling by Wirth et al. [4] suggested that mobile dislocations could more easily interact with a truncated SFT and eventually destroy it, which is important when trying to model the formation of cleared channels in irradiated copper. The experimental characterization of the different annealing conditions listed above is finished, with the analysis of the data expected to be completed over the coming months. Initial results from the samples irradiated at 200°C to 0.3 dpa are presented in Figure 4 showing images of the SFT microstructure in the as-irradiated condition and after post-irradiation annealing at 350 and 450°C. The size distributions for the as-irradiated condition and the four different annealed conditions listed above are shown in Figure 5. The size distributions and images show that the size distribution increases with annealing temperature, but even at 450°C the SFT are still present in a significant density.

Another issue that is being investigated in this collaboration concerns the clearing of defects within the dislocation channels in both pure copper and CuCrZr. In the case of pure copper, many of the channels have been found to be essentially free of the stacking fault tetrahedra observed at a very high density in the regions adjacent to the channels. Some debris remains inside the channels left over from the passage and interaction of many dislocations. In contrast, the channels found in the deformed CuCrZr exhibited a somewhat higher residual population of dislocation segments and dipoles as well as the original defects and precipitates, but overall the channels are still relatively clear of the defects produced during irradiation. Since it is not known how many dislocations have moved through a given channel, it is not possible using the current data to make quantitative comparisons between individual channels within a given sample, let alone different samples or samples from different materials.

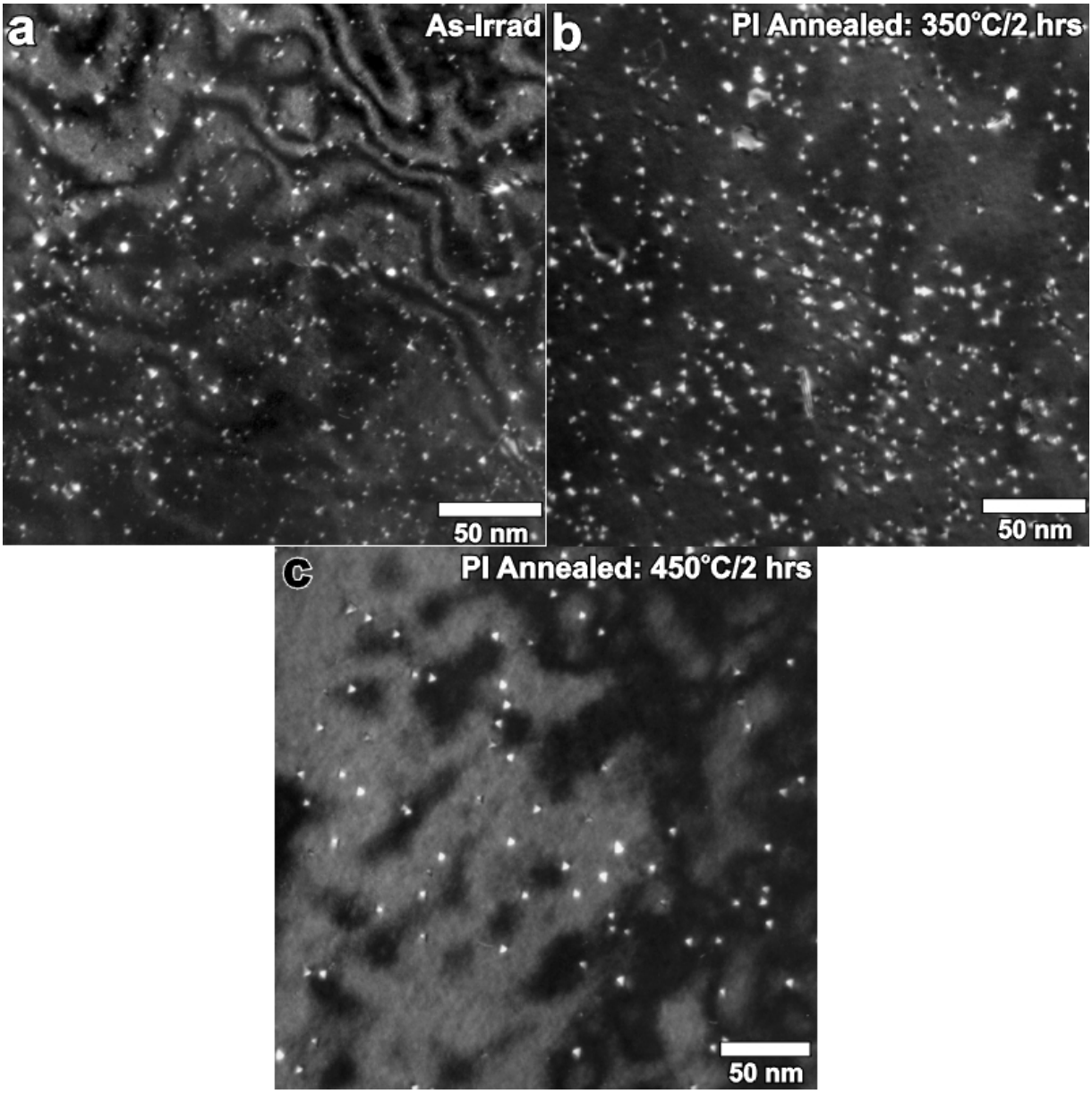

Figure 4. Examples of the SFT microstructure after post-irradiation annealing are shown above. The density decreased as the annealing temperature increased, and the size distributions shown in Figure 5 indicate a significant shift in the size distributions.

As further work is conducted to investigate the phenomenon of dislocation channeling, there is a growing recognition concerning the difficulty of trying to quantify the spacing, size and extent of dislocation channeling using TEM. Very few observations have ever captured the point at which a channel has been initiated, and the strain gradients that occur from grain to grain in a tested polycrystalline sample mean that the limited data obtained from one grain cannot necessarily be applied globally to the entire sample. A final point to consider is that the grain size in many pure metals and single phase alloys examined in these irradiation experiments ranges from several microns up to ~30 mm. A typical TEM foil is generally only 100-200 nm thick, so the very thin volume of material characterized in the TEM limits the chances of finding the point at which a channel is initiated and how it propagates into the grain interior. A greater

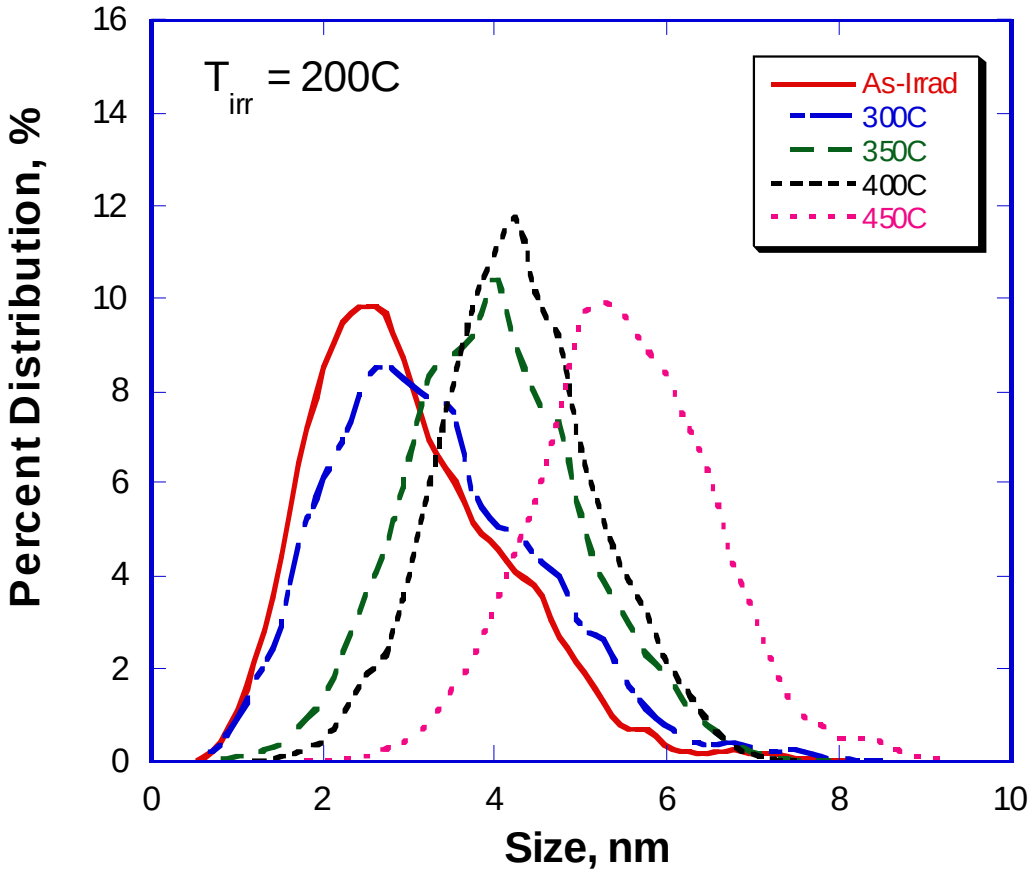

Figure 5. Size distributions from pure copper, irradiated at 200°C and annealed for 2 hours at the temperatures indicated on the plot.

effort is therefore needed to utilize bulk methods in conjunction with TEM and other techniques to explore this more fully, possibly including in-situ straining in the TEM to try and capture channel initiation events.

FUTURE WORK

The collaboration between PNNL and Risø will continue to examine some of the issues described above. A new set of experiments has been initiated involving the in-situ straining of pure copper, and the samples from that experiment will be available mid-2003. Subsequent irradiations will irradiate CuCrZr under the same conditions, then later experiments are slated to irradiate Fe and a ferritic steel. The main goal of these experiments is to compare the differences in microstructure and mechanical behavior that result from applying tensile strain from the start of irradiation cycle and comparing it side by side to samples that were not loaded until near the end of the irradiation cycle. Additional work will delve further into the issue of where channels are initiated in polycrystalline materials, in particular investigating the role of interfaces such as grain boundaries and twin boundaries.

REFERENCES

[1] B. N. Singh, D. J. Edwards and P. Toft, Journal of Nuclear Materials, 299, 205-218 (2001).

[2] D. J. Edwards and B.N. Singh, “Overaging of Outokumpu CuCrZr,” DOE/ER-0313/28, Fusion Semi-Annual Progress Report, for the period ending June 30, 2001, 176-182.

[3] D. J. Edwards and B.N. Singh, “Overaging of Outokumpu CuCrZr at 600°C,” DOE/ER-0313/31, Fusion Semi-Annual Progress Report, for the period ending December 31, 2001, 118-122.

[4] B. D. Wirth, V. V. Bulatov and T. Diaz de la Rubia, “Dislocation-Stacking Fault Tetrahedron Interactions in Cu,” Journal of Engineering Materials and Technology, 124, 329-334 (2002).

5.0 REFRACTORY METALS AND ALLOYS

No contributions.

6.0 AUSTENITIC STAINLESS STEELS

INFLUENCE OF CARBON AND DPA RATE ON NEUTRON-INDUCED SWELLING OF Fe-15Cr-16Ni-0.25Ti IN FFTF at ~400°C - T. Okita and N. Sekimura (University of Tokyo), F. A. Garner (Pacific Northwest National Laboratory)* and W. G. Wolfer (Lawrence Livermore National Laboratory)

OBJECTIVE

The purpose of this effort is to determine the influence of dpa rate and composition on the void swelling of simple austenitic Fe-Cr-Ni alloys.

SUMMARY

Contrary to the swelling behavior of fcc Fe-15Cr-16Ni and Fe-15Cr-16Ni-0.25Ti alloys irradiated in the same FFTF-MOTA experiment, Fe-15Cr-16Ni-0.25Ti-0.04C does not exhibit a dependence of swelling on dpa rate at ~400°C. The transient regime of swelling is prolonged by carbon addition, however.

Introduction

In an earlier report it was shown that two simple, annealed austenitic alloys, Fe-15Cr-16Ni and Fe-15Cr-16Ni-0.25Ti, when irradiated in FFTF-MOTA at ~400°C over a wide range of dpa rates, exhibited a very strong influence of dpa rate on void swelling (1). While the steady state swelling rate of ~1%/dpa was unaffected by dpa rate, the transient regime was strongly affected, with a progressive shortening of the transient duration as the dpa rate decreased, as shown in Figure 1. This counterintuitive dependence was shown to be mirrored in other previously published experiments conducted on more complex commercial alloys. (2-4).

Also contained in the FFTF-MOTA experiment was Fe-15Cr-16Ni-0.25Ti-0.04C, also in the annealed condition. This allows the possibility to study the possibly synergistic effects of two important variables, dpa rate and carbon.

Experimental Details

Relatively pure Fe-15Cr-16Ni, Fe-15Cr-16Ni-0.25Ti and Fe-15Cr-16Ni-0.25Ti-0.04C (at %) with no added solute were prepared by arc melting from high purity Fe, Ni, Cr and Ti. The binary alloys was rolled to sheets of 0.25 mm thickness, cut into 3 mm disks and annealed for 30 minutes at 1050°C in high vacuum.

Two sets of identical specimens are placed in sealed, helium-filled packets at each of seven different capsule positions of the Materials Open Test Assembly (MOTA), ranging from below the core to above the core of the Fast Flux Test Facility (FFTF). The packets in general contained four identical specimens of each of the two alloys. The three alloys were located side-by-side in the same packet. Two or more identically-loaded packets were placed in each capsule, with the dpa rate dependent on the axial location in MOTA.

With the exception of the below-core canister, the temperatures in MOTA capsules are actively controlled to ±5°C of the nominal target, although the nominal target temperatures varied a little from capsule to capsule.

The first irradiation sequence occurred in Cycle 11 of MOTA-2A for 2.58×10^7 sec, and a subset of specimen packets was then removed. Other identical specimen packets continued in Cycle 12 of MOTA-2B for 1.71×10^7 sec. The dose rates in the various capsules ranged from 8.9×10^{-9} to 1.7×10^{-6} dpa/sec. The dose levels attained by the specimens varied from 0.23 to 43.8 dpa in Cycle 11 and an additional

* Pacific Northwest National Laboratory (PNNL) is operated for the U.S. Department of Energy by Battelle Memorial Institute under contract DE-AC06-76RLO-1830.

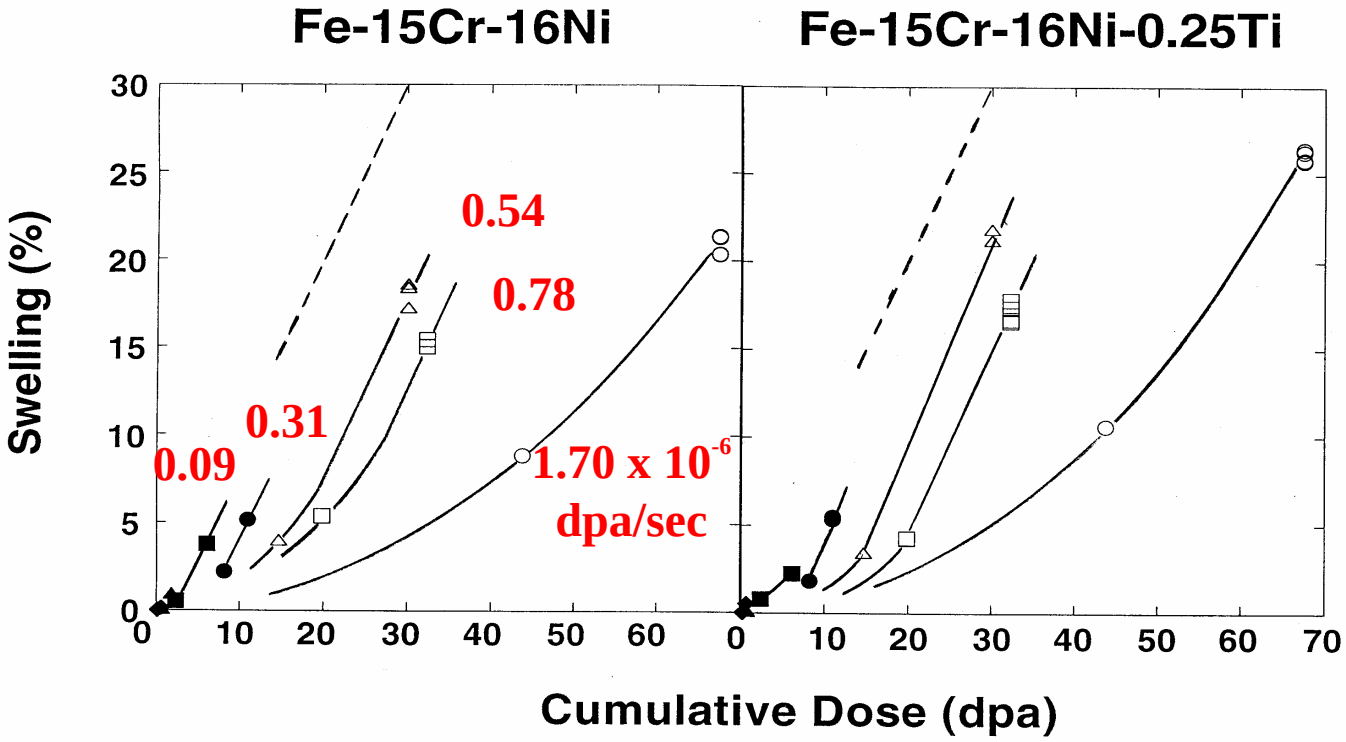

Figure 1. Swelling of simple model f.c.c. Fe-Cr-Ni alloys in FFTF-MOTA at ~400°C, as observed by Okita and coworkers (1), showing that the transient regime of swelling increases progressively as the dpa rate increases.

0.38 to 24.0 dpa in Cycle 12. Table 1 summarizes the irradiation conditions for the fourteen combinations of temperature, dpa and dpa rate.

The starting and post-irradiation densities were measured using an immersion density technique known to be accurate to ±0.2 % change in density. In some cases it was not possible to clearly identify and retrieve all four specimens, but in general there were at least two identical specimens measured in each capsule. Determination of microstructural evolution in the specimens using a transmission electron microscope has been completed for the ternary and quaternary alloys, but has not yet been initiated for the carbon-doped alloy from MOTA-2B. An earlier study by Sekimura and Ishino addressed the microstructure of some of the MOTA-2A specimens, however (5). Both the current density change and earlier microscopy data are presented in Figure 2.

Results

As shown in Figure 2, the swelling of the carbon-doped alloy at ~400°C appears to show no obvious influence of the dpa rate. As observed in the two simple undoped alloys, the range of swelling between identical specimens is relatively small, indicating the reproducibility of the swelling phenomenon. Surprisingly, the swelling of the fourteen data ensemble appears to be following a general, lower-swelling trend somewhat characteristic of the undoped alloys at the highest dpa rate.

Discussion

There are two major features of these results. First, carbon additions clearly suppress the onset of swelling at ~400°C, an effect not observed to result from the addition of Ti alone. Second, carbon additions suppress the early termination of the transient regime, especially at lower dpa rates where the

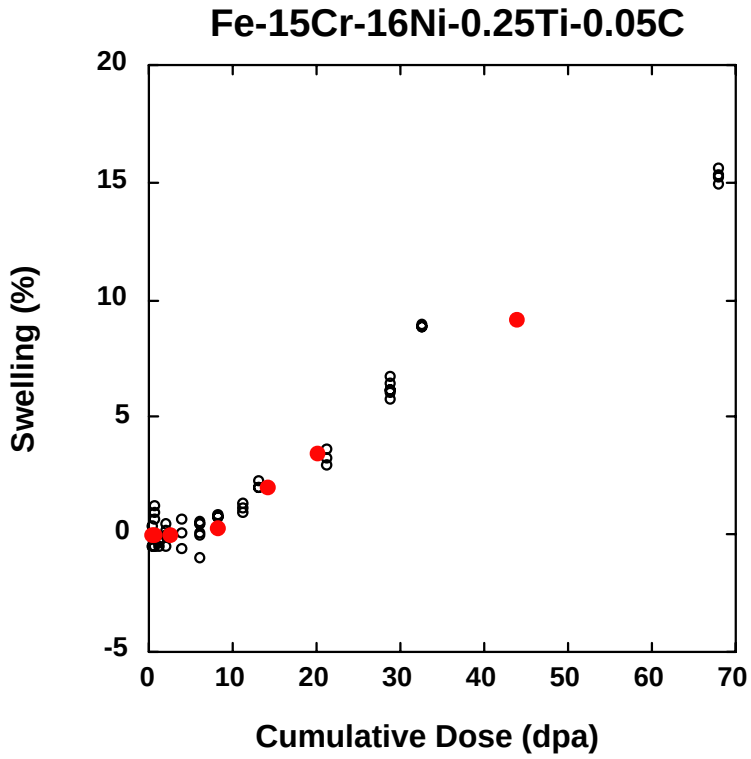

Figure 2. Swelling of simple model f.c.c. Fe-15Cr-16Ni-0.25Ti-0.05 in FFTF-MOTA at ~400°C, showing that the swelling is relatively independent of dpa rate. The red data were obtained from irradiation in MOTA-2A only and the black data from irradiation in both MOTA-2A and 2B.

undoped alloys exhibited very short transient durations.

Currently, there are no microstructural observations for the MOTA-2B carbon-doped specimens to determine the origins of this surprising result. In the undoped alloys microstructural observations of both 2A and 2B specimens showed that the flux sensitivity of the transient regime arose primarily from the flux sensitivity of Frank loop evolution (1). Higher dpa rates produced higher densities of smaller loops which were more resistant to unfaulting and network formation, thereby delaying the development of a dislocation network. Attainment of a stable network was found to be coincident with the termination of the transient regime in these carbon-free alloys (1).

As shown in Figure 3, Sekimura and Ishino (5) earlier examined by microscopy another set of the MOTA-2A specimens at three irradiation temperatures including the ~400°C specimens discussed in this report. Note that the influence of Ti addition is very small at ~400°C but increases at higher temperatures, while carbon additions to the Ti-modified alloys suppress swelling at all temperatures in the range 400-600°C.

Sekimura and Ishino did not address the effect of carbon on Frank loop characteristics at ~400°C for MOTA-2A specimens, so we can not at this point invoke a specific role for carbon's possible influence to delay swelling via its action on the evolution on Frank loops. Microstructural examination of the MOTA-2B specimens may allow the identification of such a role for carbon.

Table 1. Irradiation conditions experienced by carbon-doped specimens in FFTF cycles 11 and 12 (MOTA-2A and MOTA-2B). Note that in three of the seven cases the specimens irradiated in both cycles did not experience completely identical conditions with single cycle packages.

Dose Rate, dpa/sec		Dose, dpa		Temperature, ˚C	
# 11	#12	#11	#11 & #12	#11	#11 & #12
1.7 x 10^{-6}	1.4 x 10^{-6}	43.8	67.8	427	408
7.8 x 10^{-7} *1	9.5 x 10^{-7}	20.0 *1	32.4	390	387
5.4 x 10^{-7}	8.4 x 10^{-7}	14.0	28.8	430	424
8.2 x 10^{-7}	-----	21.1	-----	430	-----
3.2 x 10^{-7} *2	3.5 x 10^{-7}	8.22 *2	13.1	373	373
3.1 x 10^{-7} *3	3.0 x 10^{-7}	8.05 *3	11.1	411	410
1.5 x 10^{-7}	1.3 x 10^{-7}	3.87	6.12	430	431
9.1 x 10^{-8}	2.1 x 10^{-7}	2.36	6.36	430	431
4.6 x 10^{-8}	4.2 x 10^{-8}	1.18	1.91	434	437
2.7 x 10^{-8}	6.6 x 10^{-8}	0.71	1.87	434	437
1.4 x 10^{-8}	1.4 x 10^{-8}	0.37	0.61	436	444
8.9 x 10^{-9}	2.2 x 10^{-8}	0.23	0.61	436	444

Note: The swelling data of the underlined irradiation conditions come from TEM observation, while the other are density measurements.

*1: 6.0 x 10^{-7} dpa/sec and 15.6 dpa for #11 in 2 cycle irradiation specimens
*2: 2.7 x 10^{-7} dpa/sec and 6.90 dpa for #11 in 2 cycle irradiation specimens
*3: 2.2 x 10^{-7} dpa/sec and 5.69 dpa for #11 in 2 cycle irradiation specimens

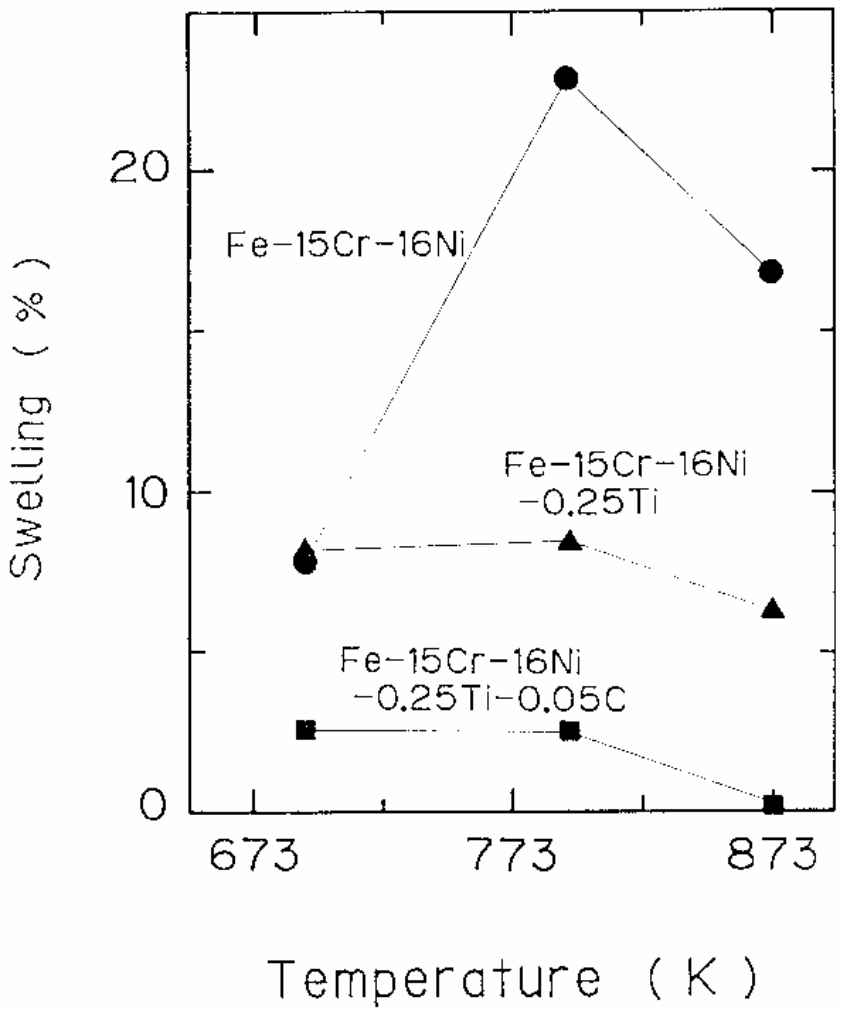

Figure 3. Cavity volume fraction determined by microscopy of three simple austenitic alloys after irradiation in FFTF-MOTA-2A at three different temperatures (5).

Conclusions

The addition of 0.04% carbon to Fe-15Cr-16Ni-0.25Ti leads to a reduction of neutron-induced swelling at ~400°C. Another consequence of carbon addition is that the strong influence of the dpa rate observed in the carbon-free alloy completely disappears in the carbon-doped alloy. The microstructural reasons for this behavior are not yet clear.

REFERENCES

[1] Okita, N. Sekimura, F. A. Garner, L. R. Greenwood, W. G. Wolfer and Y. Isobe, "Neutron-Induced Microstructural Evolution of Fe-15Cr-16Ni Alloys at ~ 400°C During Neutron Irradiation in the FFTF Fast Reactor," 10th International Conference on Environmental Degradation of Materials in Nuclear Power Systems – Water Reactors, 2001, issued on CD format, no page numbers. Also in Fusion Materials Semiannual Progress Report for Period Ending June 30, 2001, vol. 30, pp. 148-164.

[2] J. L. Seran and J. M. Dupouy, “The Swelling of Solution Annealed 316 Cladding in Rapsodie and Phenix,” Effects of Radiation on Materials: 11th International Symposium ASTM STP 782, 1982, pp. 5-16.

[3] J. L. Seran and J. M. Dupouy, “Effect of Time and Dose Rate on the Swelling of 316 Cladding in Phenix,” Proceedings Conference on Dimensional Stability and Mechanical Behavior of Irradiated Metals and Alloys, Vol. 1, BNES, 1983, pp. 25-28.

[4] G. M. Bond, B. H. Sencer, F. A. Garner, M. L. Hamilton, T. R. Allen and D. L. Porter, “Void Swelling of Annealed 304 Stainless Steel at ~370-385°C and PWR-Relevant Displacement Rates,” 9th International Conference on Environmental Degradation of Materials in Nuclear Power Systems – Water Reactors, 1999, pp. 1045-1050.

[5] N. Sekimura and S. Ishino, “The Effect of Titanium Addition on Microstructural Evolution in Austenitic Steel Irradiated with Fast Neutrons in FFTF,” J. of Nucl. Mater. 179-181 (1991) 542-545.

7.0 MHD INSULATORS, INSULATING CERAMICS AND OPTICAL MATERIALS

STUDY OF THE LONG-TERM STABILITY OF Y_2O_3 MHD COATINGS FOR FUSION REACTOR APPLICATIONS -- B. A. Pint and L. D. Chitwood (Oak Ridge National Laboratory)

OBJECTIVE

The objective of this task is to assess the long-term, high-temperature compatibility of high electrical resistance coatings with lithium at high temperatures. Electrically insulating coatings on the first wall of magnetic confinement reactors are essential to reduce the magnetohydrodynamic (MHD) force that would otherwise inhibit the flow of the lithium coolant. Initial experimental work was conducted on bulk ceramics to determine basic lithium compatibility and maximum-use temperatures of candidate ceramics such as AlN and Y_2O_3. As the next step, coatings of Y_2O_3 are now being evaluated.

SUMMARY

Two batches of Y_2O_3 coatings (12.5μm thick) were formed on V-4Cr-4Ti substrates using electron-beam assisted, physical vapor deposition (EB-PVD). The performance of the first batch of coatings was previously reported[1] and was promising. However, additional results on the second batch showed spallation after extended capsule exposures in Li at 700° and 800°C. These observations may be the result of an incompatibility between Y_2O_3 and Li, problems with the processing technique, or batch to batch variation in coating performance. A vacuum rig has been built to measure coating electrical resistance up to 800°C.

PROGRESS AND STATUS

Introduction

Previous work[2,3] using capsules tests of bulk ceramics in Li showed that Y_2O_3 was an attractive MHD coating candidate. Bulk, polycrystalline Y_2O_3 specimens showed little mass change after 1000h exposures in Li at 700° and 800°C. Also, its resistivity at 700°C was sufficient for the MHD coating application.[4] Therefore, Y_2O_3 coatings were fabricated to examine their performance before and after exposure to Li.

Experimental Procedure

The Y_2O_3 coatings were made by EB-PVD at Lawrence Livermore National Laboratory by A. Jankowski and J. Hayes. Ten 12.5mm diameter x 1mm thick V-4Cr-4Ti substrates polished to a 1μm finish were coated with Y_2O_3 in two batches (designated A and B) by rastering an electron beam over a pressed powder Y_2O_3 target. Using laser profilometry, the thickness of the as-received coatings was determined to be 12.5μm. The experimental procedure for lithium exposures has been outlined elsewhere.[5,6] Coated specimens from both batches were exposed for various times at 700° and 800°C, Table I. Two specimens were exposed to 3, 100h cycles to check the effect of thermal cycling on coating adhesion. One specimen was tested at 700°C and the other at 800°C, Table I. Specimen dimensions and mass were measured before and after exposure (0.02mg accuracy). After exposure, the first specimen (100h at 700°C) was distilled in vacuum at 500-550°C to remove residual Li from the specimen. (The same procedure was used

Table I. Summary of results from lithium exposures.

Conditions		Batch	Mass Change	Comments
700°C	100h	A	-0.77 mg	vacuum distilled
	1000h	A	1.72	no visible change, spalled after handling
	2000h	B	-2.28	remnants only
	3 x 100h	B	0.66	flaky spall
800°C	100h	A	1.03	no visible change
	1000h	A	1.48	no visible change
	2000h	B	-4.19	no coating remained
	3 x 100h	B	1.34	no visible change

to clean the bulk specimens.) However, the V-4Cr-4Ti substrate oxidized due to the relatively low vacuum possible in the distillation system. To avoid this problem, subsequent specimens were cleaned by submerging them in methanol for 24h at room temperature. Previously, coatings were characterized using field emission gun, scanning electron microscopy (SEM), auger electron spectroscopy (AES) and x-ray diffraction (XRD) with 300kV Cu Kα radiation. Coating resistance was measured up to 500°C with a vacuum pressure of $\approx 10^{-6}$ Torr to limit oxidation of the V-4Cr-4Ti substrate.[1]

Results and Discussion

Results for the eight specimens exposed to Li are shown in Table I. The results for batch A specimens and the 800°C cycled specimen were reported previously.[1] The three specimens from batch B that were exposed subsequently all showed near total loss of the coating (after 2000h at 700°C and 2000h at 800°C) or partial spallation of the coating (3 x 100h at 700°C). Thus no resistance measurements could be made after these exposures.

The mass change data for these experiments are not easily explained. Depending on the density assumed for EB-PVD Y_2O_3, the coating should have had a starting mass of no more than ≈3.1mg. Thus the mass gains observed when the coating was adherent of 1.0-1.7mg suggests a substantial reaction with Li or the V-4Cr-4Ti substrate. However, the V-4Cr-4Ti substrate has a mass of ≈700mg so the total mass change may be dominated by any change in the substrate. There are several possible explanations for the observed mass changes:

1) The mass loss of 4.2mg after 2000h at 800°C is too large to be explained by the loss of just the coating. At this time, no Li exposures of bare substrates have been performed for comparison. Some dissolution of the V alloy substrate or selective loss of certain elements (e.g. O or Ti) may have occurred during the extended exposure to Li (2000h at 800°C) resulting in an additional mass loss. Recent analysis of V-4Cr-4Ti after exposure to Li-2%Ca showed that selective attack could occur.[7] While this exposure was the longest time at the highest temperature, none of the other exposures resulted in a mass loss that could not be accounted for by loss of the coating.

2) The large mass gains for the intact coatings may reflect a reaction with the V-4Cr-4Ti substrate, possibly the uptake of N from the Li. The starting N content of the Li was measured[3] as 140ppmw giving 0.7mg N in the 5g of Li in the capsule. However, the V alloy capsule walls should have absorbed some of this total. Therefore, it is difficult to account for this mass gain by the substrate. (Future capsule experiments will use Mo capsules to reduce the possibility of the capsule affecting

the results.)
3) Previously, AES analysis had observed the formation of Y-Ti oxides on the surface of the Y_2O_3 coating after exposure to Li for 1000h at 800°C.[1] This suggests that Ti may be selectively being removed from the substrate or V alloy capsule walls. Complete conversion of Y_2O_3 to $YTiO_3$ (or another Y-Ti oxide) could increase the mass by up to 2mg but XRD results indicated complete conversion did not occur.
4) The examination by AES also revealed that there was some residual Li in the coatings after cleaning[1] and XRD analysis detected the formation of $YLiO_2$ but the mass increase due to formation of this compound would only be as much as 0.4mg for complete conversion.

A new resistance measurement rig was built using the existing vacuum system to enable higher temperature measurements. The previous system had a maximum temperature capability of ≈550°C due to its large thermal mass and small resistance heating elements. The current specimen holder (Figure 1) places the specimen on the Mo-enclosed heating element resulting in better temperature control to >800°C. In the previous report, the possible degradation of the Au electrode by residual Li in the coating during the resistance measurement at 550°C in vacuum was discussed. However, further examination by AES of that specimen after heating revealed that the electrode was largely intact but covered with carbon. Several of the surviving coated specimens were recoated with an Au electrode for examination with the new equipment but all were shorted. Further work will be done to characterize the remaining coatings by cross-sectioning them.

More testing is needed on Y_2O_3 coatings. The current results do not provide sufficient information to draw a strong conclusion about the compatibility of Y_2O_3 with Li. The formation of the $LiYO_2$ phase, which was observed in a previous study,[8] suggests that Y_2O_3 may not be sufficiently compatible. The spallation observed in these tests may be due to the thermal expansion mismatch between V-4Cr-4Ti and Y_2O_3. However, it also could be due to the coating process or batch-to-batch variation in the EB-PVD process. Additional Y_2O_3 coatings made by other processes need to be evaluated before a stronger conclusion can be made.

REFERENCES

1. B. A. Pint and L.D. Chitwood, DOE/ER-0313/32 (2002) 101.
2. B. A. Pint, J. H. DeVan and J. R. DiStefano, DOE/ER-0313/31 (2001) 132.
3. B. A. Pint, J. H. DeVan and J. R. DiStefano, J. Nucl. Mater. in press.

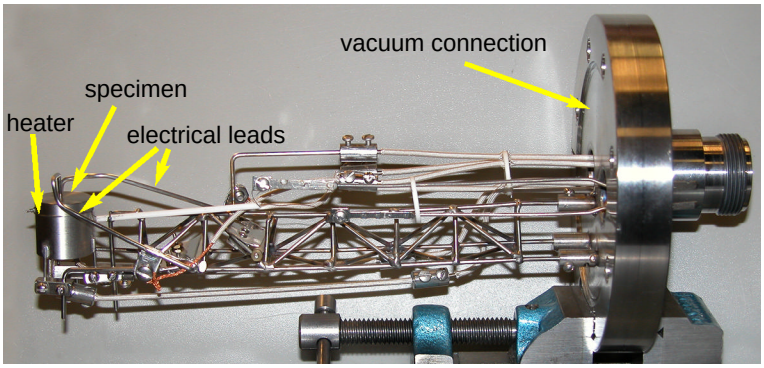

Figure 1. Specimen heater/holder that is inserted into the resistance measurement rig vacuum chamber.

4. K. Natesan, C. B. Reed, M. Uz, J. H. Park and D. L. Smith, ANL/TD/TM00-10 (2000).
5. B. A. Pint, L.D. Chitwood, J. H. DeVan and J. R. DiStefano, DOE/ER-0313/27 (2000) 49.
6. B. A. Pint, L. D. Chitwood and J. R. DiStefano, J. Nucl. Mater. 289 (2001) 52.
7. O. I. Eliseeva, Mater. Sci. 37 (2001) 910.
8. T. Mitsuyama, T. Terai, T. Yoneoka and S. Tanaka, Fusion Eng. Design 39-4 (1998) 811.

Microstructures of Y-O, Si-O, and In-Situ Formed CaO Coatings on V-4%Cr-4%Ti in Liquid 2.8 at.% Ca-Li *

J.-H. Park and K. Natesan, Energy Technology Division, Argonne National Laboratory, Argonne, IL 60439 USA

OBJECTIVE

The object of this work is development of electrically insulating coatings for vanadium alloys, one of the leading candidate materials for the first-wall/blanket structures in fusion reactors.

INTRODUCTION

In a previous study, we demonstrated the in-situ formation of a CaO insulator coating, generating defects under thermal cycling conditions, and self-healing of defects on V-Cr-Ti alloys in the liquid lithium system. [1] We also found that sintered Y_2O_3 is compatible with liquid Li.[2] These encouraging results caused us to investigate O-charged V-4Cr-4Ti with a Y film deposited by means of physical vapor deposition (PVD). We are now investigating the in-situ formation of a CaO layer on a V-4Cr-4Ti surface enriched with Y-O or Si-O. In the study of coatings on the V/Li blanket, the electrical insulation behavior should be maximized to have a thin film with high toughness and thermal conduction. What needs to be eliminated or minimized is V incorporation into the insulator film and in-situ self-healing. In this report we present microstructures for the electrical insulator coating reported previously.[3]

Also investigated was Si-O addition based on a thermodynamic evaluation. The addition of Si was tested to minimize the V incorporation in the in-situ CaO film. Our previous investigations showed that the incorporation of V into the in-situ-formed CaO was normally 15 to 35 at.%. If V is highly incorporated, the film could be conductive due to the V having a wide range of ionic valence states. Based on the thermodynamic evaluation, we determined that additions of Si could form as Ca-Si-O in the Ca-Li environment. Therefore, we performed surface modification by $Cr+Cr_2O_3$ equilibrium inside a vacuum-sealed quartz (SiO_2) chamber. When the oxygen partial pressure (pO_2) is low, such as the level corresponding to $Cr+Cr_2O_3$ equilibrium at high temperatures, the quartz becomes the source of the Si, Si-O, and Cr that are incorporated into the V-4Cr-4Ti along with O in the chemical vapor. Based on these concerns, we initiated study of the Y and Si additions to the in-situ CaO films, and we are reporting the results of short exposures.

EXPERIMENTAL PROCEDURE

PVD Y-film deposit: We O-charged a conventional argon-oxygen gas, and yttrium metal was evaporated by use of a tungsten-heating element within an ultra-high-vacuum chamber to deposit films with thicknesses of between 0.2 and 1.5 μm. Samples were annealed at 750°C for 13 h in the vacuum. The Y film reacted with the pre-charged O in the V-4Cr-4Ti to convert to Y-O. The films were analyzed and we investigated the microstructures by scanning electron microscopy (SEM), energy dispersive spectroscopy (EDS), and X-ray diffraction.

Si-O enrichment on the surface of V-4Cr-4Ti by annealing in $Cr+Cr_2O_3$ pack sealed quartz cell: We have performed the simultaneous addition of Si and O by means of $Cr+Cr_2O_3$ equilibrium inside a vacuum-sealed quartz (SiO_2) chamber at 950°C for 17 h. The above samples were exposed to 2.8 at.% Ca-Li at 600-700°C for between 99 and 747.5 h. Experimental details can be found in our previous reports.[3]

RESULTS AND DISCUSSIONS

Investigation of Y-coated V-4Cr-4Ti: Figure 1 shows a typical PVD film deposit on V-4Cr-4Ti and post-annealed specimen #33. Figure 2 shows the X-ray diffraction patterns for each step of the process:

* Work supported by the U.S. Department of Energy, Office of Fusion Energy Research, under Contract W–31–109–Eng–38.

Spectra are given for the Y-deposit, sample annealed at 750°C, and sample after exposure at 700°C in 2.8 at.% Ca-Li for 99 h. The X-ray spectrum for the exposure in the 2.8 at.% Ca-Li was identical with that for the samples exposed without Y deposit. Since the CaO film was formed and grew in-situ, it was expected that those film structures might be identical. The CaO film in Y-O coated samples was thicker than without the coating. Table 1 presents film thickness for the in-situ coatings deposited on V-4Cr-4Ti in the 2.8 at. % Ca-Li exposure for 99 h at 700°C for the Y-coated (t ≤ 0.5 μm) samples. Figure 3 shows the typical microstructure for the Y-O film prepared by conventional gas-phase oxidation after PVD Y-deposition on the V-4Cr-4Ti substrate at 500ºC in a flowing argon gas, with a trace amount of oxygen being used for the oxidation process. However, PVD film deposition started showed limitation when it desire thickness, t ≥ 1-μm film. Figure 4 shows the typical local buckling initiation during the Y-deposition, when we tried to fabricate t ≥ 2-3μm films, buckling became enlarged as we expected from the mechanical stress dissipation by the film failure. Figure 5 shows the SEM surface microstructure for YVO_3 film prepared from a thin (t = 0.35 μm) Y-metallic PVD film deposited on V-4Cr-4Ti and then annealed at 750°C for 13 h in vacuum for the specimen #47 (see Table 1).

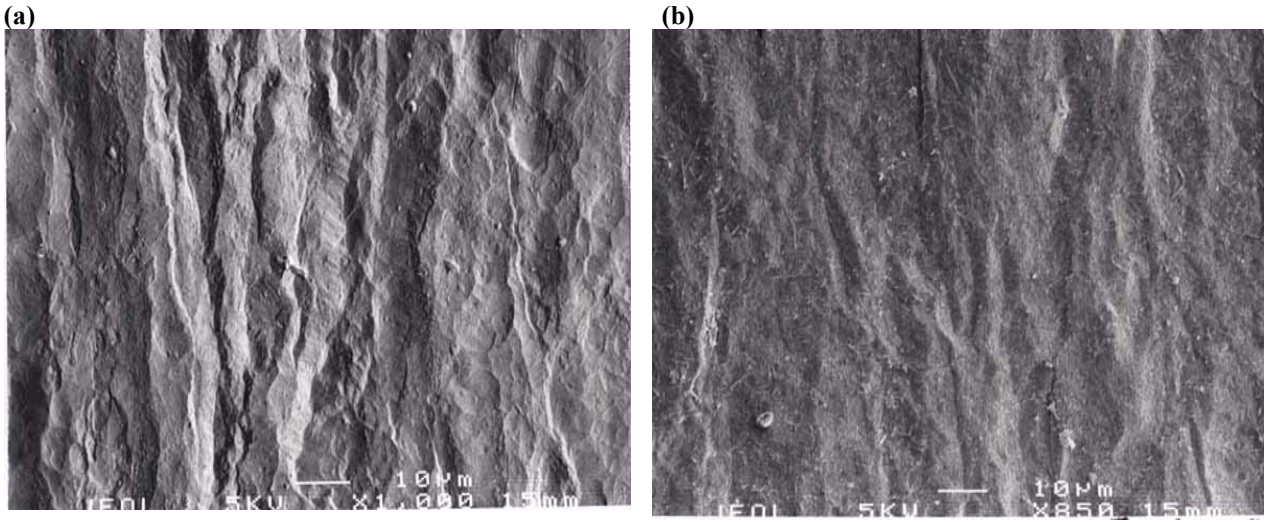

Fig. 1. SEM surface microstructure for (a) thin (t = 0.2 μm) Y-metallic PVD film deposit on V-4Cr-4Ti, and (b) sample #33 annealed at 750°C for 13 h in vacuum to convert $Y_8V_2O_{17}$ film.

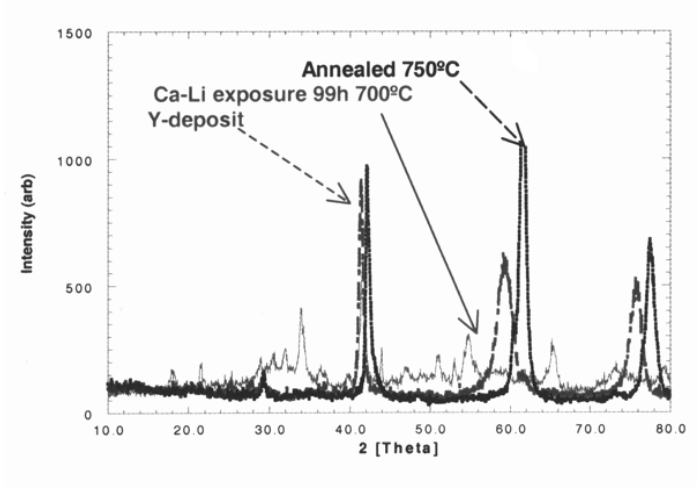

Fig. 2.

X-ray diffraction for sample #33 (see Table 1). Pattern for Y-deposit, after annealing at 750°C, and after exposure at 700°C in 2.8 at. % Ca-Li for 99 h.

Fig. 3.

Typical microstructure for the Y-O film prepared by the conventional gas phase oxidation after Y-deposition on V-4Cr-4Ti substrate at 500ºC in flowing Ar gas.

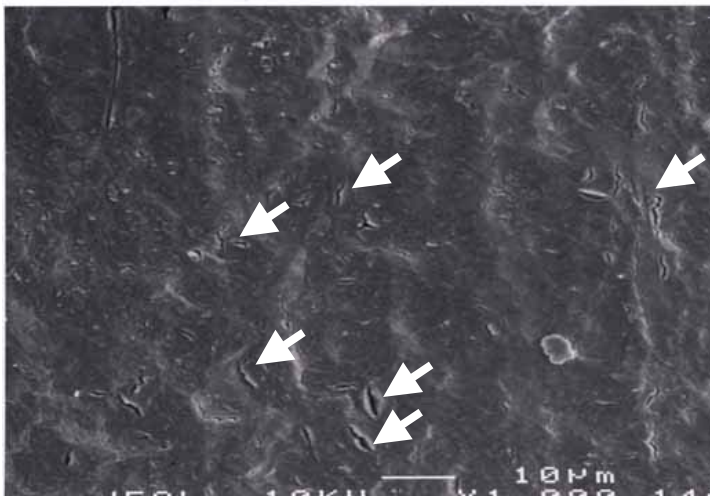

Fig. 4.

Typical microstructure for the thicker (t ≥ 1.0 μm) Y-metallic film deposit on V-4Cr-4Ti by PVD. Spots or area shown by arrows started buckling.

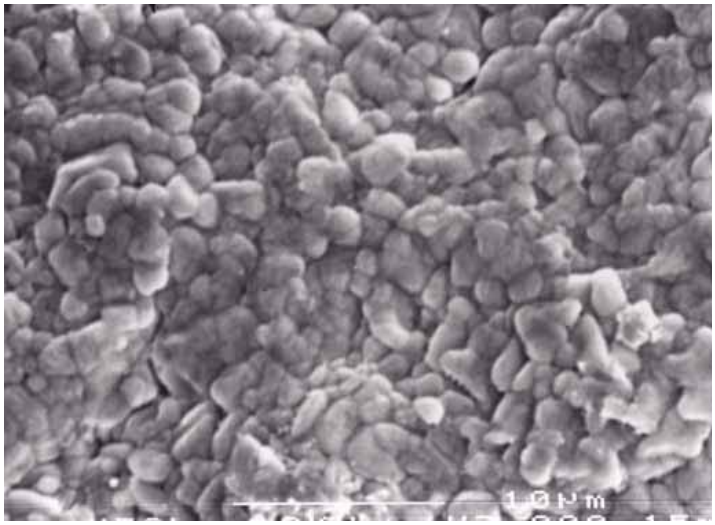

Fig. 5.
SEM surface microstructure for YVO_3 film prepared from a thin (t = 0.35 μm) Y-metallic PVD film deposited on V-4Cr-4Ti and then annealed at 750°C for 13 h in vacuum for the specimen #47 (see Table 1).

Table 1. Thickness of the in-situ coating deposited on V-4Cr-4Ti in 2.8 at. % Ca-Li exposure for 99 h at 700°C for the Y-coated (t ≤ 0.5 μm) samples.

Sample No.	O (wppm)	Y deposit (μm)	XRD annealed @750°C 13 h	Film t (μm) by SEM
33	400	0.2	$Y_8V_2O_{17}$	11.8
47	7000	0.35	YVO_3	9.5

Si-Cr-O annealed V-4Cr-4Ti: Figure 6 shows the X-ray diffraction pattern and SEM micrographs for the in-situ formed films on the V-4Cr-4Ti in 2.8 at. % Ca-Li at 600°C for 747.5 h. Shown are the patterns for the layer between the V-4Cr-4Ti and water insoluble layer in Fig. 6 (a), and for the cross-section SEM view near the V-4Cr-4Ti/CaO film in Fig.6 (b), which shows a very adherent film to the V-4Cr-4Ti substrate. Initially, O-charging was done by a $Cr+Cr_2O_3$ pack inside the vacuum-sealed quartz (SiO_2) cell.

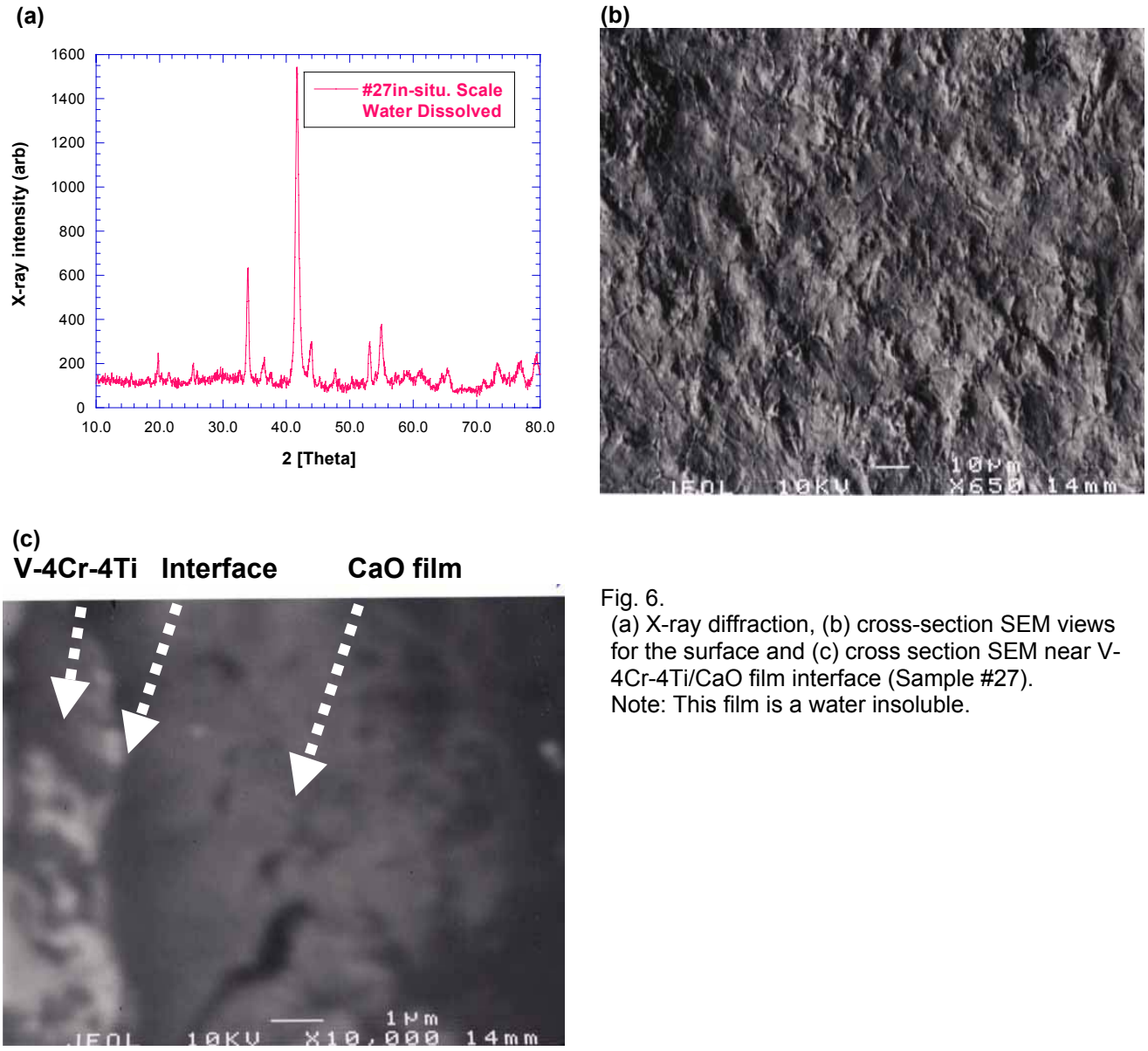

Fig. 6.
(a) X-ray diffraction, (b) cross-section SEM views for the surface and (c) cross section SEM near V-4Cr-4Ti/CaO film interface (Sample #27).
Note: This film is a water insoluble.

Table 2. Results of EDS analysis for sample surface from in-situ coating performed on V-4Cr-4Ti in 2.8 at.% Ca-Li exposure at 600ºC for 747.5 h for the samples annealed with $Cr+Cr_2O_3$ in a quartz cell.

No.	[a]O (Wppm)	Cal'd t (μm)	Meas'd t (μm)	Fraction of the element by EDS (at. fraction)					Note
				Ca	V	Ti	Cr	Si	
27	[12374]	11.154	-	0.476	0.163	0.0129	0.000	0.348	[b]Water insoluble film

[a] Brackets indicate total wt. changed during the quartz sealing cell in test with the Cr/Cr_2O_3 atmosphere. Some Si and Cr may be affected. Real O-wppm should be lower than those in brackets. This in-situ formed film was highly adhesive and insulkating based on our experience with in-situ formed films in Ca-Li environments. Currently, we do not have the electrical resistivity data required for the blanket design. [b]see Fig. 6.

Since we found the adhesion with the V-4Cr-4Ti to be water insoluble and highly resistive (only checked at ambient temperature) for sample #27 (Table 2), we calculated the free energy of formation for the Ca-Si-O shown in Fig. 4 in the previous report. As we can be seen in the previous report, the Si incorporation in the in-situ formed Ca-Si-O film of #27 sample might be effective as a buffer layer between CaO and V-4Cr-4Ti. In this film, V is 16 at.% (lowest) and Ca + Si is 83 at. % (highest); those are our targeted goals for the in-situ insulator coatings in Ca-Li environments.

FUTURE SUGGESTED WORK

We expect that Si additive could be the best choice due to its stable thermodynamic nature in liquid Li where it forms Ca-Si-O, as shown in Fig. 4 in the previous semiannual report.[3] So far we have focused on the formation of an in-situ film on the O-charged V-4Cr-4Ti. As we expected that the charged O will be consumed for the CaO-coatings or O-dissolution into the liquid metal, we expect that that adding of O into the lithium-(calcium) by CaO or Li_2O (i.e., similar idea to adding CaO) into the liquid metal might be an alternative approach to achieve thermodynamic stability of the in-situ formed films for longer time services. With both O and Ca in the lithium, the CaO layer will be much more stable. CaO does not dissolve in the lithium, but Ca does. Therefore, for CaO to be moved by the lithium, the following reaction has to occur:

$$CaO \rightarrow Ca + \underline{O}$$

The stability of CaO depends on the activity product of $a_{Ca}a_{O.}$ Therefore, we will need to keep Ca concentration in the lithium, as well as O concentration in the lithium. With only Ca concentration, the product of $a_{Ca}a_O$ is near zero. The reaction above will go to the right, and Ca will dissolve in the lithium. Therefore, addition of O to the lithium improve the performance of the CaO coating ought to be pursued.

ACKNOWLEDGMENTS

P. Johnson and B. Tani of Argonne Analytical Chemistry Laboratory provided the X-ray diffraction studies. Work supported by the U.S. Department of Energy, Office of Fusion Science, under Contract W–31–109–Eng–38. One of the authors (JHP) expresses thanks to Dr. D. K. Sze, University of California at San Diego for valuable discussions.

REFERENCES

1. J.-H. Park and T. F. Kassner, CaO Insulator Coatings and Self-healing of Defects on V-Cr-Ti Alloys in Liquid Lithium System, J. Nucl. Mater. 233-237, 476-481 (1996).

2. J.-H. Park, M. R. Fox, and G. Dragel, DOE/ER-0313/13, 260-275, and 290-294 (1992).

3. J.-H. Park, A. Sawada, K. Natesan, D. Rink, and R. F. Mattas, Progress of In-situ Coatings on the V-4Cr-4Ti in 2.8 at. % Ca-Li at 600 & 700ºC, Fusion Materials Semiannual Report Vol. #32 (2002).

8.0 BREEDING MATERIALS

No contributions.

9.0 RADIATION EFFECTS, MECHANISTIC STUDIES, AND EXPERIMENTAL METHODS

MD MODELING OF SCREW DISLOCATION - <100> LOOP INTERACTION IN Fe -

J. Marian and B. D. Wirth *(Lawrence Livermore National Laboratory)*

Objective

The objective of this study is to develop improved atomistic insight into the mechanisms of dislocation interaction with radiation produced dislocation loops, which have a Burger's vector of a<100>. This is required for the development of advanced constitutive relations for the mechanical behavior of irradiated steels and improved understanding of plastic flow localization.

Summary

Ferritic/martensitic steels considered as candidate first-wall materials for fusion reactors experience significant radiation hardening at temperatures below ~400˚C. In this work we describe the motion of screw dislocations, known to control the plastic response of *bcc* materials to external stress, and their interaction with $\langle 100 \rangle$ dislocation loops. MD simulations are used to simulate screw dislocation motion and, following a description of the computational method, we report the main physical mechanisms of the dislocation – loop interaction, including an estimate of the critical bowing angle and a first-order estimation of the induced hardening.

Introduction

Ferritic steels and alloys represent a technologically important class of materials that are widely used for structural purposes in current nuclear fission reactors and proposed as candidate materials for plasma-facing first wall structures in future fusion energy facilities. Predicting their in-service performance requires understanding the accumulation of defects and evolution of the microstructure under the severe irradiation conditions found in these environments.

Hardening in the lower temperature regime is believed to arise from the formation of dislocation loops under irradiation that pin and may also decorate dislocations, thereby impeding their glide during deformation. A number of experimental studies performed over a wide range of temperatures in ferritic model alloys have shown the existence of large interstitial loops in the bulk, which may provide a significant contribution to the hardening caused during irradiation at lower temperatures [1]. The dislocation loops are observed with both $\frac{1}{2}\langle 111 \rangle$ and $\langle 100 \rangle$ Burgers vectors, although, generally, with a predominance of $\langle 100 \rangle$ [2,3].

Ultimately, a high number density of dislocation loops in the appropriate temperature range can result in hardening by dislocation pinning, leading to a characteristic yield stress increase that can be measured experimentally using standard methods. In b.c.c. metals, screw dislocations dictate the plastic response and it is their behavior in the presence of irradiation-generated dislocation loops and the dynamics of their interactions that are key to understanding hardening in conditions relevant to fusion reactors. However, the atomistic nature of the interaction again makes these processes very difficult to study using conventional experimental techniques, whereas molecular dynamics (MD) has been successfully applied to a number of scenarios involving different lattice defects and dislocations [4,5]. In this report, we report the results of MD simulations of screw dislocation motion and interaction with a <100> dislocation loop.

Current address, Graduate Aeronautical Laboratories, California Institute of Technology, jaime@aero.caltech.edu

* Current address, Nuclear Engineering Department, University of California, Berkeley, Berkeley, CA 94720-1730, bdwirth@nuc.berkeley.edu

The MD simulations presented in this paper have been carried out with the MDCASK code [6] using the Fe-Cu potentials developed by Ackland and co-workers [7].

Results

Estimation of the hardness due to □100□loops

Based on Orowan's simple model, the most commonly used expression for the change in shear stress, □□s, induced in the dislocation glide plane by a regular array of defects is given in the following equation:

$$\Delta\tau_s = \alpha Gb(Nd)^{1/2} \qquad (1)$$

where *G* is the shear modulus, *b* the Burgers vector of the dislocations, *N* the defect number density, *d* the defect diameter and the square-root factor is the reciprocal of the average distance between obstacles. The □ factor in equation **(1)** is known as the obstacle strength and is determined as $\alpha = \cos(\psi/2)$, where □ is the angle in the line tension approximation at which the dislocation is able to break through the obstacle and continue its glide (for an impenetrable object □=0, □=1). However, relatively few measurements of the critical angle have been made for radiation-induced defects and, in practice, microstructural observations and mechanical property measurements are compared to infer values of □ for different types of defects [8]. Atomistic simulations provide a direct calculation of the dislocation-obstacle interaction and critical bowing angle, which, together with other simulation methods, can provide all of the required input to equation **(1)**. The computational elements necessary for this type of calculations are: (i) generation of a screw dislocation, (ii) introduction of an appropriate obstacle (*e.g.* a □100□ loop), and (iii) the development of the capability to reproduce the conditions required for the interaction (*i.e.* temperature, stress, etc.). In what follows, we provide a self-consistent computational framework based on MD simulations to obtain an approximate value of □□s.

Generation of a screw dislocation in □-Fe

The isotropic linear elasticity solution corrected with image summations for periodic boundary conditions is used to introduce a screw dislocation dipole into an otherwise perfect crystallite. In general, the introduction of a dipole, which is a measure intended for conserving the periodicity of the crystal, is not an appropriate initial condition for the simulations, as the dynamics of both dislocations are characterized by a strong self-annihilating bias. In order to remove one of the dislocation poles, the box must be cut accordingly, *i.e.* several atomic layers must be removed. This eliminates the periodicity in at least one direction, which further requires the use of appropriate boundary conditions. The computational boxes employed in this study were $100 \cdot a_0 \frac{\sqrt{3}}{2} \times 40 \cdot a_0\sqrt{6} \times 50 \cdot a_0\sqrt{2}$, which amount to about 10^6 atoms. In general, for these large-scale simulations, flexible boundary conditions in the form of free surfaces have been used. These free surfaces have been generated in a way that is appropriate to the application of a desired shear stress in the computational box. After cutting the box to generate the free surfaces, the dislocation density is computed to be □=2.9□10^{15} m^{-2}. Prior to any external application of stress, a relaxation of the linear-elastic dislocation configuration is performed at zero stress and a temperature-controlled equilibration at the target temperature. The stress (or more appropriately a surface traction) is applied on a skin region corresponding to the outermost atomic layers (one to three) adjacent to the free surfaces. The character and direction of the bounding surfaces and applied stress are considered concurrently to obtain the desired Peach-Köhler force (generally on {110} and {112} glide planes). In addition to this externally-induced force, image forces result from the existence of the traction-controlled (free) surfaces. These, together with the directional bias towards twinning orientations, are the sole forces exerted on the dislocation and upon which the dynamics of its motion are studied.

Dislocation-obstacle interaction

The above knowledge of the dynamic constraints is required to appropriately position the obstacle in the presumed path of the dislocation. The obstacle was chosen to be a [100](100) dislocation loop with rhombic shape containing 113 interstitials (~2 nm).

A shear stress of 750 MPa was applied to the crystallite containing both the screw dislocation and the loop at a temperature of 100 K. Since the applied stress is below the computed Peierls stress (900 MPa for this potential), the dislocation begins to glide by a double-kink mechanism on {110} planes. Two out of the eight possible {110} planes become activated and the dislocation performs a serrated glide, generating kinks on both planes as well as on one {112} plane in the twinning sense, thus effectively moving on an "apparent" single {112} plane. In these simulations, the loop is also subject to the applied stress and undergoes several structural transformations prior to interacting with the dislocation. The whole process is illustrated in **Figure 1**. The loop's corners initially transform into $\frac{1}{2}\langle 111\rangle$ segments (**Figure 1 (a)**). In **Figure 1 (b)**, the right corner of the loop is subject to secession forces as the dislocation comes closer. This is a combination of multiple factors. First, the applied external and the dislocation stress fields superimpose to exert a force on the loop corners with $\frac{1}{2}\langle 111\rangle$ geometry. Second, due to their prismatic nature, these $\frac{1}{2}\langle 111\rangle$ segments are amenable to thermally activated diffusion along the direction of the dislocation line. Indeed, in **Figure 1 (c)** a perfect $\frac{1}{2}[111]$ loop is emitted from the right section of the parent dislocation loop. At this point, the screw dislocation continues to move by a double-kink mechanism until it comes into contact with the central [100] section of the original loop. Finally, **Figure 1 (d)** shows the absorption of both the emitted loop (right side of the interaction) and the remaining $\frac{1}{2}\langle 111\rangle$ corner situated at the left side. In both cases, heavily-arched, spiral segments of different dimensions are generated, leaving a central section consisting of a [100] loop and a pinned $\frac{1}{2}[111]$ screw dislocation. In all cases, the Burgers vectors of the different screw dislocation and dislocation loop segments were determined by way of a 3D Burgers circuit analysis.

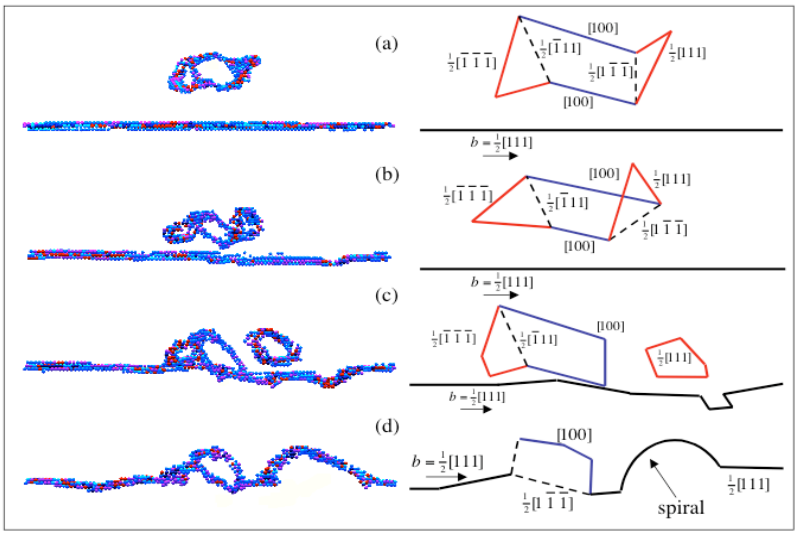

Figure 1 - Sequence of MD snapshots (left) and equivalent dislocation interpretation (right) of the interaction between a 113-SIA, rhombic [100] dislocation loop and a $\frac{1}{2}[111]$ screw dislocation at 100 K and 750 MPa of applied shear stress. The dislocation and loop cores have been visualized using the centro-symmetry deviation parameter. Details of the interaction are given in the text.

The entire interaction process lasted for 150 ps (at strain rates of the order of $\dot{\varepsilon} \approx 1.4 \times 10^{8}$ s^{-1}) but, after 200 ps of annealing, the dislocation remained pinned and the only remarkable observation was the elastic transmission of the spiral (stretching) along the dislocation line. An increase in the applied shear stress was required to force the screw dislocation through the pinning obstacle.

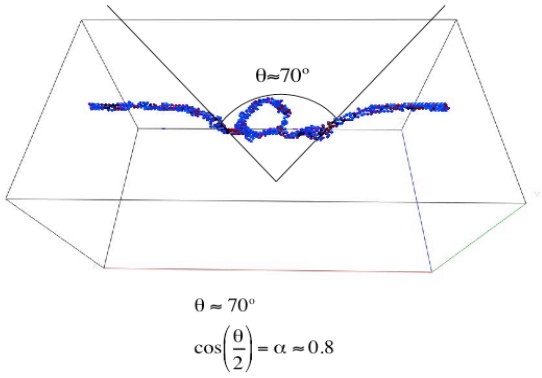

Figure 2 – Final snapshot before the dislocation breaks through the obstacle, leaving a [100] loop behind and two heavily-curved spirals along the dislocation line. The critical angle is θ=70°, necessary to estimate the obstacle strength, $\alpha = \cos(\theta/2) = 0.82$.

Estimation of the hardening

The stress was gradually increased and applied to the pinned structure described above in 50 MPa increments. Only after a value of 1.0 GPa was the screw dislocation able to traverse the [100] loop. This increment in the external stress (250 MPa) is already a first-order estimate of the value of $\Delta\tau_s$. The dislocation starts to bow around the dislocation loop until, for $\theta \approx 70°$, it can finally surpass the obstacle and continue with its normal unconstrained glide. **Figure 2** shows the last snapshot before the dislocation breaks free. From this value of θ, one can calculate the obstacle strength, α=cos(θ/2)=0.82. With this and N=1.2×10^{23} m^{-3}, d=2 nm and K_a=64 GPa[1], one can compute the change in shear stress, $\Delta\tau_s$=195 MPa, due to equation **(1)**. The computed value of α suggests a higher obstacle strength for [100] loops than other calculations quoted in the literature [10,11]. Of course, N and d have been obtained directly from our computation box and are subject to the narrow applicability window of this MD simulation. N is unphysically high, with real values being two to three orders of magnitude lower. In addition, the product Nd inside the square root in equation **(1)** should in theory be an integral over the whole size spectrum. Further, it is not clear that the continuum line tension model used to calculate α is applicable at the atomic dimension. Therefore, our results are only intended to provide a first-order estimate of $\Delta\tau_s$.

[1] Instead of G, it is more appropriate to use K_a. K_a is related to the anisotropic shear modulus and is obtained from the modified elastic compliances [9].

In uniaxial, tensile loading conditions, the resolved shear stress for polycrystalline materials that slip on {110} planes is related to the applied stress, σ_u, by [8]:

$$\sigma_u = T\tau_s \quad (2),$$

where T is the Taylor factor and a standard value of 3.06 is commonly used for microstructure–mechanical property correlations [8]. Therefore, according to equation **(2)**, we obtain $\Delta\sigma_u$=590 MPa.

The calculations presented in this section suffer from obvious limitations. There is a strong statistical uncertainty associated with the single loop and interaction geometry considered, and to the conditions under which the simulations were performed. Also, the simulations have been carried out at strain rates that, although physically reasonable in some environments, are too high for the conditions expected in fusion steels. Our values of α and $\Delta\sigma_u$ are higher than those obtained experimentally or from other micromechanical estimations. α-values as high as 0.5 and 0.6 have been reported by Nicol *et al.* [10] and Hashimoto *et al.* [12], respectively, to describe yield stress changes of ~200 MPa and ~450 MPa, but our predicted values of 0.8 and 600 MPa are about 50% too large. As well, α-values in the range of 0.5 to 0.8 must be considered suspect based on the standard value of ~0.35 used to describe network dislocation reactions [13]. In any case, this work represents the first purely-dynamical study of dislocation-obstacle interactions involving $\langle 100\rangle$ loops and screw dislocations in b.c.c. Fe and should be regarded as a first step in estimating the relevant hardening parameters by computer simulation. Recently, similar works involving edge and screw dislocations interacting with stacking fault tetrahedral, voids and precipitates have been reported [4,5,14], and it is expected that the knowledge of dislocation–obstacle interactions will significantly increase as new techniques and potentials are being developed.

Conclusions

To study the elementary hardening process in irradiated α-Fe, we have simulated the interaction between $\frac{1}{2}\langle 111\rangle$ screw dislocations and a large $\langle 100\rangle$ loop. At 750 MPa of applied stress and 100 K, the interaction results in a complex combination of dislocation loop segment absorption and pinning. The dislocation's structure becomes significantly altered, with large spiral segments being the dominant feature. When the stress is increased to 1.0 GPa, the dislocation releases from the $\langle 100\rangle$ loop at a critical angle of about 70º. These simulations permit calculation of the relevant parameters to estimate the hardening from Orowan's theory, most notably the obstacle strength of α=0.82. Our results overestimate experimental results by approximately a factor of two, which may be attributed to the limited scope in terms of time and space scales available to MD simulations or possibly the limited applicability of the continuum line tension model at the atomic level. Future work will further investigate the spectrum of dislocation – obstacle interactions and investigate the appropriate connection between the atomic mechanisms and continuum hardening relationships.

Acknowledgments

The authors are grateful to Drs. W. Cai and V. V. Bulatov for their help with the implementation of MD simulations of screw dislocation mobility. Useful discussions with Drs. A. Caro, M. Victoria and P. Derlet are acknowledged. This work has been performed under the auspices of the U.S. Department of Energy and Lawrence Livermore National Laboratory under contract W-7405-Eng-48 and within the CSN-UNESA Coordinated Research Programme under contract P000531499.

References

1. D. S. Gelles, M. L. Hamilton and R. Schäublin, in *Effects of Radiation on Materials: 20th International Symposium, ASTM STP 1405*, S. T. Rosinski, M. L. Grossbeck, T. R. Allen and A. S. Kumar, Eds., American Society for Testing and Materials, West Conshohocken, PA, 2002.
2. A. E. Ward and S. B. Fisher, *J. Nucl. Mat* **166** (1989) 227.
3. K. Suganuma and H. Kayano, *Radiat. Effects* **54** (1981) 81.
4. T. Harry and D. J. Bacon, *Acta Mater*. **50** (2002) 195; *Acta Mater*. **50** (2002) 209.
5. B.D. Wirth, V.V. Bulatov and T. Diaz de la Rubia, *Journal of Engineering Materials and Technology* **124** (2002) 329.
6. T. Diaz de la Rubia and M. W. Guinan, *Mater. Res. Forum* **174**, (1990) 151.
7. G. J. Ackland, D. J. Bacon, A. F. Calder and T. Harry, *Phil. Mag*. A **75**, (1998) 713.
8. R. E. Stoller and S. J. Zinkle, *J. Nucl. Mater*. **283-287** (2000) 349.
9. J. P Hirth and J. Lothe, *Theory of Dislocations, 2nd ed*., Krieger Publishing Co. (1982) p. 168.
10. A.C. Nicol, M.L. Jenkins and M.A. Kirk, *Mat. Res. Soc. Symp.* **650** (2001) R1.3.
11. T. Takeyama, S. Ohnuki and H. Takahashi, *Trans. Iron and Steel Inst. Japan* **21** (1981) 326.
12. N. Hashimoto, S.J. Zinkle, R.L. Klueh, A.F. Rowecliff, and K. Shiba, *Materials Research Society Symposium Proceedings Volume 650* (2001) R1.10.1.
13. P. Spatig, R. Schaublin and M. Victoria, *Materials Research Society Symposium Proceedings Volume 683E* (2001) BB1.10.1.
14. J. Marian, Ph. D. Thesis, Universidad Politécnica de Madrid (2002).

KINETIC MONTE CARLO SIMULATIONS OF THE EFFECTS OF 1-D DEFECT TRANSPORT ON DEFECT REACTION KINETICS AND VOID LATTICE FORMATION DURING IRRADIATION - H. L. Heinisch (Pacific Northwest National Laboratory)* and B. N. Singh (Risø National Laboratory, Denmark)

PURPOSE

The purpose of this computational study is to study the defect reaction kinetics of one-dimensionally migrating crowdion clusters as a function of the frequency of their direction changes, specifically to determine the sink strengths for such one-dimensionally migrating defects, as well as to demonstrate the significant role crowdion clusters may have in the formation and stability of void lattices.

SUMMARY

Within the last decade molecular dynamics simulations of displacement cascades have revealed that glissile clusters of self-interstitial crowdions are formed directly in cascades. Also, under various conditions, a crowdion cluster can change its Burgers vector and glide along a different close-packed direction. In order to incorporate the migration properties of crowdion clusters into analytical rate theory models, it is necessary to describe the reaction kinetics of defects that migrate one-dimensionally with occasional changes in their Burgers vector. To meet this requirement, atomic-scale kinetic Monte Carlo (KMC) simulations have been used to study the defect reaction kinetics of one-dimensionally migrating crowdion clusters as a function of the frequency of direction changes, specifically to determine the sink strengths for such one-dimensionally migrating defects. The KMC experiments are used to guide the development of analytical expressions for use in reaction rate theories and especially to test their validity. Excellent agreement is found between the results of KMC experiments and the analytical expressions derived for the transition from one-dimensional to three-dimensional reaction kinetics. Furthermore, KMC simulations have been performed to investigate the significant role of crowdion clusters in the formation and stability of void lattices. The necessity for both one-dimensional migration and Burgers vectors changes for achieving a stable void lattice is demonstrated.

PROGRESS AND STATUS

This is an extended abstract of a paper submitted for publication in Philosophical Magazine as part of the proceedings of the First International Conference on Multiscale Materials Modeling, Queen Mary University of London, June 17-20, 2002.

We have used KMC simulations to study the effects of Burgers vector direction changes on the reaction kinetics of crowdion clusters, making many simplifying assumptions in order to isolate the relationships among the variables of interest. In these KMC defect reaction kinetics "thought experiments," sink strengths are determined as a function of the average length, L, of the1-D path segments traversed by migrating crowdion clusters before they change their Burgers vector. The crowdion cluster does a 1-D random walk along a particular close-packed direction, then changes its Burgers vector and performs a random walk along a different close-packed direction. In this way it migrates in all three dimensions, but on a path made up of segments of 1-D walks. In our simulations we characterize such migration in terms of the average of the total lengths, minimum to maximum, of the paths traversed by the defect during n_{dc} hops in the absence of any defect interactions, where n_{dc} is the number of hops made between direction changes. Thus, in our simulations we define L as the average 1-D path length for defects that change direction regularly after every n_{dc} hops.

The usual test cell is a cube containing fcc lattice points with a volume of about $1\mu m^3$, assuming the lattice parameter of Cu. (The phenomena being investigated are not expected to differ qualitatively for fcc and bcc lattices.) The lattice points represent positions in the cell, and all defects, fixed or mobile, are

* Pacific Northwest National Laboratory (PNNL) is operated for the U.S. Department of Energy by Battelle Memorial Institute under contract DE-AC06-76RLO-1830.

"associated" with a lattice site, even defects that are not localized at a lattice point in the real material, such as SIA dumbbells and crowdions. In the KMC all mobile defects are assumed to migrate by hopping from their present lattice site to a nearest neighbor lattice site. Defects are the interacting entities in the model; individual atoms are not specifically dealt with.

Sink Strengths

Initial KMC studies of sink strength as a function of L were performed with 10^4 immobile spherical absorbers of capture radius R and number density N = 10^{22} m^{-3} randomly arranged on lattice sites within the volume. A mobile defect representing a crowdion cluster is introduced into the central volume of the cell at a random position and is followed until it is absorbed by an absorber. The mobile defect performs a 1-D random walk along a randomly chosen close-packed direction ([110] fcc), changing to another randomly chosen close-packed direction each time it has completed a fixed number of hops, n_{dc}. When the mobile defect comes within the capture radius R of an absorber, it is absorbed without changing the size or position of the absorber, and the defect lifetime *j*, the total number of hops before absorption, is recorded. Each simulation is performed for a set of 10^3 mobile defects. The sink strength k^2 is defined as the inverse of the square of the mean free path, and it is determined in the simulations for 1-D migrating defects in a field of spherical absorbers from the expression

$$k^2 = 2/a^2\langle j \rangle , \qquad (1)$$

where *a* is the hop distance along [110] and $\langle j \rangle$ is the average defect lifetime in hops for the set of migrating defects.

Sink strengths k^2 were determined for migrating defects in a field of spherical absorbers as a function of L. The individual data points in Figure 1 indicate the sink strengths determined in the simulations as a function of L for various values of R and N=10^{22} m^{-3}. Since N is constant, the volume fraction of absorbers decreases with decreasing R. The sink strengths for pure 3-D (L = *a*) are at the far left, and the sink strengths approach pure 1-D values on the right (large L). The region between 1-D and 3-D, and especially the region of transition to 3-D, are the most important to understand, because that is where the behavior in the real case is expected to lie. For each value of R the sink strengths remain almost constant at the "3-D value" until about L=R. Thus, the transition of sink strengths from 1-D to 3-D depends on R as well as L.

In conjunction with these KMC simulations, an analytical expression for sink strengths for 1-D migrating defects as a function of L interacting with spherical absorbers was developed by Trinkaus et al. (2002) strictly from theoretical considerations. It has the form

$$k_m^2 = 0.5\, k_1^2\{1 + [1 + 4/(L^2 k_1^2/4 + k_1^4/k_3^4)]^{1/2}\}, \qquad (2)$$

where the sink strengths k_1^2 and k_3^2 are for pure 1-D and pure 3-D defect migration, respectively, and they can be expressed analytically in terms of continuum models. However, to compare the analytical expression eq. 2 to the simulation results, it is necessary to account for the effects of discreteness of the crystal lattice. Hopping on a discrete lattice at the "3-D limit," n_{dc} = 1 (L=*a*), the defect makes random hops to nearest neighbor sites. The nature of the defect's migration path is still a series of 1-D segments, but the segments are only one hop in length in this limiting case. Thus, the values for k_3^2 used in eq. 2 were taken to be the sink strength values extracted from the simulations for L=*a*. The expression in eq. 2, modified for the discrete simulations, is used to plot the solid line curves in Figure 1. The agreement between the analytical expression and the simulation results is excellent.

Void Lattices

Simulations of void lattice formation were performed using the same basic KMC model, starting from a random array of small voids and introducing randomly positioned crowdion and vacancy clusters that

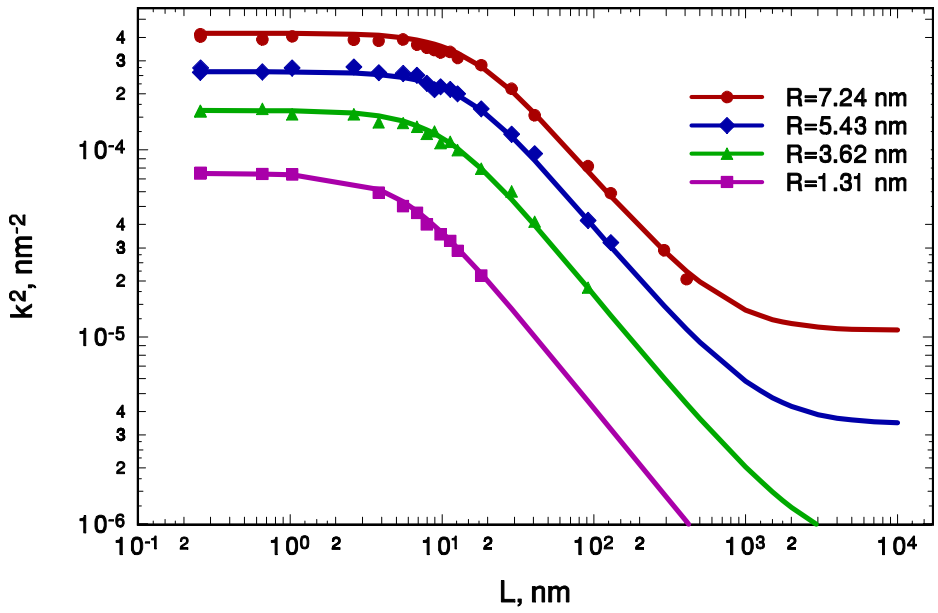

Figure 1. Sink strengths as a function of L, the average 1-D path length of 1-D/3-D migrating defects, for spherical absorbers of various radii. The points are results of the KMC simulations and the lines are calculated from Equation 2.

interact with the voids. Periodic boundaries are imposed, and the mobile defects interact only with the voids.

Many initial scenarios for void lattice formation from a set of randomly distributed voids were explored before success – quantifiable void ordering – was achieved. An initial minimum density of small, randomly-positioned voids seems to be a prerequisite for forming a void lattice. Starting with a low density of random large voids will lead to a void lattice only if the voids can be efficiently moved into position by collisions or destroyed and regrown, which are highly unlikely processes in such a situation where the shadow effect of already aligned voids is weak. The most likely scenario starts with a high enough concentration of small voids that there is a small void very near every position a lattice void will occupy. Then, by the shadow effect, the crowdion clusters will select the lattice, destroying the voids not in lattice positions and allowing the others to grow.

In radiation experiments void lattices are observed to form in small local regions of ordering which grow in extent with increasing dose. This implies that initial ordering takes place locally, perhaps as a result of the shadow effect caused by one significantly larger void (or perhaps two or more large voids correlated along a close-packed direction) occurring as a result of statistical fluctuations. To test this, simulations were performed in a fcc cell with a cube edge of 120 atomic lattice parameters, starting with a 1000 small voids and a "seed" consisting of 14 much larger voids arranged in a fcc super-lattice. Simulations were also done with the same initial conditions but with a seed consisting of a single large void in the center of the cell, and also with no seed. After irradiating with 6×10^5 crowdion clusters with $n_{dc} = 2 \times 10^4$ hops ($L \approx$ cell cube edge) and 5×10^5 vacancy clusters, very similar ordered lattices of voids were produced in all three cases, but with a void lattice parameter somewhat smaller than that of the 14 void seed. Figure 2 shows the initial configuration and the ordered configuration after irradiation in the simulation with no

seed. In the cells with seeds, the irradiation caused the seed voids to dissolve or move to fit the smaller void lattice parameter, and they became indistinguishable from the other lattice voids.

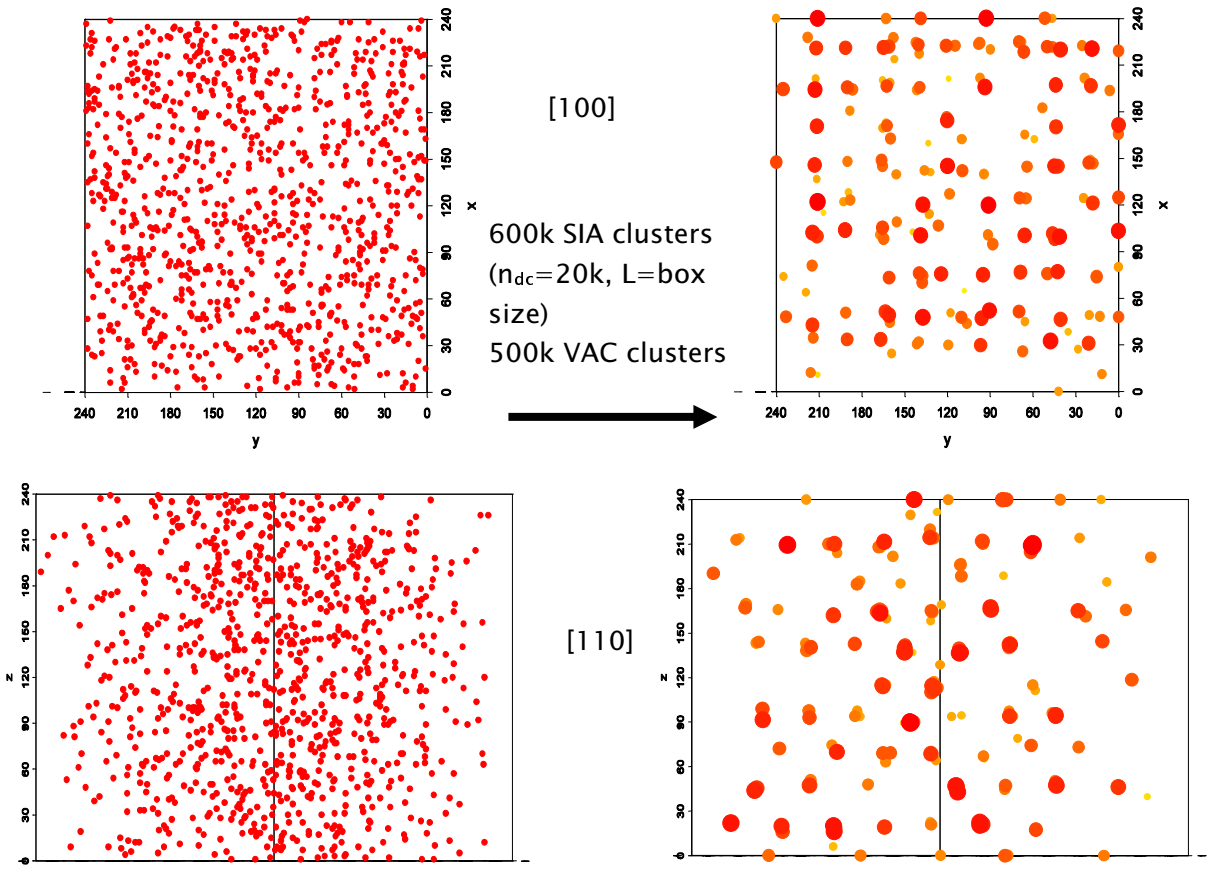

Figure 2. The initial (left) and final (right) configuration of voids after irradiation by 1-D migrating crowdion clusters having n_{dc} = 20 000 and vacancies migrating in 3-D. Initially the box contains 1000 small voids randomly distributed. The size and shading of circles in the final configuration reflects the relative sizes of the remaining voids. The top picture on each side shows a view along a [100] direction, and the bottom has views along a [110] direction.

Conclusions

KMC computer simulations applied to very specific, physically idealized defect migration situations are helping us understand the important role played by the crowdion clusters produced in displacement cascades in shaping the microstructure evolution of irradiated metals and alloys. By performing simulations that isolate the essential elements of their one-dimensional migration and Burgers vector changes and exploring them in terms of defect reaction kinetics, we have gained insight into how to incorporate their properties into the complex and comprehensive analytical rate theories of radiation-induced microstructures. In this way the KMC simulations have provided a direct link between the atomic-scale characterization of the properties of cascade-produced defects and their utilization in the global description of microstructure evolution.

By simulating the formation of void lattices in idealized KMC models, we have attempted to determine the microstructure conditions and cluster kinetics under which void lattices can form and to relate this

information to experimental measurements of the spacing of void lattices and the void size. In this way, void lattice experiments may provide a direct link, through the KMC modeling, for investigating characteristics of the primary defect production.

ACKNOWLEDGEMENTS

This work was supported by the Office of Fusion Energy Sciences of the U.S. Department of Energy and the European Fusion Programme.

FINDING POSSIBLE TRANSITION STATES OF DEFECTS IN SILICON-CARBIDE AND ALPHA-IRON USING THE DIMER METHOD – F. Gao, W. J. Weber and L. R. Corrales (Pacific Northwest National Laboratory)[*] G. Henkelman and H. Jónsson (University of Washington)

EXTENDED ABSTRACT

This is an extended abstract of a paper submitted for publication in the proceedings of the 6th COSIRES Conference, June 23-27, 2002, Dresden, Germany, to be published in Nucl. Inst. and Methods B.

The 'dimer' method was employed to search for possible transition states and their saddle point energies for interstitials and small interstitial clusters in SiC and α-Fe. The dimer method is a technique for finding saddle points in the potential energy surface within a solid, without knowledge of the final state of transition, and without the use of second derivatives of the potential, has been recently developed by Henkelman and Jónsson [1]. In addition to the calculation of activation energies of point defect and cluster migration along the <111> direction in α-Fe, the activation energies for the directional change of interstitial clusters is investigated.

The dimer method, described in detail elsewhere [1], involves two atomic images of the system, separated by a very small 3N-dimensional unit vector. The energy of this dimer and the force on the midpoint, as well as the curvature of the potential at the dimer, can be calculated from the forces acting on the two images. The net force on the dimer is minimized by rotation of the dimer, and the dimer is translated so as to move up the potential surface. Saddle points are located through a series of rotations and translations of the dimer. Upon finding a saddle point, the dimer is returned to the starting configuration, and it is randomly assigned a new orientation as a starting configuration for another saddle point search. In principle, all saddle points surrounding the initial configuration can be found. In practice, the same saddle point or symmetrically equivalent saddle points are often found, and occasionally no saddle points are located after a reasonable expenditure of computer time. Once the saddle point is found, the minimum energy path to the next energy basin can be determined, and the changes in atom positions during the transition can be followed.

Silicon Carbide

The transition states and mechanisms for migration of interstitials in SiC are studied in a cubic box of 125 unit cells consisting of 1000 atoms with periodic boundary conditions. The lowest energy configuration for the C interstitial, based on the potentials used here, is the C^{+}-C<100> dumbbell at a C site, with a formation energy of 3.04 eV. This minimum state is used as the initial configuration for the saddle point searches. The dimer run consisted of 800 randomly chosen initial dimer orientations about this minimum. In SiC, the potential migration pathways for the C interstitial are found to consist of the first neighbor jump via a Si site, having an activation energy of 0.81 eV, or second neighbor jumps from a C site directly to another C site with activation energies on the order of 1.5 eV. The results for SiC are somewhat difficult to interpret, because the dimer method finds multiple shallow saddle points along a single transition path. The interatomic potential used for SiC in these calculations was developed by Gao and Weber [2] based on the Brenner formalism [3]. Tersoff potentials lead to similar behavior. Perhaps better potentials for SiC need to be developed.

Interstitials in α-Fe

For interstitials and interstitial clusters in α-Fe, supercells containing from 2000 to 8192 atoms are employed to ensure that the effects of interactions of a cluster with its periodic images are negligible. For single interstitials the <110> dumbbell is used as an initial configuration for saddle point searches. Of 500 dimer searches, 425 converge to saddle points with an energy of 0.16 eV, which corresponds to the

[*] Pacific Northwest National Laboratory (PNNL) is operated for the U.S. Department of Energy by Battelle Memorial Institute under contract DE-AC06-76RLO-1830.

configuration change from a <110> dumbbell to a <111> crowdion. Fifteen searches converge to other saddle points, but they are not associated with the originally minimum configuration. Sixty searches fail to find saddle points within 500 iterations. Continuing searches starting from the final configuration of the previous run (i.e. <111> crowdion) result in two significant saddle points, one representing the directional change from the <111> crowdion to a <110> dumbbell and another one corresponding to an energy barrier for migration along the <111> direction. The energy path for a single interstitial is shown in Figure 1, where the relative coordination is used such that the distance from the <110> dumbbell to the final <111> configuration is one unit. It can be seen that the migration of a single interstitial consists of two mechanisms. One involves rotation from the stable <110> dumbbell to a metastable <111> crowdion with an energy of 0.163 eV, and the other is the migration of a crowdion along the <111> direction with the activation energy of 0.0022 eV. These mechanisms are similar to those observed in the MD simulations of defect diffusion [4,5].

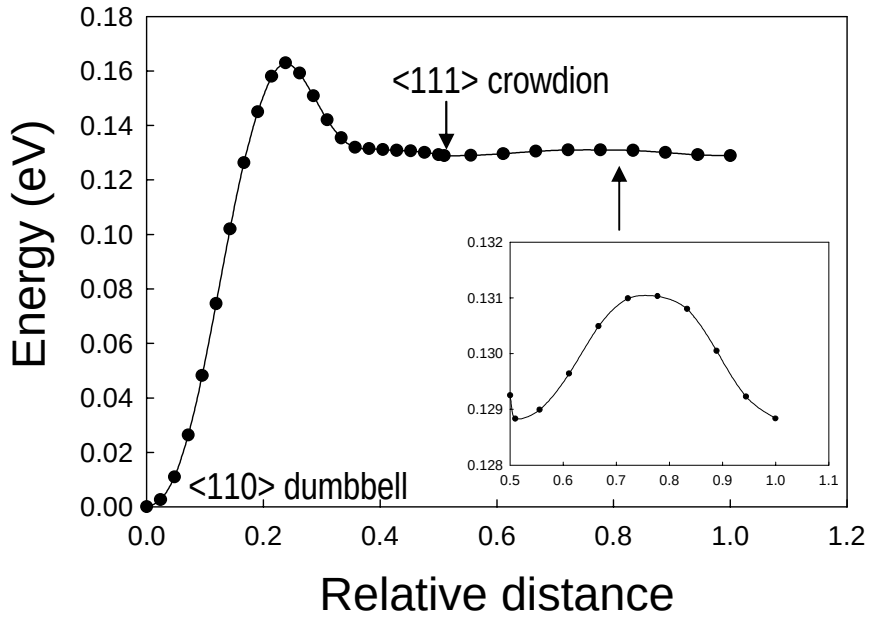

Figure 1. The minimum path traced out as the interstitial changes its direction from the initial <110> dumbbell to a <111> crowdion and migration along the <111> direction.

Interstitial Clusters in α-Fe

One of the important applications of the dimer method in this paper is to search for the transition states of interstitial clusters. Cluster sizes containing up to 10 SIAs are studied, and all initial states are set as compact <111> crowdion cluster configurations. The minimum paths associated with the saddle points, which relate to the migration along <111> direction and the directional change of clusters, have been traced out for interstitial clusters. It is found that the activation energies for migration along the <111> direction vary with cluster size and range from 0.0022 to 0.039 eV, in reasonable agreement with previous studies using MD simulations [6].

The minimum energy paths corresponding to saddle points for directional changes are shown in Figure 2, where the reaction coordinate is scaled so that the distance between two minima is unity. The paths that do not terminate back at zero energy correspond to configuration changes from a <110> dumbbell to a <111> crowdion for a single interstitial and from <111> crowdions to <110> dumbbells for di- and tri-interstitial clusters. The energy barriers for these processes, which represent the energy for directional

change, E_{dc}, from the <111> direction to another, are plotted in Figure 3, together with the binding energy per defect in a cluster for comparison. As shown, the energy for directional change is very high in comparison with the migration energy along <111> direction and generally increases with increasing cluster size. The value for E_{dc} is 0.163 eV, 0.133 eV and 0.342 eV for N=1, 2 and 3, respectively, which are smaller than the migration energy of a single vacancy (0.78 eV for the potential used). These clusters can easily change their direction by activation at room temperature. The energy of the directional change for a cluster of size 4 and 5 is about 1 eV, and these clusters may change their direction at high temperatures. When the cluster size is larger than 5, E_{dc} is in excess of 2 eV, so that the directional

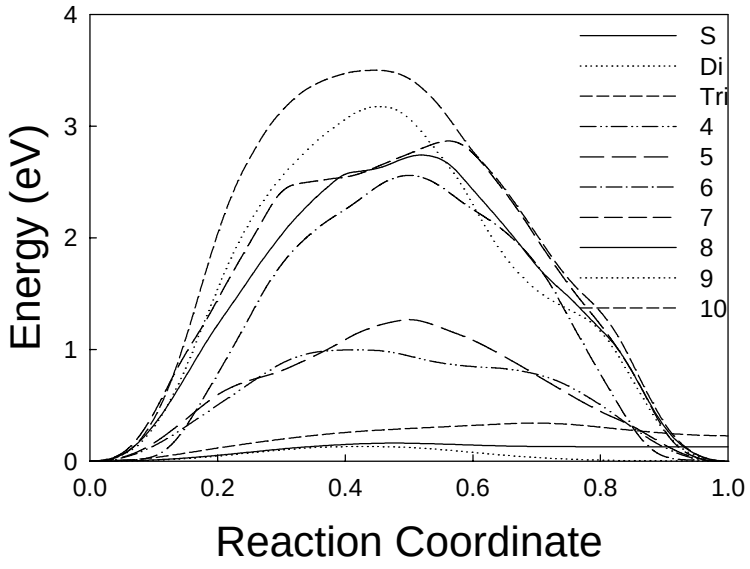

Figure 2. The minimum paths for the directional change for a cluster size up 10 SIAs, where the reaction coordinate has been scaled so that 0 represents the initial minimum and 1 indicates the final state.

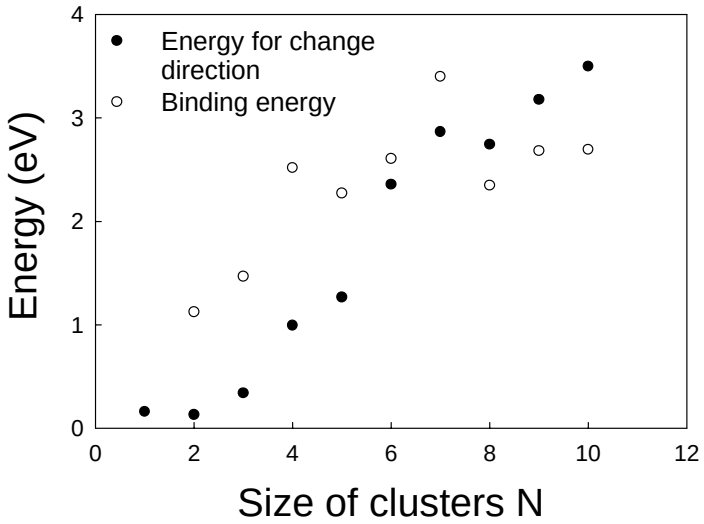

Figure 3. The energy barriers of the directional change for interstitial clusters in α-Fe, together with the binding energy per defect in a cluster for comparison.

change by thermally activated process becomes impossible, even at very high temperatures. It is interesting to note that the binding energy is larger than E_{dc} for cluster sizes up to seven, above which it is smaller than E_{dc}. This may suggest that any cluster size larger than seven may not change its direction before they dissociate into small clusters. Detailed analysis shows that single interstitial, di- and tri-interstitial clusters change their direction via <110> configurations. When the size of a cluster is larger than three, the situation becomes more complicated, and the mechanism for directional change is completely different from that for small clusters. It is found that the directional change for clusters larger than three is a two-step process, consisting of translation along the <100> direction and rotation into an equivalent <111> configuration [7].

ACKNOWLEDGMENTS

This research is supported by the U.S. Department of Energy Offices of Basic Energy Sciences and Fusion Energy Sciences under Contract DE-AC06-76RLO 1830.

REFERENCES

[1] G. Henkelman and H. Jónsson, J. Chem. Phys. 111 (1999) 7010.

[2] F. Gao and W. J. Weber, Nucl. Instr. and Meth. B, 191 (2002) 504.

[3] D. W. Brenner, Phys. Rev. B 42 (1990) 9458.

[4] F. Gao, D. J. Bacon, A. V. Barashev and H. L. Heinisch, Mat. Res. Soc. Symp. Proc. 540 (1999) 703.

[5] B. Wirth, G. R. Odette, D. Maroudas, G. E. Lucas, J. Nucl. Mater. 224 (1997) 185.

[6] Yu. N. Osetsky, D. J. Bacon, A. Derra, B. N. Singh, S. I. Golubov, J. Nucl. Mater. 276 (2000) 65.

[7] F. Gao, H. Heinisch, R. J. Kurtz, Yu. N. Osetsky, W. J. Weber and R. G. Hoagland, to be presented at the TMS Meeting, March 2-6, 2003, San Diego CA.

NUCLEATION AND GROWTH OF HELIUM-VACANCY CLUSTERS IN IRRADIATED METALS. PART. I. A GROUP METHOD FOR AN APPROXIMATE SOLUTION OF TWO DIMENSIONAL KINETIC EQUATIONS DESCRIBING EVOLUTION OF POINT DEFECT CLUSTERS. S. I. Golubov, R. E. Stoller, S. J. Zinkle (Oak Ridge National Laboratory)*.

OBJECTIVE

The objective of the study is to develop a new grouping method for an approximate solution of two dimensional kinetic equations describing gas-assisted vacancy cluster formation in irradiated materials.

SUMMARY

Nucleation, growth and coarsening of point-defect clusters or secondary phase precipitates are of interest for many applications in solid-state physics. As an example, clusters nucleate and grow from point defects in solids through irradiation. In typical nucleation, growth and coarsening problems, a master equation (ME) is constructed that summarizes the large number of ordinary differential equations (ODE) needed to describe the evolution process. To solve the large number of ODEs in the case when it is one dimensional, e.g. clustering of vacancies and self-interstitial atoms (SIAs) under irradiation in a form of voids or dislocation loops, a grouping method was originally proposed by Kiritani [1] in 1972. In 2001 Golubov et al. [2] have shown that Kiritani's method is not adequate and developed a new grouping method. The gas-assisted nucleation of voids or bubble formation is typical of problems that require solving two-dimensional ME, which has not been subjected to any specific grouping method of the type mentioned. This work intends to fill this gap. In the present work the grouping method proposed by Golubov et al. [2] is generalized for the case of the two-dimensional one. An application of the method to the problem of helium-assisted void/bubble formation under irradiation is presented.

PROGRESS AND STATUS

1. INTRODUCTION

Precipitation of helium introduced into metals by (n,α) reactions occurring in fission and fusion reactors can lead to essential changes of the structure materials. It has been established that helium atoms assist the nucleation and growth of cavities in irradiated materials leading to swelling and change their mechanical properties. The literature contains several partial treatments of the problem at hand [2-24]. However an accurate treatment of the problem is a complicated issue thus main part of work has been done in a semi quantitative way. An exception attempt to solve the problem quantitatively has been done by Ghoniem et al. (see e.g. [22]) by using a kind of grouping method for numerical solution of a kinetic equation (KE) in a form of Fokker-Planck equation. The method developed there for two-dimensional (2-D) kinetic equation is based essentially on the same approach as it has been done in the Kiritani's one [1] in a case of one-dimensional KE, namely the evolution of clusters grouped was treated in terms of an average cluster concentration in a group. However, as it has been shown [2] for the case of one-dimensional kinetic equation, such an approach does not allowed keeping identity of the group KEs with the original ones. The main point is that the approximation of the size distribution function (SDF) within a group is failed satisfying certain conservation laws, which follow for KE and are crucially important in the problem under consideration. In the framework of the Kiritani's method the group equations has been designed by an ad hoc procedure to satisfy the conservation laws, which results in distortion of the physical mechanisms operated in the original KE. It can be shown that in the framework of the method developed in [22] the group equations do not satisfy the conservation of the total numbers of vacancies and He atoms accumulated in the clusters.

As it is shown in [2] the simplest correct grouping method in the case of one-dimensional KE may be developed when size distribution function (SDF) within a group is approximated by a linear function. It may be shown that the same approach is also valid a case when the dimensionality of KE is 2-D or higher. A grouping method based on this approach is presented in the present work.

---

* The work has been done in collaboration with A.M. Ovcharenko and C.H. Woo (Department of Mechanical Engineering, The Hong Kong Polytechnic University, Hong Kong)

2. MASTER EQUATION

To describe the evolution of point defect clusters or secondary phase precipitates a kinetic equation in form of the continuity equation in a phase space of a certain dimensionality defined by the vector $\vec{x}$ is normally used

$$\frac{df(\vec{x},t)}{dt} + \nabla J(\vec{x},t) = 0 \tag{1}$$

where $f(\vec{x},t)$ and $J(\vec{x},t)$ are the number density of clusters of size $\vec{x}$ and flux of the clusters in $\vec{x}$-space at time t. The ME is normally considered in two approaches. One is based on an assumption that variable size is discreet, i.e. the vector components, x_i, are described by integer values. The second one is the so called Fokker-Planck (FPE) equation where the flux $J(\vec{x},t)$ is expanded into Taylor series and the variable $\vec{x}$ is treated as a continuous one (see e.g. [22]). Kinetic equation based on the first approach, which is normally referred as a master equation (ME), is more general compare to that of FPE. Moreover it also allows a more detail and flexible description for the reaction kinetics of the smallest clusters. For these reasons the ME will be considered as a basic one in the present work.

In a discreet space of cluster size the variables x and m are used describe a cluster of a certain composition in the case of 2-D ME. Thus in a case of He-void cluster the variable x and m are related to a number of vacancies and He atoms in a particular cluster, respectively. A specific form of ME depends on the mechanisms, which are responsible for evolution of the clusters under irradiation (or ageing). It is commonly accepted that in many cases it is well enough to assume that the cluster of size x,m can change its size only by absorption of monomers, e.g. vacancies, self-interstitial atoms (SIAs), impurities and so on. In the case the ME can be presented as follows

$$\frac{df(x,m,t)}{dt} = \left[J_x(x-1,m,t) - J_x(x,m,t)\right] + \left[J_m(x,m-1,t) - J_m(x,m,t)\right], \begin{cases} x \geq x_{\min} \\ m \geq m_{\min} \end{cases}, \tag{2}$$

where

$$\begin{aligned} J_x(x,m,t) &= P_x(x,t) f(x,m,t) - Q_x(x+1,m,t) f(x+1,m,t), \\ J_m(x,m,t) &= P_m(x,t) f(x,m,t) - Q_m(x,m+1,t) f(x,m+1,t), \end{aligned} \tag{3}$$

and the coefficients $P_x(x,t), Q_x(x,m,t), P_m(x,t), Q_m(x,m,t)$ are the rates of capture/evaporation reactions between the monomers and clusters leading to a change in the cluster size x and m, respectively, $x_{\min}, m_{\min}$ are minimal sizes of the clusters. For example in a case of secondary phase precipitates the values of $x_{\min}, m_{\min}$ may be taken to be equal $x_{\min} = m_{\min} = 0$ (accept the point of $x = m = 0$). In a case of gas-vacancy clusters the choice of the parameters $x_{\min}, m_{\min}$ is slightly different and will be discussed later.

The ME in a form of Eq. (2) is essentially a set of rate equations for clusters of each size in a size-range of practical interest. It was already pointed out (see e.g. [1]) that for practical purposes it is necessary to consider clusters containing a large number of point defects (or atoms) that makes difficulties for numerical solution even in the case 1-D kinetic equation. In the case of 2-D ME the situation is even more difficult since the total number of equations need to be solved are drastically increased compare to that of 1-D ME. Below it is shown that the grouping method developed in [2], which may be easily generalized for the case under consideration, allows solving the problem.

Note that a specific form of the coefficients $P_x(x,t), Q_x(x,m,t), P_m(x,t), Q_m(x,m,t)$ is depended on the problem of interest. An advantage of the method developed in [1] is that it may be formulated without fixing a specific form of the fluxes $J_x(x,m,t), J_m(x,m,t)$. This is the reason as to why in the following the grouping method mentioned is presented prior discussion of the mechanisms related to the gas assistant void nucleation problem. An application of the grouping method to the problem of evolution of He vacancy clusters will be presented next to illustrate use of the method.

3. BASIC EQUATIONS.

3.1. Conservation laws

Since the ME has a form of continuity equation it may be easy shown that the ME obeys certain conservation laws. As it has been shown in [2] two of them play crucial role in the case when a grouping method is used for numerical calculations. First is the conservation law for the total number of the clusters, *N(t)*. It follows from Eq. (2) that *N(t)*, which given by

$$N(t) = \sum_{x=x_{\min}}^{\infty} \sum_{m=m_{\min}}^{\infty} f(x,m,t), \tag{4}$$

is described by the following equation

$$\frac{dN(t)}{dt} = \sum_{m=m_{\min}}^{\infty} J_x(x_{\min}-1,m,t) + \sum_{x=x_{\min}}^{\infty} J_m(x,m_{\min}-1,t), \tag{5}$$

The second one is related to a conservation of the total number of monomers, *x* and *m*, accumulated in the clusters, $S(t),\ M(t)$, which are given by

$$S(t) = \sum_{x=x_{\min}}^{\infty} \sum_{m=m_{min}}^{\infty} xf(x,m,t), \quad M(t) = \sum_{x=x_{\min}}^{\infty} \sum_{m=m_{min}}^{\infty} mf(x,m,t). \tag{6}$$

Multiplying Eq. (2) on x (or *m*) and summing it over *x* and *m* one can find the following equations

$$\begin{aligned} \frac{dS(t)}{dt} &= \sum_{m=m_{\min}}^{\infty} \left\{ J_x(x_{\min}-1,m,t) + \sum_{x=x_{\min}-1}^{\infty} J_x(x,m,t) \right\} + \sum_{x=x_{\min}}^{\infty} xJ_m(x,m_{\min}-1,t), \\ \frac{dM(t)}{dt} &= \sum_{x=x_{\min}}^{\infty} \left\{ J_m(x,m_{\min}-1,t) + \sum_{x=x_{\min}-1}^{\infty} J_m(x,m,t) \right\} + \sum_{m=m_{\min}}^{\infty} mJ_x(x_{\min}-1,m,t). \end{aligned} \tag{7}$$

Eq. **(5)** shows that, in the framework cluster evolution described by the ME, $N(t)$ changes only due to the boundary fluxes, $J_x(x_{\min}-1,m,t),\ J_m(x,m_{\min}-1,t)$. In contrast to this the conservation laws described by Eqs. (7) depend on the fluxes $J_x(x,m,t), J_m(x,m,t)$ in whole phase space of sizes *x* and *m*. Because of this, as it has been shown in [2] for the case of 1-D ME, the simplest approximation for the SDF inside of a group when clusters grouped are treated in terms of an average cluster concentration in a group, cannot satisfy to both conservation laws simultaneously. The situation is the same in the case of 2-D ME. Thus one may conclude that in the case under consideration the simplest grouping method has to be based on a linear approximation of SDF inside a group in respect to both variables *x* and *m* and such a method is presented in this work.

3.2. Grouping of the clusters in x, m space

Let us introduce a description of the groups in the case under consideration. Follow to [1,2] the clusters are grouped within of a group of widths $\Delta x_i = x_i - x_{i-1},\ \Delta m_j = m_j - m_{j-1}$, which include the clusters of the sizes

$$\begin{aligned} x &= x_{i-1} + k,\ \left(k = 1,..,\Delta x_i\right), \\ m &= m_{j-1} + n,\ \left(n = 1,..,\Delta m_j\right), \end{aligned} \tag{8}$$

respectively, where the subscript i indicates the number of a group in $x-$space and the subscript j indicates the number of a group in $m-$space. Thus each group consists of $n_{i,j} = \Delta x_i \Delta m_j$ numbers of clusters of different sizes and is defined by the double index "*ij*". It can be shown that the mean sizes of clusters within an *ij* group, $< x >_i, < m >_j$, are equal to

$$< x >_i = x_i - \frac{1}{2}\left(\Delta x_i - 1\right),$$
$$< m >_j = m_j - \frac{1}{2}\left(\Delta m_j - 1\right), \tag{9}$$

respectively. Note that in a case when $\Delta x_i = 1$ or $\Delta m_j = 1$ $< x_i >= x_i$ and $< m >_j = m_j$, respectively.

3.3. The grouping method

Follow [2] let us approximate the SDF, $f(x,m,t)$, by a linear function within a group i, j of the type

$$f_{i,j}(x,m) = L_0^{i,j} + L_{1x}^{i,j}(x - < x >_i) + L_{1m}^{i,j}(m - < m >_j). \tag{10}$$

The total number clusters in the i, j group, $N_{i,j}$, and total number of vacancies and gas atoms accumulated in the clusters, $S_{i,j}, M_{i,j}$ are given by

$$N_{i,j} = \sum_{k=1}^{\Delta x_i}\sum_{n=1}^{\Delta m_j} f(x_{i-1}+k, m_{j-1}+n),$$
$$S_{i,j} = \sum_{k=1}^{\Delta x_i}\sum_{n=1}^{\Delta m_j}\left(x_{i-1}+k\right) f(x_{i-1}+k, m_{j-1}+n), \tag{11}$$
$$M_{i,j} = \sum_{k=1}^{\Delta x_i}\sum_{n=1}^{\Delta m_j}\left(m_{j-1}+n\right) f(x_{i-1}+k, m_{j-1}+n).$$

Summing the ME (2) over *x* and *m* within the *ij*[th] group one may find that

$$\frac{dN_{i,j}}{dt} = \sum_{n=1}^{\Delta m_j}\left[J_x(x_{i-1}, m_{j-1}+n) - J_x(x_i, m_{j-1}+n)\right] + \\ + \sum_{k=1}^{\Delta x_i}\left[J_m(x_{i-1}+k, m_{j-1}) - J_m(x_{i-1}+k, m_j)\right]. \tag{12}$$

On the other side multiplying the Eq. **(2)** on x (or *m*) and summing it over *x* and *m* within the group one may find

$$\frac{dS_{i,j}}{dt} = \sum_{n=1}^{\Delta m_j}\left[\left(x_{i-1}+1\right)J_x(x_{i-1}, m_{j-1}+n) - x_i J_x(x_i, m_{j-1}+n) + \sum_{k=1}^{\Delta x_i - 1} J_x(x_{i-1}+k, m_{j-1}+n)\right] + \\ + \sum_{k=1}^{\Delta x_i}\left(x_{i-1}+k\right)\left[J_m(x_{i-1}+k, m_{j-1}) - J_m(x_{i-1}+k, m_j)\right], \tag{13}$$

$$\frac{dM_{i,j}}{dt} = \sum_{k=1}^{\Delta x_i}\left[\left(m_{j-1}+1\right)J_m(x_{i-1}+k, m_{j-1}) - m_j J_m(x_i+k, m_j) + \sum_{n=1}^{\Delta m_j - 1} J_m(x_{i-1}+k, m_{j-1}+n)\right] + \\ + \sum_{n=1}^{\Delta m_j}\left(m_{j-1}+n\right)\left(J_x(x_{i-1}, m_{j-1}+n) - J_x(x_i, m_{j-1}+n)\right), \tag{14}$$

Substituting Eq. (10) into Eq. (11) one can obtain

$$
\begin{aligned}
N_{i,j} &= L_0^{i,j}\Delta x_i \Delta m_j, \\
S_{i,j} &= \left(L_0^{i,j} < x >_i + L_{1x}^{i,j}\sigma_i^2\right)\Delta x_i \Delta m_j, \\
M_{i,j} &= \left(L_0^{i,j} < m >_j + L_{1m}^{i,j}\sigma_j^2\right)\Delta x_i \Delta m_j,
\end{aligned}
\tag{15}
$$

where σ_i^2, σ_j^2 are dispersions of cluster sizes in the group, which are given by

$$
\begin{aligned}
\sigma_i^2 &= \frac{1}{\Delta x_i}\left[\sum_{\alpha=x_{i-1}+1}^{x_i}\alpha^2 - \frac{1}{\Delta x_i}\left(\sum_{\alpha=x_{i-1}+1}^{x_i}\alpha\right)^2\right], \\
\sigma_j^2 &= \frac{1}{\Delta m_j}\left[\sum_{\alpha=m_{j-1}+1}^{m_j}\alpha^2 - \frac{1}{\Delta m_j}\left(\sum_{\alpha=m_{j-1}+1}^{m_j}\alpha\right)^2\right].
\end{aligned}
\tag{16}
$$

It is followed from Eqs. **(15)** that the coefficients $L_0^{i,j}, L_{1x}^{i,j}, L_{1m}^{i,j}$ may be expressed through the moments $N_{i,j}, S_{i,j}, M_{i,j}$ as follows

$$
\begin{aligned}
L_0^{i,j} &= \frac{1}{\Delta x_i \Delta m_j} N_{i,j}, \\
L_{1x}^{i,j} &= \frac{1}{\Delta x_i \Delta m_j \sigma_i^2}\left(S_{i,j} - N_{i,j} < x >_i\right), \\
L_{1m}^{i,j} &= \frac{1}{\Delta x_i \Delta m_j \sigma_j^2}\left(M_{i,j} - N_{i,j} < m >_j\right).
\end{aligned}
\tag{17}
$$

Differentiating Eqs. (15) over time and using Eqs. (12), (14) and (15) one can find the following equations for the coefficients $L_0^{i,j}, L_{1x}^{i,j}, L_{1m}^{i,j}$ may be written in the following form

$$
\begin{aligned}
\frac{dL_0^{i,j}}{dt} = \frac{1}{\Delta x_i \Delta m_j}\Bigg\{&\sum_{n=1}^{\Delta m_j}\Big[J_x(x_{i-1}, m_{j-1}+n) - J_x(x_i, m_{j-1}+n)\Big] + \\
&\sum_{k=1}^{\Delta x_i}\Big[J_m(x_{i-1}+k, m_{j-1}) - J_m(x_{i-1}+k, m_j)\Big]\Bigg\},
\end{aligned}
\tag{18}
$$

$$
\begin{aligned}
\frac{dL_{1x}^{i,j}}{dt} = -\frac{(\Delta x_i - 1)}{2\Delta x_i \Delta m_j \sigma_i^2}\Bigg\{&\sum_{n=1}^{\Delta m_j}\Big[J_x(x_{i-1}, m_{j-1}+n) + J_x(x_i, m_{j-1}+n) - 2 < J_x >_{i,n(j)}^*\Big] \\
+\frac{1}{\Delta x_i - 1}&\sum_{k=1}^{\Delta x_i}\Big[\big(\Delta x_i + 1 - 2k\big)\big(J_m(x_{i-1}+k, m_{j-1}) - J_m(x_{i-1}+k, m_j)\big)\Big]\Bigg\},
\end{aligned}
\tag{19}
$$

$$\frac{dL_{1m}^{i,j}}{dt}=-\frac{\left(\Delta m_j-1\right)}{2\Delta x_i\Delta m_j\sigma_i^2}\left\{\sum_{k=1}^{\Delta x_i}\left[J_m(x_{i-1}+k,m_{j-1})+J_m(x_{i-1}+k,m_j)-2<J_m>_{i(k),j}^{*}\right]\right.$$
$$\left.+\frac{1}{\Delta m_j-1}\sum_{n=1}^{\Delta m_j}\left[\left(\Delta m_j+1-2n\right)\left(J_x(x_{i-1},m_{j-1}+n)-J_x(x_i,m_j+n)\right)\right]\right\}, \tag{20}$$

where $<J_x>_{i,n(j)}^{*}$ and $<J_m>_{i(k),j}^{*}$ are the mean J_x flux inside ij^{th} group at a given size of m ($m=m_{j-1}+n$) and the mean J_m flux inside ij^{th} group at a given size of x ($x=x_{i-1}+k$), respectively, which are given by

$$<J_x>_{i,n(j)}^{*}=\frac{1}{\left(\Delta x_i-1\right)}\sum_{k=1}^{\Delta x_i-1}J_x(x_{i-1}+k,m_{j-1}+n),\quad \Delta x_i>1, \tag{21}$$

$$<J_m>_{i(k),j}^{*}=\frac{1}{\left(\Delta m_j-1\right)}\sum_{n=1}^{\Delta m_j-1}J_m(x_{i-1}+k,m_{j-1}+n),\quad \Delta m_j>1. \tag{22}$$

Eqs. (18) - (20) describe the evolution of the SDF within the group approximation. Thus instead of solving $n_{ij}=\Delta x_i\Delta m_j$ numbers of MEs for the group it is necessary to solve the three equations only. On the other side in the limiting cases when $\Delta x_i=1$ or $\Delta m_j=1$ the right hand sides of Eqs. (19) or (20) become equal to zero that results in $L_{1x}^{i,j}=0$ or $L_{1m}^{i,j}=0$. In the case when both widths are equal to unit, i.e. $\Delta x_i=\Delta m_j=1$, both coefficients $L_{1x}^{i,j}$, $L_{1m}^{i,j}$ are equal to zero whereas Eq. (18) transforms to Eq. (2), that is $f(x_i,m_j)=L_0^{i,j}$. This property of the group equations is important allowing to calculate SDF using arbitrary group widths, $\Delta x_i,\Delta m_j$, including the limiting cases when $\Delta x_i=1$ or $\Delta m_j=1$.

Note that the group equations described by Eqs. (18) - (20) still require time consuming numerical calculations due to the summation on the right hand sides of the equations. However the equation may be simplified because the summations can be done analytically if to take an approximation that all capture/evaporation efficiencies, namely $P_x(x,m),Q_x(x,m),P_m(x,m),Q_m(x,m)$, are equal within a group (similar approximation was used in the original Kiritani's method [1]). Using this approximation and taking into account that SDF within a group linear depends on x and m (see Eq. (10)) one can find that Eqs. (18) - (20) may be finally presented in the following form

$$\frac{dL_0^{i,j}}{dt}=\frac{1}{\Delta x_i}\left[J_x(x_{i-1},<m>_j)-J_x(x_i,<m>_j)\right]+\frac{1}{\Delta m_j}\left[J_m(<x>_i,m_{j-1})-J_m(<x>_i,m_j)\right]. \tag{23}$$

$$\frac{dL_{1x}^{i,j}}{dt}=-\left(\frac{\Delta x_i-1}{2\sigma_i^2\Delta x_i}\right)\left\{\ J_x(x_{i-1},<m>_j)+J_x(x_i,<m>_j)-2J_x(<x_i>-\frac{1}{2},<m>_j)\ \right\}$$
$$+\frac{1}{\Delta m_j}\left\{\ \left[J_m(<x>_i+1,m_{j-1})-J_m(<x>_i,m_{j-1})\right]-\left[J_m(<x>_i+1,m_j)-J_m(<x>_i,m_j)\right]\ \right\}. \tag{24}$$

$$\frac{dL_{1m}^{i,j}}{dt} = -\left(\frac{\Delta m_j - 1}{2\sigma_j^2 \Delta m_j}\right)\left\{ J_m(< x >_i, m_{j-1}) + J_m(< x >_i, m_j) - 2J_m(< x >_i, < m >_j - \frac{1}{2}) \right\}$$
$$+\frac{1}{\Delta x_i}\left\{ \left[J_x(x_{i-1}, < m >_j + 1) - J_x(x_{i-1}, < m >_j)\right] - \left[J_x(x_i, < m >_j + 1) - J_x(x_i, < m >_j)\right] \right\}. \quad (25)$$

Eqs. (23) - (25) describe the evolution of the SDF within the group approximation. Note that last two equations are highly symmetrical, e.g. one may obtain Eq. (25) from Eq. (24) by using a simple permutation of fluxes J_x , J_m with corresponding change of the variables x to m and m to x and the multiplier $\frac{\Delta x_i - 1}{2\sigma_i^2 \Delta x_i}$ to $\frac{\Delta m_j - 1}{2\sigma_j^2 \Delta m_j}$.

3.4. The grouping method in the cases of 1-D and 3-D ME

In the case of 1-D ME, i.e. when $f(x,m) = f(x)$, Eqs. (23) - (25) are transformed to the equations (37) and (38) derived in [2] for the case of 1-D ME. Actually in this case the flux J_m and coefficient $L_{1m}^{i,j}$ are equal to zero, $J_m = 0$, $L_{1m}^{i,j} = 0$, that transforms Eqs. (23), (24) in

$$\frac{dL_0^{i,j}}{dt} = \frac{1}{\Delta x_i}\left[J_x(x_{i-1}) - J_x(x_i)\right],$$
$$\frac{dL_{1x}^{i,j}}{dt} = -\left(\frac{\Delta x_i - 1}{2\sigma_i^2 \Delta x_i}\right)\left\{ J_x(x_{i-1}) + J_x(x_i) - 2J_x(< x_i > - \frac{1}{2}) \right\}. \quad (26)$$

It is easy to show that Eqs. (26) coincide with the equations (37) and (38) in [2] taking into account that the mean flux $< J >_i^*$ in [2] (see Eq. (38)) is equal to $J_x(< x_i > - \frac{1}{2})$ in the case when the capture/evaporation efficiencies, namely $P_x(x,m)/Q_x(x,m)$, are taken to be equal within a group. Note, as it already has been pointed out in [25], the multiplier $-1/\Delta x_i$ in the right hand side of Eq. (38) in [2] was lost**.**

On the other side it is worthy to emphasize that the symmetry of Eqs. (23) - (25) allows one easily to generalized the grouping method on a case when dimensionality of the ME is higher than two. For example in the case of 3-D ME, i.e. when the SDF depends on three variable ($f(x,m,n)$) the approximation of SDF within a group (see Eq. (10)) is given by

$$f_{i,j,k}(x,m) = L_0^{i,j,k} + L_{1x}^{i,j,k}(x - < x >_i) + L_{1m}^{i,j,k}(m - < m >_j) + L_{1n}^{i,j,k}(n - < n >_k). \quad (27)$$

In the case one can easily find that Eq. (23) takes a form

$$\frac{dL_0^{i,j,k}}{dt} = \frac{1}{\Delta x_i}\left[J_x(x_{i-1}, < m >_j, < n >_k) - J_x(x_i, < m >_j, < n >_k)\right]$$
$$+\frac{1}{\Delta m_j}\left[J_m(< x >_i, m_{j-1}, < n >_k) - J_m(< x >_i, m_j, < n >_k)\right] \quad (28)$$
$$+\frac{1}{\Delta n_k}\left[J_n(< x >_i, < m >_j, n_{k-1}) - J_n(< x >_i, < m >_j, n_k)\right].$$

where $J_l(x,m,n)$ is the flux of the clusters in l direction ($l = x, m, n$). The same way one can generalize Eqs. (24) and (25). For example one can find that Eq. (24) takes a form

$$\frac{dL_{1x}^{i,j,k}}{dt} = -\left(\frac{\Delta x_i - 1}{2\sigma_i^2 \Delta x_i}\right)\left\{\begin{array}{l} J_x(x_{i-1}, < m >_j, < n >_k) + J_x(x_i, < m >_j, < n >_k) \\ -2J_x(< x_i > -\frac{1}{2}, < m >_j, < n >_k) \end{array}\right\}$$

$$+\frac{1}{\Delta m_j}\left\{\begin{array}{l} \left[J_m(< x >_i + 1, m_{j-1}, < n >_k) - J_m(< x >_i, m_{j-1}, < n >_k)\right] \\ -\left[J_m(< x >_i + 1, m_j, < n >_k) - J_m(< x >_i, m_j, < n >_k)\right] \end{array}\right\} \qquad (29)$$

$$+\frac{1}{\Delta n_k}\left\{\begin{array}{l} \left[J_n(< x >_i + 1, < m >_j, n_{k-1}) - J_n(< x >_i, < m >_j, n_{k-1})\right] - \\ \left[J_n(< x >_i + 1, < m >_j, n_k) - J_n(< x >_i, < m >_j, n_k)\right] \end{array}\right\}.$$

The equations for the coefficients $L_{1m}^{i,j}$, $L_{1n}^{i,j}$ can be easily obtained from Eq. (29) by permutation of fluxes J_x, J_m, J_n with corresponding change of the variables *x, m* and *n* and the multiplier $\frac{\Delta x_i - 1}{2\sigma_i^2 \Delta x_i}$ to $\frac{\Delta m_j - 1}{2\sigma_j^2 \Delta m_j}$ or $\frac{\Delta n_k - 1}{2\sigma_k^2 \Delta n_k}$, respectively, on the right hand side of the equation. The grouping equations in the case when dimensionality of the ME is higher than three may be obtained by the same way.

4. MODEL DESCRIPTION

In order to use the grouping method one need to set up a model of interest. As can be seen from the ME and Eqs. (23) - (25) a model is fully determined by a choice of the fluxes $J_x(x,m,t), J_m(x,m,t)$. In this paper He-assisted vacancy clustering in irradiated metals is considered only. For the sake of simplicity in the following the process is considered taking into account single mechanism of He transport only, namely via migration of He atoms in a form of the interstitials.

4.1. Flux $J_x(x,m,t)$

In the first Eq. **(3)** $P_x(x,t)$ and $Q_x(x,m,t)$ are the rate of a vacancy absorption and the sum of corresponding rates of SIAs absorption (in the case of irradiation) and vacancy emission from the clusters of size x containing *m* He atoms. In the following the SIAs are considered having two configurations, namely the dumbbell configuration, which is 3-D diffusing defect, and crowdion configuration, which is 1-D diffusing defect. Last configuration is chosen to represent the SIA clusters, which are normally generated in irradiated metals under cascade damage conditions. Such a simplification is taken due two reasons: (a) the 1-D reaction kinetics is not very sensitive to the size of the SIA clusters, (b) in the case of crowdions the ME still keeps the form of Eq. (2). In the case when concentrations of 3-D diffusing point defects, $C_v(t), C_i(t)$, and 1-D diffusing crowdions, $C_g(t)$, are measured in atomic fractions the rates $P_x(x,t)$ and $Q_x(x,m,t)$ may be written as follows [26]

$$P_x(x) = wx^{1/3} D_v C_v(t),$$

$$Q_x(x,m) = wx^{1/3}\left[D_i C_i + D_v \exp\left(-E_v^b(x,m)/kT\right)\right] + Q_x^g(x,t) = Q_x^i(x,m) + Q_x^v(x,m) + Q_x^g(x,t), \qquad (30)$$

$$Q_g(x,t) = 2\Lambda D_g C_g \left(\frac{3\sqrt{\pi}\Omega}{4}\right)^{2/3} x^{2/3}, \quad \Lambda = \sqrt{\frac{k_g^2}{2}},$$

where $w=\left(48\pi^2/\Omega^2\right)^{1/3}$ (Ω is the atomic volume), D_v, D_i and D_g are the diffusion coefficients of 3-D diffusing vacancies and SIAs and 1-D diffusing crowdions, respectively; $E_v^b(x,m)$ is a binding energy of vacancy with a cluster of size *x* containing m gas atoms, k_B is the Boltzmann constant, T is absolute temperature. The value k_g^2 in the last equation is the total sink strength for the crowdions, which is given by [26]

$$k_g^2 = 2\left(\frac{\pi\rho d_{abs}}{4}+\sqrt{\frac{2}{l(2R_g-l)}}+\sigma_v N_v+\sigma_{vc}N_{vc}+\sigma_{ic}N_{ic}\right)^2, \tag{31}$$

where $\sigma_v=\pi R_v^2$, R_v and N_v are the void radius and density, d_{abs} is the capture diameter of dislocations for the absorption of the SIA clusters, σ_{vc},σ_{ic} and N_{vc},N_{ic} are the mean cross-sections of the sessile vacancy and SIA clusters and number densities of these clusters, respectively; R_g, l are the grain radius and distance from the grain boundary, respectively. The cross section of voids, $\sigma_v N_v$, can be easy calculated using SDF

$$\sigma_v N_v=\sum_{x=2}^{\infty}\sum_{m=0}^{\infty}Q_g(x,t)f(x,m,t)+Q_g(1,t)\sum_{m=1}^{m_0}f(1,m,t). \tag{32}$$

Binding energy

The binding energy of vacancies with the clusters, $E_v^b(x,m)$, is a key "parameter" controlling nucleation of the clusters. Assuming that that the volume of a cluster, *V*, does not depend on the parameter *m*, i.e. it obeys the equation $V=x\Omega$ (Ω is atomic volume), and taking into account that the pressure produced by *m* He atoms in a spherical cluster containing *x* vacancies, $p(x,m)$, may be presented as $p(x,m)=\left(k_BT/\Omega\right)\left(m/x\right)Z(m/x,T)$, where $Z(T,m/x)$ is so called compressibility factor, one can find that the $E_v^b(x,m)$ may be written as

$$E_v^b(x,m)=E_v^f-\frac{\alpha}{x^{1/3}}+\left(\frac{m}{x}\right)Z\left(\frac{m}{x},T\right)k_BT, \tag{33}$$

where E_v^f is the vacancy formation energy, $\alpha=2\gamma\left(4\pi\Omega^2/3\right)^{1/3}$ and γ is the free surface energy. The function $Z(T,m/x)$ depends on an approach used to calculate the equation of state (EOS) of He. Several approximations to the EOS have been proposed so far. In the following two equations of state are tested. The first one is so called hard sphere EOS [27], which results in the function $Z_{hs}(m/x,T)$ given by

$$\begin{aligned} Z(T,m/x)_{hs}&=\frac{\left(1+y+y^2-y^3\right)}{\left(1-y\right)^3},\\ y&=\left(\frac{\pi d^3}{6\Omega}\right)\frac{m}{x}, \end{aligned} \tag{34}$$

where *d* is the hard sphere diameter of He atom . The diameter *d* is a temperature dependent function, which is given by $d=0.3135\bullet\left[0.8542\text{-}0.03996\bullet\ln(\mathrm{T}/9.16)\right]$ nm.

The second EOS was derived by Manzke et al [28] by using Beck's potential and interpolation between a quasi-harmonic approximation with anharmonic corrections for solid fcc He, which results in the function $Z_m(m/x,T)$,

which after a simplification (combining the first and last terms in Eq. (3) in [28] and taking into account that the multiplier $Z_m^{'}V_m$ in the last one is equal to $Z_m^{'}V_m$ =-50) can be presented as

$$Z_m(T,m/x)=\left(1-\rho\right)\left(1+\rho-52\rho^2\right)+\frac{b}{V_m}\rho\left(1-\rho\right)^2+Z_m\rho^2\left(3-2\rho\right), \tag{35}$$

where

$$\begin{aligned}
&\rho=\left(\frac{V_m}{\Omega}\right)\frac{m}{x},\\
&V_m=56\mathrm{T}^{-1/4}\exp(-0.145\ \mathrm{T}^{1/4}),\\
&Z_m=0.1225\ V_m\mathrm{T}^{\ 0.555},\\
&b=170\mathrm{T}^{-1/3}\ -1750\mathrm{T}^{-1}.
\end{aligned} \tag{36}$$

In Eqs. (36) V_m is the He atomic volume of the melt measured in cubic angstroms. Note that Eqs. (36) are written here assuming that the volume of the cluster containing *x* vacancies, *V*, is equal to $V=x\Omega$.

4.2. Flux $J_m(x,m,t)$

In the second Eq. (3) $P_m\left(x,m,t\right)$ is the rate of a He atom absorption by a cluster of size x and $Q_m\left(x,m,t\right)$ is a rate of resolution of He atoms from the clusters of size x containing *m* He atoms. The rate $P_m\left(x,m,t\right)$ may be calculated the same way as used for point defects whereas an equation for the rate $Q_m\left(x,m,t\right)$ depend on a mechanism responsible for resolution of He atoms form the clusters. In a case of so called radiation resolution mechanism (see e.g. [6]) the rate $Q_m\left(x,m,t\right)$ is linear dependent on the number of He atoms in a cluster. Taking into account the radiation resolution mechanism only $P_m\left(x,m,t\right)$ and $Q_m\left(x,m,t\right)$ may be written as

$$\begin{aligned}
P_m(x)&=wx^{1/3}D_{He}C_{He},\\
Q_m(x,m)&=Am,
\end{aligned} \tag{37}$$

where $C_{He}(t)$ and D_{He} are the concentration and diffusion coefficient of He atoms in the interstitial position and *A* is a parameter characterizing intensity of the radiation resolution mechanism.

Equations (30) - (37) fully determine the model under consideration. All capture/evaporation rates need to be used to calculate the fluxes $J_x(x,m,t),J_m(x,m,t)$ can be calculated using these equations together with the equations for the concentrations of the mobile defects, which are presented in the next section.

4.3. Equations for the concentrations of mobile defects

As it has been already shown in [26] the rate equations for point defect concentrations of mobile defects, $C_v(t),C_i(t),C_g(t)$, are given by

$$\begin{aligned}
\frac{dC_v}{dt}=&\left\{G_v+Q_m(1)f(1,1,t)+Q_x(2,0)f(2,0,t)+\sum_{x=2}^{\infty}\sum_{m=0}^{\infty}Q_x^v(x+1,m)f(x+1,m,t)+D_vC_{v0}Z_v\rho_d\right\}\\
&-\left[\mu_RD_iC_iC_v+\mu_R^{He}D_{He}C_{He}C_v+D_vC_vZ_v\rho_d+P_x(1)f(1,0,t)+\sum_{x=1}^{\infty}\sum_{m=0}^{\infty}P_x(x)f(x,m,t)\right],
\end{aligned} \tag{38}$$

$$\frac{dC_i}{dt} = G_i - \mu_R D_i C_i C_v - D_i C_i Z_i \rho_d - \sum_{x=2}^{\infty} \sum_{m=0}^{m_{\max}} Q_x^i(x) f(x,m,t) - Q_x^i(1) \sum_{m=1}^{m=m_0} f(1,m). \tag{39}$$

$$\frac{dC_g(t)}{dt} = G_g(t) - D_g C_g(t) k_g^2(t), \tag{40}$$

where G_v, G_i, G_g are the generation rates of vacancies, SIAs (in dumbbell and crowdion configurations) and He atoms, respectively, μ_R is the coefficients describing reactions between SIA and vacancy, Z_v, Z_i are the capture efficiencies of dislocations for vacancies and SIAs, respectively, ρ is the dislocation density, C_{v0} is the thermal equilibrium vacancy concentration, m_0 is the maximum number of He atoms in the clusters of the smallest size, $f(1,m)$. The generation rates vacancies and SIAs are given by

$$\begin{aligned} G_v &= G_{NRT}(1-\varepsilon_r), \\ G_i &= G_{NRT}(1-\varepsilon_r)(1-\varepsilon_i^g), \\ G_g &= G_{NRT}(1-\varepsilon_r)\varepsilon_i^g, \end{aligned} \tag{41}$$

where G_{NRT} is the generation rate calculated using NRT model, ε_r is a fraction of point defects recombined during cooling phase of cascades, ε_i^g is a fraction SIAs generated in a the form of crowdions. Note that vacancy clustering in a form of dislocation loops or stacking fault tetrahedra, which also takes place during cooling phase of cascades, is not considered in this work.

Equation for the concentration of He atoms in the interstitial position may be written in the same manner

$$\begin{aligned} \frac{dC_{He}}{dt} &= \left\{ G_{He} + \sum_{x=2}^{\infty} \sum_{m=1}^{m_{\max}} Q_m(m) f(x,m,t) + \sum_{m=1}^{m=m_0} \left[Q_m(m) + m Q_x^i(1) \right] f(1,m) \right\} \\ &- \left[\mu_R D_{He} C_v C_{He} + D_{He} C_{He} Z_{He} \rho_d + \sum_{x=2}^{\infty} \sum_{m=0}^{m_{\max}-1} P_m(x) f(x,m,t) + P_m(1) \sum_{m=1}^{m=m_0-1} f(1,m) \right], \end{aligned} \tag{42}$$

where G_{He} is the generation rate of He atoms, μ_R^{He} is the coefficients describing reaction between He atom and vacancy, Z_{He} is the capture efficiencies of dislocations for He atoms.

The terms in the figure brackets on the right hand side of Eqs. (38) and (42) describe the generation of vacancies and interstitial He atoms via irradiation and due to reactions of the smallest clusters with the mobile defects. Note that the capture/evaporation terms on the right hand side Eq. (42) for the clusters of the smallest size are written separately to show explicitly limitation in increase of number of He atoms in the clusters (see last term in the square brackets) and the replacement reaction caused by interaction o the clusters with SIAs (see last term in the figure brackets).

4.4. Initial and boundary conditions

The initial conditions for the mobile defects and boundary conditions for the SDF are taken to have the following form

$$\begin{aligned} &C_v(t)_{|t=0} = C_{v0}, \quad C_i(t=0)_{|t=0} = C_g(t=0)_{|t=0} = C_{He}(t)_{|t=0} 0, \\ &f(x,m,t)_{|t=0} = C_{v0}\delta(x-1)\delta(m) + C_{He}^{\mathrm{Im}}\delta(x-1)\delta(m-1), \quad (x \geq 1), \\ &f(x=1,0,t) = C_v(t), \quad f(x=\infty,m,t) = 0, \end{aligned} \tag{43}$$

where C_{He}^{Im} is the concentration of He pre implanted in a metal before irradiation. Thus in the following it is assumed that all pre implanted He atoms take the substitution configuration, i.e. takes a form of the (1,1) cluster. Note that such an assumption is a kind of simplification since during an implantation a kind of SDF of He-vacancy clusters has to be formed. However the clusters produced normally via pre implantation are very small and practically this SDF is not measured. Thus for the sake of simplicity it looks reasonable to use the initial condition given by the third Eq. (43). Note that the calculations of type presented in this work can be easily carried out taking into account an arbitrary initial SDF. Moreover in principle a SDF produced during pre implantation can be calculated by using the same type of calculations.

5. RESULTS AND DISCUSSION

In the calculations a nickel type of metal is considered under irradiation with the parameters close to that taking place in fast breeder reactors. The set of main parameters used in the calculations is given in the Table 1.

Table 1. Parameters used in the calculation.

Temperature, T	473-973K
NRT displacement rate, G_{NRT}	10^{-6} dpa/s
Recombination fraction, ε_v	0.75
Fraction of crowdions, ε_i^g	0; 0.1
Effective displacement rates, $G_v=G_i+G_g= G_{NRT}(1-\varepsilon_r)$	2.5 *10^{-7} dpa/s
Helium generation rate, G_{He}	(1 -100) ppm/dpa
Recombination coefficients, $\mu_R = \mu_R^{He}$	5.0*10^{+20} m^{-2}
Atomic volume, Ω	1.205*10^{-29} m^{-3}
Vacancy diffusion coefficient, D_v	
pre-exponent coefficient	1.0*10^{-06} m^2/s
migration energy	1.10 eV
SIA diffusion coefficient, D_i	
pre-exponent coefficient	1.0*10^{-08} m^2/s
migration energy	0.15 eV
He diffusion coefficient, D_{He}	
pre-exponent coefficient	1.0*10^{-08} m^2/s
migration energy	0.15 eV
Dislocation density, ρ_d	10^{13} m^{-2}
Free surface energy, γ	(1 – 2)* *10^3 mJ/ m^2
Dislocation capture efficiency for vacancies, Z_v	1.00
Dislocation capture efficiency for SIAs, Z_i	1.25
Dislocation capture efficiency for He atoms, Z_{He}	0
Rate of radiation resolution, A	0

5.1. Homogeneous nucleation

In the case of absent of gas impurities the nucleation of 3-D vacancy clusters occurs via so called homogeneous mechanism, which has been developed in great details (see e.g. [29]-[31]). Gas-assistant mechanism of the nucleation operate simultaneously with the previous one thus in order to emphasize the He effect on the nucleation and growth of the clusters it is useful to present a brief description of the process in the limiting case when there are not He atoms in irradiated material, which is described by the equations given above at $C_{He}^{\mathrm{Im}} = 0,\ G_{He} = 0$.

As can be seen from Eq. (33) the surface energy γ is the main parameter at m=0, which controls the binding energy $E_b(x, m = 0)$. The value of γ in Ni is somewhat close to 2000 mJ/m^2 and slightly depends on temperature [31] but in some cases (see e.g. [31]) it has been taken to be essentially lower (e.g. 1000 mJ/m^2 [7]). To illustrate an

influence of the parameter γ on the nucleation of the clusters in the following the value γ is chosen to be in a range of 1000 -2000 mJ/m^2. The corresponding binding energy in the case m=0 is presented in Fig. 1. As can be seen from the plot the binding energy $E_b(x, m=0)$ essentially decreases with increase of γ that, in its turn, has to result in decrease of nucleation rate of the clusters. The calculated results illustrating such dependence are presented in Figs. 2 -6.

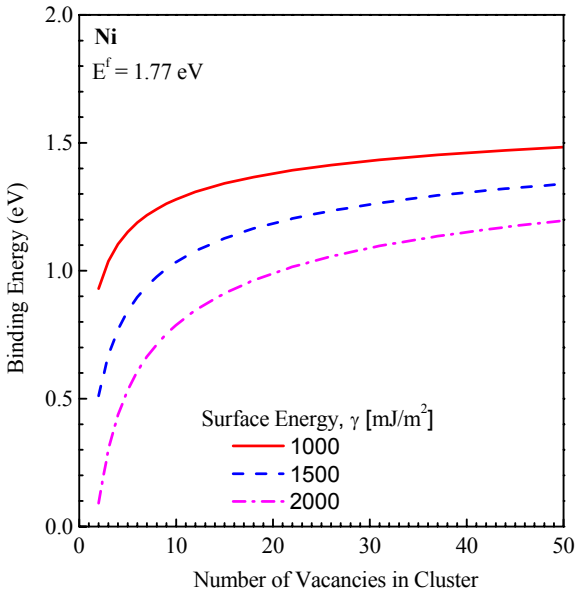

Fig. 1. The binding energy of a vacancy with voids at different values of the free surface energy.

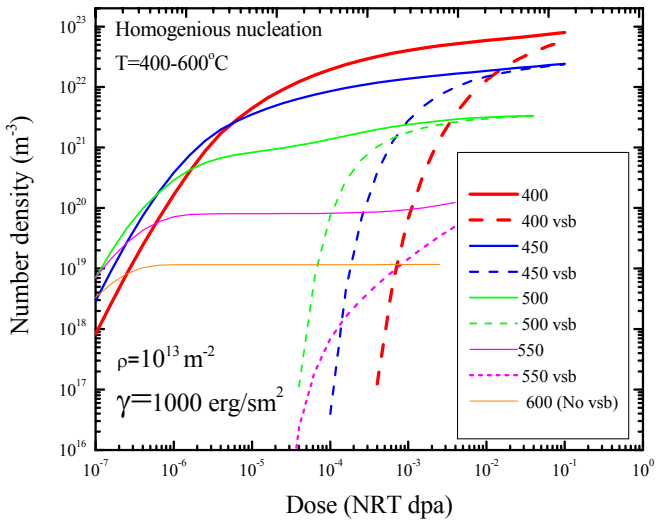

Fig. 2. Dose dependence of total number density of void under irradiation in the temperature range of 400-600°C in the case of homogeneous nucleation. The solid lines represent the total density of all vacancy clusters whereas the non-solid lines represent the total density of so called "visible" clusters, which are defined here as the cluster with the sizes of x>20. Note that there are no visible clusters at 600°C.

The dose dependence of number density of void nucleated under irradiation in the temperature range of 400-600°C and =1000 (the value γ here and in the following is measured in mJ/m^2) is presented in Fig. 2. The solid lines represent the total density of vacancy clusters whereas the non-solid lines represent the total density of visible clusters. Note that there are no visible clusters at 600°C that means the nucleation rate is equal to zero. This can be clearly seen from Fig. 3 and 4 where the dose dependence of swelling corresponding to the irradiation conditions presented on Fig. 2 and the size distribution functions calculated at 10^{-2} dpa are presented. As can be seen from Fig. 3 vacancy accumulation in the clusters is delay already at T=550°C and completely saturated at a very low level at T=600°C. The temperature dependence of the visible density of the clusters, which represent the terminal cluster density nucleated during irradiation, is presented in Fig. 5.

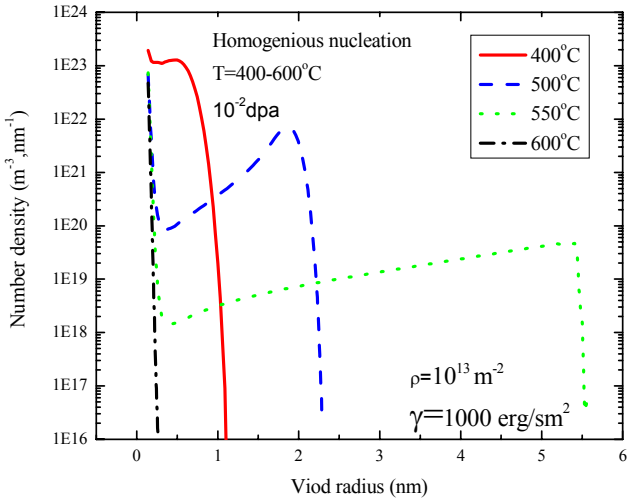

Fig. 3. Size distribution functions of the clusters at irradiation dose of 10^{-2} dpa in the case of homogeneous nucleation.

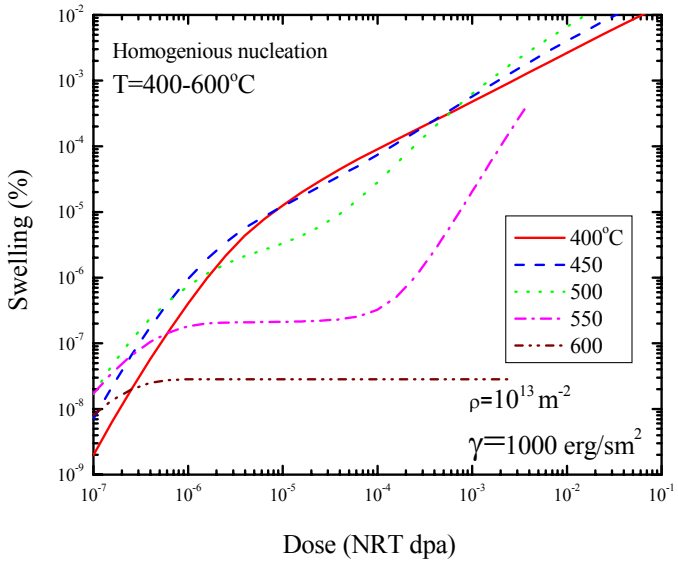

Fig. 4. Dose dependence of swelling in the case of homogeneous nucleation. Note that swelling is saturated at 600°C.

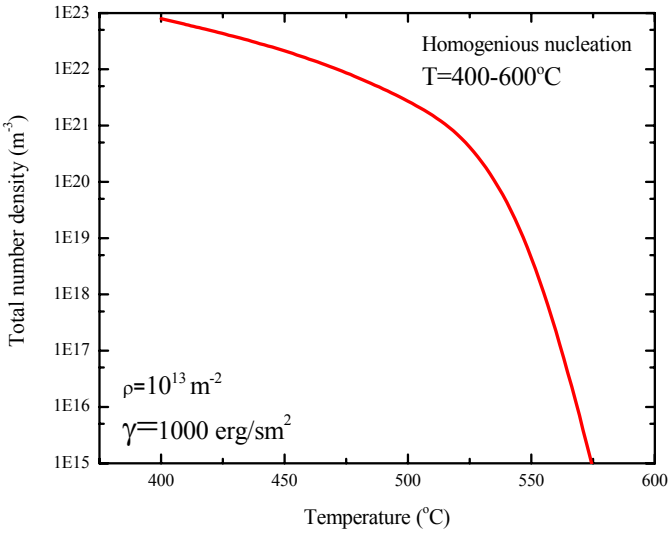

Fig. 5.Temperature dependence of the terminal cluster density in the case of homogeneous nucleation.

The dose dependence of the number density of the clusters calculated at γ=1500 and 2000 are presented in Fig. 6 and 7. As can be seen from the Fig. 2, 6 and 7 the increase of γ shifts drastically the temperature interval where the homogeneous nucleation mechanism is effective towards to low temperatures. It is shown bellow that the situation is quite different when the helium generation it taken into account.

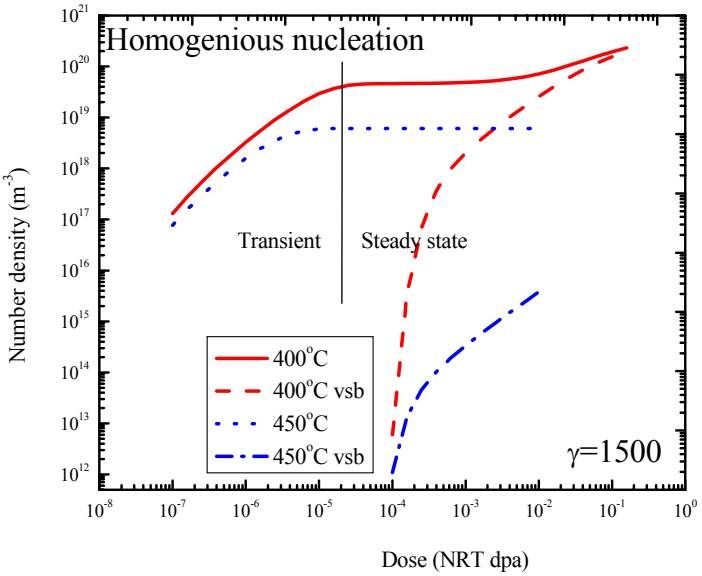

Fig. 6. Dose dependence of the cluster density in the range of 400° - 450°C at $\gamma = 1500$ in the case of homogeneous cluster nucleation. Note that the vertical line marks the beginning of the steady state for point defect concentrations.

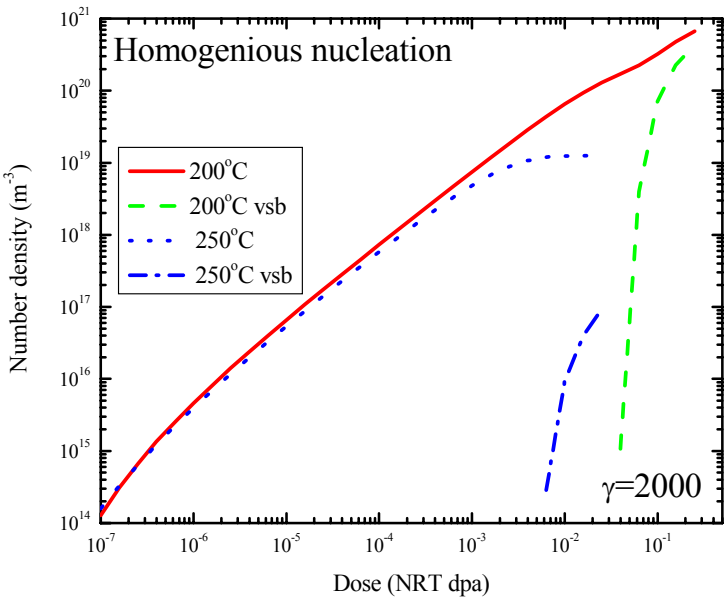

Fig. 7. Dose dependence of the cluster density in the range of 200°-250°C at $\gamma = 2000$ in the case of homogeneous cluster nucleation..

5.2. Evolution of helium-vacancy clusters

Binding energy

As can be seen from Eq. (33) the binding energy of vacancies with a cluster s increases in the case when He atoms filled in the cluster. The binding energy calculated by using EOS described by Eq. (35) as a function of *x* and *m* at different temperatures and values of the surface energy, γ , is shown in Fig.8a -8c. In Figs. 8a and 8b the binding energy is presented for the lowest value of the surface energy of γ=1000 at 300° and 600°C, respectively. It can be seen (see the projections on *x,m* plane) that the binding energy is slightly increased with increasing temperature that is related to an increase of the pressure produced by the gas atoms inside of the clusters. On the other side as can be seen from Figs. 8b and 8c the binding energy is essentially decreases with increase of the surface energy from 1000 to 2000. Note that for the sake simplicity the value of the binding energy for the clusters presented in Figs. 8 are taken to be equal to E_v^f when it is larger than the formation energy of vacancy, E_v^f , since there are no difference between those clusters which obey the inequality $E_b(x,m) \geq E_v^f$ in respect of their ability to evaporate vacancies (all of them are practically thermally stable at temperatures of interest). Note that the function $E_b(x,m)$ calculated by using EOS (34) is very close to that presented in Figs. 8.

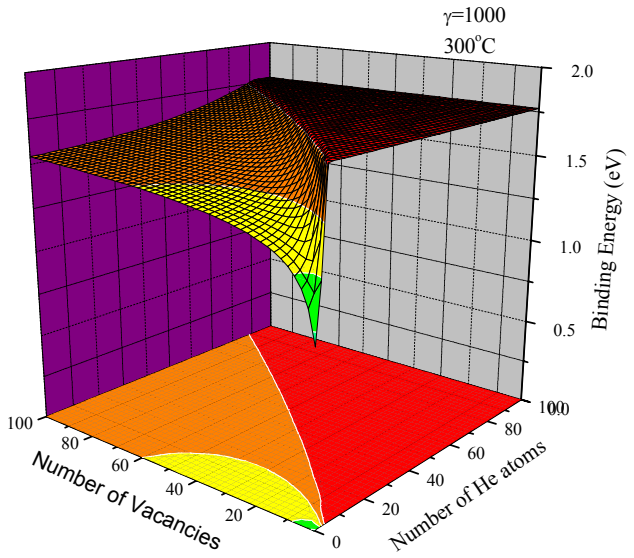

Fig. 8a.The binding energy of a vacancy with He-vacancy clusters at T=300°C and γ= 1000.

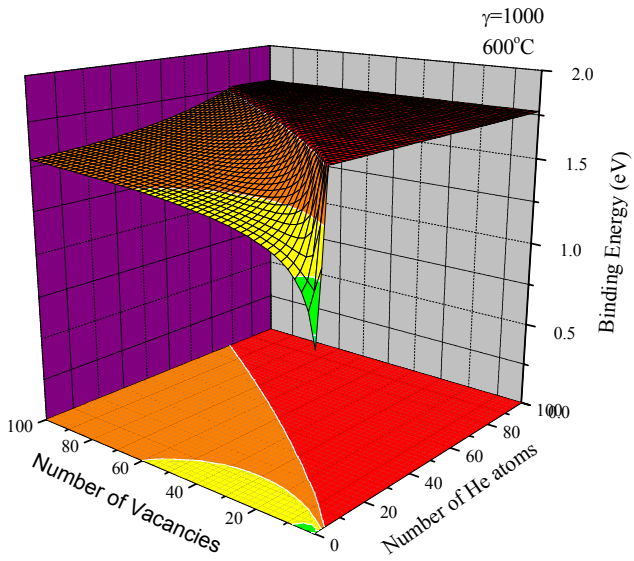

Fig. 8b.The binding energy of a vacancy with He-vacancy clusters at T=600°C and γ= 1000.

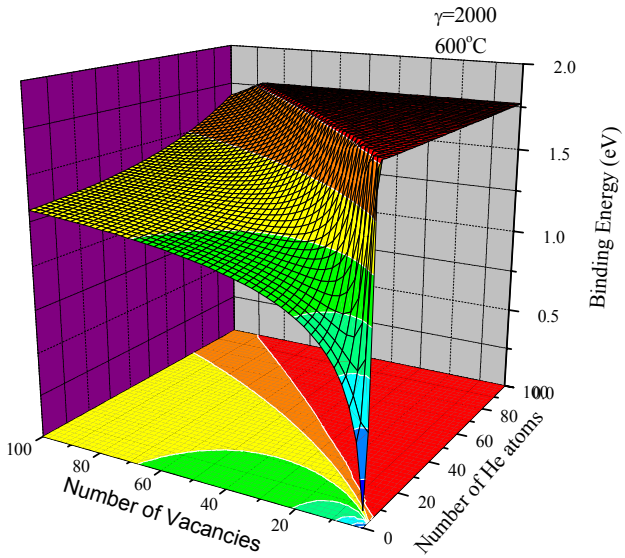

Fig. 8c.The binding energy of a vacancy with He-vacancy clusters at T=600°C and γ= 2000.

Cluster evolution under irradiation

The cluster evolution, which takes place under irradiation, depends on material parameters on one side and irradiation conditions on another side. Full scale study of the process is a complicated problem and it is not the issue for the present work. As it already has been emphasized the main objective here is to present some preliminary results of He-vacancy cluster evolution obtained by using the grouping method developed. For the sake of simplicity in the following the results calculated in the framework of the standard rate approach for a particular case, when He atoms are generated concurrently with point defects and $C_{He}^{\mathrm{Im}} = 0$, are presented only.

It has been shown above the homogeneous mechanism void nucleation is failed at high temperatures. In the case of γ=1000 (see Fig. 2) the homogeneous nucleation does not occur already at T=600°C. Thus one may conclude that the cluster nucleation at T=600°C in the case when generation of He atoms takes place occurs due to formation of He-vacancy clusters. Due to the reason this temperature is chosen for the calculations and the results obtained are presented below.

Figure 9 shows the dose dependence of the total number density ($x \geq 1$ excluding vacancy concentration) and density of visible clusters ($x > 20$) of the clusters, N_{vis}, obtained by the calculations for three different He generation rates, namely 1, 10 and 100 ppm/dpa. For a comparison the total number density calculated in the case of homogeneous nucleation is also presented. As can be seen nucleation of the clusters occurs practically in the pure homogeneous way at low doses, when number of He atoms generated is small. However already at a dose of order of 10^{-6} dpa the gas atoms start to accelerate the cluster formation providing finally nucleation of the visible clusters, which are stable and grow at the irradiation conditions considered. Stability of the clusters can be clearly seen on Fig. 10 where the dose dependence of swelling is presented. Thus one can conclude that generation of gas atoms leads to increase of the upper temperature limit for the nucleation that is shown in Fig. 11.

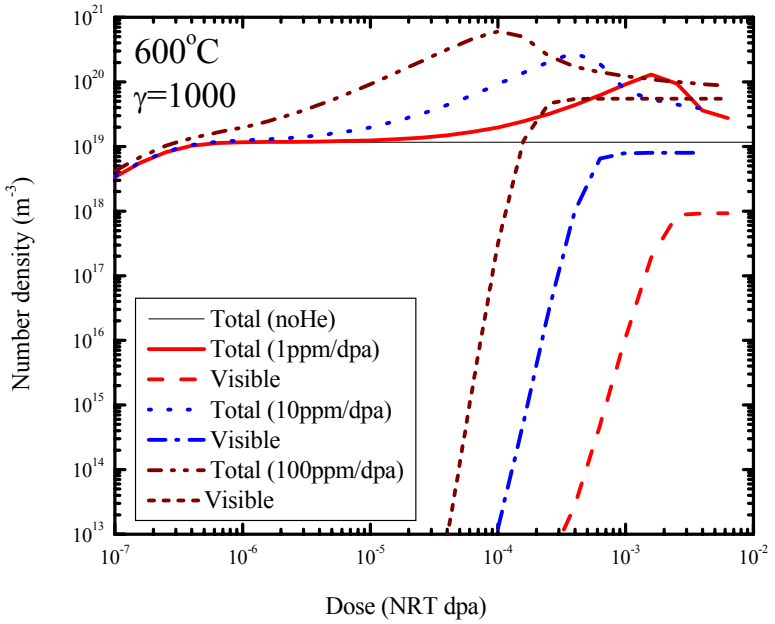

Fig. 9. Dose dependence of the cluster density at different He generation rates under irradiation at 600°C. Note that the curve drown by the thin line corresponds to the total cluster density in the case of homogeneous nucleation.

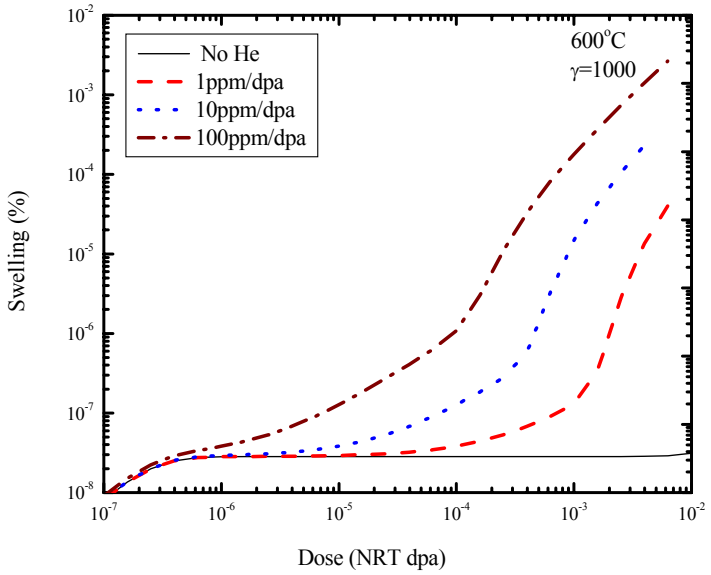

Fig. 10. Dose dependence of swelling at different He generation rates under irradiation at 600°C. Note that the curve drown by the thin line corresponds to the swelling in the case of homogeneous nucleation.

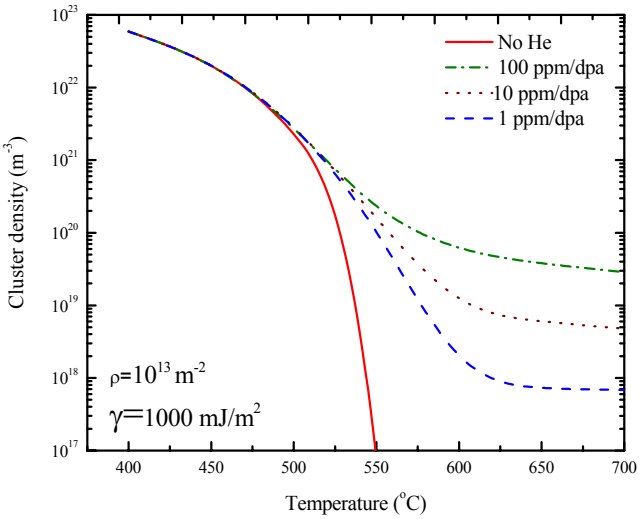

Fig. 11. Temperature dependence of the cluster density under irradiation in the temperature range of 400-600°C. The solid curve corresponds to the homogeneous nucleation, the other curves correspond to the cases of the He generation rates G_{He}=1, 10 and 100 ppm/dpa.

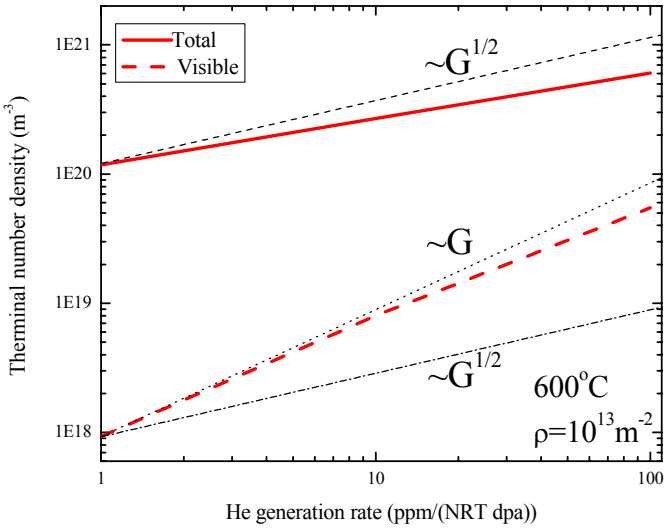

Fig. 12. Dependence of the cluster density on the He generation rate under irradiation at 600°C. Note that the solid line corresponds to a maximum of the total number density of the clusters.

Figure 12 shows the dependence of the cluster density on the He generation rate, where the thick solid and dashed lines correspond to a maximal value of the total number density and number density of the visible clusters, respectively (see Fig. 9). As can be seen the maximal magnitude of the total number density increases with the generation rate increase with increasing the generation rate G_{He} . However the increase is rather week (less than that of the square root (see the upper thin line)). In contrast the number density of visible clusters increases much strongly being very close to that described by the linear one (the corresponding linear and square root dependences are also shown on the plot). Thus one can conclude that the dependence $N_{vis}(G_{He})$ that agrees quite well with that predicted by Trinkaus [12, 13].

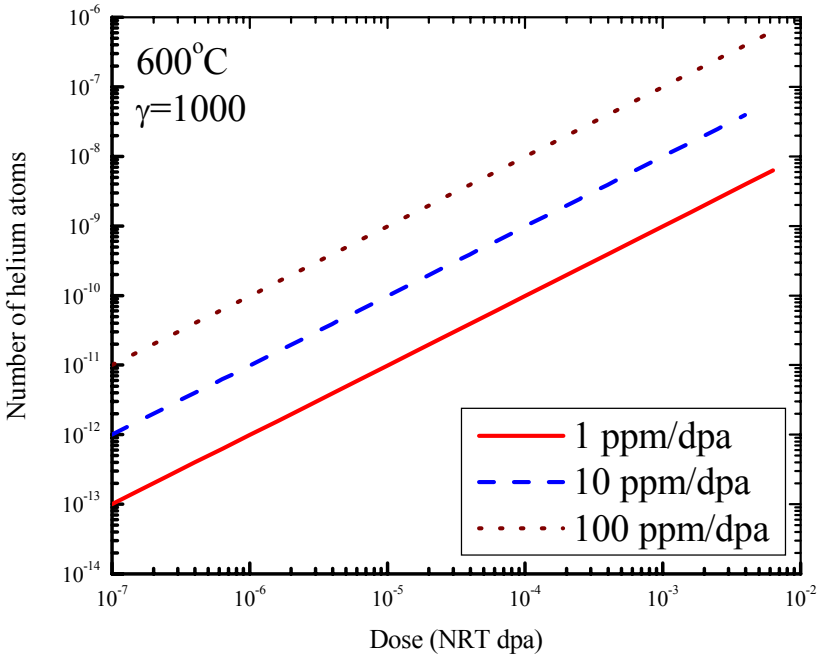

Fig. 13. Dose dependence of total number of He atoms accumulated in crystal calculated at different He generation rates under irradiation at 600°C.

It is worthy to emphasize again that the group method developed in this work provides conservation of the totals number density of the clusters and the total number of point defects (vacancies and He atoms) accumulated in the clusters. An example of this can be seen in Fig. 13 where the dose dependence of the total number of He atoms accumulated in crystal, i.e. the value $M(t) = \sum_{x=1}^{\infty}\sum_{m=1}^{\infty} mf(x,m,t) + C_{He}(t)$, is presented. As can be seen in all cases considered the magnitude $M(t)$ is linear increased with dose increase as it has to be when He atoms are generated with constant rate.

As can be seen from Fig. 9 nucleation of the stable clusters occurs faster at higher magnitude of the He generation rate. Such a behavior takes place because it is necessary to accumulate a certain concentration of He atoms to provide the nucleation process, what requires different irradiation doses at different magnitudes of the He generation rates. Correspondingly an evolution of SDF of the clusters is quite different in the cases considered that can be seen on Figs. 14 where the SDF calculated with different He generation rates after irradiation to a dose of 10^{-3} dpa are presented. As can be seen from Fig.14a the evolution of the clusters at the lowest rate of G_{He}=1 ppm/dpa is still at the nucleation stage (maximum of SDF is still located at the smallest sizes) whereas at higher rates G_{He} it already corresponds to the growth stage (Figs. 14b and 14c). Note that the variation in the number of He atoms in the clusters (the width of SDF in *m*-space) is less in the case of the highest generation rate, i.e. at $G_{He} = 100\ ppm/dpa$.

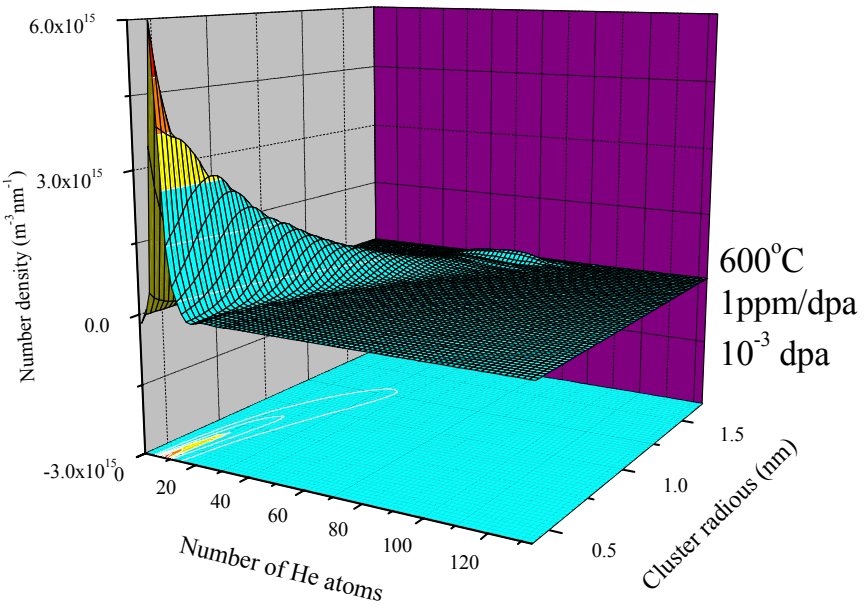

Fig. 14a. Size distribution function of the clusters at 10^{-3} dpa for the case of $G_{He} = 1\ ppm/dpa$.

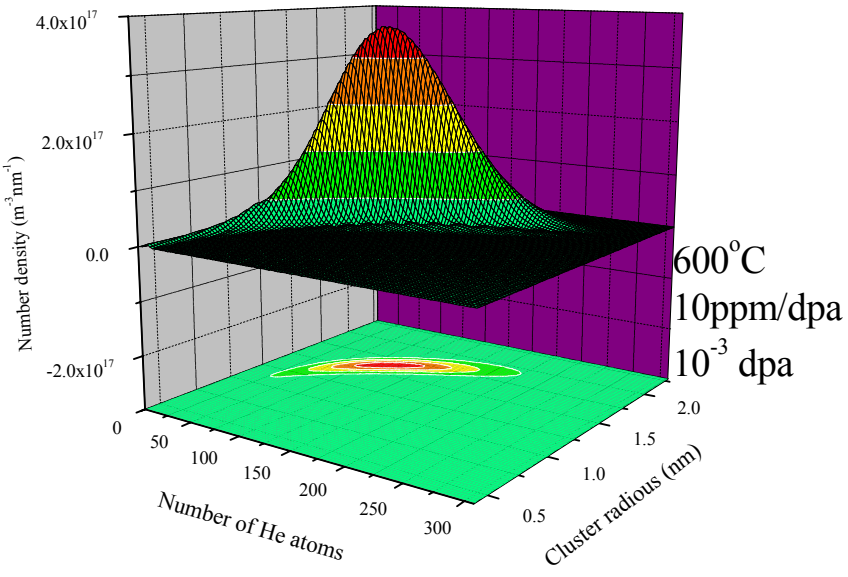

Fig. 14b. Size distribution function of the clusters at 10^{-3} dpa for the case of $G_{He} = 10\ ppm/dpa$.

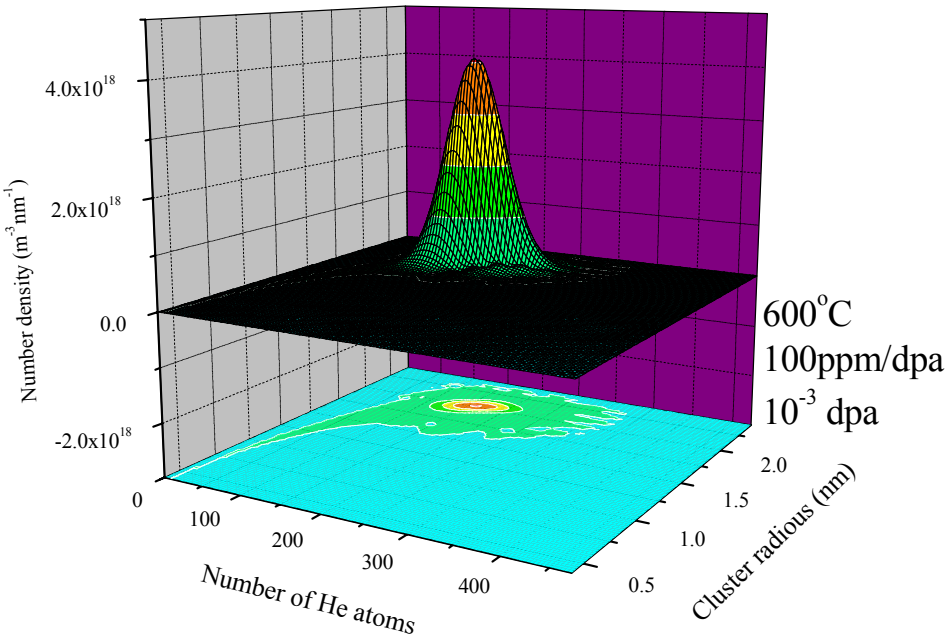

Fig. 14c. Size distribution function of the clusters at 10^{-3} dpa for the case of $G_{He} = 100\ ppm/dpa$.

The EOS effect

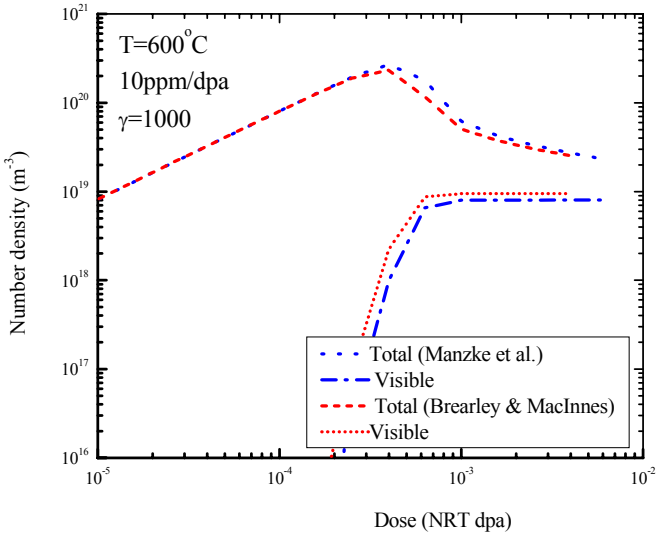

Fig. 15. Dose dependence of the cluster density calculated at 600°C and $G_{He} = 10\ ppm/dpa$ by using equation of state of He given by Eqs. (34) and (35).

All results presented above are obtained by using the equation of state of He derived by Manzke et al. (see Eq. (35)). Fig. 15 shows a comparison between the results obtained for the dose dependence of the cluster density calculated at $G_{He} = 10\ ppm/dpa$ by using the EOSs given by Eqs. (34) and (35). As can be seen the hard sphere EOS leads to a slightly higher density of the visible clusters since the hard sphere EOS provide higher stability of the clusters compare to that obtained by using the EOS described by Eq. (35). The results obtained for other values of the He generation rates are similar. Note that the total number density of the clusters obtained by using Eq. (35) is higher compare to that obtained by using the hard sphere EOS in contrast to that taking place for the visible ones.

Surface energy effect

As it has been shown above the free surface energy, γ, plays a crucial role in the case of homogeneous cluster nucleation. In order to test sensitivity of the cluster evolution to γ under irradiation with concurrent generation of He atoms the cluster evolution has been calculated for three values of γ at He generation rates to be equal 10 and 100 ppm/dpa. The results calculated are presented on Figs. 16. As can be seen at both generation rates the number density of visible clusters decreases with increasing magnitude of free surface energy however the effect is rather small. Note that similar to that found in the calculations with different EOS (see Fig. 15) the total number density of the clusters obtained in the case of the most stable clusters (γ=1000) is lower compare to that obtained in the case of when the clusters are less stable (γ=1500 and 2000).

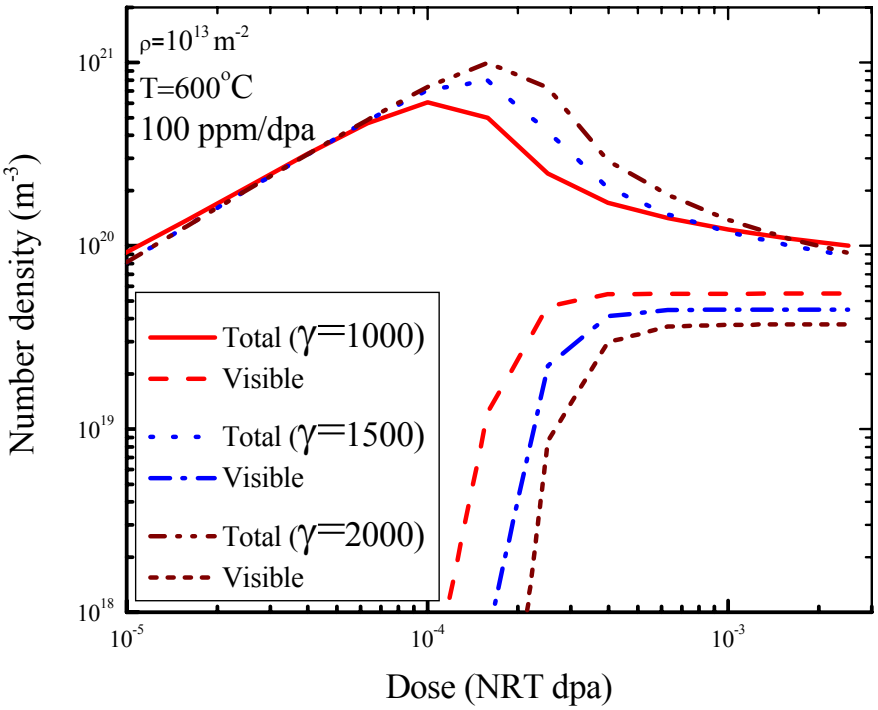

Fig. 16a. Dose dependence of the cluster density under irradiation at $G_{He} = 100\,ppm/dpa$ calculated for different values of the surface energy.

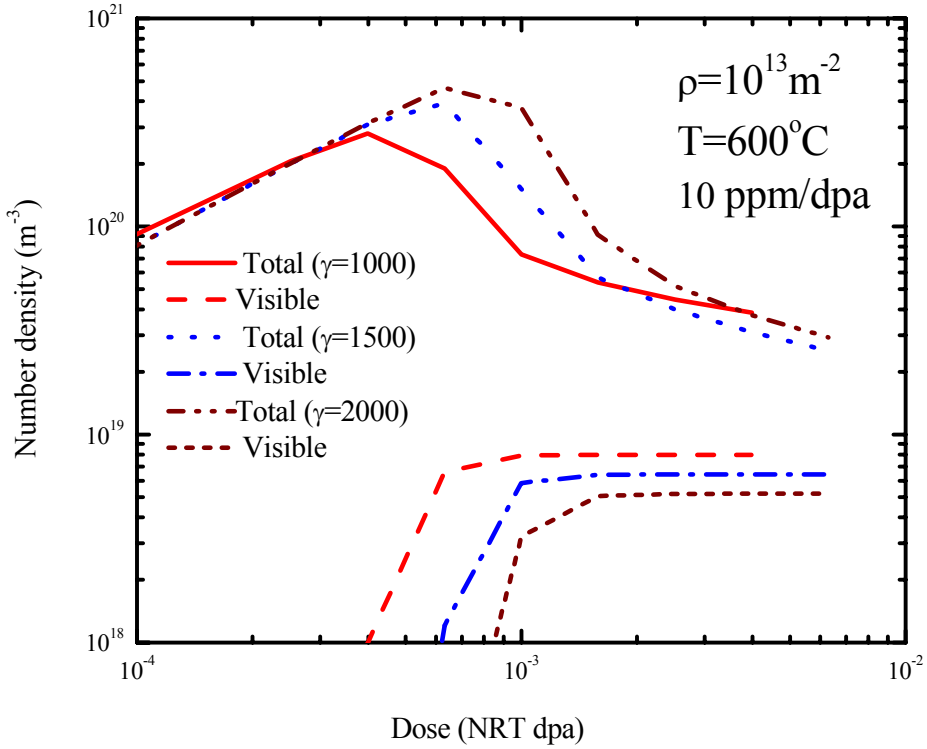

Fig. 16b. Dose dependence of the cluster density under irradiation at $G_{He} = 10\ ppm/dpa$ calculated for different values of the surface energy.

.

CONCLUSIONS

1. A new grouping method for an approximate solution of two dimensional kinetic equations describing evolution of point defect clusters is developed. It is shown that the method can be easily generalized to solve a kinetic equation of highest dimensionality. An ability of the method is demonstrated describing an evolution of helium–vacancy clusters under irradiation.
2. Preliminary results of the calculations of evolution of helium–vacancy clusters under irradiation are presented for a case when: (a) a concurrent generation of He atoms taking place with different rate in the range of 1-100 ppm/dpa, (b) the sink strength of defects others than the cluster is constant with dose. The results calculated are compared with those obtained in the case when there is no He generation.
3. It is found that the terminal cluster is very close to linear in the He generation rate. It is also shown that in the case of He assisted evolution of vacancy clusters: (a) nucleation of the clusters is not very sensitive to the value of surface energy in contrast to that taking place when the homogeneous nucleation operates, (b) The so called hard sphere equation of state of He [27] and that derived by Manzke et al. [28] lead to quite similar results for He-vacancy cluster evolution.

REFERENCES

1. M. Kiritani, J. Phys. Soc. Japan 35 (1973) 95.
2. S.I. Golubov, A.M. Ovcharenko, A.V. Barashev, and B.N. Singh, Philos. Mag. Series A. 81, No.3 (2001) 643-658.
3. K. Russell, Acta Metall. 19 (1971) 753.
4. K. Russell, Scripta Metall. 6 (1972) 209.
5. K. Russell, Scripta Metall. 7 (1973) 755.
6. K. Russell, The theory of void nucleation in metals, Acta Metall. 26 (1978) 1616.
7. S.I. Maydet and K. Russell, Numerical simulation of void nucleation in irradiated metals, J. Nucl. Mater. 82 (1979) 271.
8. J.L. Katz and H. Wiedersich, J. Nucl. Mater. 46 (1973) 41.
9. H. Wiedersich, J.J. Barton and J.L. Katz, J. Nucl. Mater. 51 (1974) 287.
10. B.T.M. Loh, Acta Metall. 20 (1972) 1305.
11. H. Trinkaus, J. Nucl. Mater. 118 (1983) 39.
12. H. Trinkaus, J. Nucl. Mater.133&134 (1985) 105;
13. H. Trinkaus, Radiation Effects. 101 (1986) 101.
14. A.J.E. Foreman and B.N. Singh, J. Nucl. Mater. 141 - 143 (1986) 672.
15. H. Trinkaus, B.N. Singh and A.J.E. Foreman, J. Nucl. Mater. 174 (1990) 80.
16. B.N. Singh and H. Trinkaus, J. Nucl. Mater. 186 (1992) 153.
17. B.N. Singh and A.J.E. Foreman, The Physics of Irradiation Produced Voids (ed. By R.S. Nelson) HMSO, London (1975) p.205.
18. B.N. Singh and A.J.E. Foreman, J. Nucl. Mater. 122&123 (1992) 537.
19. A.J.E. Foreman, Harwell Rep. AERE-R 8389.
20. N. Ghoniem, H. Gurol, Radiation Effects 55 (1981) 209
21. N. Ghoniem, S. Sharafat, J.M. Williams, and L.K. Mansur, J. Nucl. Mater. 117 (1983) 96.
22. S. Sharafat, N. Ghoniem, UCLA/ENG-8947 (1989) PPG-1225.
23. S. Sharafat, N. Ghoniem, J. Nucl. Mater. 122 (1-3) (1984) 531.
24. R.E. Stoller and G.R. Odette, J. Nucl. Mater. 131 (1985) 118.
25. A.M. Ovcharenko S.I. Golubov, C.H. Woo, Hanchen Huang, GMIC++: Grouping method in C++: an efficient method to solve large number of Master equations, Computer Physics Communications (in press).
26. Singh B.N., Golubov S.I., Trinkaus H., Serra A., Osetsky Yu.N., Barashev A.V., J. Nucl. Mater., 251 (1997) 107-122.
27. I.R. Brearley and D.A. MacInnes, J. Nucl. Mater. 95 (1980) 239.
28. R Manzke, W. Jäger, H. Trinkaus, G. Crecelius, and R. Zeller, Solid State Communications 44, No.4 (1982) 481.

10. DOSIMETRY, DAMAGE PARAMETERS, AND ACTIVATION CALCULATIONS

No contributions.

11. MATERIALS ENGINEERING AND DESIGN REQUIREMENTS

No contributions.

12. IRRADIATION FACILITIES AND TEST MATRICES

No contributions.